



Patrick Bottke, Dipl.-Chem.

ZUR LITHIUM–SELBSTDIFFUSION IN
KRISTALLINEN FESTKÖRPERN

—

Die Detektion von extrem langsamen und schnellen
Diffusionsprozessen mittels Kernresonanzspektroskopie

D I S S E R T A T I O N

zur Erlangung des akademischen Grades

Doktor der Naturwissenschaften (Dr. rer. nat.)

eingereicht an der

Technischen Universität Graz

Betreuer

Univ.-Prof. Dr. Martin Wilkening

Institut für Chemische Technologie von Materialien

Graz, August 2015

Eidesstattliche Erklärung

Ich erkläre an Eides statt, dass ich die vorliegende Arbeit selbstständig verfasst, andere als die angegebenen Quellen/Hilfsmittel nicht benutzt, und die den benutzten Quellen wörtlich und inhaltlich entnommenen Stellen als solche kenntlich gemacht habe. Das in TUGRAZonline hochgeladene Textdokument ist mit der vorliegenden Dissertation identisch.

Datum

Unterschrift

Kurzfassung

Eine der wichtigsten Aufgaben unserer Gesellschaften ist es, Konzepte und Systeme zur Speicherung von elektrischer Energie aus erneuerbaren Quellen bereitzustellen. In Anbetracht der aktuellen Entwicklung von elektrochemischen Energiespeichersystemen sehen wir uns einer der größten Herausforderungen seit Jahrzehnten gegenübergestellt. Da die Leistungsfähigkeit von Lithium-Ionen-Batterien eng mit den Transporteigenschaften des Ions Li^+ verknüpft ist, sind grundlegende Untersuchungen von Li-Sprungraten und Li-Aktivierungsenergien entscheidend bei der Entwicklung von neuen Elektrodenmaterialien und Elektrolyten. Neben Materialien die direkt in Batterien genutzt werden können, sind Modellspezies zum besseren Verständnis der Ionen(selbst-)diffusion besonders hilfreich. Sie ermöglichen einen vorzüglichen Einblick in die Komplexität des Ionentransports in Festkörpern, die sich durch verschiedene Morphologien auszeichnen. Dabei sind Methoden, die in der Lage sind Sprungprozesse auf atomarer Ebene zu beobachten, zu solchen, die sensitiv für makroskopischen Ladungstransport sind, die ideale Ergänzung, um ein möglichst komplettes Bild der *bulk*-Dynamik zu erhalten. In dieser Hinsicht bietet die Kernresonanzspektroskopie wesentliche Vorteile gegenüber anderen Methoden, insofern, dass die Ionenbeweglichkeit im Kristallgitter beobachtet wird und die Einflüsse von Oberfläche, Korngrenzen und kristallographischen Phasengrenzen vernachlässigbar sind. Die vorliegenden Ergebnisse sind zum großen Teil an den Leitmotiven der DFG Forschergruppe 1277 „Mobilität von Lithium-Ionen in Festkörpern“ ausgerichtet, die sich u. a. folgenden Themen widmet: i) langsame Li-Bewegung, ii) Li-Diffusion in nanokristallinen Materialien, iii) Li-Diffusionspfade, iv) Dimensionalitätseffekte.

Die Doktorarbeit zeigt, wie Li-NMR *time domain*-Methoden und hochauflösende Techniken genutzt werden können, um lokale Strukturen zu charakterisieren und diese mit den zugrundeliegenden Ionensprüngen zu korrelieren. Die studierten Materialien umfassen dabei Festkörper mit extrem guter bis hin zu sehr schlechter Ionenleitfähigkeit. In den Rahmen dieser Arbeit gehörte insbesondere die eingehende Untersuchung der Li^+ -Diffusivität von Anodenmaterialien basierend auf TiO_2 , wie z. B. Anatas mit mesoporöser Form und als Nanoröhre. Während ultralangsamem Li-Austausch im Li_2ZrO_3 erfolgreich mit 2D- ^6Li -MAS-NMR nachgewiesen werden konnte, wurden zahlreiche, zueinander komplementäre *time domain*-Methoden angewendet, um Informationen über die extrem schnellen Li-Austauschprozesse in oxidischen Granaten, wie z. B. $\text{Li}_{6,5}\text{La}_3\text{Zr}_{1,75}\text{Mo}_{0,25}\text{O}_{12}$, zu erhalten. Granate werden gegenwärtig als Festkörperelektrolyte für Lithium-Ionen-Batterien in Betracht gezogen. Im Fall des LLZMO konnten mit Hilfe von ^7Li stimulierter Echo NMR

zusätzlich die Li-Migrationspfade und der Beitrag des $24 d \leftrightarrow 96 h$ -Sprungs zur insgesamt sehr hohen Leitfähigkeit des Materials erfasst werden. Für Li_2ZrO_3 , auf der anderen Seite, war es möglich, die niedrigsten Diffusionskoeffizienten, die jemals durch 2D-EXSY-NMR gemessen wurden, zu bestimmen und mit Werten aus der Leitfähigkeitsspektroskopie zu bestätigen. Die beiden Beispiele veranschaulichen die Möglichkeiten der NMR zum Studium der Ionendynamik mit Sprungraten vom Sub-Hz-Regime bis zum GHz-Bereich. In allen Fällen konnten sehr zuverlässig mikroskopische Aktivierungsenergien oder Li Sprungraten bestimmt werden. Derartige Untersuchungen werden helfen, neue Materialien im Hinblick auf ihre Anwendungsmöglichkeiten in einer lithiumbasierten Batterie mit Insertionsmaterialien oder einer reinen Festkörper-Lithium-Batterie zu entwickeln bzw. anzupassen.

Abstract

One of the most important topics of our modern society is to develop concepts and devices to store electric energy from renewable sources. Considering the development of electrochemical energy storage systems we are currently faced with one of the largest challenges since decades. Considering rechargeable lithium-based batteries the performance is tightly linked with Li^+ ion transport properties. Thus, basic research focusing on the measurement of jump rates and activation energies is definitely needed to support the development of advanced electrode materials and electrolytes. Besides materials that can be directly used as in batteries, ionic (self-)diffusion phenomena can be best understood with the help of suitable model compounds. They can greatly help gaining insights into the complexity of ion transport in solids with different morphologies. Additionally, the use of methods that are capable to monitor jump processes from an atomic-scale point of view complement those being sensitive to macroscopic, long-range ion transport. In this respect nuclear magnetic resonance (NMR) spectroscopy offers some advantages over other methods in that it probes bulk ion dynamics and is therefore not affected by surface effects, grain boundaries or crystallographic phase boundaries. The present PhD thesis was part of the DFG Research Unit 1277 “Mobile Li Ions in Solids” that focusses on the following (selected) Leitmotifs: i) slow Li motions, ii) Li diffusion in nanocrystalline materials, iii) Li diffusion pathways, iv) dimensionality effects.

The thesis shows how Li NMR time domain methods and high-resolution techniques can be used to probe local structures and to study the associated elementary steps of ion hopping. The model compounds chosen comprise extremely good as well as very poor ion conductors. This also included, for instance, the in-depth study of Li^+ diffusivity in TiO_2 -based anode materials such as mesoporous Li_xTiO_2 and anatase nanotubes. While ultraslow Li exchange was successfully probed in Li_2ZrO_3 by means of high-resolution 2D ^6Li MAS NMR, several time domain methods were applied to collect information on very fast ion exchange in oxide garnets such as $\text{Li}_{6.5}\text{La}_3\text{Zr}_{1.75}\text{Mo}_{0.25}\text{O}_{12}$ being currently considered as solid electrolytes in Li-based batteries. In the case of LLZMoO 7Li stimulated echo NMR was used to directly follow the Li migration pathway and to show that the Li sites $24d$ and $96h$ do participate in ion hopping. For Li_2ZrO_3 , on the other hand, it was possible to record one of the lowest diffusion coefficients ever reported by exchange NMR. The two examples illustrate the possibilities by NMR to measure ion dynamics with rates from the sub-Hz regime up to the GHz range. In each case, reliable microscopic activation energies or Li jump rates were probed. This greatly helped understand the materials in view of their applications in batteries taking advantage of mobile Li ions.

Der Glaube ist zum Ruhen gut,
Doch bringt er nicht von der Stelle.
Der Zweifel in ehrlicher Männerfaust,
Der sprengt die Pforten der Hölle.

Theodor Storm
Der Zweifel

In Gedenken an

Jutta Bottke (geb. Barembruch)

★ 11. Mai 1955 † 15. Februar 1993

und für

Marlene (geb. Freese)

★ 19. Juni 2013

Inhaltsverzeichnis

Vorwort	xv
Einleitung und Motivation	1
1 Grundlagen: Diffusion in Festkörpern und spektroskopische Methoden	3
1.1 Festkörper-NMR-Spektroskopie	6
1.1.1 NMR-Spin-Gitter-Relaxation	10
1.1.2 Quadrupolare NMR-Spin-Gitter-Relaxation	12
1.1.3 BPP-Modell nach BLOMBERGEN, PURCELL and POUND	15
1.1.4 Strukturelle Unordnung und niederdimensionale Diffusion	17
1.2 Impedanzspektroskopie	22
1.2.1 Grundlagen	22
1.2.2 Leitfähigkeitsspektren	23
2 Experimentelles: Techniken, Geräte und Synthesewege	25
2.1 Kernresonanzmethoden und Ausstattung	26
2.1.1 Relaxometrie	26
2.1.2 SAE NMR	29
2.1.3 1D MAS und 2D EXSY MAS NMR	31
2.2 Impedanz- und Leitfähigkeitsspektroskopie	34
2.3 Synthese von Titandioxid Nanoröhren [TiO ₂ (nt)] mit Anatas-Modifikation	34
2.4 Lithium-Interkalation – chemisch und elektrochemisch	36
2.5 Elektrochemische Charakterisierung	38
3 Ergebnisse: Zur Li-Diffusion in kristallinen Festkörpern	41
3.1 Hochauflösende ^{7,6} Li NMR	42
3.1.1 P1 <i>Ultraslow Li Exchange Processes in Diamagnetic Li₂ZrO₃ As Monitored by EXSY NMR</i>	43
3.1.2 Leitfähigkeitsmessungen an mikro- und nanokristallinem Li ₂ ZrO ₃	49
3.1.3 1D/2D ^{7,6} Li MAS NMR an paramagnetischen Kathodenmaterialien	52
3.1.4 P2 <i>Low-Temperature Synthesis, Characterization, and Stability of Spinel-Type Li₂NiF₄ and Solid-Solutions Li₂Ni_{1-x}Co_xF₄</i>	54

3.1.5	P3 <i>Synthesis of ternary transition metal Fluorides Li_3MF_6 via a sol-gel route as candidates for cathode materials in lithium-ion batteries</i> . . .	63
3.1.6	2D ^6Li MAS EXSY NMR an $\beta\text{-Li}_3\text{VF}_6$	72
3.2	Li-Diffusion in Titandioxiden und Titanaten	76
3.2.1	P4 <i>Li ion dynamics in TiO_2 anode materials with an ordered hierarchical pore structure – insights from ex situ NMR</i>	78
3.2.2	TiO_2 Anatas Nanoröhren – Synthese, Zyklenstabilität als Anode und NMR-Messungen zur Dynamik	86
3.2.3	P5 <i>Small Change—Great Effect: Steep Increase of Li Ion Dynamics in $\text{Li}_4\text{Ti}_5\text{O}_{12}$ at the Early Stages of Chemical Li Insertion</i>	95
3.3	Oxidische Granate als Festkörperelektrolyte für Lithium-Ionen-Batterien . .	106
3.3.1	P6 <i>Structure and dynamics of the fast lithium ion conductor “$\text{Li}_7\text{La}_3\text{Zr}_2\text{O}_{12}$”</i>	108
3.3.2	P7 <i>Ion dynamics in solid electrolytes: NMR reveals the elementary steps of Li^+ hopping in oxide garnets</i>	124
4	Zusammenfassung und Ausblick	141
	Literaturverzeichnis	143
	Anhang	146
A	Verwendete Computerprogramme	147
B	Konferenzbeiträge und Veröffentlichungen in Fachzeitschriften	149
B.1	Vorträge	149
B.2	Posterbeiträge	149
B.3	Veröffentlichungen in Fachzeitschriften	150
C	Lebenslauf	154

Vorwort

Das Studium von ionischen Sprungprozessen in Festkörpern nimmt eine stetig wachsende Stellung in den modernen Materialwissenschaften ein. Die in dieser kumulativen Dissertationsschrift enthaltenen Arbeiten zeigen eine Auswahl von Studien, die im Zeitraum von 2010 bis 2015 an den Universitäten Hannover und Graz entstanden sind. Unter den Kernpublikationen sind zwei veröffentlichte und eine eingereichte Arbeit.

Die Untersuchungen widmen sich der gezielten Erfassung der Dynamik und Geometrie von Li^+ -Bewegungsprozessen in kristallinen und nanostrukturierten oxidischen Festkörpern. Mit dem Methodenarsenal der Kernresonanzspektroskopie können sowohl extrem langsame als auch sehr schnelle Teilchenbewegungen studiert werden. Die Arbeiten sind eingebettet in die Thematik der Forschergruppe molife „Mobilität von Li-Ionen in Festkörpern“, die seit 2010 von der Deutschen Forschungsgemeinschaft gefördert wird. Zu den Leitmotiven von molife gehören insbesondere die Untersuchungen von langsamen Ionenbewegungen, das Studium der Li-Selbstdiffusion in meso- und nanostrukturierten Ionenleitern und die Erfassung schneller Diffusionsprozesse.

Meine Arbeiten zur Dissertation begannen im Teilprojekt 7 der FOR 1277 „Nanostrukturierte Ionenleiter“; im Laufe der Promotionszeit sind auch die anderen Themen der Forschergruppe in meinen Interessensmittelpunkt gerückt. Mit dem Wechsel meines Betreuers, Martin Wilkening, von der Universität Hannover an die TU Graz, fiel auch der Aufbau einer neuen Arbeitsgruppe in die Dissertationszeit. Durch den Zugang zu neuen Geräten an der TU Graz konnte das Arbeitsthema der Dissertation noch einmal erweitert werden. Ab 2012 nahm somit der Stellenwert von anwendungsorientierten Fragestellungen im Bereich der elektrochemischen Energiespeicher zu, die über das grundlagenorientierte Fragenportfolio von molife deutlich hinausgingen. Trotzdem blieben die festkörperspektroskopischen Methoden (Kernresonanz- und Impedanzspektroskopie) während der gesamten Zeit Schwerpunkt dieser Arbeit.

Für die Möglichkeit dieser spannenden Entwicklung möchte ich ganz besonders meinem Betreuer Herrn Prof. Dr. Martin Wilkening danken. Schon in Hannover hat er mir viel Vertrauen geschenkt und seine Begeisterung für die Wissenschaft mit mir geteilt. Daraus ist nicht nur eine für diese Arbeit sehr fruchtbare Diskussionsebene entstanden, sondern auch der Wunsch, mit ihm an die TU Graz zu wechseln. Teil des Aufbaus einer neuen Arbeitsgruppe im Ausland zu sein und die feinen Unterschiede zwischen Österreich und Deutschland zu erleben, hat mir viel Erfahrung und schöne Erinnerungen beschert.

Ich möchte mich herzlich bei Herrn Prof. Dr. Hansjörg Weber für die stete Hilfsbereitschaft bei technischen Fragestellungen und die fachlichen Diskussionen in der NMR-Halle bedanken. Außerdem danke ich ihm für die Bereitschaft, die Rolle des Zweitgutachters dieser Arbeit übernommen zu haben.

Es gab aber auch viele temporäre Begleiter auf dieser langen Reise, die durch sehr willkommenen Wissensaustausch und/oder die Bereitstellung von Probenmaterial entscheidend zur Entstehung dieser Arbeit beigetragen haben. Die meisten von ihnen sind oder waren mal Mitarbeiter, aber auch ehemalige Kollegen aus Hannover oder Graz, selbst wenn Sie mit ganz anderen Themengebieten betraut waren, haben den Prozess der eigenen Promotion positiv beeinflusst.

Sehr dankbar bin ich außerdem für die herzliche Aufnahme im Arbeitskreis von Prof. Dr. P.G. Bruce und die finanzielle Unterstützung durch das PROMOS Reisestipendium des DAAD, welches meinen Aufenthalt vom 02.02. – 30.03.2011 in St. Andrews (Schottland) erst ermöglicht hat. Speziell möchte ich hier Dr. Yu Ren danken, der mir in dieser Zeit viel beigebracht hat.

Den aktuellen Arbeitskollegen gebührt selbstverständlich der selbe wissenschaftliche Dank, viel mehr möchte ich jedoch die entspannte und zugleich motivierende Atmosphäre im Arbeitskreis hervorheben, die ich immer in guter Erinnerung behalten werde.

Gute Freunde, Verwandte und die eigene Familie sind selbstverständlich die wichtigsten Personen für jeden Menschen und ich bin sehr dankbar, dass es sie alle gibt. Gordon danke ich für die Durchsicht dieser Arbeit und meiner Partnerin für die vielen Kleinigkeiten des Alltags, die man während des Schreibens aus den Augen verliert. Danke Irina. Die Erfahrung machen zu dürfen, dass einem niemand der Liebsten eine echte Hilfe beim Verfassen einer Doktorarbeit ist, verdanke ich dem Leben, welches uns außerdem eine wundervolle Tochter geschenkt hat. Herzlichen Dank dafür.

Patrick Bottke,
Graz, im August 2015

Einleitung und Motivation

Die Erschließung neuer Wege zur Energieumwandlung und -speicherung stellen die Gesellschaften des 21. Jahrhunderts vor gewaltige Herausforderungen. Um unsere Abhängigkeit von fossilen Brennstoffen zu verringern, bedarf es neuer Energiekonversions- und Energiespeichersysteme.^[1,2] Im Falle der elektrochemischen Energiespeicherung liegt der Fokus auf lithiumbasierten Systemen. Lithium ist neben Wasserstoff das leichteste nutzbare Element und somit in Festkörpern eines der schnellsten Ladungsträger.

Nur neue Materialien können für eine beschleunigte Entwicklung und damit zu einer Verbesserung der Leistungsfähigkeit von Akkumulatoren führen. Einhergehend damit müssen wir dafür Sorge tragen, dass die grundlegenden festkörperelektrochemischen Abläufe in modernen Batteriesystemen im Detail verstanden werden, um gezielt nach neuen Materialien suchen zu können bzw. diese zu entwickeln.

Kristalline und nanokristalline Li-Ionenleiter sind ein exzellentes Beispiel für die Vielfältigkeit der Herausforderungen an die modernen Materialwissenschaften. Die 1990 von Sony eingeführte Lithium-Ionen-Batterie hat unsere heutige Gesellschaft maßgeblich geprägt. Um die Mobilität von elektronischen Geräten wie Laptops und Mobiltelefonen weiter zu steigern, wurde und wird weltweit ein immenser Forschungsaufwand betrieben. Ohne die Fortschritte der letzten Jahrzehnte wären Smartphones, Tablets und Elektroautos mit praktikabler Laufzeit bzw. Reichweite jedoch weiterhin *science fiction* oder zumindest Konzeptstudien geblieben. Während konventionelle Li-Ionen-Batterien mit flüssigen, entflammaren Elektrolyten arbeiten, sind Festkörperbatterien, denen eine lange Lebenszeit und erhöhte Sicherheit zugeschrieben werden, gänzlich aus festen Komponenten aufgebaut.

Bei Elektronikbauteilen wie dem Kondensator war der Begriff *all solid state* wegen der Kapazität pro Volumen und aus Sicherheitsgründen schon lange vor den ersten Smartphones ein Qualitätsmerkmal. Im Idealfall sollen Festelektrolyte für Li-Ionen-Batterien alle Anforderungen, die ein komplexes, elektrochemisches System mit sich bringt, erfüllen. Neben einer sehr hohen Ionenleitfähigkeit und einer Li^+ -Überföhrungszahl nahe 1, muss der elektronische Isolator reproduzierbar, kostengünstig und umweltfreundlich hergestellt werden können. Zudem sollen die Durchtrittswiderstände an den Komponentengrenzen möglichst niedrig sein. Neben den außerordentlich guten Transporteigenschaften ist elektrochemische Stabilität gegenüber Li-Metall in einem möglichst großen Potentialfenster zwingend, damit die heutigen Insertionsmaterialien auf der Anodenseite durch reines Lithium ersetzt werden können.

Aber nicht nur Materialien die besonders hohe Kapazitäten ermöglichen und hohe Leitfähigkeiten mit sich bringen werden gesucht, sondern auch solche, die als Barriere für die mobilen, kleinen Ionen wie z. B. H^+ , Li^+ (s.o.), und F^- dienen.

Das genaue Studium der grundlegenden Bewegungsmechanismen der mobilen Spezies ist eine der zentralen Fragestellungen in diesen Forschungsgebieten. Belastbare Informationen, die z. B. Auskunft über lang- und kurzreichweitige Li-Ionenbewegungen geben bzw. auf Diffusionspfade hinweisen, sind außerordentlich hilfreich bei der Suche nach neuen Materialien. Hierbei sind vor allem elementspezifische Informationen über Bewegungsprozesse von entscheidender Bedeutung. Während mit Leitfähigkeitsmessungen nur unter erheblichem Aufwand zwischen unterschiedlichen Ladungsträgern unterschieden werden kann, bietet die kernmagnetische Resonanzspektroskopie Möglichkeiten die Li- und F-Bewegungen im *bulk* über einen großen Zeitbereich direkt zu erfassen.

Gemeinsames übergeordnetes Ziel der folgenden Arbeiten*, die in dieser Schrift zusammengefasst sind, ist es, Li-Ionenbewegungsprozesse in Festkörpern möglichst präzise und quantitativ in Modellsubstanzen (mit Anwendungsbezug) zu beschreiben. Insbesondere galt es absolute Sprungraten und Aktivierungsenergien zu ermitteln, die den Ionentransport in Abhängigkeit der Kristallstruktur und Morphologie der Proben bestimmen.

Dabei wurden Materialien mit extrem langsamen Li-Diffusionsprozessen (Li_2ZrO_3 , potentieller Werkstoff für Kernfusionsreaktoren), mit sehr alterungsresistenten Eigenschaften (verschiedene Modifikationen und Morphologien von Titandioxid und Titanat, als Interkalationsmaterial für Anoden von Li-Ionen-Batterien) bis hin zu Kandidaten für Festelektrolyte (Granate des Typs LLZMoO, mit sehr hoher Diffusivität) auf die Li-Dynamik untersucht. Das Methodenrepertoire erstreckte sich dabei über relaxometrische NMR-Messungen, *spin alignment echos*, 2D Austausch-Experimente und die klassische Aufnahme von (hochaufgelösten) $^{6,7}Li$ - (MAS)-NMR-Spektren und wurde durch Impedanz- bzw. Leitfähigkeitsspektroskopie sowie elektrochemische Charakterisierungsmethoden ergänzt.

* Achsenbeschriftungen der noch nicht publizierten Graphen sowie stichwortartige Erläuterungen in den Abbildungen sind in englischer Sprache. Da in den Abbildungen als Dezimaltrennzeichen der Punkt verwendet wird, wurde der Einheitlichkeit halber auch im Text auf diese Schreibweise zurückgegriffen, obwohl die Dissertation in deutscher Sprache verfasst wurde. Die in dieser Arbeit präsentierten Ergebnisse sind zum Großteil wissenschaftliche Veröffentlichungen in internationalen Fachzeitschriften und somit Ursprung für die teilweise Verwendung der englischen Sprache bzw. derer Schreibweise.

1 Grundlagen: Diffusion in Festkörpern und spektroskopische Methoden

Unter dem Begriff Diffusion versteht man den Ausgleich von Konzentrationsunterschieden bis hin zum praktisch vollständigen Durchmischen, der durch die Bewegung von Atomen, Molekülen oder Ionen entsteht. In jeder Substanz finden temperaturbedingt ungeordnete atomare und molekulare Bewegungen statt, die je nach Aggregatzustand und Art der diffundierenden Teilchen andere Ausmaße annehmen. In Festkörpern dominieren im Allgemeinen Schwingungen um die Gleichgewichtslage, in Flüssigkeiten und Gasen hingegen machen translatorische und rotatorische Verschiebungen den Hauptanteil der Molekülbewegungen aus. Besonders kleine Teilchen wie zum Beispiel das Li-Ion sind in auch in vielen Festkörpern besonders beweglich. Hier spricht man dann von festen Li-Ionenleitern. Der Stoffaustausch erfolgt vom Ort höherer Konzentration zum Ort niedrigerer Konzentration. Diffusion erfolgt, im Gegensatz zur Konvektion, ohne Strömung des Mediums, indem sich die Teilchen befinden. Die translatorische Diffusion lässt sich durch das 1. FICKSche Gesetz beschreiben:

$$\mathbf{j} = -D^{\text{tr}} \cdot \nabla c \quad (1.1)$$

Hierbei ist \mathbf{j} der Teilchenstrom (Anzahl der Teilchen pro Fläche und Zeiteinheit), die Größe D^{tr} wird als makroskopischer Diffusionskoeffizient oder Tracerdiffusionskoeffizient (entsprechend der Methode mit der er bestimmt werden kann) bezeichnet und ∇c steht für den Gradienten der Konzentration. Die Einheit für D^{tr} ist m^2/s und die gemessenen Werte unterscheiden sich je nach Aggregatzustand des Mediums, in dem die Atome, Ionen, Teilchen diffundieren, um etwa vier Zehnerpotenzen für die oberen Grenzen. In Gasen zeigt sich die höchste und Festkörpern die niedrigste Diffusivität. Typische Werte liegen dabei in folgenden Größenordnungen 10^{-5} für Gase, 10^{-9} für Flüssigkeiten und 10^{-13} (siehe S. 108ff und S. 124ff) ... 10^{-22} (siehe S. 43ff) für Festkörper. D^{tr} ist in anisotropen Medien richtungsabhängig und wird nur durch eine symmetrische 3×3 -Matrix (Tensor *zweiter* Stufe) richtig beschrieben. Bei isotropen Diffusionsvorgängen ist er als Proportionalitätsfaktor D^{tr} (Tensor *nullter* Stufe bzw. Skalar) direkt zugänglich. Unter der Voraussetzung, dass die diffundierenden Teilchen keine chemischen Reaktionen eingehen,

die Teilchenzahl also erhalten bleibt, gilt die Kontinuitätsgleichung.

$$\frac{\partial c}{\partial t} + \nabla \mathbf{j} = 0 \quad (1.2)$$

Setzt man diese in Gleichung 1.1 ein, so erhält man das zweite FICKSche Gesetz,

$$\frac{\partial c}{\partial t} = \nabla (D^{\text{tr}} \cdot \nabla c) \quad (1.3)$$

auch Diffusionsgleichung genannt. Der skalare Diffusionskoeffizient ist unabhängig von der Konzentration, somit auch vom Ort und man erhält:

$$\frac{\partial c}{\partial t} = D^{\text{tr}} \cdot \Delta c \quad (1.4)$$

Aus Gleichung 1.4 lässt sich für eindimensionale Diffusion in eine beliebige Richtung x folgender Ausdruck herleiten:

$$\frac{\partial c}{\partial t} = D^{\text{tr}} \frac{\partial^2 c}{\partial x^2} \quad (1.5)$$

Diese lineare partielle Differentialgleichung zweiter Ordnung kann für bestimmte Anfangs- und Grenzwerte gelöst werden. Um ein anschauliches Bild von eindimensionaler Diffusion zu bekommen, stellt man sich am besten einen dünnen Film an der Oberfläche eines einseitig unendlich ausgedehnten Festkörpers vor. In diesem können Teilchen, die sich zum Zeitpunkt $t = 0$ am Ort $x = 0$ befinden sollen nur entlang der so festgelegten x -Achse diffundieren. Die Konzentration zur Zeit t ist dann gegeben durch:

$$c(x, t) = \frac{M_D}{\sqrt{\pi D^{\text{tr}} t}} \cdot \exp\left(-\frac{x^2}{4D^{\text{tr}} t}\right) \quad (1.6)$$

Diese Funktion wird unter anderem zur Ermittlung des Diffusionskoeffizienten über das Radiotracerverfahren benötigt, wobei das Konzentrationsprofil beim Eindringen radioaktiver Isotope in einen Festkörper beobachtet wird. M_D steht für die Teilchendichte (Anzahl der Teilchen pro Flächeneinheit) im dünnen Film zur Zeit $t = 0$. Auf Grund des zu kurzlebigen Radioisotops von Lithium kann diese Methode jedoch nicht zur Untersuchung von Li-Diffusionsparametern angewendet werden. Massentracer-Verfahren sind aber möglich und Bestandteil aktueller Forschung, siehe Teilprojekt 6 der FOR 1277.

Gleichung 1.6 hat die Form einer GAUSS'schen Wahrscheinlichkeitsdichte und zeigt, dass sich die Diffusion aus einer ungerichteten, statistischen Bewegung zusammensetzt. Dieser auch als BROWNSche Molekularbewegung bekannte Prozess ist allein von der Temperatur abhängig, sodass auch das Temperaturverhalten des Diffusionskoeffizienten in vielen Fällen

durch einen ARRHENIUSansatz beschrieben werden kann:

$$D^{\text{tr}} = D_0^{\text{tr}} \cdot \exp\left(-\frac{E_A}{k_B T}\right) \quad (1.7)$$

Hier ist D_0^{tr} der präexponentielle Faktor, E_A die Aktivierungsenergie (hier Energie pro Teilchen), k_B die Boltzmann-Konstante und T die Temperatur. In Festkörpern sind Defekte wie z.B. Leerstellen Grundvoraussetzung für Diffusion. Deshalb setzt sich die Energie, die ein diffundierendes Teilchen für eine langreichweitige Bewegung braucht aus zwei Bestandteilen zusammen. Ein Anteil wird für die Bildung der Defekte und der andere für die Migration dieser Defekte benötigt (Messmethode Impedanz siehe Kap. 2.2).

Die EINSTEIN-SMOLUCHOWSKI-Beziehung^[3] verknüpft den Selbstdiffusionskoeffizienten D^{SD} mit der Verschiebung der Teilchen auf einem kubischen Gitter. Bei langen Beobachtungszeiten ($t \rightarrow \infty$) gilt:

$$D^{\text{SD}} = \frac{\langle \mathbf{R}^2 \rangle}{2d \cdot t} \quad (1.8)$$

$\langle \mathbf{R}^2 \rangle$ ist das mittlere Verschiebungsquadrat der diffundierenden Teilchen, d ist die Dimension der Verschiebung und D^{SD} wird als *mikroskopischer Diffusionskoeffizient*, *Selbstdiffusionskoeffizient* oder *Diffusionskoeffizient der unkorrelierten Diffusion* bezeichnet. Beschreibt diese Gleichung tatsächlich einen ausschließlich aus unkorrelierten Einzelsprüngen bestehenden Prozess, ist der Diffusionskoeffizient mit dem makroskopischen Diffusionskoeffizienten D^{tr} identisch. Um reale Bedingungen wie die vorliegende Gittergeometrie und den Diffusionsmechanismus erfassen zu können, wird der Korrelationsfaktor f eingeführt:

$$D^{\text{tr}} = f \cdot D^{\text{SD}} \quad (1.9)$$

Dabei gilt immer $0 \leq f \leq 1$. Bei $f = 1$ liegt ausschließlich unkorrelierte Diffusion vor. Unter der Annahme eines kubischen Gitters haben alle Sprünge zwischen direkt benachbarten Gitterplätzen einen konstanten Abstand r und Gleichung 1.8 vereinfacht sich zu:

$$D^{\text{SD}} = \frac{r^2}{2d \cdot \tau} \quad (1.10)$$

Die neu eingeführte Verweilzeit τ eines Teilchens an einem Gitterplatz (bzw. τ^{-1} die mittlere atomare Sprungrate) komplettiert die mikroskopischen Größen, die nötig sind, um Gleichung 1.9 lösen zu können. Sprungraten können z. B. durch $T_{1(\rho)}$ -Experimente der NMR-Spektroskopie direkt gemessen werden.

1.1 Festkörper-NMR-Spektroskopie

Um das Prinzip der NMR-Spektroskopie (engl. *Nuclear Magnetic Resonance*) zu verstehen, müssen zunächst die fundamentalen Eigenschaften der materiauaufbauenden Elementarteilchen veranschaulicht werden. Diese Bausteine haben z. B. eine definierte Ruhemasse und elektrische Ladung, aber auch ihr Spin ist eine unveränderbare Größe. Den Spin kann man sich ganz vereinfacht als eine Art „innere Rotation“ vorstellen. Bewegen sich elektrische Ladungen, wird dadurch ein magnetisches Feld erzeugt und die LORENZkraft zwingt die Teilchen auf eine gekrümmte Bahn um die Feldrichtung. Im Fall der Atomhülle sind diese Bedingungen mit den auf Kreisbahnen geführten Elektronen erfüllt. Auch wenn dies eine klassische und stark vereinfachte Darstellung ist, kann man so das magnetische Bahnmoment (Bahndrehimpuls) der meisten Elektronen erklären. Die Größe des magnetischen Dipols lässt sich aus dem Produkt von Stromstärke (abhängig von Anzahl und Geschwindigkeit der Elektronen im betrachteten System) und umflossener Fläche (wird durch die jeweilige Atomhülle gegeben) berechnen.

Der für die NMR entscheidende Impuls (Spindreh- oder auch Eigendrehimpuls L ; kurz Spin oder Kernspin) liegt aber auch ohne eine gekrümmt-translatorische „Bewegung“ vor. Hier soll nicht weiter auf die quantenmechanischen Eigenschaften von Elektronen und Nukleonen eingegangen werden, es kann aber festgehalten werden, dass die angesprochene „innere Rotation“ dafür sorgt, dass alle Atomkerne charakteristische magnetische Spin-Dipole besitzen. Es handelt sich dabei um permanente Dipole, die auch als Elementarmagnete bezeichnet werden. Das resultierende magnetische Moment μ ist über das gyromagnetische Verhältnis γ des jeweiligen Atomkerns mit dem Kernspin verknüpft, der als Kernspinvektor I (in Lehrbüchern häufig auch als Kernspinquantenzahl bezeichnet) ausgedrückt wird (Gleichung 1.11). Eine gute Grundlage für das Vektormodell, sowie die NMR-Spektroskopie an sich bietet das Buch von M. Levitt.^[4]

$$\mu = \gamma \cdot L = \gamma \cdot I \quad (1.11)$$

Die Kernspinquantenzahl des Atomkerns ist eine quantenmechanische Größe und nimmt nur diskrete Werte an. In einem äußeren stationären, homogenen Magnetfeld $B_0 \neq 0$ (das laut Definition die z -Richtung des Koordinatensystems festlegt) bestimmt sie die möglichen Beträge der messbaren Komponente I_z selbst, weil die magnetische Quantenzahl $m_I = I, I - 1, \dots, -I$ die Anzahl der Einstellmöglichkeiten des Kernspinvektors I festlegt:

$$|I| = \sqrt{I(I+1)}\hbar \quad (1.12)$$

mit $I = 0, 1/2, 1, 3/2, \dots$ und $\hbar = \text{PLANCKSches Wirkungsquantum}$

$$I_z = m_I \cdot \hbar \quad \text{bzw.} \quad \mu_z = \gamma \cdot \hbar \cdot m_I \quad (1.13)$$

Die Protonen/Neutronen-Anzahl (gg, ug, gu, uu; mit g=gerade und u=ungerade) des Atomkerns bestimmt, ob I Null, halb oder ganzzahlig ist. Für Kerne mit gerader Anzahl beider Nukleonen (z. B. ^{12}C) ist I gleich Null und es gibt kein magnetisches Moment, das durch ein äußeres Magnetfeld in eine Vorzugsrichtung gebracht werden kann. ^7Li besitzt einen Kernspin $I = 3/2$ und damit vier Werte für m_I die in einem statischen Feld B_0 vier Energiebeiträge E_m für die möglichen Zustände des Kernspinvektors liefern:

$$E_m = -\mu_z B_0 = \gamma \hbar m_I B_0 \quad (1.14)$$

Die PLANCKSche Beziehung (Gleichung 1.15) ist immer genau dann erfüllt, wenn die Auswahlregel des Drehimpulserhaltungssatzes $\Delta m = \pm 1$ (bei einem Photonenspin von $S = 1$) von Quanten eines elektromagnetischen Feldes erfüllt wird. Nur in diesem Fall ist ein Übergang zwischen den Energieniveaus (siehe auch Abb. 1.1) des Kernspins möglich. Auf diesem Resonanzphänomen beruht die NMR und die Gleichungen 1.16 und 1.17 liefern die Resonanzbedingung.

$$\Delta E = h\nu \quad (1.15)$$

$$\Delta E = \hbar\omega_0 \quad (1.16)$$

$$\Delta E = \hbar\gamma B_0 \quad (1.17)$$

Wird eine Probe einer Substanz mittels NMR untersucht, enthält diese eine hohe Anzahl Atomkerne, deren Kernspins alle dem gleichen äußeren Magnetfeld ausgesetzt sind. Auf Grund des thermodynamischen Gleichgewichts stellt sich ein definiertes Verhältnis zwi-

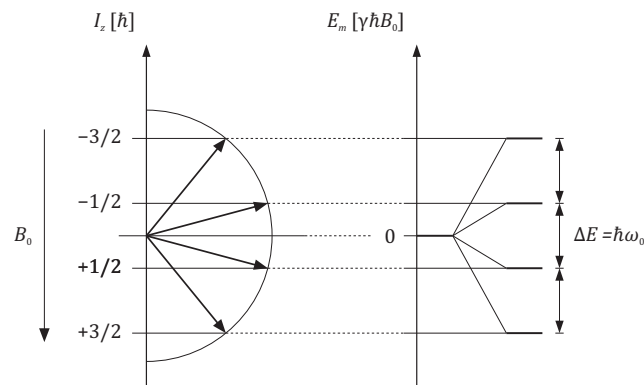


Abbildung 1.1: Zeemanaufspaltung: Kernspinverhalten am Beispiel von ^7Li ($I = 3/2$) in einem Magnetfeld B_0 , das die z-Achse des Koordinatensystems darstellt (wegen der gleichzeitigen Betrachtung der Energiewerte nach unten weisend). Die Richtungsquantelung für das magnetische Kernmoment μ nach Gleichung 1.13 liefert über die magnetische Quantenzahl im Magnetfeld vier mögliche Orientierungen I_z für einen solchen Spin. Dadurch entstehen vier diskrete Energieeigenwerte E_m mit konstanten Abständen ΔE .

schen den Besetzungszahlen der Energieniveaus ein. Dabei wird die Besetzung energetisch höherer Zustände durch thermische Bewegung, also bei höherer Temperatur begünstigt. Dieses Verhältnis wird nach Boltzmann für zwei Benachbarte Zustände m und $m - 1$ mit den Besetzungszahlen N_m und N_{m-1} für die Energieeigenwerte E_m und E_{m-1} wie folgt beschrieben:

$$\frac{N_m}{N_{m-1}} \sim \exp \left[\frac{(E_m - E_{m-1})}{k_B \cdot T} \right] \quad (1.18)$$

mit $(E_m - E_{m-1}) = \Delta E$ und $k_B = \text{BOLTZMANN-Konstante}$

Die Winkelgeschwindigkeit $\omega_0 = -\gamma \cdot B_0$, auch LAMORfrequenz genannt, ist bei gegebenem γ (^7Li -Kerne mit $\gamma = 1.4 \cdot 10^8 \text{ Ts}^{-1}$) nur von der Stärke des äußeren Magnetfeldes abhängig und somit eine für das jeweilige Experiment leicht zu berechnende Konstante. Mit dieser Geschwindigkeit präzedieren die einzelnen Magnetischen Momente μ_i um die z-Achse. Diese Bewegung ist bildlich formuliert der fortwährende Versuch der magnetischen Momente, sich nach der durch das statische Feld B_0 vorgegebenen Vorzugsrichtung auszurichten. Die Ausbildung eines Drehmoments $T = \mu \times B = \mu \cdot B \cdot \sin \theta$ in einem Magnetfeld ist hierfür, wie auch für alle NMR-Experimente die Grundlage. Es besteht dabei keinerlei Phasenbeziehung zwischen den Momenten, sodass deren Ausrichtung auf ihrem Präzessions-Kegel statistisch verteilt ist und keine makroskopische Magnetisierung M in x- oder y-Richtung zu beobachten ist. Im thermodynamischen Gleichgewicht ($M = M_0$) addieren sich also nur die z-Komponenten $\mu_{i,z}$ eines Ensembles mit N Kernspins.

$$\mathbf{M} = \sum_{i=1}^N \mu_i = \sum_{i=1}^N (0, 0, \mu_{i,z}) \quad (1.19)$$

Unter der Annahme eines zeitlich konstanten Magnetfeldes mit $B_z = B_0 = \text{const.}$ und $B_x = B_y = 0$, gilt auch $M_x(t) = M_y(t) = 0$ und $M_0 \parallel B_0$.

Während eines NMR-Experiments wird der Magnetisierungsvektor M durch ein zeitabhängiges Radiofrequenzfeld (*rf*-Feld) der Resonanz- bzw. Lamorfrequenz ω_0 mit gezielten Zeitpulsen beeinflusst. Das Radiofrequenzfeld wirkt hierbei wie ein zweites senkrecht zu B_0 aufgebautes Magnetfeld, welches sich mit der Geschwindigkeit der Präzessionsbewegung des Magnetisierungsvektors „mitdreht“ (theoretisch auch durch ein um die Probe rotierendes Spulenpaar realisierbar – in der Praxis mit Werten für ω_0 bis 1 GHz unvorstellbar). So ist eine optimale Interaktion mit den einzelnen Kernspins möglich und es können definierte Energieniveauwechsel induziert werden. Die anschließende Relaxation des Kernspinsystems zurück ins thermodynamische Gleichgewicht liefert durch ihre substanzspezifischen Zeiten die Ergebnisse eines NMR-Experiments.

Im Laborkoordinatensystem **LKS** sind die komplexen Bewegungen, die ein magnetisches Moment μ bzw. die sich ergebende makroskopische Magnetisierung M ausführen, sehr schnell unübersichtlich. Besonders wenn sie durch ein gepulstes *rf*-Feld beeinflusst ihre Orientierung ändern. Deshalb werden in der NMR rotierende Koordinatensysteme **RKS** (siehe Abbildung 1.2) zur besseren Veranschaulichung der Bewegung bzw. Orientierung von Magnetisierungsvektoren verwendet.

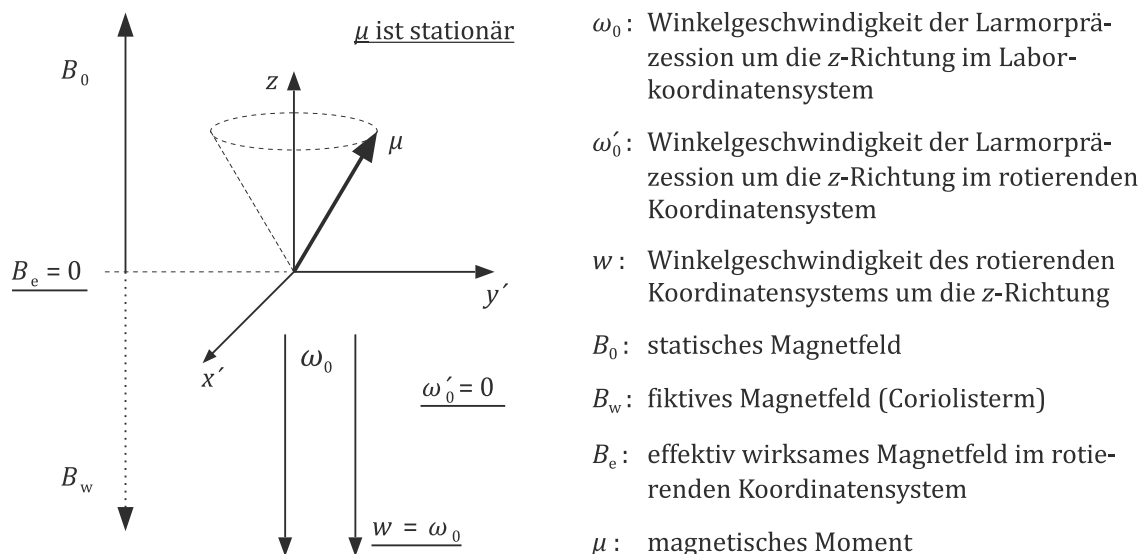


Abbildung 1.2: Entspricht die Winkelgeschwindigkeit eines rotierenden Koordinatensystems w der Larmorpräzession ω_0 im Laborkoordinatensystem, so ist $\omega'_0 = 0$ und μ wird stationär (Rotation immer um die durch B_0 festgelegte Vorzugsrichtung; per Definition die z-Achse). Das fiktive Magnetfeld B_w wirkt dem statischen Magnetfeld B_0 hierbei entgegen und hat bei $w = \omega_0$ den selben Betrag, sodass ein effektiv wirksames Magnetfeld B_e im rotierenden Koordinatensystem nicht vorhanden bzw. gleich Null ist.

Das Konzept von LKS und RKS sowie die Verwendung eines zeitabhängigen, linear polarisierten Magnetfeldes $B_1^{lin} \perp B_0$ (B_1^{lin} bisher als *rf*-Feld benannt) mit der Oszillationsfrequenz ω_0 und dessen Realisierung durch zwei Spulen in der x,y -Ebene (im hier betrachteten Fall parallel zur x -Achse orientiert), wird am elegantesten durch Animationen (im Internet) veranschaulicht. B_1^{lin} kann als Überlagerung zweier in der x,y -Ebene mit den Frequenzen ω_0 und $-\omega_0$ zirkular polarisierten Felder $B_1(\omega_0)$ und $B_1(-\omega_0)$ aufgefasst werden.

$$B_1^{lin} = B_1(\omega_0) + B_1(-\omega_0) \tag{1.20}$$

Im RKS sind die jeweiligen Winkelgeschwindigkeiten entsprechend um den Betrag ω_0 „langsamer“, d.h. B_1^{lin} dreht sich hier mit $-\omega_0$ um die z-Achse. Durch diese Betrachtungsweise gilt einerseits $B_1(-2\omega_0)$ und außerdem ein statisches Feld $B_1(0)$ für das rotierende

Koordinatensystem. Dieses Feld (im Folgenden als B_1^r bezeichnet) erfüllt zu jeder Zeit die Resonanzbedingung und lässt M in der yz -Ebene mit der Winkelgeschwindigkeit $\omega_1 = \gamma B_1^r$ um die x -Achse rotieren, sofern die Amplitude des rf-Feldes hinreichend groß ist. Dies wird durch entsprechende Verstärker gewährleistet. Das Vorzeichen des gyromagnetischen Verhältnisses γ bestimmt also nicht nur die Präzessionsrichtung von M und somit die Drehrichtung des RKS, sondern auch ob der gegen (ccw) oder mit dem Uhrzeigersinn (cw) rotierende Anteil von B_1^{lin} mit M in Resonanz tritt ($\gamma > 0$ entspricht cw und $\gamma < 0$ entspricht ccw). Im Folgenden wird deshalb nur noch die Komponente B_1^r berücksichtigt und das rotierende Koordinatensystem als Grundlage vorausgesetzt.

1.1.1 NMR-Spin-Gitter-Relaxation

Zwei Bedingungen müssen erfüllt sein, um eine Probe mittels NMR zu untersuchen. Erstens muss ein statisches Magnetfeld B_0 vorhanden sein, damit sich die magnetischen Kerndipole (oder auch quadrupolare Kerne wie ^7Li , siehe 1.1.2) parallel zur Vorzugsrichtung (gegeben durch das Magnetfeld) ausrichten und sich somit eine makroskopische Magnetisierung M der Probe ausbildet. Diese wird durch die zweite grundlegende Voraussetzung eines transversal zur Vorzugsrichtung eingestrahlten HF-Feldes, welches nach Gl. 1.15 die richtige Energie aufweist, gezielt beeinflusst. Die anschließende Relaxation des Spinsystems wird in Form eines zeitlichen Verlaufs von M über Empfängerspulen als induzierter Strom registriert.

$$M(t) = M_0 \cdot e^{-\frac{t}{T_2^*}} \quad (1.21)$$

Dieses idealisierte Zeitgesetz mit der charakteristischen Konstante T_2^* stellt den sogenannten FID (*free induction decay*) dar. Wird also M_0 durch einen bzw. mehrere aufeinander folgende $90^\circ |x'$ -Pulse auf die y' -Achse gekippt, wird zum Zeitpunkt $t = 0$ (direkt nach dem letzten Puls) ein $M_{0,y}$ und das anschließende Abnehmen der makroskopischen Magnetisierung $M_y(t)$ mit der Zeit beobachtet. Dafür verantwortlich sind lokale Inhomogenitäten, die jeden einzelnen Kern und somit jedes einzelne μ ein etwas anderes lokales Magnetfeld spüren lassen, wodurch die magnetischen Momente beginnen zu dephasieren bis sie willkürlich in der x',y' -Ebene verteilt sind. $M_y(t)$ ist jetzt gleich Null.

Auch nach vollständiger Relaxation der Magnetisierung in der x',y' -Ebene ist das System also noch nicht wieder im thermodynamischen Gleichgewicht. Hierfür ist ein anderer Relaxationsmechanismus notwendig. Die so genannte Spin-Gitter-Relaxation **SGR** ermöglicht den erneuten Aufbau einer makroskopischen Magnetisierung M in z -Richtung. Hierbei werden Übergänge der einzelnen Momente zwischen den m -Niveaus durch Selbstdiffusion induziert. Andere Bewegungsprozesse atomarer oder molekularer Art kommen auch für eine derartige lokale Resonanz in Betracht, werden hier jedoch vernachlässigt, da auch die Versuchsbedingungen darauf ausgelegt sind, die Li-Ionen-Diffusion zu beobach-

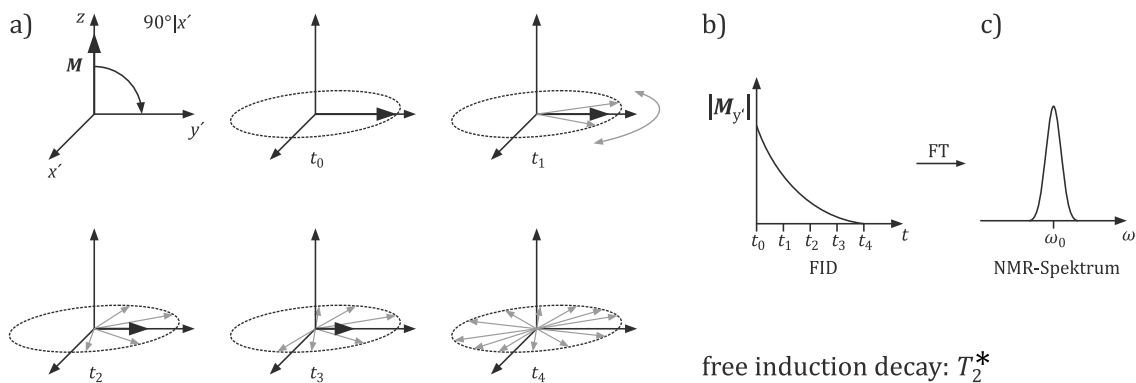


Abbildung 1.3: Von der Entropierelaxation (a) über den FID (b) zum Spektrum (c): Die Aufnahme eines FIDs kann mit einer isothermen, adiabatischen Expansion eines idealen Gases in Vakuum verglichen werden. $dE/dt = 0 \wedge dS/dt > 0$ Bei einer solchen Entropierelaxation nimmt zwar die Entropie des Systems zu, aber der Energiewert bleibt erhalten. D. h. das Spinsystem bleibt im künstlich angeregten Bereich. Die magnetischen Momente bleiben zu jeder Zeit t in der $x'y'$ -Ebene, aber dephasieren mit der Zeit, sodass die makroskopische Magnetisierung in y' -Richtung abnimmt. Aus dem FID wird durch Fourier-Transformation (FT) das NMR-Spektrum berechnet.

ten. Aufgrund der elektrischen Ladung von Ionen ist das an ihre Bewegung gekoppelte elektromagnetische Feld und somit auch die Wahrscheinlichkeit die NMR spezifische Resonanzbedingung zu erfüllen größer als von Atomen und Molekülen.

Die Diffusion von Ionen in Festkörpern wird dann möglich, wenn sich in der Probe Fehlstellen befinden. Beim Vorliegen eines leeren Gitterplatzes kann z. B. ein benachbartes Ion auf diesen Gitterplatz springen. Dies ist nur ein Mechanismus für das Wandern eines Atoms | Ions | Teilchens. Nulldimensionalen Punktdefekte treten in jedem Festkörper oberhalb von 0 K auf und verstärken sich bei steigender Temperatur weiter. Auch höherdimensionale Defekte, wie eindimensionale Vernetzungen oder zweidimensionale Grenzflächen (z.B. Bruchstellen von Kristallen), stellen häufig Bereiche erhöhter Diffusivität dar. Durch *high energy ball milling* (HEBM) können solche Defekte gezielt eingebracht werden, um die Diffusivität von z. B. Li^+ in einem (Model-)System vom Einkristall über mikrokristallines und nanokristallines Pulver bis hin zum röntgenamorphen Material zu studieren.

$$M(\tau) = M_0 \cdot \left[1 - \exp\left(-\frac{\tau}{T_1}\right) \right] \quad (1.22)$$

Die sogenannte Spin-Gitter-Relaxationszeit, bzw. die $1/T_1$ -Rate hängt also stark von der Temperatur ab und gibt direkten Aufschluss über die Diffusivität in der untersuchten Probe. Hohe Sprungraten bzw. hohe Diffusivität ergibt kleine T_1 -Zeiten. Umgekehrt deuten größere Werte von T_1 auf weniger Sprünge pro Zeit bzw. geringere Diffusivität hin.

Das einfach-exponentielle Zeitgesetz setzt ideale Bedingungen voraus. Der Wiederaufbau der makroskopischen Magnetisierung in z -Richtung und die charakteristische Konstante

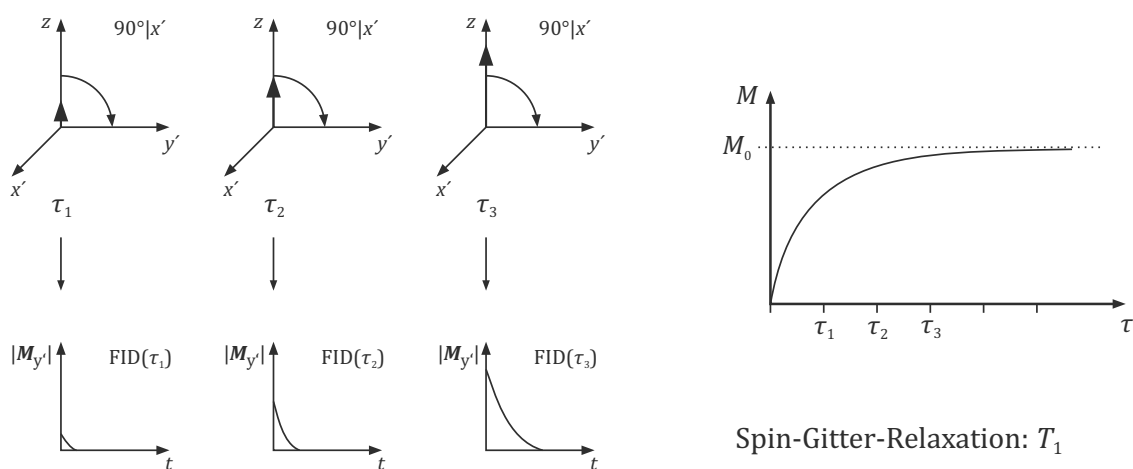


Abbildung 1.4: Spin-Gitter-Relaxation (T_1): Aus Gleichung 1.22 ergibt sich für den Zeitpunkt $\tau = T_1$ eine Magnetisierung von 63 % der Gleichgewichtsmagnetisierung M_0 , hier bei τ_1 . Für eine 99 %ige Sättigung dieses auch *saturation recovery* genannten Experiments muss eine Wartezeitenliste mit $\tau_{\max} = 5 \cdot T_1$ genutzt werden. Die Anzahl und Abstände der Listeneinträge sind entscheidend für einen zuverlässigen Fit der Messpunkte und somit entscheidend für die Genauigkeit der berechneten T_1 -Zeit.

T_1 sind hier von τ und nicht von t abhängig. Ausgehend von der maximalen makroskopischen Magnetisierung M_0 in z -Richtung wird der Wiederaufbau der Magnetisierung durch definierte Evolutionszeiten τ nach mehreren 90° x' -Pulsen gemessen, indem ein erneuter Puls die zum Zeitpunkt τ wiederaufgebaute Magnetisierung in die $x'y'$ -Ebene kippt und der entsprechende FID aufgenommen wird. Durch die Wahl mehrerer geeigneter Evolutionszeiten ist es möglich, den vollständigen Wiederaufbau der Magnetisierung als exponentiellen Anstieg gegen den Grenzwert M_0 darzustellen (siehe Abb.1.4). Die Messung einer Spin-Gitter-Relaxation ist also die Folge von mehreren FID-Messungen zu unterschiedlichen Wartezeiten τ . Aus der Auftragung lässt sich schließlich die stoffspezifische und temperaturabhängige Zeit T_1 ablesen. Für Festkörper gilt im Allgemeinen: $T_2^* \ll T_1$

Somit ist der FID geeignet, um die Spin-Gitter-Relaxation mit beschriebener Methode zu bestimmen. Die Verknüpfungen zwischen SGR-Zeit und den einzelnen charakteristischen Größen des zugrunde liegenden Bewegungsprozesses, wie Aktivierungsenergie, Selbstdiffusionskoeffizient und Sprungfrequenz, werden im Abschnitt 2.1 noch erklärt.

1.1.2 Quadrupolare NMR-Spin-Gitter-Relaxation

Atomkerne wie ${}^7\text{Li}$ zeigen auf Grund ihres Kernspins $I \geq 1$ neben der magnetischen Dipol-Dipol Wechselwirkung elektrische Quadrupolwechselwirkung. Ohne näher auf die physikalischen Hintergründe eingehen zu wollen, kann hier festgehalten werden, dass von der Ku-

gelsymmetrie verschiedene Kernladungen (zigarrenförmige oder oblatenförmige Ladungsverteilungen) Quadrupolmomente zur Folge haben. Über eine Taylor-Reihenentwicklung der Energieverteilung ergibt sich der sogenannte Quadrupolterm E_2 , welcher durch geschickte Wahl der Randbedingungen stark vereinfacht werden kann und so Zugang zum Quadrupolmoment Q_z liefert.

$$E_2 = \frac{1}{4} V_{zz} e Q_z \quad (1.23)$$

mit e = Elementarladung, V_{zz} = elektrischer Feldgradient und

$$Q_z = \frac{1}{e} \int [3z^2 - r^2] \rho(r) d\tau \quad (1.24)$$

wobei $\rho(r)$ die Kernladungsdichteverteilung ist.

Die Richtungsquantelung des Drehimpulses I überträgt sich auf die zulässigen Orientierungen des Kernquadrupolmoments Q_z gegenüber des elektrischen Feldgradienten V_{zz} und hat dementsprechend auch eine Energiequantelung von E_2 zur Folge. Der Drehimpuls I widersetzt sich auch hier analog zur Neuorientierung im magnetischen Feld einer Ausrichtung parallel zum elektrischen Feld und das resultierende Drehmoment T lässt den Kern mit der Winkelgeschwindigkeit ω um die Symmetrieachse des elektrischen Feldgradienten präzedieren. Die Tatsache, dass der Feldgradient V_{zz} eine skalare Größe ist, macht eine graphische Darstellung der physikalischen Zusammenhänge schwierig. Deshalb wird hier auf eine Veranschaulichung der elektrischen Quadrupolwechselwirkung verzichtet. Man kann sich jedoch einfach vorstellen, dass der entsprechende Sondenkern im Fall von ${}^7\text{Li}$ vier Möglichkeiten der Orientierung im elektrischen Feld hat und das System (Kern + umgebendes Kristallgitter) versucht seine Energie durch Reorientierung des Kerns zu minimieren. Analog zu magnetischen Wechselwirkungen können auch hier Übergänge im Kernspinsystem induziert werden und so zur Relaxation beitragen. Diesen Mechanismus nennt man quadrupolare Spin-Gitter-Relaxation. Wird im NMR-Spektrum eine Aufspaltung des Signals in ein Triplett beobachtet, liegt dieser Mechanismus dominierend vor und lässt sich durch eine teilweise Aufhebung der Äquidistanz der Kernzeeman-Niveaus erklären.

Die Aufspaltung zum Triplett (Kerne mit $I = 3/2$) ist in der Praxis dann besonders stark zu beobachten, wenn es sich bei der untersuchten Probe um Material mit hohem kristallinen Anteil handelt. Das für ${}^7\text{Li}$ typische Auftreten eines Paares "innerer Satelliten" und "äußerer Flanken" um die Zentrallinie nimmt daher mit steigendem Anteil amorpher Bereiche ab. Das heißt die quadrupolare Spin-Gitter-Relaxation ist im Spektrum "nur dann" zu erkennen, wenn es sich um ein echtes Gitter handelt, in dem alle Kerne dem selben elektrischen Feldgradienten ausgesetzt sind. Beim Vergleich verschiedener Proben einer Substanz kann so zusätzlich zu den Relaxationszeiten die Ordnung im "Kristallsystem" gegenüber gestellt

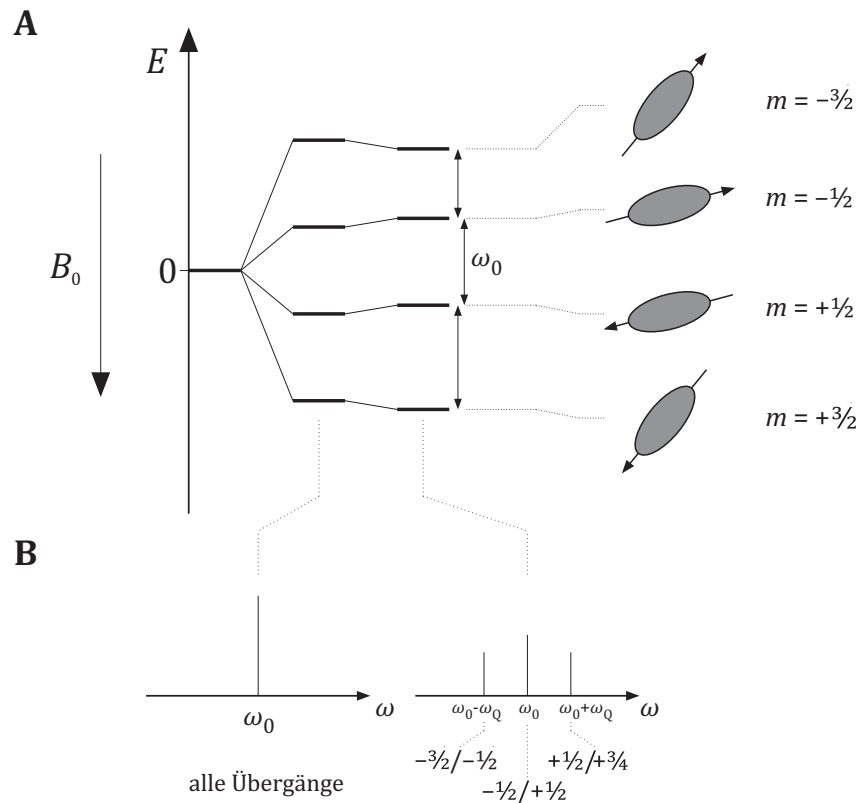


Abbildung 1.5: Auswirkungen des Kernquadrupolmoments Q_z auf die resultierenden Spektren: In A sind die Energieeigenwerte ohne (Äquidistanz von ω_0) und mit Einfluss durch ein positives Kernquadrupolmoment $Q_z > 0$ gezeigt. B zeigt die daraus resultierenden Spektren. Im Ersten fallen alle Übergänge zu einer Linie zusammen, weil alle Übergänge durch diese eine Frequenz induziert werden können. Die elektrischen Quadrupole mit den Orientierungen $m = \pm 1/2$ und $m = \pm 3/2$ haben jeweils die gleiche energetische Ausrichtung hinsichtlich des Feldgradienten V_{zz} und können somit als Paar betrachtet werden. Paar $_{1/2}$ erhöht die Energieeigenwerte der Kern-Zeeman-Niveaus und Paar $_{3/2}$ erniedrigt sie. Dadurch sind die Übergänge nicht mehr äquidistant und das entsprechende Spektrum zeigt ein Linientriplett. Der Übergang von $m = +1/2$ zu $m = -1/2$ bildet die Zentrallinie, welche weiterhin bei der ursprünglichen Frequenz ω_0 liegt. Die Lage der anderen beiden Übergänge mit ihrer Verschiebung $\Delta\nu = \pm 2|Q_z|$ zur Zentrallinie ist im rechten Spektrum gezeigt. Für $Q_z < 0$ wären diese genau vertauscht, weil das Paar $_{1/2}$ hier energieerniedrigend wäre.

werden. Die hierfür aus technischen Gründen besser geeignete *Solid-Echo*-Plusfolge ist z. B. auch in dem freien eBook^[5] von Bernhard Blümich gezeigt.

1.1.3 BPP-Modell nach Blombergen, Purcell and Pound

Korrelationsfunktionen überbrücken die Lücke zwischen Theorie und Experiment und sind in vielen Gebieten der Spektroskopie gebräuchlich. In der NMR-Spektroskopie wird durch die Autokorrelationsfunktion $G(t)$ und Modelle wie z.B. das von BLOEMBERGEN, PURCELL und POUND (BPP-Modell) ein direkter Zusammenhang zwischen Fluktuationen der lokalen Magnetfelder $B_0^{\text{lok}}(\tau)$ um den makroskopischen Mittelwert B_0 und Größen wie Selbstdiffusionskoeffizient, Aktivierungsenergie und deren Temperaturabhängigkeit hergestellt.

Von (Zeit-)Autokorrelation wird im Allgemeinen gesprochen, wenn Werte **einer** physikalischen Größe, die auf den ersten Blick statistisch unabhängig voneinander scheinen, einen zeitlichen Zusammenhang aufweisen. Im Fall der lokalen Magnetfelder an den einzelnen Sondenkernen in einer NMR-Probe werden die lokalen Schwankungen durch mikroskopische Bewegungen hervorgerufen. Und auch wenn diese statistisch verteilt über die gesamte Probe ablaufen, d.h. zu jeder Zeit an jedem Sondenkern eine im Rahmen des Effekts beliebige Abweichung vorliegen kann, ist die Geschwindigkeit mit der sich $B_0^{\text{lok}}(\tau)$ ändert nie unendlich groß. $G(t)$ (im Folgenden nur noch Korrelationsfunktion genannt) beinhaltet im Idealfall alle möglichen Spin-Gitter Interaktionen (hier nicht im einzelnen aufgeführt) und liefert mit der sogenannten Korrelationszeit τ_c eine für das "Gedächtnis" des Systems charakteristische Zeitkonstante.

Für die diffusionsinduzierte Relaxation sind hauptsächlich homonukleare und/oder heteronukleare dipolare Wechselwirkungen zwischen den Kernspins (siehe 1.1.1) bzw. Wechselwirkungen zwischen Kernen mit Quadrupolmomenten und elektrischen Feldgradienten (siehe 1.1.2) verantwortlich. τ_c entspricht daher in etwa der mittleren Verweilzeit eines Teilchens auf einem (Gitter-) Platz und τ_c^{-1} kann als mittlere Sprungrate angenommen werden.

$$G(t) = G(0) \exp\left(-\frac{t}{\tau_c}\right) \quad (1.25)$$

Gleichung 1.25 kann unter der Annahme eines homogenen Festkörpers, in dem dreidimensionale, voneinander unabhängige Bewegungen von Teilchen stattfinden, abgeleitet werden (gilt auch für Flüssigkeiten und Gase). Dafür müssen folgende Grenzfälle gelten,

- $G(t = 0) = \langle B_0^{\text{lok}}(0) B_0^{\text{lok}}(t \rightarrow 0) \rangle = \langle B_0^{\text{lok}}(0)^2 \rangle$
(Erhaltungsgröße, maximale Abweichung von $\langle B_0 \rangle^2$ und konstant)
- $G(t = \infty) = \langle B_0^{\text{lok}}(0) B_0^{\text{lok}}(t \rightarrow \infty) \rangle = \langle B_0 \rangle^2$
(Mittelwert der Produkte ist gleich dem Produkt des Mittelwerts)

die zur räumlichen Mittlung und folgendem Korrelationsintegral führen:

$$\bullet G(t) = \langle B_0^{lok}(0) B_0^{lok}(t) \rangle = \lim_{T \rightarrow \infty} \frac{1}{T} \int_0^T B_0^{lok}(\tau) B_0^{lok}(\tau + t) d\tau$$

Die Annahme der Äquivalenz von räumlicher und zeitlicher Mittlung ist bei Inhomogenitäten in der Probe nicht bzw. nur für sehr kleine Volumenelemente gegeben. Anders ausgedrückt kann im Fall von z.B. Schichtverbindungen oder auch amorphen Festkörpern davon ausgegangen werden, dass sich das Verhalten nur durch Potentialbarrieren oder eine Verteilung von Korrelationszeiten beschreiben lässt.

Das BPP-Modell hingegen geht von isotroper, dreidimensionaler Diffusion aus und setzt von vornherein eine einfach-exponentiell abklingende Korrelationsfunktion wie Gl. 1.25 voraus. Die Fouriertransformation liefert die zugehörige lorentzförmige Spektraldichtefunktion:

$$J(\omega) = \int_{-\infty}^{+\infty} G(t) \exp(-i\omega t) dt \quad (1.26)$$

und Einsetzen der Korrelationsfunktion (Gl. 1.25) in Gl. (1.26) führt in erster Näherung zur spektralen Dichte:

$$J(\omega) = G(0) \frac{\tau_c}{1 + \omega^2 \tau_c^2} \quad (1.27)$$

In Abb. 1.6 werden diese Zusammenhänge anschaulich dargestellt. (a) zeigt, warum die Korrelationszeit τ_c im Fall des BPP-Modells mit der mittleren Verweilzeit des diffundierenden Ions oder Atoms in etwa identisch ist. Die Temperaturabhängigkeit von τ_c zeigt sich durch schneller abklingende Korrelationsfunktionen (b) und breitere spektrale Dichten (c) für höhere Temperaturen. Zusammengefasst in einem Arrhenius-Ansatz (Gleichung 1.28 mit $\tau_\infty =$ Korrelationszeit bei unendlicher Temperatur)

$$\tau_c^{-1} = \tau_\infty^{-1} \exp\left(-\frac{E_A}{k_B T}\right) \quad (1.28)$$

kann über die Flankensteigungen direkter Zugang zur Aktivierungsenergie E_A erhalten werden (siehe Abb. 1.6.d). Hochtemperaturflanke (HT-Flanke) und Tieftemperaturflanke (TT-Flanke) haben nach dem BPP-Modell die gleiche Steigung, d.h. für alle Resonanzfrequenzen werden symmetrische Kurven erhalten. Andersherum betrachtet kann diese Symmetrie als Bestätigung für die im BPP-Modell gemachten Annahmen der isotropen, dreidimensionalen Diffusion angesehen werden. Finden während einer LAMORpräzession besonders viele Sprünge statt (HT-Flanke mit $\omega\tau_c \ll 1$), hat das springende Teilchen in dieser Zeit eine besonders lange Strecke zurückgelegt (Aufsummierung der einzelnen

Sprunglängen; nicht als Strecke vom Startpunkt zu verstehen). Die Aktivierungsenergie dieser Flanke entspricht der *langreichweitigen* Diffusion. Auf der Seite der TT-Flanke finden im gleichen Zeitintervall viel weniger Sprünge statt und die zugehörige Aktivierungsenergie gilt für *kurzreichweitige* Diffusion. Sind beide Flanken also gleich steil, müsste die Potentiallandschaft in der untersuchten Probe nach bisherigen Ausführungen in jedem beliebig großen Volumenelement homogen sein. Eine andere Möglichkeit wird in Abschnitt 1.1.4 erläutert.

Dadurch, dass die HT-Flanke ($\omega\tau_c \ll 1$) frequenzunabhängig ist,

$$\frac{1}{T_1} \propto \tau_c \propto \exp\left(+\frac{E_A}{kT}\right) \quad (1.29)$$

die TT-Flanke ($\omega\tau_c \gg 1$) jedoch frequenzabhängig

$$\frac{1}{T_1} \propto \frac{1}{\omega^2\tau_c} \propto \frac{1}{\omega^2} \exp\left(-\frac{E_A}{kT}\right), \quad (1.30)$$

verschieben sich die Ratenmaxima $(\omega_0\tau_c)_{\max} = 0.62 \approx 1$ bei niedrigeren Frequenzen zu tieferen Temperaturen. Bei vielen Proben bzw. Messungen ist weder das Ratenmaximum noch die HT-Flanke im Bereich der experimentellen Möglichkeiten zugänglich. Die frequenzabhängige Messung in Kombination mit dem Arrhenius-Ansatz ist somit eine wertvolle Methode zur nahezu direkten Bestimmung der Sprungraten.

Über die Einstein-Smoluchowski-Beziehung (Gleichung 1.8) lässt sich der mikroskopische Diffusionskoeffizient bzw. der Selbstdiffusionskoeffizient bestimmen.

1.1.4 Strukturelle Unordnung und niederdimensionale Diffusion

Allen vorausgegangenen Betrachtungen wurde das BPP-Modell zugrunde gelegt, welches auch die Grundlage für moderne bildgebende Verfahren wie *magnetic resonance imaging* (MRI) ist.^[6–10] Reale Proben zeigen aber immer Abweichungen vom idealen Verhalten, sodass die Kurven der Arrhenius-Auftragung in der Praxis mehr oder weniger symmetrisch sein können. In diesen Fällen beeinflussen Korrelationseffekte und Dimensionalitätseffekte die Steigungen der Flanken bzw. die über das NMR-Experiment messbaren Aktivierungsenergien. Dadurch ist auch die "exakte" Bestimmung von τ_c nur noch am Ratenmaximum möglich. Es gibt grundsätzlich zwei Arten der Abweichung vom BPP-Modell.

Niederdimensionale Diffusion

In Schichtstrukturen bei denen nur zweidimensionale Diffusion vorliegt, erniedrigt sich die Aktivierungsenergie der HT-Flanke. Hier ist die Sprungrate wesentlich höher als die LAMORfrequenz, es handelt sich also um langreichweitige Diffusion und diese ist in den einzelnen Schichten begünstigt (geringere Potentialbarrieren). Die kurzreichweitige

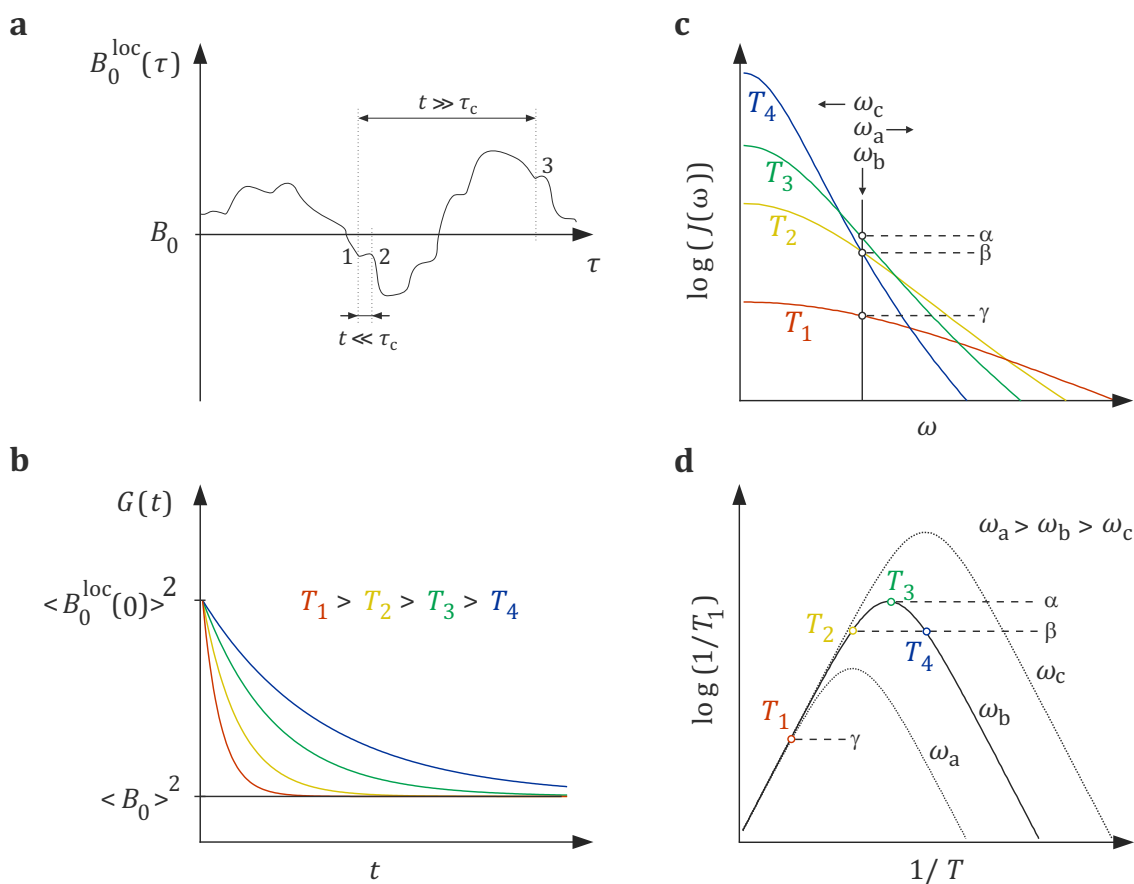


Abbildung 1.6: Die Graphen a–d veranschaulichen die Zusammenhänge von mikroskopischer Bewegung (a) zur Korrelationsfunktion $G(t)$ (b), zur Spektral Dichtefunktion $J(\omega)$ (c) und der Auftragung von $\log(1/T_1)$ gegen $1/T$ (d). In (a) ist das lokale Magnetfeld eines exemplarischen Sondenkerns zur Zeit τ im Vergleich zum angelegten Magnetfeld bei einer nicht definierten Temperatur gezeigt. In b–d sind vier Beispielttemperaturen T_{1-4} gewählt worden. Angenommen T_1 ist die maximal mögliche Temperatur (entweder für den Probenkopf oder die Probe selbst) und T_4 die minimal mögliche Temperatur, dann ist aus (d) leicht abzulesen, welche Frequenz ω geeignet ist, um das Ratenmaximum, sowie die Hoch- und Tieftemperaturflanke aufzunehmen. Beim gewählten Beispiel ω_b lassen sich nur wenige Punkte auf der TT-Flanke aufnehmen und bei ω_c würde bei T_4 bereits das Ratenmaximum gemessen werden. Diese Ergebnisse würden bei üblichen Feldstärken von einigen Tesla und einem Temperaturbereich von ca. 150 K – 500 K auf eine extrem hohe Diffusivität hinweisen, sodass diese T_1 -Messreihe idealerweise bei ω_a aufgenommen werden sollte. In der Praxis werden die Ratenmaxima mit z. B. knapp 117 Millionen Sprüngen pro Sekunde (Resonanzfrequenz für ${}^7\text{Li}$ bei einem 7 Tesla Magneten) nur von sehr schnellen Ionenleitern erreicht und deutlich überschritten. Die HT-Flanke ist daher mit T_1 -Experimenten im experimentellen Rahmen häufig nicht messbar. Um auch bei noch stärkeren Magneten den direkten Zugang zu Sprungraten einer definierten Temperatur (am Ratenmaximum ausgelesen) zu erhalten, kann das für die Relaxation effektive Feld in $T_{1\rho}$ -Experimenten um ca. 3 Größenordnungen herabgesetzt werden.

Diffusion deren Aktivierungsenergie an der TT-Flanke abzulesen ist, verändert sich im Vergleich zum BPP-Modell nicht. Es sind **beide** Flanken frequenzabhängig.

Tabelle 1.1: Übersicht der Frequenzabhängigkeiten^[11,12]

	$\omega_0\tau \ll 1$	$\omega_0\tau \gg 1$
3D	$\propto \tau$	$\propto \tau^{-1}\omega_0^{-2}$
2D	$\propto \tau \ln \frac{1}{\omega_0\tau}$	$\propto \tau^{-1}\omega_0^{-2}$
1D	$\propto \tau(\omega_0\tau)^{-1/2}$	$\propto \tau^{-1}\omega_0^{-2}$

Tab.1.1 zeigt das asymptotische Verhalten der Spin-Gitter Relaxationsrate $1/T_1(\tau, \omega_0)$ in Abhängigkeit der Dimensionalität des Diffusionsprozesses für Hoch- und Tieftemperaturflanke.

Strukturelle Unordnung und Coulomb-Wechselwirkungen

Auch bei Verbindungen mit heterogenen Potentiallandschaften, d.h. bei lokal stark unterschiedlichen Potentialbarrieren (strukturelle Unordnung; keine Schichten oder Kanäle) sind die Bedingungen des BPP-Modells nicht mehr erfüllt. Amorphe und defektreiche kristalline Systeme zeigen auf der TT-Flanke eine niedrigere Steigung als auf der HT-Flanke.

Man stelle sich zunächst die Potentiallandschaft eines perfekt kristallinen Systems als sinusförmige Welle in alle Raumrichtungen vor. Zur Veranschaulichung spielt es hier keine Rolle, dass diese Voraussetzungen auch für Einkristalle bei 0 K eigentlich für keine Kristallstruktur gelten. Senken sind also Gitterplätze und Berge zu überwindende Barrieren, verkörpert durch das Gitter selbst. Je ungeordneter die Struktur durch das Auftreten von Defekten wird, desto mehr Barrieren werden erniedrigt. Durch das statistische Auftreten der Defekte entstehen allerdings nur lokal sprungbegünstigte Bereiche. Diffundierende Teilchen benötigen hier kleinere Aktivierungsenergien als über das BPP-Modell abgeschätzt. Anders ausgedrückt bringen bei niedrigen Temperaturen nur wenige Teilchen die vom BPP-Modell geforderte Aktivierungsenergie auf, dürften deshalb nicht oder nur sehr selten springen, wodurch auch nur sehr selten Übergänge der m -Niveaus induziert werden könnten (Resonanzbedingung). Die abweichende Steigung der TT-Flanke zeigt jedoch, dass die T_1 -Zeiten bei niedrigen Temperaturen kleiner als vom Modell vorhergesagt sind. Diese erhöhte SGR beruht auf kurzreichweitiger Diffusion in den lokal defekten Bereichen. Je mehr Fehlstellen in die ein Teilchen mit geringem Energieaufwand springen kann desto höher die Abweichung.

Für längere Wegstrecken bzw. Teilchen mit höherer Sprungrate (HT-Flanke) stimmt E_A bzw. T_1 weiterhin mit dem BPP-Modell überein. Das Ratenmaximum ist hier bereits durchlaufen worden und die Vorteile der strukturellen Unordnung sind nicht mehr vorhanden. Abweichungen vom BPP-Modell können z. B. durch nicht einfach-exponentielle Korrelationsfunktionen dargestellt werden (Dreidimensionale Diffusion). Das reale Verhalten

lässt sich dann näherungsweise durch eine gestreckte Exponentialfunktion, wie die häufig verwendete Kohlrausch-Williams-Watts^[13] Funktion beschreiben.

$$G'(t) = G_0 \exp(-(t/\tau_c)^\gamma) \quad (1.31)$$

mit $0 < \gamma < 1$

In seltenen Fällen können reale Proben das symmetrische Bild des BPP-Modells aufweisen, weil sie entweder eine sehr ideale Struktur besitzen oder zufällig Abweichungen gleicher Größe für beide Flanken vorhanden sind. Die Möglichkeit besteht also auch bei niederdimensionaler Diffusion in ungeordneten Systemen. Eine Probe muss somit nicht zwangsläufig, wie weiter oben behauptet, vollkommen homogen sein und vollkommen unkorrelierte, dreidimensionale Diffusion aufweisen, um BPP-Verhalten zu zeigen. Nicht nur deswegen, sondern auch wegen der meist experimentell unzugänglichen HT-Flanke, werden durch NMR ermittelte Aktivierungsenergien mit Werten aus der Impedanzspektroskopie verglichen. Durch Leitfähigkeitsmessungen (Beispiel: Abb.1.9) bei niedrigen Frequenzen erhält man ohne "Temperaturprobleme" Werte der langreichweitigen Diffusion und kann durch den Vergleich mit der relaxometrischen NMR-Messungen Rückschlüsse auf Bewegungsprozesse in der Probe führen. Weitere NMR-Methoden wie z. B. SAE NMR und 2D MAS EXSY NMR können die Untergrenzen der Relaxometrie *umgehen* und so den

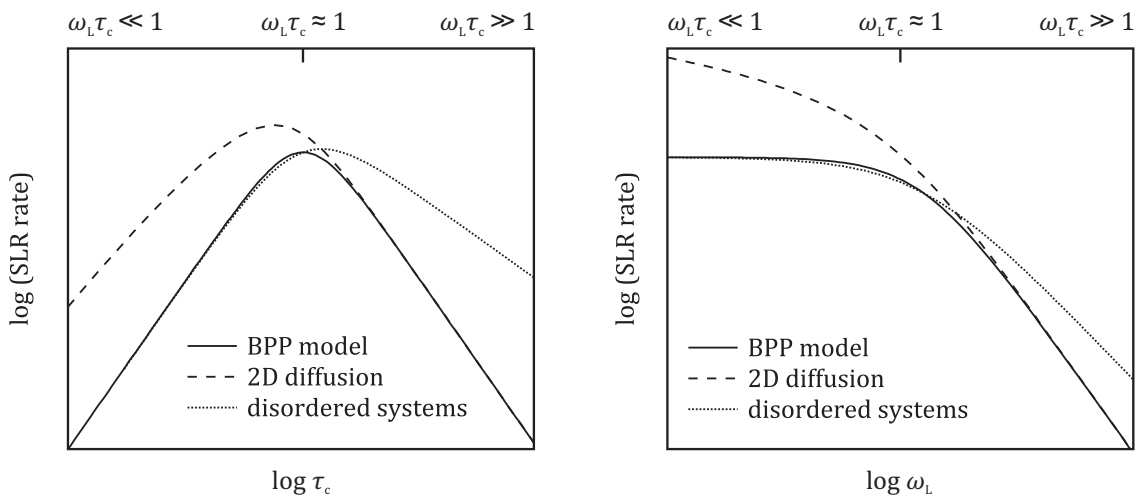


Abbildung 1.7: Spin-Gitter-Relaxationsraten und Abweichungen vom BPP-Modell. Auf der linken Seite ist die Abhängigkeit der Spin-Gitter-Relaxationsrate von der Korrelationszeit und auf rechten Seite von der Larmorfrequenz dargestellt. In beiden Fällen sind die Abweichungen vom BPP-Modell für Systeme mit zweidimensionaler Diffusion (2D und 1D Diffusion) und ungeordnete Systeme wie sie zum Beispiel durch Hochenergiekugelmahlen entstehen, skizziert.^[14] Erklärungen siehe Text.

Bereich von messbaren Probenmaterialien nach unten (kleinere Diffusionskoeffizienten) deutlich erweitern. Korngrößen und amorphe Anteile der Probe bzw. deren Kristallinität, bestimmt über Röntgendiffraktometrie und Rasterelektronenmikroskopie bzw. SAED, sowie Aufenthaltswahrscheinlichkeiten und Pfade der Li-Kationen aus der Neutronenstreuung vervollständigen schließlich das Bild der Dynamik eines Materials.

Abbildung 1.8 greift ein Model^[15–17] auf, dass für die teilweise sehr unterschiedlichen Ergebnisse bei den Aktivierungsenergien und Diffusionskoeffizienten, die durch SGR NMR auf der Tieftemperaturflanke und Leitfähigkeitsmessungen im selben Temperaturbereich erhalten werden, eine Erklärung bietet. Die Zuordnung des Transportmechanismus ist im beschriebenen Fall zwar meistens wie in Abb. 1.8 gezeigt und spiegelt die Einteilung in mikros- und makroskopische Methoden wider, da es sich bei der Impedanz aber nicht um eine nukleare Methode handelt, müssen hier auch noch Effekte, die durch zusätzliche mobile Spezies auftreten können, ausgeschlossen oder in ihrem Anteil bestimmt werden.

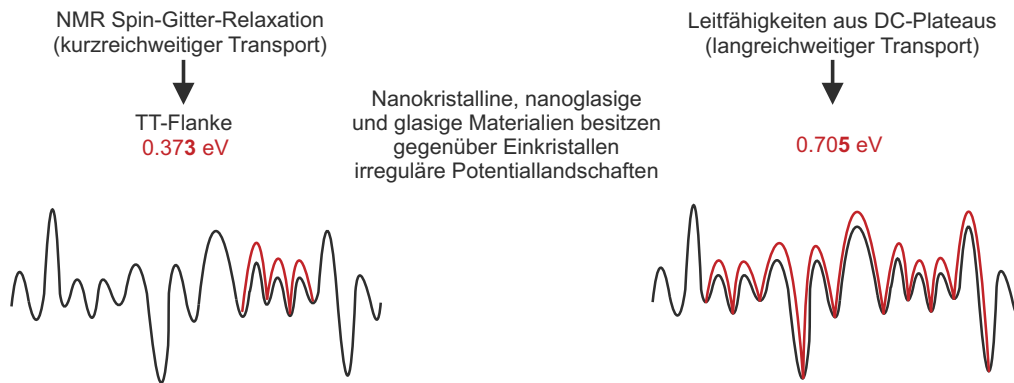


Abbildung 1.8: Der Vergleich zwischen NMR Spin-Gitter-Relaxation und Impedanzspektroskopie zeigt Aktivierungsenergien von glasigem β -Eukryptit für kurzreichweitigen und langreichweitigen Transport. Die schematische Visualisierung einer Potentiallandschaft, soll dabei helfen, sich die unterschiedlich hohen Energiebarrieren in einem ungeordneten System vorzustellen. Die Zuordnung der Messmethoden zu den beobachteten Transportprozessen entspricht nicht dem vollständigen Potential von NMR- und Impedanz-Experimenten, spiegelt aber die üblichen Ergebnisse, bedingt durch Limitierungen im experimentellen Aufbau und/oder der Probeneigenschaften, wider. Werte von HT-Flanken der NMR-Relaxometrie und aus AC-Plateaus der Leitfähigkeitsspektroskopie könnten das umgekehrte Bild zeigen.

Als ein Beispiel sei die Überführungszahl genannt, die das Verhältnis zwischen ionischer und elektronischer Leitung in einem Festkörper angibt. Aber auch Fremdionen wie Na^+ tragen in „reinen“ Lithium-Ionen-Leitern zur Leitfähigkeit bei.

NMR-Methoden, die bis hier nicht ausführlich vorgestellt wurden, aber Teil dieser Arbeit sind, werden in den Kapiteln 2 und 3, sowie in den jeweils weiterführenden Referenzen beschrieben.

1.2 Impedanzspektroskopie

Wie im vorherigen Abschnitt (Abb. 1.8) schon veranschaulicht wurde, können mit der Impedanzspektroskopie d. h. über die Plateaus der Gleichstromleitfähigkeiten bei verschiedenen Temperaturen Diffusionskoeffizienten für den langreichweitigen Transport bestimmt werden. Dafür wird die NERNST-EINSTEIN-Relation

$$D^{NE} = \frac{\sigma_{dc} \cdot k_B \cdot T}{N \cdot q^2} \quad (1.32)$$

für ionische Leiter genutzt. Wobei σ_{dc} die Ionenleitfähigkeit, N die Anzahl der Ionen pro Einheitsvolumen und q die Ladung der Ionen bezeichnet. Ebenso wie bei den NMR-Messungen wird auch der Ladungsdiffusionskoeffizient D^{NE} mit dem Tracerdiffusionskoeffizienten D^{tr} verknüpft:

$$D^{tr} = H_V \cdot D^{NE} \quad (1.33)$$

Den Zusammenhang bekommt man über das HAVEN-Verhältnis H_V , welches im Idealfall einen Wert von eins hat, aber auch etwas größere oder kleinere Werte annehmen kann. Korrelierte Bewegung der Ladungsträger, elektronische Beiträge zur Leitfähigkeit oder z.B. Leerstellenpaare die zur Diffusion beitragen, sind hier alle zusammengefasst. Addieren sich starke Effekte, kann das HAVEN-Verhältnis auch Werte deutlich größer als eins annehmen.

1.2.1 Grundlagen

Die Impedanzspektroskopie beruht auf der einfachen Annahme, dass eine an die Probe angelegte Wechselspannung mit der Amplitude U_0 in einem Wechselstrom mit der Amplitude I_0 resultiert. Es werden also Wechselstromwiderstände der zu analysierenden Materialien bestimmt. Bei einer Messung (definierte, konstante Temperatur) werden viele, zuvor im Messprogramm festgelegte Messpunkte eines Frequenzbereichs aufgenommen. Weil die Frequenzen $\nu = \omega/2\pi$ von Wechselspannung und Wechselstrom jedoch um δ_I phasenverschoben sind, ist das Einführen von komplexen Größen notwendig, die im Folgenden mit einem * gekennzeichnet werden.

$$U^*(\omega) = U_0 \cdot \exp(i\omega t) \quad (1.34)$$

$$I^*(\omega) = I_0 \cdot \exp(i(\omega t - \delta_I)) \quad (1.35)$$

Hierbei ist $i = \sqrt{-1}$ die imaginäre Einheit. Der Wechselstromwiderstand wird analog zum OHMSchen Gesetz $U = R \cdot I$ bestimmt und als Impedanz Z^* bezeichnet:

$$U^*(\omega) = Z^*(\omega) \cdot I^*(\omega), \quad \text{mit} \quad Z^*(\omega) = Z_0 \cdot \exp(i\delta_I) \quad (1.36)$$

Der komplexe Leitwert wird als *Admittanz* Y^* bezeichnet und ist wiederum analog der Kehrwert der Impedanz:

$$Y^* = \frac{1}{Z^*} \quad (1.37)$$

Die spezifischen Leitfähigkeiten σ^* und Widerstände ρ^* sind definiert über:

$$Z^* = \rho^* \cdot \frac{b_z}{A} \quad \text{und} \quad Y^* = \sigma^* \cdot \frac{A}{b_z} \quad (1.38)$$

Wobei A die Querschnittsfläche und b_z die Dicke der Proben bezeichnet. Dadurch kann Gleichung 1.36 als

$$\underline{j_e} = \underline{\sigma^*} \cdot \underline{E} \quad (1.39)$$

geschrieben werden. Hier ist $\underline{\sigma^*}$ der Leitfähigkeitstensor, wodurch z.B. verschieden dicke Tabletten direkt miteinander verglichen werden können, da die Dimensionen der Probe nicht mehr mit eingehen. Die Stromdichte $\underline{j_e} = I/A$ im Material ist die Antwort des Systems auf das elektrische Feld $\underline{E} = U/b_z$, welches von außen angelegt wird.

1.2.2 Leitfähigkeitsspektren

In dieser Arbeit wird nur ein sehr kleiner Bereich des möglichen Frequenzspektrums betrachtet. Die Gleichstromleitfähigkeit σ_{dc} gehört zum *Impedanzbereich*, welcher mit Frequenzen unterhalb einiger 10 MHz erst am Anfang des gesamten Spektrums der Analysemethoden liegt. Daran schließen sich noch der *Radiofrequenzbereich* (von einigen 10 MHz bis zu einigen GHz), der *Mikrowellenbereich* (von einigen GHz bis ca. 150 GHz) und der (*Fern-*)*Infrarotbereich* (oberhalb von 150 GHz) an.

Die Kontaktierung der Proben mit Elektroden, wie z.B. Silber oder Graphit (aufgetragen als Paste), wodurch eine schnelle Probenvorbereitung unterschiedlicher Materialien für den immer gleichen Messplatz möglich ist, findet nur im Impedanzbereich Anwendung. Um doppelte Probenvorbereitung zu vermeiden und die Messungen jederzeit auch auf den *Radiofrequenzbereich* erweitern zu können, ist die Bedampfung der Proben mit oder das Aufputtern von Gold bzw. Platin sinnvoll. Als internes Standardverfahren hat sich hier auf Grund des Preis/Leistungsverhältnisses das Aufputtern von 50 nm Gold als Elektroden durchgesetzt.

Bei *Leitfähigkeitsspektren* (Beispiel in Abb. 1.9) wird der Realteil σ' der spezifischen Leitfähigkeit $\sigma^* = \sigma' + i\sigma''$ gegen die Frequenz ν oder $\omega = 2\pi\nu$ doppelt logarithmisch aufgetragen.

Hochfrequenz-Plateaus werden erst oberhalb von 100 GHz erreicht, wo die Leitfähigkeit durch phononische Beiträge bestimmt ist, welche nicht in jedem Fall heraus gerechnet

werden können, sodass dieses Plateau nicht immer zur Auswertung herangezogen werden kann. Spektren in dieser Arbeit wurden nur bis ca. 10 MHz aufgenommen, weshalb hier auch nicht weiter auf den *dispersiven Bereich* eingegangen wird. Es sei nur kurz angemerkt, dass mit steigender Frequenz auch die *ac*-Leitfähigkeit monoton bis zum infraroten Frequenzbereich ansteigt. Dieses als *Dispersion* bekannte Verhalten zeigt sich bei vielen Festkörpern und ist auf die nicht-idealen Phänomene wie z.B. Wechselwirkungen zwischen den Ionen oder Fehlstellen im Gitter zurückzuführen. Bei noch tieferen Frequenzen kann ein *dc-Leitfähigkeitsplateau* $\sigma_{dc} = \sigma'(0)$ beobachtet werden. In den meisten Fällen zeigt $\sigma_{dc}T$ Arrhenius-Verhalten mit einer Aktivierungsenergie $E_{A,dc}$.^[18]

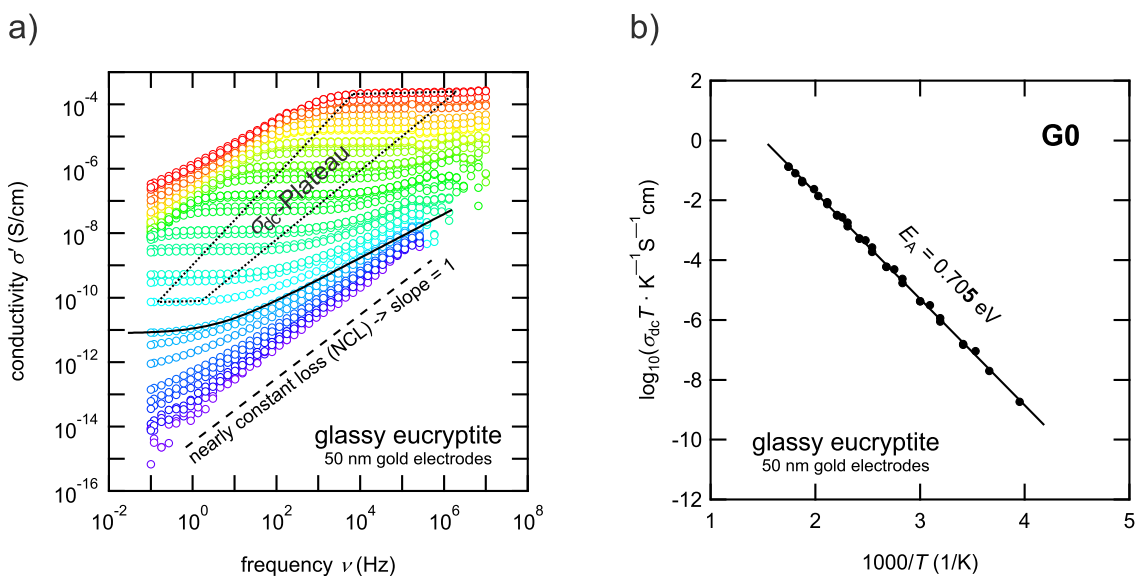


Abbildung 1.9: a) Leitfähigkeitsspektren von glasigem β -Eukryptit. Probenvorbereitung: Rundgeschliffenes Glasplättchen mit einem Durchmesser von 1 cm und einer Stärke von ca. 2 mm. Temperaturbereich: $-100\text{ }^{\circ}\text{C}$ (lila) bis $+300\text{ }^{\circ}\text{C}$ (rot), wobei Werte für σ_{dc} nur oberhalb von $-10\text{ }^{\circ}\text{C}$ direkt abgelesen werden können (siehe markierter Bereich). Die Leitfähigkeitsspektren können auch mit einem *powerlaw*^[19] (schwarze Linie) angefitet werden, um einen Wert für σ_{dc} abzuschätzen. In b) sind diese Werte multipliziert mit der Temperatur in Kelvin logarithmisch gegen die inverse Temperatur aufgetragen. Aus diesem Arrhenius-Plot kann die Aktivierungsenergie E_A direkt abgelesen werden.

2 Experimentelles: Techniken, Geräte und Synthesewege

In diesem Kapitel werden die angewandten experimentellen NMR-Methoden (siehe Abb. 2.1) im Detail vorgestellt. Dabei wird jeweils kurz auf Vor- und Nachteile der jeweiligen Methode, sowie die sich daraus ergebende Nutzbarkeit zur Charakterisierung von Materialien eingegangen. Die theoretischen Grundlagen werden dabei nur dann herangezogen, wenn sie für das Verständnis des durchgeführten Experiments unabdingbar sind. Weiterführende Referenzen werden in den folgenden Abschnitten trotzdem nur teilweise gegeben, da die Veröffentlichungen in Kapitel 3 die jeweilige Literatur zitieren.

Der Großteil der durchgeführten Messungen basiert auf sogenannten *time-domain* Kernresonanzmethoden und hochauflösenden EXSY NMR-Messungen. Impedanzspektroskopische und elektrochemische Messungen ergänzen teilweise die durchgeführten NMR-Studien. Diese Hilfsmittel komplettieren das eingesetzte Methodenrepertoire. Standardcharakterisierungen wie XRD, ICP-OES, (HR)TEM und AAS wurden an manchen Proben ebenfalls durchgeführt. Diese Messungen wurden jedoch fast alle in Auftrag gegeben und werden hier deshalb nicht weiter erläutert.

Da es sich bei den untersuchten Proben ausschließlich um Festkörper handelt, wird teilweise der Begriff Festkörper-NMR bzw. *solid state NMR* verwendet. Auch wenn sich die Anforderungen an die Probenvorbereitung, der Fokus der Analyse und die erhaltenen Ergebnisse stark von der Flüssig-NMR unterscheiden, handelt es sich hierbei nicht um eine spezielle Methode. Es werden sogar teilweise die gleichen „Programme“, sogenannte Pulssequenzen verwendet, wie sie zum Beispiel auch für die Strukturaufklärung von organischen Molekülen üblich sind.

Eine Studie zur Dynamik eines bestimmten Ions in einem Festkörper (in dieser Arbeit ausschließlich Li^+ , aber auch für folgende Ionen interessant: H^+ , F^- und Na^+) nutzt diese Pulssequenzen zur Aufnahme von vielen Spektren. Meist wird dabei nur ein Parameter pro Temperatur variiert. Über den gesamten Temperaturbereich können aber leicht Hunderte wenn nicht sogar Tausende Spektren zur Charakterisierung des Materials nötig werden. Abgesehen von den Fragestellungen, Strukturaufklärung oder dynamische Eigenschaften des Probenmaterials, zeigt sich hier der in der Praxis größte Unterschied von der Flüssig-NMR zur Festkörper-NMR – die Messzeit. Die vollständige Untersuchung eines Materials kann durchaus Wochen oder Monate dauern.

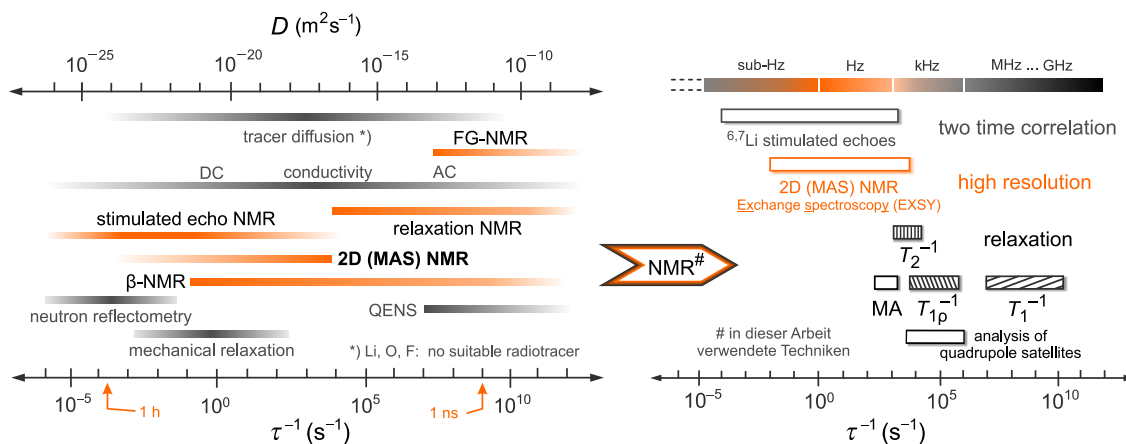


Abbildung 2.1: Etablierte makroskopische und mikroskopische Methoden zur Untersuchung von Selbst-Diffusion (links) und die in dieser Arbeit verwendeten NMR-Techniken (rechts). Nukleare und nicht-nukleare Methoden wurden nicht besonders gekennzeichnet. Leitfähigkeitsmessungen sind aber im Gegensatz zur NMR eine nicht-nukleare Methode. [14,20]

2.1 Kernresonanzmethoden und Ausstattung

Für die NMR-Messungen standen während der Entstehung dieser Arbeit insgesamt fünf verschiedene Bruker-Spektrometer zur Verfügung. Die zwei Geräte der Serie MSL (*Multipurpose Solids and Liquids*) wurden mit Kryomagneten der Firma Oxford betrieben. Deren nominale ${}^1\text{H}$ -Frequenzen betragen 200 MHz, was einer Magnetfeldstärke von $B_0 = 4.7$ Tesla entspricht (MSL 100) und 400 MHz ($B_0 = 9.4$ Tesla) am MSL 400. Beide Spektrometer werden in Hannover im Arbeitskreis von Prof. Heitjans betrieben. Außerdem konnten dort zwei Bruker-Spektrometer der Serie AVANCE III genutzt werden. Die zugehörigen Kryomagneten waren ebenfalls von der Firma Bruker und entsprachen folgenden Ausführungen: 600 MHz Ultrashield Plus und 300 MHz Ultrashield, beide als Variante WB (engl. für *wide bore*) geeignet für 89 mm Durchmesser Probenköpfe. Der 300 MHz Messplatz wurde am 25.01.2012 nach Graz transportiert, wo einige Monate später (August – Oktober) auch noch ein 500 MHz WB Ultrashield Plus AVANCE III Spektrometer installiert wurde (Abb. 2.2).

2.1.1 Relaxometrie

Die theoretischen Grundlagen für die Bestimmung der Li-Dynamik eines Festkörpers mittels NMR relaxometrischen Messungen wurden im Kapitel 1.1.1 anhand des Beispiels der T_1 -Zeit (longitudinale Relaxation) schon gezeigt. Da die Feldstärken der heutigen Kryomagneten immer im oberen einstelligen und ab 500 MHz Magneten sogar im zweistelligen Tesla-Bereich liegen (500 MHz bzw. 600 MHz für $\omega_{0,1\text{H}}$ resultieren aus 11.7 bzw.



Abbildung 2.2: 500 MHz Spektrometer in Graz. Foto vom 05.09.2012. Der Ultrashield Plus Magnet ist schon vollständig aufgebaut, evakuiert und eingekühlt. Die leeren Heliumkannen sind im Hintergrund zu sehen. Die Konsole und die Palette mit den Probenköpfen und dem Zubehör (rechte Bildhälfte) sind noch originalverpackt. Der PC zur Ansteuerung des Arbeitsplatzes ist noch auf dem Schreibtisch im Vordergrund aufgebaut. Die linke Bildhälfte zeigt ein 500 MHz Flüssig-NMR-Spektrometer mit ungeschirmten Magneten der Firma Oxford.

14.1 Tesla), ergeben sich für die NMR aktiven Kerne Resonanzfrequenzen von einigen MHz (z. B. 5.3 MHz für ^{197}Au bei 7 Tesla) bis zu aktuell 1 GHz für Protonen in einem 23.5 Tesla Magneten. Für die Relaxometrie dieser Arbeit wurden die Kerne $^{7,6}\text{Li}$ verwendet. Im Bereich von 4.7 – 14.1 Tesla ergeben sich Resonanzfrequenzen von 29.4 – 233.2 MHz. Die T_1 -Messungen (Spin-Gitter-Relaxation) sind in Abbildung 2.1 absichtlich etwas breiter eingezeichnet, da die Messungen des nicht-diffusiven Bereichs (Untergrund) bei tiefen Temperaturen (*rigid lattice*) über die diffusionsinduzierte Erhöhung der Raten ($1/T_1$) bei höheren Temperaturen und bei Temperaturen oberhalb des Ratenmaximums auch niedrigere und höhere Sprungraten detektieren können. Die mittlere Verweilzeit des Lithiums auf seinem Gitterplatz sollte für diese Technik und den messbaren Temperaturbereich zwischen 1 μs und 1 ns liegen, um die Dynamik des Diffusionsprozesses präzise erfassen zu können.

Bruker *single X*-Hochtemperaturprobenköpfe und Probenköpfe gleicher Bauart, jedoch mit Teflon-Probenkammer anstatt Keramik, decken gemeinsam einen Temperaturbereich von ca. -150°C bis ca. 350°C (zusätzlicher *booster* für die Heizeinheit erforderlich, sonst nur max. 220°C möglich) ab. Schnelle und sehr schnelle Li-Ionen-Leiter liefern in diesem

Temperaturbereich ein Ratenmaximum und ausreichend Datenpunkte zur Bestimmung der Aktivierungsenergie aus der HT-Flanke (siehe Abb. 1.6). Um die Relaxometrie auch für „langsamere“ Materialien zugänglich zu machen, wurde die sogenannte *spin-lock*-Technik entwickelt, bei der die Vorteile eines modernen Kryomagneten und dessen hohes Feld B_0 mit einem um mehrere Größenordnungen kleineren Feld $B_{\text{lock}} = B_1$ kombiniert wird.

T_1 und $T_{1\rho}$ -NMR Der technische Aufbau ist für beide Methoden exakt gleich (siehe Abb. 2.3). Für Messungen im Laborkoordinatensystem wie auch im rotierenden Koordinatensystem ist der erste gesendete Plus P_1 ein 90° -Puls, der die makroskopische Magnetisierung je nach Eintrag der Phasenliste auf die x' -, $-x'$ -, y' - oder $-y'$ -Achse des Koordinatensystems kippt. Im Falle der T_1 -Messungen hat davor noch eine Pulsfolge von $90^\circ|x$ -Pulsen zu erfolgen (meistens 10 sogenannte Zerstörungspulse), damit sich $M(t)$ eine definierte Wartezeit wieder aufbauen kann, um dann direkt nach P_1 in der x,y -Ebene als $M_{x,y}$ detektiert werden zu können. Beim *spin lock* Verfahren wird die $T_{1\rho}$ -Zeit im rotierenden Koordinatensystem bestimmt. D. h. es wird immer M_0 (vollständig relaxierte Probe; in der Praxis $5 \times T_1$ Wartezeit vor jedem Scan) in die x', y' -Ebene gekippt und dann eine definierte Zeit t_{lock} "gewartet", bevor die in dieser Ebene verbliebene Magnetisierung detektiert wird. Dabei verhindert ein zweiter Radiofrequenzpuls P_2 geringerer Leistung (typischerweise zwischen ca. 5 und 30 Watt; vgl. $P_1 = 200$ Watt oder mehr), dass das Spinensemble in der Ebene dephasiert. M' wird dadurch, je nach voreingestellter Phase in Richtung x' , $-x'$, y' oder $-y'$ festgehalten. Detektiert wird in genau dieser Richtung. Eine

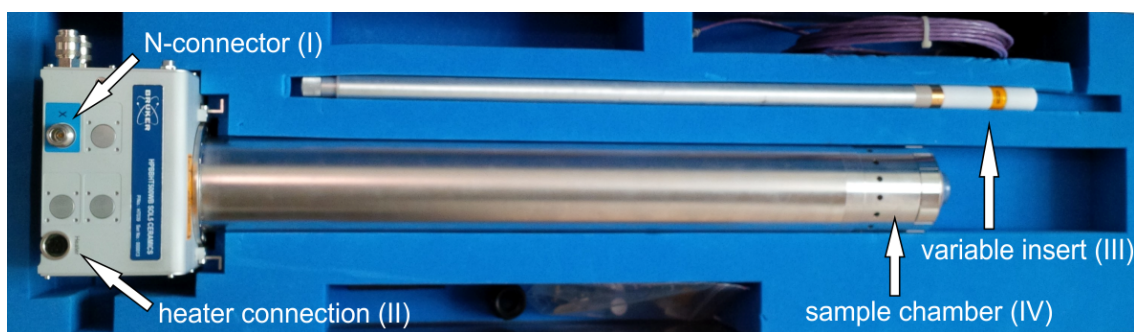


Abbildung 2.3: Ein *single-X*-Probenkopf der Firma Bruker verfügt über einen Anschluss (I) für den Hochleistungsradiofrequenzverstärker des Spektrometers, über eine Heizwendel im Inneren des Dewars, durch den das *VT gas* (Anschluss auf der Rückseite) zur Probenkammer (IV) geleitet wird, eine Buchse (II) für den Anschluss des Heizverstärkers und wechselbare *inserts* (III; Kondensator mit oder ohne Dämpfungswiderstand) zur Änderung des Frequenzbereichs. Im Inneren der Probenkammer befindet sich eine Spule mit 5 mm Innendurchmesser, die gleichzeitig als Probenhalterung dient. Das Gehäuse und die elektronischen Bauteile werden über trockene Druckluft oder Stickstoff-Gas gekühlt. Ein Thermoelement des Typs E dient zur Temperaturmessung nahe der Spule.

Liste mit variablem t_{lock} d. h. mit unterschiedlich langen *locking* Pulsen, ergibt einen im Idealfall einfach exponentiellen Zerfall von M' .

$$M' = M_0 \cdot e^{-(t_{\text{lock}}/T_{1\rho})^\gamma} \quad (2.1)$$

Der Streckfaktor γ korrigiert Abweichungen realer Proben. Dieser kann Werte größer null und kleiner eins annehmen, wobei 0.5 ein Indiz für das Ratenmaximum ist und γ für den nicht diffusionsinduzierten Bereich häufig Werte von fast eins annimmt. Streckfaktoren die deutlich von diesem Verhalten abweichen sind ein Hinweis für einen schlechten Fit. Dies kann der Fall sein, wenn z. B. ein zweiter Relaxationsprozess mit zunehmender Temperatur aktiviert wird und die Transienten doppelt exponentiell gefittet werden müssten. Wenn die Relaxationsraten dieser Prozesse sehr ähnlich sind, können zusätzliche Experimente nötig sein, um das Verhalten der Probe besser zu verstehen und die Daten richtig zu fitten.

Details zur Pulssequenz, Spektraldichte- und Korrelationsfunktion sind z. B. in den Referenzen^[21-27] gegeben und werden in den jeweiligen Publikationen im Kapitel 3 erklärt bzw. mit Referenzen belegt.

T_2 -Messungen nehmen den Zerfall der Magnetisierung in der x, y -Ebene direkt nach einem $90^\circ |x$ -Puls auf. Diese Technik nutzt die Spin-Spin-Relaxation (SSR) und ist geeignet um noch langsamere Bewegungsprozesse zu erfassen, als mit den oben aufgeführten SGR-Methoden. Typische Sprungraten liegen hierbei im unteren kHz-Bereich. Damit wird die Lücke zwischen SGR-Messungen im rotierenden Koordinatensystem und der einfachen Linienformanalyse geschlossen. Das *motional averaging* (MA) der „Zentral“linie liefert Sprungraten von mehreren Hundert Hz bis hin zu wenigen kHz.

MA Die bewegungsinduzierte Verschmälerung der Zentrallinie eines NMR-Spektrums kann erfasst werden, indem die Linienbreiten auf halber Linienhöhe FWHM (*full width at half maximum*) ausgelesen werden und gegen die Temperatur aufgetragen werden. Im geeigneten Temperaturbereich wird eine Kurve mit Linienbreiten erhalten, die bei niedrigen Temperaturen das starre Gitter widerspiegeln (einige kHz) und bei hohen Temperaturen die natürliche Linienbreite zeigen (*extreme narrowing*). Dazwischen findet das *motional narrowing* statt. Dieser Verlauf kann mit den (halb-)empirischen Funktionen von Hendrickson und Bray^[28], Waugh und Fedin^[29] oder anderen Modellen angepasst werden, um Aktivierungsenergien abzuschätzen.

2.1.2 SAE NMR

Spin-Gitter und Spin-Spin Relaxationsmessungen liefern Informationen über Transportprozesse mit Sprungraten vom kHz- (selten einstellig) bis hin zum dreistelligen MHz-Bereich. Diese Grenzen der Relaxometrie und die theoretisch komplexe Interpretation der erhal-

tenen Raten und Flankensteigungen, stehen der experimentell einfachen Aufzeichnung und der nahezu relaxationsmodellunabhängigen Bestimmung der Korrelationszeit τ_c am Ratenmaximum ($\omega_0\tau_c \approx 1$ im Falle von T_1 - und $\omega_1\tau_c \approx 0.5$ für $T_{1\rho}$ -Messungen) gegenüber.

Linienformanalysen, wie das MA der Zentrallinie oder die Analyse der *electric quadrupolar interactions*, in Form von Quadrupolsatelliten, liefern nicht voraussetzungsfrei Hinweise auf die Sprungraten und müssen über die gleichen Temperaturbereiche wie die relaxometrischen Methoden durchgeführt werden.

Die Methode des Spin-Alignment-Echos (SAE) erlaubt es langreichweitige Li-Diffusionsprozesse aus atomarer Sichtweise zu untersuchen. Darin sind gleich drei Vorteile gegenüber der Relaxometrie enthalten. (i) SAE-NMR-Messungen geben direkten, modellunabhängigen Zugang zu Sprungraten. (ii) Die Zwei-Zeiten-ein-Teilchen Korrelationsfunktion ist in der Lage, auch sehr langsame Bewegungsprozesse (bis in den sub-Hertz-Bereich) zu detektieren. (iii) Die Messmethode ist unabhängig vom externen Magnetfeld (gutes S/N vorausgesetzt).

Entwickelt wurde die Zwei-Zeiten Spin-Alignment-NMR von Spiess, um ultralangsame Bewegungen von Deuteronen zu beobachten^[30,31]. Der ^2H -Kern bietet sich auf Grund seines großen Kernquadrupolmoments an, da die Wechselwirkung dessen mit den elektrischen Feldgradienten (EFG) des umgebenen Gittergitters in Wechselwirkung tritt. Die Dipol-Dipol Kopplungen sind hier, anders als bei z. B. ^7Li , vernachlässigbar klein. Nichtsdestotrotz hat sich die SAE-NMR auch für Kerne mit kleinerem Q_z und $I > 1$ etabliert.^[32-34]

Das Prinzip ist sehr ähnlich zu Austausch-Experimenten, wie sie in 2.1.3 behandelt werden und beruht auf einer Dreipulsfolge nach Jeener und Broekaert^[35]

$$\beta_{1\phi_1} - t_p - \beta_{2\phi_2} - t_m - \beta_{1\phi_3} - t \quad (2.2)$$

wobei für die Pulslängen gilt $\beta_1 = 90^\circ$ und $\beta_2 = \beta_3 = 45^\circ$. ϕ_i sind die entsprechenden Pulsphasen und t_p sowie t_m bezeichnen die Evolutions- und Mischzeit des Experiments.

Während der Evolutionszeit wird ein stimuliertes Echo erzeugt, dessen Intensität als Funktion der Mischzeit aufgenommen wird. Die abgespeicherten Phaseninformationen erlauben es dabei zu beobachten, ob die Sondenkerne (in dieser Arbeit ^7Li) während der Mischzeit verschiedenen EFGs ausgesetzt waren. Springen die Ionen also zu elektrisch inäquivalenten Gitterplätzen, wird eine Echodämpfung auftreten. Listen geeigneter Mischzeiten liefern Echo-Zerfallskurven, die die Zwei-Zeiten-ein-Teilchen Korrelationsfunktion repräsentieren.

$$S_2 \propto \exp[-(t_m/\tau_{\text{SAE}})^\gamma] \cdot A \quad (2.3)$$

Der Einfluss von t_p und eine detailliertere Beschreibung der Methode wird durch Wu et al. und Böhmer et al. gegeben.^[32,36–38] Außerdem sind in Abschnitt 3.3.1 die experimentellen Details und Grundlagen der Technik für die Ergebnisse einer aktuellen SAE-NMR-Studie dieser Arbeit gegeben.

Alle statischen Methoden vereinen die Vorteile der einfachen Probenvorbereitung bei sicherer Handhabung auch von luftempfindlichen Materialien durch Abschmelzen in Glasampullen. Die nötigen Probenköpfe sind zudem relativ preisgünstig.

2.1.3 1D MAS und 2D EXSY MAS NMR

Die breiten statischen Linien von Festkörperspektren beruhen auf einer Reihe von Wechselwirkungen, die bei Molekülen in Lösung durch die schnelle Bewegung (Translation und vor allem Rotation) ausgemittelt werden. Für ein beliebiges Spinsystem können die Felder, die darauf wirken, zunächst als interne und externe Hamiltonoperatoren betrachtet werden. Die Summe daraus ist der Gesamt-Hamiltonoperator.

$$\hat{H}_{\text{ges}} = \hat{H}_{\text{ext}} + \hat{H}_{\text{int}} \quad (2.4)$$

Die externen Felder haben für diese Arbeit eine große Bedeutung. Das externe statische Magnetfeld B_0 und die Zeeman-Aufspaltung sind Summanden von \hat{H}_{ges} . Die Technik des *magic angle spinnings* (MAS) hat darauf jedoch keine Auswirkungen.

Wird \hat{H}_{int} für die Flüssig- und für die Festkörper-NMR betrachtet (Gleichungen 2.5 und 2.6), wird schnell klar, warum statisch aufgenommene Spektren von Pulverproben nahezu immer nur eine breite NMR-Linie liefern.

$$\hat{H}_{\text{int}} = \hat{H}_{\text{CS}}^{\text{iso}} + \hat{H}_{\text{J}} \quad (2.5)$$

$$\hat{H}_{\text{int}} = +\hat{H}_{\text{CS}}^{\text{aniso}} + \hat{H}_{\text{D, hetero}}^{\text{aniso}} + \hat{H}_{\text{D, homo}}^{\text{aniso}} + \hat{H}_{\text{Q}}^{\text{iso}} + \hat{H}_{\text{Q}}^{(1)\text{aniso}} + \hat{H}_{\text{Q}}^{(2)\text{aniso}} \quad (2.6)$$

Durch die Rotation einer Pulverprobe im magischen Winkel zum externen Magnetfeld können die anisotropen Wechselwirkungen bis zur ersten Ordnung vollständig ausgemittelt werden, wenn die Rotationsfrequenz deutlich größer ist als die anteilige Verbreiterung der statischen Linie. Abb. 2.4 zeigt die technische Umsetzung für die Auslöschung des Terms $(3 \cos^2 \theta - 1)$, den alle genannten Hamiltonoperatoren enthalten. \hat{H}_{int} vereinfacht sich so zu

$$\hat{H}_{\text{int}} = \hat{H}_{\text{CS}}^{\text{iso}} + \hat{H}_{\text{Q}}^{\text{iso}} + \hat{H}_{\text{Q}}^{(2)\text{aniso}} \quad (2.7)$$

und die NMR-Linien eines 1D MAS NMR-Spektrums werden deutlich schmaler. Dadurch können auch einzelne Gitterplätze bei zueinander geringer chemischer Verschiebung aufgelöst werden (siehe z. B. Seite 43ff).

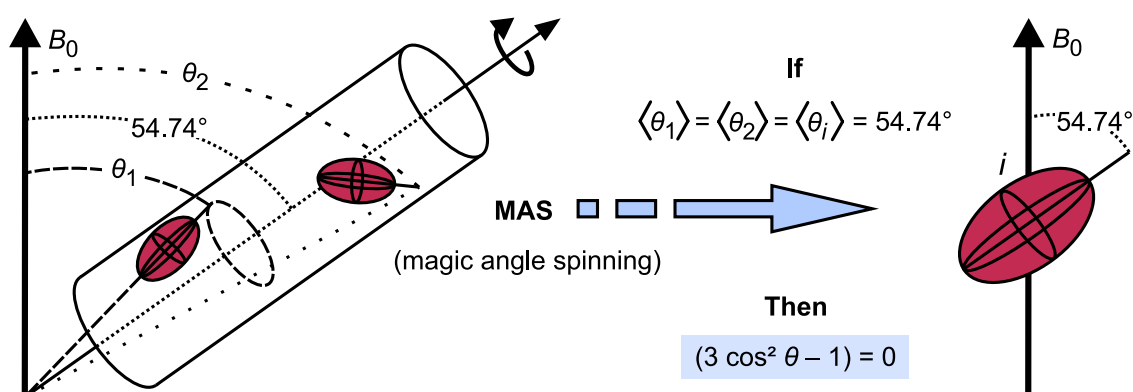


Abbildung 2.4: Die schematische Darstellung eines MAS-Rotors im Magnetfeld B_0 und zwei ausgewählte Kernspins mit willkürlicher Ausrichtung zu B_0 (links). Bei hinreichend schneller Rotation nehmen die Winkel θ_i einen gemittelten Wert von 54.74° an und die Hamilton-Operatoren, die proportional zu $(3 \cos^2 \theta - 1)$ sind, werden 0 und fallen aus \hat{H}_{int} heraus (rechts). Geeignete Probenköpfe erreichen aktuell bis zu 100 kHz Rotationsfrequenz.

2D EXSY MAS NMR Die Aufnahme von zweidimensionalen Spektren mit einer indirekten Dimension F1 und einer direkten Dimension F2 für den selben Sondenkern ermöglicht die Beobachtung von Austauschprozessen zwischen magnetisch inequivalenten Gitterplätzen. Bei einer Modellsubstanz mit nur zwei unterschiedlichen Gitterplätzen, die von Lithium besetzt werden können, tritt dann der Idealfall ein, dass aus den beobachteten Sprüngen direkt die durchschnittliche Sprungrate berechnet werden kann. Das zugrundeliegende Experiment ist ein phasensensitives Nuclear Overhauser Enhancement Experiment*. Da es bei Isotopen mit geringer natürlicher Häufigkeit, wie es bei ^6Li der Fall ist, keinen NOE sieht (und auch keine anderen unerwünschten Wechselwirkungen wie z. B. Spin-Spin), sondern echten Austausch, kann das E in NOESYph (Bruker-Pulsprogramm) doppelt gedeutet werden und das Experiment bekommt den *Zusatz: und Exchange Spectroscopy. Die Pulssequenz und die Auftragung des 2D Spektrums nach doppelter Fourier-Transformation (FT) sind in Abbildung 2.6 dargestellt.

Bei mikrokristallinem Li_2ZrO_3 z. B. ist die T_1 -Zeit (^7Li NMR Messungen) auch für einen Festkörper sehr lang (s. S. 43). Die Wartezeit zwischen den einzelnen scans müsste mindestens 25 Minuten betragen, damit die longitudinale Magnetisierung wieder vollständig aufgebaut wird. Die Zerstörungspulsfolge aus dem *satrect1* Experiment wurde daher mit NOESYph kombiniert, um die Messzeit von etwa 5 Wochen auf 6 – 8 Tage (je nach Mischzeit t_m) zu reduzieren. Die neue Pulsfolge ist in Abb. 2.5 skizziert.

Das Experiment selbst besteht aus drei Phasen. Die Zeit zwischen dem ersten und dem zweiten Puls ist die Präparationszeit t_p , die automatisch berechnet wird. Sie hängt von der spektralen Weite der indirekten Dimension und den slices auf dieser F1-Achse (Bruker Bezeichnung) ab. Anders ausgedrückt, von der Anzahl Spektren, die in F2 aufgenommen

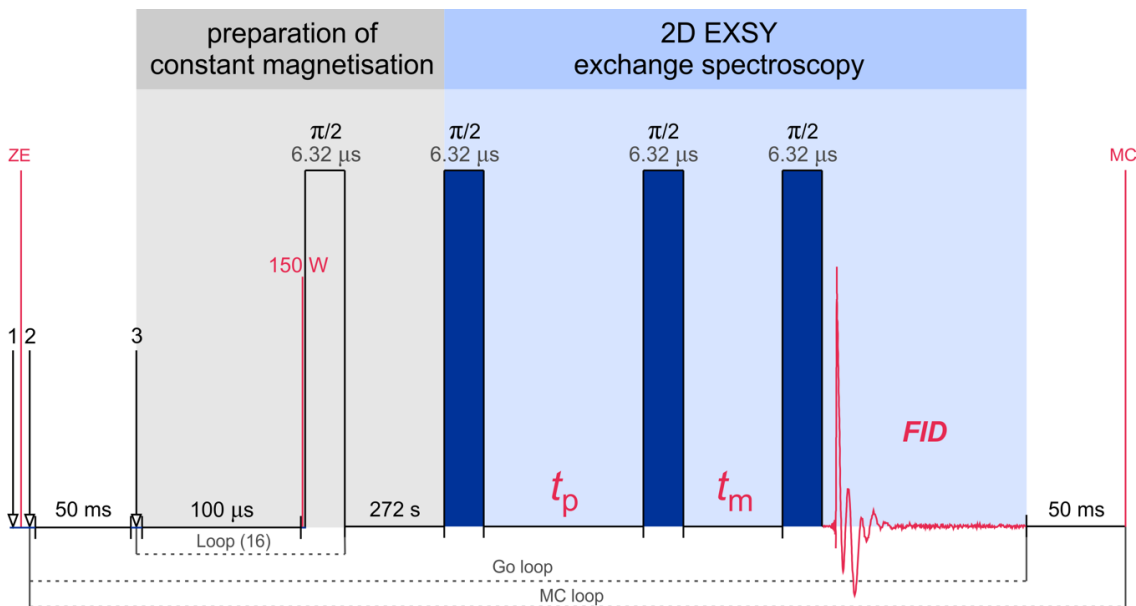


Abbildung 2.5: Pulssequenz für Austauschexperimente an Materialien mit sehr langen T_1 -Zeiten. Die Variablen und der FID gehören einem Experiment am Li_2ZrO_2 . Die genutzte Magnetisierung entsprach der von $1 \times T_1$.

werden, um F1 zu konstruieren. Dafür wird die *acquisition time* der indirekten Dimension durch die Anzahl *slices* geteilt und inkrementell abgearbeitet.

Das fertige 2D Spektrum wird als *contour plot* (2D mit Höhenlinien) oder dreidimensional dargestellt. In Abb. 2.6 sind Pulssequenz, Fourier-transformierte 2D *contour plots* und der Wechsel eines Sondenkerns von einem Gitterplatz mit ω_1 zu einem anderen mit ω_2 gezeigt. Die Hauptintensitäten (*peaks* des 1D Spektrums) liegen auf der Diagonalen dieser Auftragung und sind auch ohne Austausch immer vorhanden. Finden während der Mischzeit t_m Platzwechsel statt, wachsen proportional zusätzliche *peaks*, die sogenannten *cross peaks*, auf den Schnittpunkten der Horizontalen und Vertikalen durch die Hauptintensitäten heraus. In Materialien mit mehr als zwei magnetisch unterschiedlichen Positionen kann so also auch bestimmt werden, welche Plätze an den Diffusionsprozessen beteiligt sind.

Um nur Austausch zu beobachten, sollte die zu untersuchende springende Spezies verdünnt im Material vorliegen. D. h. die nächsten Nachbarn müssen mit hoher Wahrscheinlichkeit Ionen anderer Elemente oder andere Isotope sein. Für ^2H ist dies sehr gut erfüllt und für ^6Li gilt diese Näherung in den meisten Systemen auch noch hinreichend. Es gibt aber auch Materialien, wie z. B. Li_3N , in denen die Lithiumdichte so hoch ist, dass selbst bei Messungen an ^6Li NOEs aufgenommen werden bzw. *spin*-Diffusion für das Auftreten von *cross peaks* verantwortlich ist.

- EXSY pulse sequence identical to NOESY experiment (NOE = nuclear Overhauser effect)
dipole-dipole coupling through space

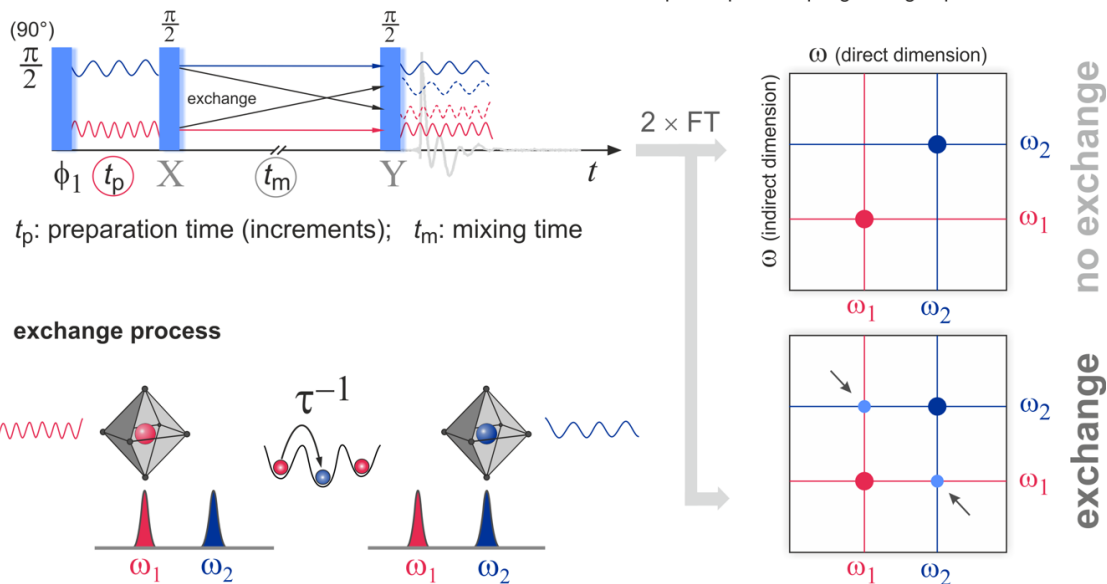


Abbildung 2.6: Schematische Darstellung von NOESY bzw. EXSY Pulssequenz und der Aufbau des 2D Spektrums ohne und mit *cross peaks*. Außerdem zwei magnetisch unterschiedliche Gitterplätze mit ω_1 (rot) und ω_2 (blau), die auch so als Hauptintensitäten auf der Diagonalen des *contour plots* liegen.

2.2 Impedanz- und Leitfähigkeitsspektroskopie

Für die Impedanzspektroskopie (Messungen der Impedanz, Admittanz, Kapazität, etc. werden in dieser Arbeit nicht gezeigt) bzw. Leitfähigkeitsmessungen wurde ein Geräte-Paket *Concept 80* der Firma Novocontrol verwendet. Der Alpha-A Impedanz Analyser und die aktive Messzelle ZGS ermöglichen einen Frequenzbereich von 3 μHz bis 20 MHz. Der zweite Analyser (Agilent 4991E) erweitert diesen Bereich im Zusammenspiel mit einer Novocontrol Eigenbau Messzelle bis zu Frequenzen über 1 GHz. Die Temperatur kontrolliert das System über das Quatro Cryosystem und die Software WinDETA (Novocontrol). Der Messbereich dieser Arbeit beinhaltet Temperaturen von 173 K bis 523 K.

2.3 Synthese von Titandioxid Nanoröhren [TiO₂(nt)] mit Anatas-Modifikation

Die Synthese der Anatas Nanoröhren wurde nach einer leicht abgewandelten Vorschrift aus dem Arbeitskreis von Prof. Dr. Peter G. Bruce (St. Andrews / SCHOTTLAND) durchgeführt. Die Originalvorschrift beschreibt die Darstellung von Nanoröhren der Modifikation TiO₂(B).

Bis zu diesem Zeitpunkt war es nicht gelungen, die Anatas-Modifikation als Hauptprodukt oder gar phasenrein herzustellen. Untersuchungen an *meso*-strukturiertem Titandioxid (Veröffentlichung siehe Seite 78) zeigen, dass TiO₂(B) in dieser Morphologie eine niedrigere Aktivierungsenergie für den Lithiumtransport besitzt als die Anatasmodifikation. Die elektrochemische Interkalation von Lithium bewirkt außerdem die Umwandlung von Anatas zu TiO₂(B). Bei den Nanoröhren stellte sich heraus, dass es während der Synthese ein sehr empfindliches Gleichgewicht gibt, das über den pH-Wert in einem Aufarbeitungsschritt gesteuert werden muss, um die Anatas Nanoröhren zu erhalten.

Insgesamt erfolgt die Synthese von [TiO₂(nt)] in drei Schritten: (i) Hydrothermalsynthese, (ii) Ionenaustausch und (iii) Kalzinierung. Die Formierung von Nanoröhren findet bereits während der Hydrothermalsynthese statt und ist in Abb. 2.7 im Detail illustriert. Das Zwischenprodukt ist ein Titanat der Zusammensetzung Na_{2-x}H_xTi_nO_{2n+1} · yH₂O und wird im Schritt (ii) zunächst in *dest.* Wasser suspendiert und wieder abfiltriert, bevor das Suspendieren in 0.1 M HCl für jeweils mindestens 24 Stunden so lange wiederholt wird, bis der pH-Wert leicht sauer ist. Dieser Prozess wäscht die Natronlauge aus der Probe bzw. ermöglicht den Ionenaustausch von Na⁺-Ionen mit H⁺. Die anschließende Kalzination (iii) überführt das vorgetrocknete Titanat in TiO₂. Röntgendiffraktogramme des Zwischenprodukts geben Aufschluss über den Fortschritt des Ionenaustauschs und die Modifikation des Endprodukts (110228).

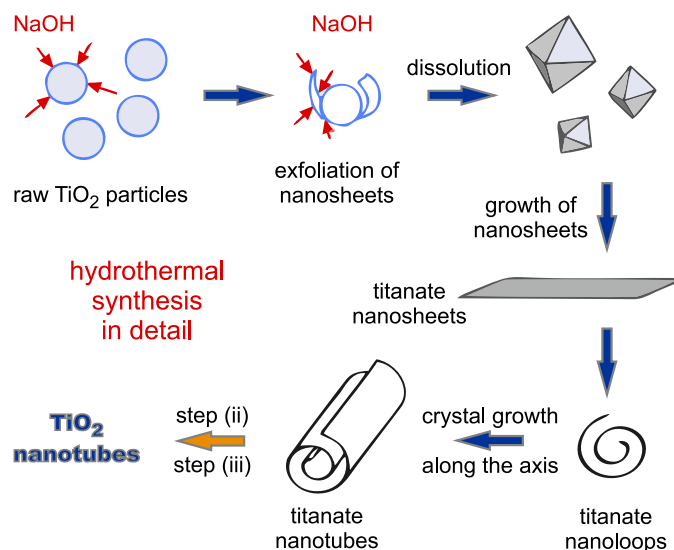


Abbildung 2.7: Schematischer Ablauf der Entstehung des Vorläuferprodukts für die TiO₂-Nanoröhren. Das während der Hydrothermalsynthese entstehende Titanat liegt schon als Nanoröhre vor und hat die Zusammensetzung Na_{2-x}H_xTi_nO_{2n+1} · yH₂O. Schritt (ii) und (iii) siehe Text.

2.4 Lithium-Interkalation – chemisch und elektrochemisch

Die Anodenmaterialien von Lithium-Ionen-Batterien wie z. B. auch die $\text{TiO}_2(\text{nt})$ sind sogenannte Interkalationsmaterialien. D. h. sie dienen als „Speicher“ für Lithium, welches während der Einlagerung auf Zwischengitterplätze bzw. freie Gitterplätze wandert und in Schichten, Kanälen oder Röhren Platz findet. Die Struktur des Wirtsgitters bleibt dabei idealerweise unbeeinflusst. Da das Lithium nicht elementar als ein Atom Li^0 , sondern als Li^+ interkaliert wird, die Ladungsneutralität aber gewahrt bleiben muss, um diesen Prozess fortführen zu können, sollten Anodenmaterialien elektronische Leiter sein. Im Falle einer wiederaufladbaren Batterie werden die Elektronen hierfür vom Ladegerät über die Stromabnehmer (Kontakt zwischen Batteriegehäuse und Elektrode) zur Anode „geschoben“ bzw. wandern beim Entladen durch einen Verbraucher wieder zur Kathodenseite.

Das „Beladen“ der Anode mit Lithium beim (ersten) Ladevorgang einer (Halb-)Zelle wird elektrochemische Interkalation genannt (Details siehe auch Abschnitt 2.5). Durch den technischen Aufbau sind Additive wie Leitruf und Binder zur Herstellung einer Anode (Interkalationsmaterial auf Stromabnehmer) nötig. Die chemische Interkalation erfolgt am Rohmaterial in trockenem *n*-Hexan mit *n*-Butyl-Lithium (BuLi).

Mit Hilfe dieser zwei Varianten wurden aus dem Produkt 110228 (siehe Abschnitt 2.3 und Abb. 3.7) Proben mit unterschiedlichen Interkalationsgraden hergestellt. Die jeweiligen Synthesewege sind im Ergebnisteil angegeben, im Folgenden wird eine beispielhafte Durchführung der Methoden beschrieben:

Chemische Interkalation

Vorbereitungen:

- Trocknen des Rohmaterials (1. 60 °C im Trockenschrank, 2. 120 °C unter Vakuum)
- Frisches, trockenes Hexan in der Glovebox mit 3 °A Molsieb rühren (ca. 1.5 Std)

Durchführung:

- Trockenes Rohmaterial in Hexan suspendieren
- Tropfenweise BuLi zugeben
- Je nach Partikelgröße des Rohmaterials für wenige Minuten bis einige Tage rühren*
- Abfiltrieren oder Dekantieren des abgesetzten Produkts und Trocknen unter Vakuum

* Im Falle von nanostrukturierten Titandioxidreicht reichen wenige Minuten für die vollständige Reaktion. Nach ca. 10 min war die Lösung absolut klar und die $\text{TiO}_2(\text{nt})$ waren nicht mehr farblos, sondern blau. Diese Beobachtung zeigt, dass sich Ti^{3+} -Zentren gebildet haben. Zur Sicherheit wurde einige Stunden weitergerührt.

Elektrochemische Interkalation

Vorbereitungen:

- Trocknen des Rohmaterials (60 °C im Trockenschrank)
- Elektrodenslurry* herstellen
- Elektrodenslurry auf Stromabnehmer rakeln†
- Trocknen im Trockenschrank bei 60 °C
- Ausstanzen oder Schneiden der Elektroden für den gewünschten Zelltyp‡
- Trocknen der Elektroden im Hochvakuum (Temp. je nach Material 60–120 °C)
- Zusammenbau der Halb-Zellen in der Glovebox

Durchführung:

- Elektrochemische Charakterisierung der ersten Zyklen (falls noch unbekannt)
- Mit kleiner C-Rate bis zum gewünschten SOC (*state of charge*) laden
- Zellen in der Glovebox wieder öffnen
- Elektrodenmaterial vom Stromabnehmer abkratzen und Elektrolytreste auswaschen
- Trocknen unter Vakuum

Da die typische Masse an Elektrodenmaterial in Swagelock- und Knopfzellen nur wenige mg beträgt, müssen auch bei unüblich dicken Elektroden mehrere Zellen gebaut werden, um genügend Probenmaterial für die NMR-Untersuchungen herzustellen. Ein weiterer Nachteil ist das in der Probe verbleibende *carbon black*, das alle Proben wie es der Name schon sagt, schwarz färbt. Der Interkalationsgrad von Titandioxiden kann anhand der Intensität der Blaufärbung mit dem bloßem Auge abgeschätzt werden. Dies funktioniert nicht bei zugesetztem Leitruf. Proben, die Kontakt mit Luft bekommen, werden innerhalb von Sekunden wieder wieder farblos. Diese Kontrollmöglichkeit einer Probenveränderung vor und nach den NMR-Messungen entfällt für elektrochemisch hergestellte Proben. Diese entsprechen jedoch den (potentiellen) Elektrodenmaterialien einer Lithium-Ionen-Batterie.

* Gemisch aus Rohmaterial, Binder und Leitruf in geeignetem Lösungsmittel

† Auch *Doctor blade*-Technik, ist die Aufbringung des feuchten, viskosen Gemischs von Aktivmasse, Additiven und Lösungsmittel mit definierter gleichmäßiger Schichtdicke von typischerweise 50 – 200 μm .

‡ Es gibt drei übliche Bauarten: (i) *coin-cells* sind große Knopfzellen, wie sie z. B. auch aus flachen elektronischen Geräten verwendet werden; (ii) Swagelock-Zellen; (iii) *pouch-bag*-Zellen, die den Vorteil haben, dass sie in beliebigen Formaten hergestellt werden können. Die beiden ersten Typen sind in Abb. 3.8 gezeigt.

2.5 Elektrochemische Charakterisierung

Zum Testen von Elektrodenmaterialien werden sogenannte Halbzellen hergestellt. Dabei handelt es sich im Prinzip auch um vollständige Batterien. Es wird jedoch üblicherweise reines Lithiummetall als Anode (negative Elektrode) verwendet. Soll also wie im Fall des Titandioxids ein Anodenmaterial getestet werden, ergibt sich eine sehr kleine Potentialdifferenz zwischen der Anode Lithium und der Kathode TiO_2 . Da elementares Lithium das elektronegativste Potential der elektrochemischen Spannungsreihe besitzt, werden alle zu testenden Elektroden als Kathode an die jeweiligen Messgeräte angeschlossen. Die verwendeten Elektrolyte müssen dabei nicht identisch mit denen in einer Vollzelle sein. Und vor allem die eingesetzten Separatoren sind aufgrund der Dendritenbildung des Lithiums deutlich dicker als in handelsüblichen Batterien. Deshalb wird auch bei Kathodenmaterialien, die gegenüber Lithium die typische Zellspannung von Lithium-Ionen-Batterien erreichen oder sogar überschreiten, nicht von Vollzellen gesprochen.

Die zwei üblichen Methoden zur Charakterisierung von Elektrodenmaterialien sind die zyklische Voltametrie (CV) von engl. *cyclic voltammetry*, wobei die Spannung mit einer kleinen, konstanten Vorschubgeschwindigkeit von z. B. $5 \mu\text{V}$ das Potentialfenster „abtastet“ und dabei die Stromstärke gemessen wird. Sofern es keine Nebenreaktionen wie z. B. die Zersetzung eines für die anliegende Spannung ungeeigneten Elektrolyten gibt, kann so nicht nur das Potentialfenster für neue Materialien bestimmt werden, sondern auch die Ein- (Interkalation) bzw. Auslagerung (Deinterkalation) des Lithiums ins bzw. aus dem Material mit einer oder mehreren Spannungen verknüpft werden. Als Beispiel sei die stufenweise (De-)Interkaltion aus/in Graphit genannt (siehe Abb. 2.8). Da das Zyklovoltamogramm nicht nur Spannung U und Stromstärke I gegeneinander aufträgt, sondern durch die gewählte Vorschubgeschwindigkeit auch noch die Zeit für den Lithiumionentransport beinhaltet, können aus den Flächenintegralen (bis zur Stromnulllinie) der entstandenen Peaks auch direkt die Lade- und Entladekapazitäten der getesteten Elektroden in Amperestunden Ah oder sogar in Wattstunden Wh berechnet werden. Bei genauer Einwaage der Aktivmasse werden ebenso die spezifischen Kapazitäten erhalten.

Die Methode der zyklischen Voltametrie wird auch als potentiostatisches Zyklieren bezeichnet. Die Charakterisierung von elektrochemischen Reaktionen ist nur möglich, wenn der konkret ablaufende Reaktionsmechanismus berücksichtigt wird. Ein Überblick findet sich in der Literatur.^[39,40] Es können drei unterschiedliche Szenarien für den Reaktionsverlauf unterschieden werden:

- **reversible Reaktion**

Hierbei ist die Reaktionskinetik des Ladungsdurchtritts so groß, dass sich an der Phasengrenze ein dynamisches Gleichgewicht einstellt. Der Gesamtprozess ist damit lediglich durch den Massentransport limitiert. Der sich ergebende Strom-Spannungs-Graph ist durch Stromstärke-Maxima bzw. -Minima (Redoxpeaks) charakterisiert, die um die entsprechenden Oxidations- bzw. Reduktionspotentiale zu finden sind.

- **irreversible Reaktion**

Bei irreversiblen Verhalten ist der Ladungsdurchtritt kinetisch stark gehemmt oder das Reaktionsprodukt reagiert mit anderen Bestandteilen des Elektrolyten oder der Elektrode weiter. Dadurch ist die Lage der Redoxpeaks stark von der Vorschubgeschwindigkeit abhängig.

- **quasi-reversible Reaktion**

In diesem Fall bestimmen sowohl Ladungsdurchtritt als auch Massentransport die Reaktionskinetik. Durch die Wahl der Vorschubgeschwindigkeit ist es möglich, zwischen ladungsdurchtritts- bzw. massentransportdominiertem Verhalten zu wechseln.

Um die Zyklenfestigkeit von Elektrodenmaterialien zu testen werden ebenso standardisierte Bedingungen* genutzt und die Zellen werden viele Male mit einem definierten konstanten Strom geladen und entladen. Dabei ist eine Zelle per Definition entladen, wenn die positive Elektrode vollständig mit Lithium beladen ist. Die Charakterisierung von wiederaufladbaren Batterien oder einzelnen Elektroden mittels Lade-Entlade-Zyklisierung

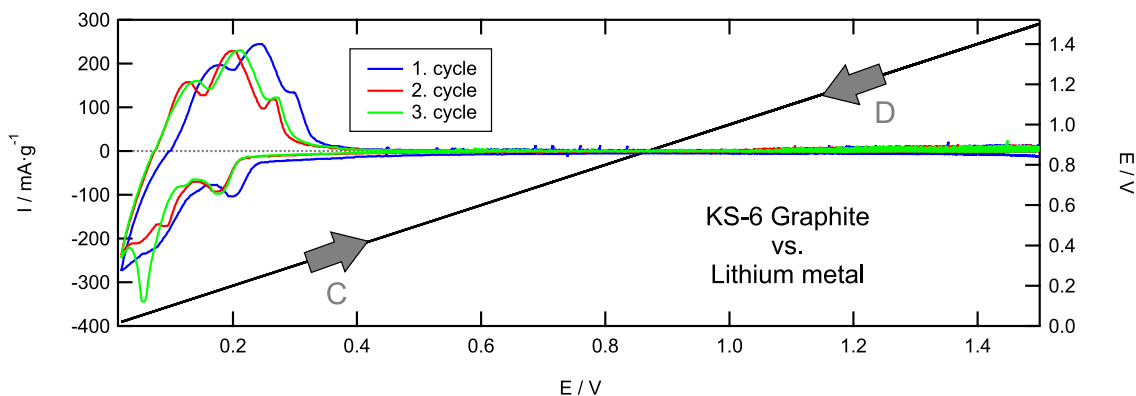


Abbildung 2.8: Zyklovoltamogramm eines Flockengraphits gegen Lithiummetall als Anode. Es wurden drei vollständige Zyklen von 1500 mV bis zum Umkehrpunkt bei 20 mV und zurück bis 1500 mV durchlaufen. Während des Entladevorgangs (Pfeil D) der Zelle werden Elektronen und Lithiumkationen aus der Anode zur Kathode transportiert und in die Graphitstruktur eingelagert (interkaliert). Die dabei gemessenen Ströme sind negativ. Die positiven Strompeaks sind während des Ladens der Zelle (Pfeil C) entstanden und zeigen die nötigen Potentiale zur Deinterkalation des Lithiums während der einzelnen Zyklen. Dieses Ergebnis ist in einem Praktikum für Studenten entstanden.

* Innerhalb einer Testreihe von Elektroden mit z. B. unterschiedlichen Verhältnissen von Binder, Leitruß und Aktivmasse (aus einer Charge Elektrodenmaterial), werden für den Aufbau der Halbzellen immer die selben Elektrolyte und Separatoren in den zum Zelltyp passenden Mengen bzw. Dicken benutzt. Analog können Testreihen für folgende Variablen gefahren werden: Elektrodendicke, Binder, Leitruß, Separator und Elektrolyt.

wird auch als Galvanostatische Zyklisierung bezeichnet. Da das System hier aus dem Gleichgewicht gebracht wird, indem ihm ein Strom aufgezwungen wird. Messgröße und experimentelle Variable sind im Vergleich zur potentiostatischen Zyklisierung also genau vertauscht.

Aussagen über die Kinetik lassen sich mit dieser Methode nur indirekt und qualitativ treffen, vorrangig werden Lade- und Entladekennlinien, Stromausbeute und Zyklenstabilität bestimmt. Dafür werden die experimentellen Daten unterschiedlich gegeneinander aufgetragen. Ein wichtiger Messparameter ist die sogenannte C -Rate. Eine C -Rate von C/t gibt die konstante Stromstärke an, die notwendig ist, ein galvanisches Element innerhalb einer Dauer von t Stunden mit der vollen theoretischen Kapazität dieses Elements zu laden bzw. entladen. Die theoretische Kapazität lässt sich dabei mit dem Faradayschen Gesetz berechnen.

Für Interkalationsmaterialien können nach Armand^[41] aus der Kennlinie Rückschlüsse auf eine mögliche Phasenumwandlungen während des Lade-/Entladevorgangs geschlossen werden. So ist für einen Zwei-Phasen-Prozess ein Plateau im Lade-Entlade-Graphen charakteristisch (siehe S. 78ff). Einphasenprozesse weisen hingegen kein Plateau auf und sind durch einen kontinuierlichen Anstieg der gemessenen Spannung gekennzeichnet.

3 Ergebnisse: Zur Li-Diffusion in kristallinen Festkörpern

Li-Bewegungsprozesse in kristallinen und amorphen Festkörpern mit einer starren Matrix können Selbstdiffusionskoeffizienten zeigen, die sich über einen dynamischen Bereich von vielen Größenordnungen erstrecken. Während Li-Sprungraten von z. B. 1 s^{-1} charakteristisch sind für Ionenleiter mit äußerst niedriger Leitfähigkeit, zeigen Festkörper mit extrem schneller Li-Diffusivität Werte im Bereich von 10^9 s^{-1} .

Die NMR-Spektroskopie bietet eine Reihe von Verfahren an, mit denen Li-Translationsprozesse mit Raten vom sub-Hz bis über den GHz-Bereich hinaus erfasst werden können. In Abb. 2.1 sind bekannte NMR-Techniken und andere nukleare sowie nicht-nukleare Methoden mit ihren jeweiligen Zeitfenstern dargestellt.

Zur Detektion von ultralangsamem Diffusionsprozessen eignen sich z. B. i) die Aufzeichnung von Zwei-Zeiten-Korrelationsfunktionen mit Hilfe stimulierter Echos (Publikation 7; Seiten 124ff) bzw. ii) die Durchführung von mischzeitabhängigen 2D Austauschexperimenten unter hinreichend schneller Probenrotation (Publikation 1; Seiten 43ff). Insbesondere können 1D und 2D ^6Li MAS NMR-Messungen zur Charakterisierung der lokalen magnetischen Strukturen in dia- und paramagnetischen Verbindungen herangezogen werden (Publikationen 2 und 3; Seiten 54ff und 63ff).

Sehr schnelle Bewegungsprozesse werden üblicherweise mit NMR relaxometrischen Messungen im Laborkoordinatensystem erfasst (Publikationen 6 und 7; Seiten 108ff und 124ff). Moderate bis schnelle Prozesse können mit *spin-lock* Verfahren, die im rotierenden Koordinatensystem gemessen werden, analysiert werden. Mit dieser Technik sind die Anodenmaterialien mesoporöses- TiO_2 und $\text{Li}_4\text{Ti}_5\text{O}_{12}$ (LTO) studiert worden (Publikationen 4 und 5; Seiten 78ff und 95ff).

Im Idealfall liefern alle Techniken Hinweise auf Aktivierungsenergien und absolute Li-Sprungraten. Zusätzlich enthalten SAE-NMR-Messungen und relaxometrische Studien Informationen über die Form der zugrundeliegenden Bewegungskorrelationsfunktion und den Einfluss von Korrelationseffekten^[18]. Frequenzabhängige Relaxationsmessungen geben Aufschluss über die Dimensionalität des Bewegungsprozesses^[18,42]. Selbst einzelne Spektren können durch die Analyse der Quadrupolsatelliten und durch die Linienbreite der Zentralintensität bei verschiedenen Temperaturen, wertvolle Hinweise auf die Dynamik des Materials liefern.

3.1 Hochauflösende ${}^{7,6}\text{Li}$ NMR

Dieser Abschnitt fasst die Publikationen 1 – 3 zu einem Block zusammen, wobei die erste und die letzte Publikation durch die Zusätze Z1 und Z3 ergänzt werden. Im Inhaltsverzeichnis sind die Publikationen (kursiv) und die ergänzenden Unterabschnitte fortlaufend nummeriert.

3.1.1 P1: **Ultraslow Li Exchange Processes in Diamagnetic Li_2ZrO_3 As Monitored by EXSY NMR**

Bottke, P., Freude, D., and Wilkening, M. *J. Phys. Chem. C* **117**, 8114–8119 (2013).

3.1.2 Z1: Leitfähigkeitsmessungen an mikro- und nanokristallinem Li_2ZrO_3

3.1.3 1D/2D ${}^{7,6}\text{Li}$ MAS NMR an paramagnetischen Kathodenmaterialien

3.1.4 P2: **Low-Temperature Synthesis, Characterization, and Stability of Spinel-Type Li_2NiF_4 and Solid-Solutions $\text{Li}_2\text{Ni}_{1-x}\text{Co}_x\text{F}_4$**

Kohl, J., Nakhal, S., Ferro, N., Bottke, P., Wilkening, M., Bredow, T., Heitjans, P., and Lerch, M. *Z. Anorg. Allg. Chem.* **639**, 326–333 (2013).

3.1.5 P3: **Synthesis of ternary transition metal fluorides Li_3MF_6 via a sol-gel route as candidates for cathode materials in lithium-ion batteries**

Kohl, J., Wiedemann, D., Nakhal, S., Bottke, P., Ferro, N., Bredow, T., Kemnitz, E., Wilkening, M., Heitjans, P., and Lerch, M. *J. Mater. Chem.* **22**, 15819–15827 (2012).

3.1.6 Z3: 2D ${}^6\text{Li}$ MAS EXSY NMR an $\beta\text{-Li}_3\text{VF}_6$

P1: Es gibt bisher nur sehr wenige Studien an diamagnetischen Materialien, die sich der Herausforderung stellen, platzspezifische Li-Austauschraten über hochauflösende ${}^6\text{Li}$ -MAS 2D EXSY NMR zu messen. Derartige Experimente erlauben die Sichtbarmachung von Diffusionspfaden bzw. die experimentelle Bestimmung der Diffusionsmechanismen. Li_4SiO_4 war die erste Modellsubstanz, die von Stebbins und Mitarbeitern^[43] mit mischzeitabhängigen 2D-Experimenten untersucht wurde.

Li_2ZrO_3 stellt ebenfalls ein geeignetes Modellsystem dar, das sich durch genau zwei magnetisch und kristallographisch inequivalente Li-Positionen auszeichnet. Die äußerst langen SLR-Zeiten verursachen eine Messdauer von mehreren Tagen für ein Austauschexperiment. Dennoch ist es möglich gewesen, dass der 2-Platzsprungwechsel in kristallinem Li_2ZrO_3 präzise erfasst werden konnte. Um RT sind extrem geringe Austauschraten von 1 min^{-1} gemessen worden. Dies entspricht nach der EINSTEIN-SMOLUCHOWSKI-Gleichung einem Diffusionskoeffizienten in der Größenordnung von $10^{-22} \text{ m}^2/\text{s}$. Impedanzmessungen bestätigen das Ergebnis und sind als Anhang zur Publikation 1 gezeigt.

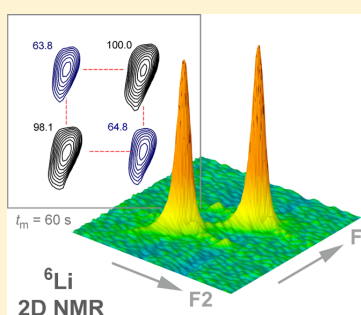
Ultraslow Li Exchange Processes in Diamagnetic Li_2ZrO_3 As Monitored by EXSY NMR

P. Bottke,^{*,†} D. Freude,[‡] and M. Wilkening[†]

[†]Institute for Chemistry and Technology of Materials, Graz University of Technology, Stremayrgasse 9, 8010 Graz, Austria

[‡]Institutes of Experimental Physics, University of Leipzig, Linnéstraße 5, 04103 Leipzig, Germany

ABSTRACT: Two-dimensional (2D) ${}^6\text{Li}$ exchange magic angle spinning (MAS) nuclear magnetic resonance (NMR) spectroscopy was used to probe extremely slow lithium hopping processes in a polycrystalline powder sample of lithium zirconate, Li_2ZrO_3 . In agreement with the crystal structure of Li_2ZrO_3 , the ${}^6\text{Li}$ MAS NMR spectra recorded are composed of two signals (-0.10 and 0.26 ppm) with equal intensity. They reflect the two magnetically (and electrically) inequivalent Li sites in Li_2ZrO_3 . The mixing-time dependent 2D MAS NMR spectra, which were acquired at a bearing gas temperature of ca. 310 K, clearly reveal off-diagonal intensities indicating Li exchange processes with exchange rates as low as 60 jumps/hour. To our knowledge, this is by far one of the slowest Li solid-state diffusion processes ever probed by ${}^6\text{Li}$ 2D exchange MAS NMR spectroscopy (submitted to *J. Phys. Chem. C*, 2013).



INTRODUCTION

Diffusion of small ions, such as H^+ , Li^+ , and F^- , plays a crucial role in the various subdisciplines of materials science. While in some research areas extremely fast ion conductors are needed,^{1,2} which is certainly the fact when lithium-ion based energy systems^{3–11} have to be developed, there are also applications known for which solids, acting as long-lasting barriers for ion transport, are necessary. For instance, this is true for semiconductor research and the development of tritium breeding blankets being one of the topics of nuclear fusion research. Promising blanket materials should offer a slow release of lithium but a fast release of tritium after neutron irradiation. Lithium zirconate, Li_2ZrO_3 , is thought to act as such a blanket material. The crystallographic structure reveals two magnetically inequivalent Li sites¹² ($\text{Li}(1)$ and $\text{Li}(2)$), which are equally populated (see Figure 1). Temperature-dependent conductivity measurements, static Li nuclear magnetic resonance (NMR) spectra, and Li NMR spin–lattice relaxation rates (see below) point to an extremely low Li^+ mobility. By using fast magic-angle spinning (MAS) NMR it was possible to resolve the two spectral components and to follow their evolution by 2D ${}^6\text{Li}$ exchange NMR spectroscopy (EXSY).

Here, ${}^6\text{Li}$ MAS NMR measurements are preferred over ${}^7\text{Li}$ ones because of both the smaller magnetogyric ratio ($39.73 \times 10^6 \text{ rad s}^{-1} \text{ T}^{-1}$) of ${}^6\text{Li}$ (spin-1 nucleus, natural abundance of 7.6%) and the smaller quadrupole moment $Q({}^6\text{Li}) = -0.0808 \times 10^{-30} \text{ m}^2$ as compared to ${}^7\text{Li}$ (spin-3/2, 92.4%) with $103.98 \times 10^{-30} \text{ m}^2$ and $Q({}^7\text{Li}) = -4.01 \times 10^{-30} \text{ m}^2$. While the former leads to much weaker interfering homonuclear ${}^6\text{Li}$ dipole–dipole interactions, the smaller value of $Q({}^6\text{Li})$ drastically reduces second-order quadrupolar broadening. Hence, under MAS conditions the nuclear properties of ${}^6\text{Li}$ spins are beneficial to achieve a sufficiently high spectral

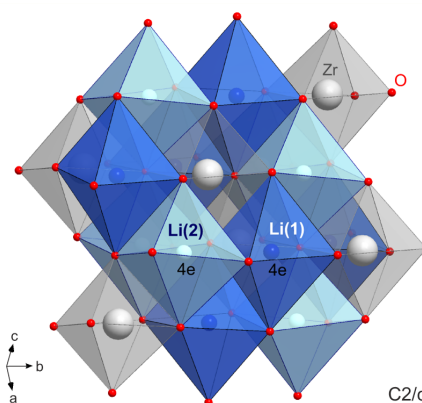


Figure 1. Crystal structure of Li_2ZrO_3 ($C2/c$ symmetry); the two crystallographically inequivalent Li sites $\text{Li}(1)$ and $\text{Li}(2)$ are indicated ($4e2$ positions). Li ions are octahedrally coordinated by oxygen and the LiO_6 -polyhedra share common edges. Li–O distances of the polyhedral are given in Figure 2.

resolution with the ideal result that signals arising from different Li sites do not or only partially overlap. Moreover, the much smaller concentration of ${}^6\text{Li}$ spins in a sample with natural abundance helps suppress effects from unwanted spin diffusion.

Since the pioneering work of Xu and Stebbins,¹³ who have determined site-specific Li jump rates in lithium orthosilicate

Received: February 6, 2013

Revised: March 27, 2013

Published: March 27, 2013

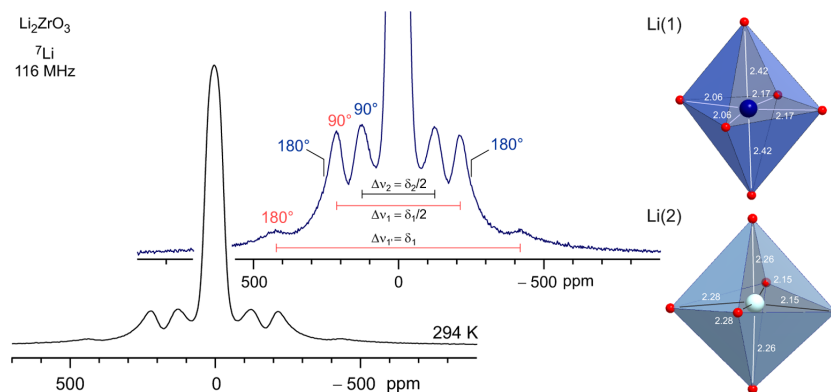


Figure 2. ${}^7\text{Li}$ NMR spectrum (116 MHz) of Li_2ZrO_3 that was recorded under static conditions at room temperature. Besides a pronounced central intensity, being the sum of the two NMR central lines of the two crystallographically different Li sites, two different quadrupole powder patterns show up. Provided two axially symmetric EFGs are assumed, from the distance of the inner and outer (if visible) singularities the electric quadrupole coupling constants δ_1 and δ_2 can be determined. The upper spectrum is a magnification of that one shown on the bottom. The LiO_6 octahedra of the two Li sites are shown on the right-hand side. Values indicate Li–O distances (in Å) according to the neutron profile refinement of Hodeau et al.¹² See text for further explanation.

(Li_4SiO_4) via 2D ${}^6\text{Li}$ NMR, exchange spectroscopy has been mainly used to probe ion dynamics in paramagnetic, see, for example, refs 14–21, rather than in diamagnetic^{13,22–26} compounds such as oxides, fluorides, and phosphates. Experiments on paramagnetic materials take advantage of large dipolar interactions between the Li nucleus and unpaired electrons of transition metals such as V, Ni, Co, Fe, etc. resulting in (i) short NMR spin–lattice relaxation (SLR) rates ranging from milliseconds to some seconds^{14,18,19} and (ii) large, site-specific NMR paramagnetic shifts.^{15,27,28} While the first circumstance drastically reduces the measurement time but limits the application of time-domain NMR techniques to study lithium-ion dynamics, the second fact makes it possible to resolve the distinct Li sites present in those materials, which is a prerequisite for the application of 2D MAS NMR. However, even under fast sample rotation, in some cases Fermi-contact interactions may become very large leading to extremely broad and unresolved NMR lines, which can make the interpretation of ${}^6\text{Li}$ NMR spectra of paramagnetic compounds extremely difficult.²⁹ In particular, this becomes a challenging task in complex materials with a large number of magnetically inequivalent Li sites. Certainly, in some cases also the large sideband manifolds, being characteristic for ${}^7\text{Li}$ MAS NMR spectra, are highly useful for data interpretation.

In the present case, we used a polycrystalline sample of Li_2ZrO_3 with a natural abundance of ${}^6\text{Li}$ in order to reduce the impeding effects of homonuclear spin-diffusion as much as possible. The latter also causes off-diagonal intensities in 2D NMR spectra that are not related to mass transfer. However, the moderate NMR sensitivity of the ${}^6\text{Li}$ nucleus and the use of rotors with a very small inner volume, which is necessary to reach high spinning frequencies, expectably lead to a poor signal-to-noise ratio. Even if large magnetic fields are used to sample ${}^6\text{Li}$ NMR spectra, a sufficiently large number of scans n_s needs to be accumulated. Note that n_s is also codetermined by the minimum number of entries of the phase cycle used. The total measurement time is then approximately given by the number of scans, the number of points in the 2D time domain in F1 direction, the mixing time used and the necessary recycle delay. The latter is determined by the NMR SLR time being a

measure of the recovery of longitudinal magnetization after perturbation the spin system with an appropriate radio frequency pulse. In the present case, ${}^6\text{Li}$ NMR SLR times of up to 270 s are found at ambient-bearing gas temperature. Thus, recycle delay times as long as 5×300 s are used in combination with mixing times of up to 60 s. Hence, for a single, constant mixing time t_m nine days or more are needed to record a 2D NMR experiment.

Usually, for each temperature the mixing time is varied and the normalized intensity of the off-diagonal intensities (the so-called cross peak intensity reflecting Li ion exchange) is plotted versus t_m . The resulting time-signal intensity curves can be approximated with exponential functions to extract the Li residence time. Altogether, in the case of Li_2ZrO_3 this would result in a complete measurement time of up to one year. Fortunately, since only two magnetically inequivalent Li sites are present from each 2D NMR experiment recorded at a given mixing time, the Li residence time τ can be deduced. As a result, in the present case, τ^{-1} is as low as $2 \times 10^{-2} \text{ s}^{-1}$ at 310 K. To our knowledge, this is by far the lowest Li^+ jump rate measured by ${}^6\text{Li}$ 2D MAS NMR.

EXPERIMENT

${}^6\text{Li}$ 2D MAS NMR spectra were recorded at 310 K on Avance III 600 and 750 solid-state NMR spectrometers (Bruker) each in combination with a shimmed cryomagnet (14.1 and 17 T, respectively). Magic-angle spinning was carried out using probes designed for 4.0 and 1.3 mm rotors (Bruker). While the saturation recovery pulse sequence has been used to determine T_1 , a NOESY pulse sequence with appropriate phase cycling (8–16 entries) was employed to record the 2D spectra. The maximum number of data points chosen in the time domain in F1 direction was 256; for F2 the corresponding value varied from 1024 to 2048. In some experiments, the NOESY sequence has been combined with the saturation recovery pulse sequence³⁰ placed at the beginning of the three-pulse 2D NMR experiment. Since the NMR SLR time T_1 is much larger than the time period determined by t_m , that is, $T_1 \gg \tau$, the saturation comb, consisting of up to 16 closely spaced 90° pulses, allows the use of relaxation delays shorter than $5 \times T_1$. This reduces

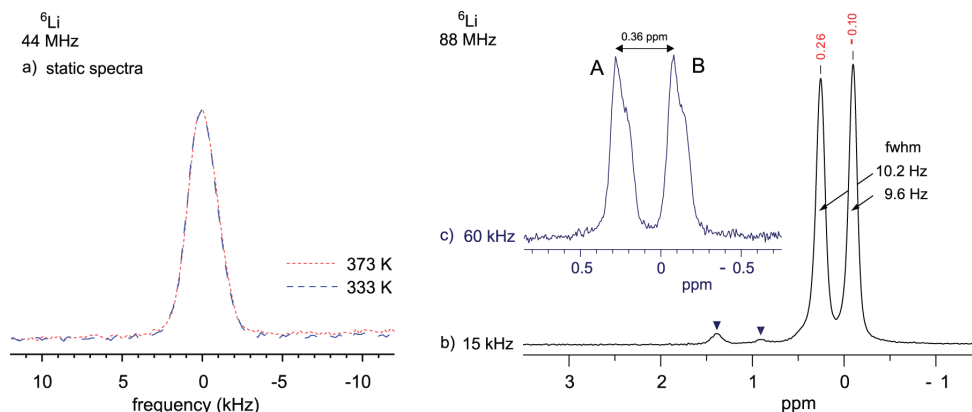


Figure 3. ${}^6\text{Li}$ NMR spectra of Li_2ZrO_3 . (a) Spectra recorded under static conditions (44 MHz) at different temperatures ranging from 294 K (not shown for the sake of clarity) to 373 K, the full width at half-maximum (fwhm) is approximately 2.2 kHz irrespective of temperature; (b,c) MAS NMR spectra recorded at two different rotation frequencies viz. 15 and 60 kHz. Chemical shifts (0.26 ppm and -0.10 ppm) of the two Li NMR signals are referenced to aqueous LiCl (1 M). The triangles indicate two NMR signals of very low intensity that arise from traces of impurities.

the measurement time not to exceed more than ten days per mixing time. 1D ${}^6\text{Li}$ MAS NMR spectra were recorded with a single pulse sequence. The 90° pulse length, determined via the pulse optimization procedure implemented in TopSpin (Bruker), was 2.3 μs . Up to 1024 scans were accumulated for one spectrum. In addition, static, variable-temperature ${}^7\text{Li}$ NMR spectra were recorded on an Avance III spectrometer (Bruker) connected to a shimmed 7 T cryomagnet. The spectra contain information on the local, electric quadrupole interaction between the electrically inequivalent ${}^7\text{Li}$ nuclei in Li_2ZrO_3 and the nonvanishing electric field gradients (EFGs) at the nuclear sites. Analysis of the 1D and the 2D Li NMR spectra was carried out with IGOR Pro (Wavemetrics), TopSpin, and Mestre Nova software.

RESULTS AND DISCUSSION

In Figure 2, typical ${}^7\text{Li}$ NMR spectra are shown recorded on nonrotating samples and at the temperatures indicated. The dipolarly broadened spectra are composed of two distinct quadrupole powder patterns reflecting the two Li subensembles according to the electrically inequivalent cation sites Li(1) and Li(2) (position 4e2) in Li_2ZrO_3 . Assuming an axially oriented EFG, that is, anticipating a vanishing anisotropy parameter ($\eta = 0$),³¹ the associated quadrupole coupling constants δ_i ($i = 1, 2$) can be precisely read out from the distance of the (first-order) singularities of the powder pattern as indicated in Figure 1.³² For δ_1 and δ_2 , we obtain 67 kHz (site α) and 36 kHz (site β), respectively. This is in fair agreement with the result of Baklanova (ca. 52 and 29 kHz, respectively) obtained from much less resolved ${}^7\text{Li}$ NMR spectra recorded at a magnetic field of 9.4 T.³³ Considering the Li–O distances of the two polyhedra shown in Figure 2, which were taken from the neutron profile refinement of Hodeau et al.,¹² the Li(1) O_6 octahedron is less symmetric than the corresponding Li(2) O_6 one. For comparison, Li–O distances of Li(1) O_6 range from 2.06 to 2.42 Å; in Li(1) O_6 the distances vary from 2.15 to 2.28 Å. Thus, in agreement with the assignment presented in ref 33 the larger coupling constant (δ_1) found might be ascribed to the elongated Li O_6 octahedron of Li(1), while δ_2 (site β) might represent the Li(2) site.

The observation that $2\Delta\nu_2(90^\circ) = \Delta\nu'_2(180^\circ)$ holds, where $\Delta\nu_2$ is the spectral distance of the 90° and $\Delta\nu'_2$ that of the 180° singularities (see Figure 2), respectively, indeed points to an axially symmetric field gradient of site α . Note that the relation $2\Delta\nu_2 = \Delta\nu'_2$ is only valid for EFG interactions with $\eta = 0$ of spin-3/2 nuclei like ${}^7\text{Li}$.^{32,34} While the 90° singularities of the two sites are clearly visible, those reflecting 180° interactions can only be seen for site α being characterized by δ_1 . The corresponding 180° singularities of site β , whose positions are also indicated in Figure 2, are hidden by the satellite intensities of the powder pattern of site α . With increasing temperature, no change of the shape of the total quadrupole powder pattern is observed. Hence, Li exchange rates are much smaller than $2\pi\Delta\nu_i$ determined by the site-specific electric quadrupole interactions.

In the present case, the central intensity of the ${}^7\text{Li}$ NMR spectrum shown in Figure 1 actually represents the sum of two central NMR lines broadened by dipole–dipole interactions. Since upon heating no averaging of dipolar interactions is observed, which should manifest in a significant narrowing of the overall width (full width at half-maximum, $\Delta\nu_{\text{central}} \approx 10$ kHz) of this signal, the average Li jump rate clearly turns out to be much smaller than $\Delta\nu_{\text{central}}$. For comparison, the ${}^6\text{Li}$ NMR spectra, recorded under static conditions at different temperatures (cf. Figure 3a), only reveal a single line that is dipolarly and quadrupolarly broadened. It is a superposition of both central and satellite intensities. The combined effect of dipole–dipole broadening and the much smaller quadrupole moment Q of ${}^6\text{Li}$ ($Q({}^6\text{Li}) \approx 1/50 \times Q({}^7\text{Li})$) excludes the determination of the ${}^6\text{Li}$ NMR quadrupole powder pattern.

However, the elimination of (i) dipole–dipole interactions and (ii) first order quadrupole interactions by fast magic-angle spinning results in a high-resolution ${}^6\text{Li}$ MAS NMR spectrum that is clearly composed of two NMR lines with different chemical shifts (σ_1 and σ_2) but of equal intensity (Figure 3b,c). The spectrum shown in Figure 3b reveals two NMR signals of minor intensity pointing to a negligible amount of impurities, such as Li_2HfO_3 , in commercially available Li_2ZrO_3 . Since the Li jump rate is also much smaller than the spectral width, which is given by the distance $\Delta\sigma = \sigma_1 - \sigma_2$ of the two MAS NMR signals on the hertz scale (here, 1 ppm equals 10 Hz), no

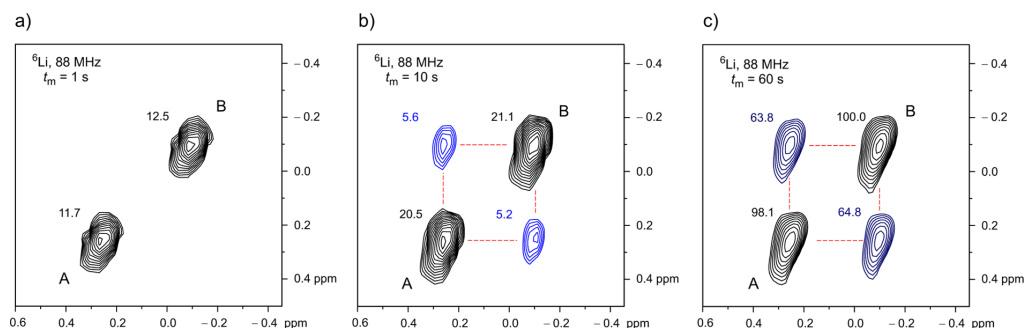


Figure 4. 2D ${}^6\text{Li}$ exchange NMR spectra of Li_2ZrO_3 recorded at different mixing times t_m ranging from 1 to 60 s. The temperature of the bearing gas used was 310 K; the rotation frequency was 12 kHz (4-mm rotor). Chemical shifts are referenced to aqueous LiCl (1 M).

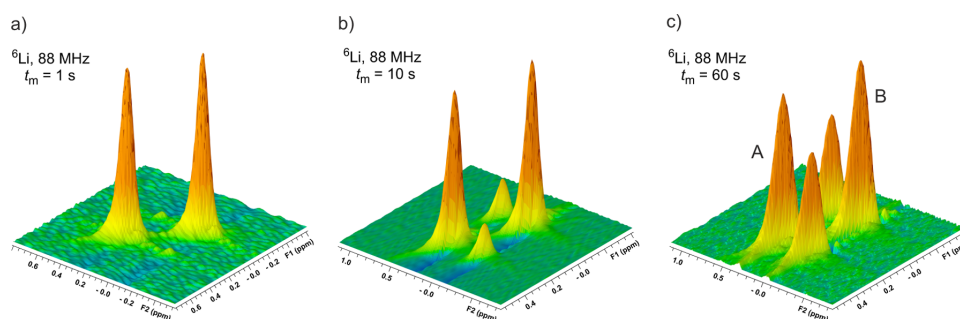


Figure 5. Three-dimensional plots of the 2D ${}^6\text{Li}$ exchange MAS NMR spectra of Li_2ZrO_3 (shown in Figure 3). While almost no cross peaks are visible at a mixing time of $t_m = 1$ s, they emerge when t_m is increased to 10 s. At $t_m = 60$ s the two-site hopping process $\text{Li}(1) \rightleftharpoons \text{Li}(2)$ clearly causes intense off-diagonal signals that can be used to calculate τ_{exch} and, thus, the Li residence time τ . Chemical shifts are referenced to aqueous LiCl (1 M).

coalescence of the two spectral components is observed even when the bearing gas temperature is increased by approximately 30 °C.

The two different chemical shift values determined might be assigned to the crystallographic Li sites in the following way. Considering the asymmetry of the $\text{Li}(1)\text{O}_6$ octahedron, the central Li(1) ion might be deshielded leading to an NMR shift (signal A in Figure 3c) toward larger frequencies and, thus, more positive ppm values. On the other hand, the NMR signal of the more symmetric $\text{Li}(2)\text{O}_6$ octahedron seems to be the result of an upfield shift, hence, the NMR line (cf. signal B in Figure 3c) appears at a lower resonance frequency, that is, at a lower ppm value. Certainly, this tentative assignment needs to be corroborated by theoretical investigations.

Interestingly, at very high MAS frequencies an asymmetric shape of the two NMR signals is found (see Figure 3c). At first glance, this feature might be attributed to second order quadrupole effects, which cannot completely be removed by MAS. The maximum second-order quadrupole splitting of the MAS spectrum of nuclei having a spin-quantum number $I = 1$ under the influence of an electric field gradient with rotational symmetry is in the order of $\nu_Q^2 / (16 \nu_L)$,³¹ where ν_L denotes the Larmor frequency. Inserting $\nu_L = 88$ MHz and $\nu_Q = \delta_i = 67$ kHz, we obtain a resulting second-order quadrupolar splitting of 3.2 Hz. The broadening revealed in Figure 2b is approximately 0.2 ppm, which equals 17.6 Hz. Interestingly, this value is much larger and points to another influence. It should be noted that the two ${}^6\text{Li}$ MAS NMR lines are subject to

the same asymmetric broadening, even though the quadrupole coupling constants differ from each other by a factor of 1.86 (see Figure 3c). One might speculate whether the asymmetry observed is due to a residual drift or to a slight inhomogeneity of the external magnetic field. However, even when drift compensation is applied and shimming effects are considered the feature remains. Nevertheless, irrespective of its origin the spectral resolution is by far good enough to carry out 2D MAS EXSY NMR. The corresponding spectra are expected to reveal any ultraslow Li exchange processes if the mixing time t_m is chosen to be sufficiently long enough.

In general, in a 2D NMR experiment, the angular NMR frequency $\omega(t')$ of a given Li ion at time t' is correlated with the frequency $\omega(t'')$ the spin is exposed to after a mixing time t_m . Off-diagonal intensities result if $\omega(t') \neq \omega(t'')$, that is, when jumps between magnetically inequivalent sites occur during the period defined by t_m . Here, at a very short t_m of only 100 ms the corresponding contour plot of the 2D exchange NMR experiment is solely composed of diagonal intensities indicating that almost no Li^+ exchange took place within the observation period. This also holds for $t_m = 1$ s (see Figure 4a). However, with increasing t_m to 10 and 60 s, respectively, off-diagonal intensities emerge clearly revealing a two-site hopping process between the Li sites differing in chemical shift (Figure 4b,c). Since we used a sample with natural abundance (the ${}^6\text{Li}/{}^7\text{Li}$ ratio is close to 7.5:92.5 ensuring a sufficiently good spatial separation of the ${}^6\text{Li}$ spins) spin-diffusion, that is, flip-flop processes that are not related to mass but to spin transfer, can

be reliably neglected to be responsible for the emergence of cross-peak intensities.

Since the 2D NMR spectra have been recorded at different recycle delays with a NOESY pulse sequence combined with a saturation recovery unit, the numbers in Figure 4 quantify the intensities I (in percent of the diagonal (I_A and I_B) and off-diagonal peaks (I_{AB} and I_{BA}) with respect to the most intense line in Figure 3c) which is set to $I_B = 100\%$. The recycle delay of the 2D NMR spectrum shown in Figure 4c was 300 s. At a Larmor frequency of 88 MHz, the site-specific spin–lattice relaxation times T_{1A} and T_{1B} of the two signals (A and B) amount to 264(8) s and 266(7) s, respectively. Because of the saturation comb used, a full relaxation delay of $5T_1$ can be avoided to keep the measurement time within an acceptable range.

In order to further illustrate the ratios (such as I_A/I_{AB}) found, in Figure 5 three-dimensional plots of the 2D experiments are shown for comparison. In all three cases, we found $I_A \approx I_B$ ($= I_{d(\text{ia})}$) and $I_{AB} \approx I_{BA}$ ($= I_{c(\text{ross})}$). Additional broadening of the diagonal NMR intensities emerging with increasing mixing time is absent. Hence, no indications for self-exchange processes¹³ are seen at the time scales and temperature of our experiments.

Since Li hopping is restricted to a two-site jump process, the exchange rate $1/\tau_{\text{exch}}$ can be estimated using the following expression

$$\frac{I_c}{I_d} = \left[1 - \exp\left(-\frac{t_m}{\tau_{\text{exch}}}\right) \right], \text{ i.e., } \tau_{\text{exch}} = -\frac{t_m}{\ln \frac{I_d - I_c}{I_d}}$$

With the intensities determined at $t_m = 60$ s we obtain $\tau_{\text{exch}} = 57(5)$ s. Using the Einstein–Smoluchowski equation

$$D_{\text{sd}} = \frac{a^2}{6\tau_{\text{exch}}}$$

and assuming a jump distance a of approximately 2 Å between the Li sites Li(1) and Li(2), this corresponds to an Li self-diffusion coefficient D_{sd} in the order of $1 \times 10^{-22} \text{ m}^2 \text{ s}^{-1}$. Taking this value as an estimate of the solid-state diffusion coefficient D , the Nernst–Einstein equation³⁵ yields an Li ion conductivity of $\sigma \approx 10^{-13} \dots 10^{-12} \text{ S cm}^{-1}$ at ca. 310 K. This is in good agreement with experimental values measured by ac impedance spectroscopy.³⁶ Hence, atomic-scale 2D exchange NMR probes the same translational process which is responsible for macroscopic Li ion transport in Li_2ZrO_3 .

SUMMARY AND OUTLOOK

Local electronic structures and Li^+ hopping in polycrystalline Li_2ZrO_3 has been studied by 1D and 2D ${}^6\text{Li}$ and ${}^7\text{Li}$ MAS NMR spectroscopy. At sufficiently long mixing times of up to 1 min, the contour plots of ${}^6\text{Li}$ EXSY NMR clearly reveal off-diagonal intensities indicating an extremely slow two-site exchange process with rates as low as ~ 60 jumps/hour. This corresponds to a self-diffusion coefficient in the order of $10^{-22} \text{ m}^2 \text{ s}^{-1}$ which is in agreement with macroscopic transport properties probed by conductivity measurements. To our knowledge, this is, so far, one of the slowest Li solid-state diffusion processes made visible by ${}^6\text{Li}$ 2D exchange MAS NMR.

To our opinion, Li_2ZrO_3 with its two distinct Li sites might serve as a promising model system for future work, for example, being geared toward the calculation of chemical shifts, electric field gradients, and dynamic parameters. The pure two-site exchange process in Li_2ZrO_3 might be beneficial to be studied

in detail by further sophisticated and newly established NMR techniques, which are sensitive to fast and slow Li dynamics as well. By using complementary methods, it would be interesting to enlighten the dynamic range over which the two-site jump process does exist.

AUTHOR INFORMATION

Corresponding Author

*E-mail: bottke@tugraz.at

Notes

The authors declare no competing financial interest.

ACKNOWLEDGMENTS

Financial support by the Deutsche Forschungsgemeinschaft (DFG) within the Research Unit FOR 1277 (WI3600 4-1 and 4-2) is highly appreciated. We thank the Graz University of Technology and the University of Leipzig (project Avance 750) for further support.

REFERENCES

- (1) Knauth, P. Inorganic solid Li ion conductors: An overview. *Solid State Ionics* **2009**, *180*, 911–916.
- (2) Murugan, R.; Thangadurai, V.; Weppner, W. Fast Lithium Ion Conduction in Garnet-Type $\text{Li}_7\text{La}_3\text{Zr}_2\text{O}_{12}$. *Angew. Chem., Int. Ed.* **2007**, *46*, 7778–7781.
- (3) Winter, M.; Besenhard, J. O.; Spahr, M. E.; Novák, P. Insertion Electrode Materials for Rechargeable Lithium Batteries. *Adv. Mater.* **1998**, *10*, 725–763.
- (4) Choi, N.-S.; Chen, Z.; Freunberger, S. A.; Ji, X.; Sun, Y.-K.; Amine, K.; Yushin, G.; Nazar, L. F.; Cho, J.; Bruce, P. G. Challenges Facing Lithium Batteries and Electrical Double-Layer Capacitors. *Angew. Chem., Int. Ed.* **2012**, *51*, 9994–10024.
- (5) Goodenough, J. B.; Kim, Y. Challenges for rechargeable batteries. *J. Power Sources* **2011**, *196*, 6688–6694.
- (6) Bruce, P. G.; Freunberger, S. A.; Hardwick, L. J.; Tarascon, J.-M. Li-O₂ and Li-S batteries with high energy storage. *Nat. Mater.* **2012**, *11*, 19–29.
- (7) Tarascon, J.-M. Key challenges in future Li-battery research. *Philos. Trans. R. Soc. London, Ser. A* **2010**, *368*, 3227–3241.
- (8) Bruce, P. G.; Scrosati, B.; Tarascon, J.-M. Nanomaterials for Rechargeable Lithium Batteries. *Angew. Chem., Int. Ed.* **2008**, *47*, 2930–2946.
- (9) Arico, A. S.; Bruce, P.; Scrosati, B.; Tarascon, J.-M.; Schalkwijk, W. V. Nanostructured materials for advanced energy conversion and storage devices. *Nat. Mater.* **2005**, *4*, 366–377.
- (10) Tarascon, J.-M.; Armand, M. Issues and challenges facing rechargeable lithium batteries. *Nature* **2001**, *414*, 359–367.
- (11) Ellis, B. L.; Lee, K. T.; Nazar, L. F. Positive Electrode Materials for Li-Ion and Li-Batteries. *Chem. Mater.* **2010**, *22*, 691–714.
- (12) Hodeau, J. L.; Marezio, M.; Santoro, A.; Roth, R. S. Neutron Profile Refinement of the Structures of Li_2SnO_3 and Li_2ZrO_3 . *J. Solid State Chem.* **1982**, *45*, 170–179.
- (13) Xu, Z.; Stebbins, J. F. Cation Dynamics and Diffusion in Lithium Orthosilicate: Two-Dimensional Lithium-6 NMR. *Science* **1995**, *270*, 1332–1334.
- (14) Verhoeven, V. W. J.; de Schepper, I. M.; Nachtegaal, G.; Kentgens, A. P. M.; Kelder, E. M.; Schoonman, J.; Mulder, F. M. Lithium dynamics in LiMn_2O_4 probed directly by two-dimensional ${}^7\text{Li}$ NMR. *Phys. Rev. Lett.* **2001**, *86*, 4314–4317.
- (15) Grey, C. P.; Dupré, N. NMR Studies of Cathode Materials for Lithium-Ion Rechargeable Batteries. *Chem. Rev.* **2004**, *104*, 4493–4512.
- (16) Cahill, L. S.; Yin, S. C.; Samoson, A.; Heinmaa, I.; Nazar, L. F.; Goward, G. R. ${}^6\text{Li}$ NMR studies of cation disorder and transition metal ordering in $\text{LiNi}_{1/3}\text{Mn}_{1/3}\text{Co}_{1/3}\text{O}_2$ using ultrafast magic angle spinning. *Chem. Mater.* **2005**, *17*, 6560–6566.

- (17) Cabana, J.; Dupré, N.; Rousse, G.; Grey, C. P.; Palacín, M. R. *Solid State Ion.* **2005**, *176*, 2205.
- (18) Cahill, L. S.; Chapman, R. P.; Britten, J. F.; Goward, G. R. ^7Li NMR and 2D Exchange Study of Lithium Dynamics in Monoclinic $\text{Li}_3\text{V}_2(\text{PO}_4)_3$. *J. Phys. Chem. B* **2006**, *110*, 7171–7177.
- (19) Cahill, L. S.; Iriyama, Y.; Nazar, L. F.; Goward, G. R. Synthesis of $\text{Li}_3\text{V}(\text{PO}_4)_2\text{F}_2$ and ^6Li , ^7Li NMR studies of its lithium ion dynamics. *J. Mater. Chem.* **2010**, *20*, 4340–4346.
- (20) Davis, L. J. M.; Heinmaa, I.; Goward, G. R. Study of Lithium Dynamics in Monoclinic $\text{Li}_3\text{Fe}_2(\text{PO}_4)_3$ using ^6Li VT and 2D Exchange MAS NMR Spectroscopy. *Chem. Mater.* **2010**, *22*, 769–775.
- (21) Wilkening, M.; Romanova, E. E.; Nakhla, S.; Weber, D.; Lerch, M.; Heitjans, P. Time-Resolved and Site-Specific Insights into Migration Pathways of Li^+ in $\alpha\text{-Li}_3\text{VF}_6$ by ^6Li 2D Exchange MAS NMR. *J. Phys. Chem. C* **2010**, *114*, 19083–19088.
- (22) Wagemaker, M.; van Eck, E. R. H.; Kentgens, A. P. M.; Mulder, F. M. Li-Ion Diffusion in the Equilibrium Nanomorphology of Spinel $\text{Li}_{4+x}\text{Ti}_5\text{O}_{12}$. *J. Phys. Chem. C* **2009**, *113*, 224–230.
- (23) Kuhn, A.; Sreeraj, P.; Pöttgen, R.; Wiemhöfer, H.-D.; Wilkening, M.; Heitjans, P. Li NMR Spectroscopy on Crystalline $\text{Li}_{12}\text{Si}_7$: Experimental Evidence for the Aromaticity of the Planar Cyclopentadienyl-Analogous Si_5^{6-} Rings. *Angew. Chem., Int. Ed.* **2011**, *50*, 12099–12102.
- (24) Vijayakumar, M.; Kerisit, S.; Rosso, K. M.; Burton, S. D.; Sears, J. A.; Yang, Z. G.; Graff, G. L.; Liu, J.; Hu, J. Z. Lithium diffusion in $\text{Li}_4\text{Ti}_5\text{O}_{12}$ at high temperatures. *J. Power Sources* **2011**, *196*, 2211–2220.
- (25) Vijayakumar, M.; Kerisit, S.; Yang, Z. G.; Graff, G. L.; Liu, J.; Sears, J. A.; Burton, S. D.; Rosso, K. M.; Hu, J. Z. Combined ^6Li , ^7Li NMR and Molecular Dynamics Study of Li Diffusion in Li_2TiO_3 . *J. Phys. Chem. C* **2009**, *113*, 20108–20116.
- (26) Hain, H.; Scheuermann, M.; Heinzmann, R.; Wünsche, L.; Hahn, H.; Indris, S. Study of local structure and Li dynamics in $\text{Li}_{4+x}\text{Ti}_5\text{O}_{12}$ using ^6Li and ^7Li NMR spectroscopy. *Solid State Nucl. Magn. Reson.* **2012**, *42*, 9–16.
- (27) Carlier, D.; Ménétrier, M.; Grey, C. P.; Delmas, C.; Ceder, G. Understanding the NMR shifts in paramagnetic transition metal oxides using density functional theory calculations. *Phys. Rev. B* **2003**, *67*, 174103–174117.
- (28) Ménétrier, M.; Vaysse, C.; Croguennec, L.; Delmas, C.; Jordy, C.; Bonhomme, F.; Biensan, P. ^7Li and ^1H MAS NMR Observation of Interphase Layers on Lithium Nickel Oxide Based Positive Electrodes of Lithium-Ion Batteries. *Electrochem. Solid State Lett.* **2004**, *7*, A140–A143.
- (29) Kohl, J.; Nakhla, S.; Ferro, N.; Bottke, P.; Wilkening, M.; Bredow, T.; Heitjans, P.; Lerch, M. Z. *Allg. Anorg. Chem.* **2013**, *639*, 326.
- (30) Fukushima, E.; ; Roeder, S. B. W. *Experimental Pulse NMR*; Addison-Wesley: Reading, 1981.
- (31) Freude, D.; Haase, J. Quadrupole Effects in Solid-State NMR. In *Nuclear Magnetic Resonance, Basic Principles and Progress*; Springer: New York, 1993; Vol. 29; pp 1.
- (32) Bredow, T.; Heitjans, P.; Wilkening, M. Electric field gradient calculations for Li_xTiS_2 and comparison with ^7Li NMR results. *Phys. Rev. B* **2004**, *70*, 115111–115122.
- (33) Baklanova, Y. V. ^1H and ^7Li NMR in $\text{Li}_{2-x}\text{H}_x\text{MO}_3$ (M = Ti, Zr). *Magn. Res. Solids* **2008**, *10*, 39–45.
- (34) Böhmer, R.; Jeffrey, K.; Vogel, M. Solid-state lithium NMR with applications to the translational dynamics in ion conductors. *Prog. Nucl. Magn. Reson. Spectrosc.* **2007**, *50*, 87–174.
- (35) Mehrer, H. *Diffusion in Solids: Fundamentals, Methods, Materials, Diffusion-Controlled Processes*; Springer: Berlin, 2007.
- (36) Hellstrom, E. E.; Gool, W. v. Li ion conduction in Li_2ZrO_3 , Li_4ZrO_4 , and LiScO_2 . *Solid State Ionics* **1981**, *2*, 59–64.

3.1.2 Leitfähigkeitsmessungen an mikro- und nanokristallinem Li_2ZrO_3

In der zuvor gezeigten Publikation, ist ein Selbstdiffusionskoeffizient in der Größenordnung $10^{-22} \text{ m}^2/\text{s}$ angegeben worden, der sich über die EINSTEIN-SMOLUCHOWSKI-Gleichung aus der Austauschrate des ${}^6\text{Li}$ 2D EXSY NMR-Experiments berechnen lässt. Dafür wurden die Sprungdistanz r und die Dimensionalität d des Prozesses mit 2 \AA und dreidimensionaler Diffusion angenommen. Des Weiteren wurden der Korrelationsfaktor f und das HAVEN-Verhältnis H_V gleich eins gesetzt, wodurch auch D^{tr} und D^{NE} denselben Wert annehmen. Über die NERNST-EINSTEIN-Relation wurden dann Leitfähigkeiten im Bereich von $\sigma \approx 10^{-13} \dots 10^{-12} \text{ S cm}^{-1}$ abgeschätzt. Diese Umrechnung kann auch in die andere Richtung genutzt werden, um Leitfähigkeiten in Sprungraten umzurechnen. Die oben genannten Parameter könnten nach hinreichenden NMR-, Tracerdiffusions- und Impedanzmessungen bestimmt werden.

Die Kristallstruktur von Li_2ZrO_3 ist spätestens seit der Arbeit von J. L. Hodeau et al.^[44] vollständig bekannt. Durch die Verfeinerung der Daten aus Neutronenbeugungsexperimenten mit Hilfe der Rietveldmethode^[45] konnten die Raumgruppe C2/c und eine monokline Elementarzelle bestätigt werden. Schon G. Dittrich und R. Hoppe^[46] hatten diese Ergebnisse, welche sie über Röntgenstrukturanalyse erhielten, veröffentlicht. Hier wurde Li_2ZrO_3 mit Li_2HfO_3 verglichen, wobei J. L. Hodeau et al. zusätzlich Li_2SnO_3 untersuchten. Die Lithiumionenleitfähigkeit von Lithiumzirkonat wurde von E. Hellstrom und W. Van Gool^[47] mittels Impedanzspektroskopie untersucht. Abb. 3.2 A zeigt den Vergleich mit den eigenen Messungen.

Die Leitfähigkeiten von den Proben A (Alfa Aesar mind. 94 %); B (kugelmahlen dunkelgrau) und C (kugelmahlen* farblos) sind in Abb. 3.1 gezeigt. A ist identisch mit der Probe, die auch für die NMR verwendet wurde. Für die Leitfähigkeitsmessungen wurden jedoch von allen drei Proben Tabletten aus dem Pulver gepresst und mit aufgesputterten Goldelektroden versehen. Außerdem wurde das Temperaturprogramm so gewählt, dass die Proben vor den eigentlichen Messungen einige Stunden bei $250 \text{ }^\circ\text{C}$ im Stickstoffstrom getrocknet wurden. Einflüsse dieser Probenvorbereitung können nicht ausgeschlossen werden. Das Trocknen erniedrigte die Leitfähigkeit der Probe A am stärksten, im untersuchten Temperaturbereich jedoch max. um eine halbe Größenordnung. Für die NMR wurde das Rohmaterial direkt verwendet.

Die hier gezeigten Leitfähigkeiten und Sprungraten in den Arrheniusdiagrammen wurden entweder direkt gemessen oder sind mit $d = 3$, $f = 1$ und $H_V = 1$ berechnet worden. Durch die Anpassung der Parameter könnte eine bessere Übereinstimmung erreicht werden, dafür sind aber zu wenige Daten aus der NMR vorhanden.

* Die Proben B und C wurden durch HEBM in einer Fritsch Pulverisette 7 aus dem Rohmaterial A hergestellt. 1 g Li_2ZrO_3 , 140 Kugeln, 600 rpm, $12 \times 30 \text{ min}$ mit je 30 min Pause zwischen den Mahlvorgängen. Die farblose Probe haftete kompakt an der Innenwand des Wolframcarbid-Mahlbechers und wurde von der dunkelgrauen Probe, die lose im Becher vorlag, teilweise bedeckt. Die Trennung der optisch und haptisch (Spatel) sehr unterschiedlichen Materialien erfolgte manuell.

Interessanterweise passt die Leitfähigkeit, die aus dem Austauschexperiment mit $t_{\text{exchange}} = 57.4$ s berechnet wurde, besser zu den Daten von Hellstrom et al. [47], die von den eigenen Ergebnissen deutlich abweichen. Die Sprungdistanz wurde hierfür auf 3.063 \AA festgelegt. Diese Anpassung (gegenüber P1) ergibt sich aus der durchschnittlichen Distanz aller möglichen Sprünge zu einem nächsten Nachbarplatz. σ_{EXSY} ist dadurch etwa halb so groß; r kann die Abweichung von den eigenen Werten also nicht erklären.

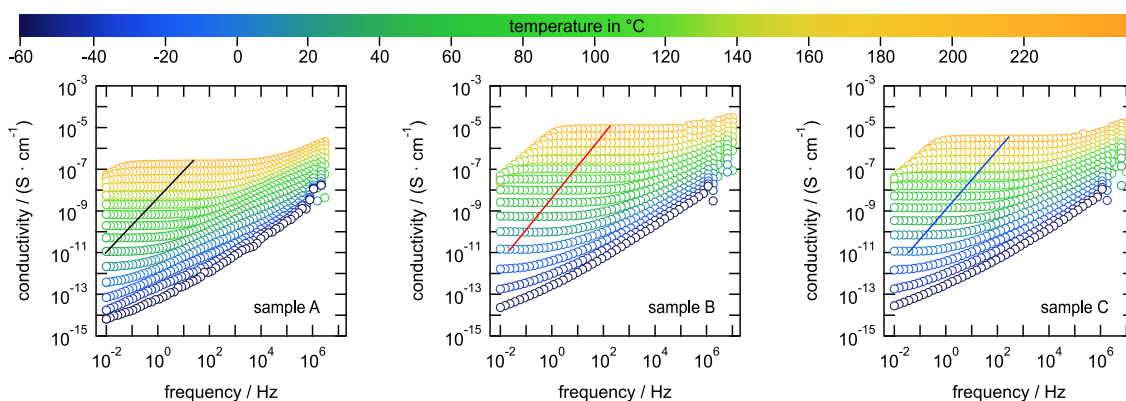


Abbildung 3.1: Leitfähigkeitsspektren von Li_2ZrO_3 . Die Proben A (mikrokristallines Rohmaterial), B (kugelmahlen, fast röntgenamorph) und C (kugelmahlen nanokristallin) zeigen gut auslesbare DC-Plateaus. Die farbigen Linien geben den in Abb. 3.2 A aufgetragenen Wert an. Das Kugelmahlen erhöht die Leitfähigkeit um ca. $1^{1/2}$ Größenordnungen.

Die höchste experimentelle Ungenauigkeit liegt in der Proben temperatur während des 2D EXSY NMR Experiments. Durch die Probenrotation erwärmt sich die Probe und durch die Gasströme *VT gas*, *bearing* und *drive* wird die Probe hauptsächlich gekühlt. *VT gas* ist das Heiz- bzw. Kühlmedium (variable Temperatur durch elektrische Heizung und Wärmetauscher im flüssigen Stickstoff), es kann die Probe aber nicht direkt temperieren. Die Temperatur des Gesamtgasstroms, der mit der Rotoraußenwand Wärme austauscht, ist entscheidend. Da *bearing* (hält den Rotor in Position) und *drive* (treibt die Rotation an) immer Raumtemperatur haben und ihr Fluss mit der gewünschten Rotationsfrequenz steigt, nimmt der Einfluss auf *VT gas* ebenso zu. Dadurch ist der Temperaturbereich der Probe gegenüber den technisch möglichen Werten für *VT gas* verschoben und zusammengestaucht. Dieses komplexe System verbietet die direkte Messung der Proben temperatur und muss mit geeigneten Referenzsubstanzen kalibriert werden. [48–50] Wenn dann alle Gasströme und auch die resultierende Rotationsfrequenz während des Experiments mit den Werten der Kalibrierung übereinstimmen, kann eine Proben temperatur angegeben werden. Je nach Rotorendurchmesser und Rotationsfrequenz herrscht außerdem ein Temperaturgradient im Probenmaterial (an der Rotationsachse kühler als nach außen hin).

Für die MAS Frequenz von 12 kHz und eine *VT gas* Temperatur von 310 K wurde nach oben genannten Vorüberlegungen eine durchschnittliche Proben temperatur von 321.7 K

bzw. 48.5°C abgeschätzt. In Abb. 3.2 A ist dieser Wert (grüner Punkt) für die berechnete Leitfähigkeit verwendet worden. Zusätzlich ist noch eine höhere Temperatur (roter Punkt) und eine niedrigere Temperatur (blauer Punkt) dargestellt. Die Temperaturen 60°C und 10°C wurden willkürlich gewählt, um auf den Ausgleichsgeraden der Daten von Hellstrom et al. bzw. Probe A zu liegen. Die zusätzliche Korrektur der Temperatur nach oben ist zwar nicht zu vernachlässigen, liegt aber im Bereich des Möglichen. Dass die Proben temperatur während der Durchführung des Experiments 10°C betrug, kann hingegen ausgeschlossen werden.

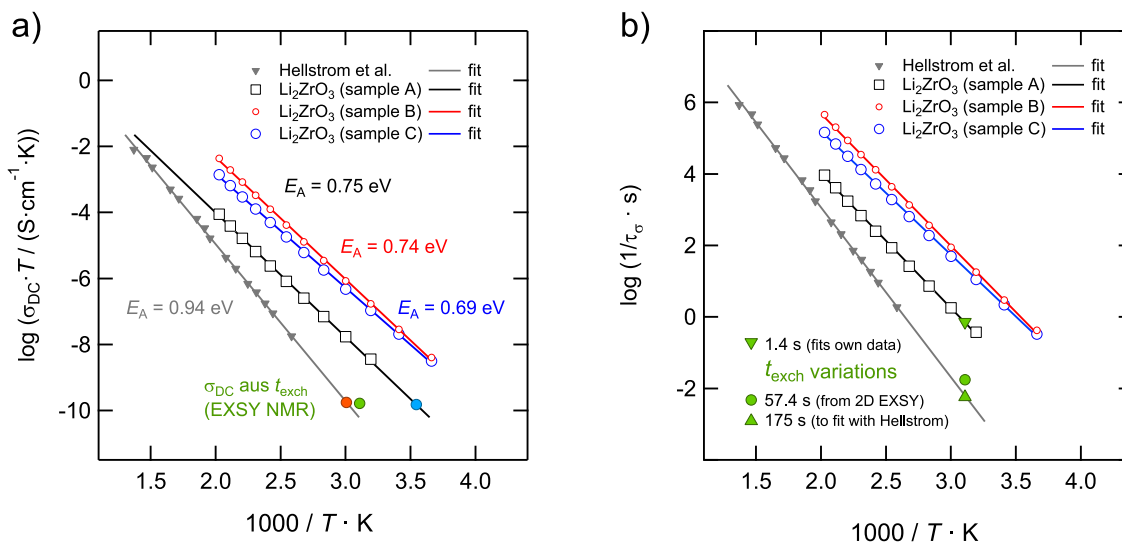


Abbildung 3.2: a) Arrhenius-Plot der Leitfähigkeiten aus Abb. 3.1 und aus der Literatur^[47]. Außerdem ist der berechnete σ_{DC} -Wert aus dem 2D-Austauschexperiment ($t_{\text{exchange}} = 57.4$ s) multipliziert mit seiner Temperatur (Details siehe Text) aufgetragen. Dabei entsprechen die vollausgefüllten Kreise 48.5°C (grün), 60°C (rot) und 10°C (blau). b) Sprungraten berechnet aus den Leitfähigkeiten von A aufgetragen gegen die inverse Temperatur. Die grün gefüllten Symbole sind für die „echte“ Proben temperatur (siehe Text) und die angegebenen Austauschzeiten eingetragen.

In Abb. 3.2 b) ergibt sich zunächst dasselbe Bild für die aus den Leitfähigkeiten berechneten Sprungraten. Der grüne Punkt für t_{exchange} hat auch hier die experimentell bestimmten Parameter und ist gleich nah an den Hellstrom-Daten. Für die grünen Dreiecke wurden die Austauschzeiten so angepasst, dass sie auf den Fits für die Sprungraten von Probe A bzw. der Literatur liegen. Nehmen wir die Proben temperatur von 48.5°C als korrekt an, ist die Austauschrate aus den 2D EXSY Messungen nur ca. 3 mal so hoch wie in der Literatur. Dies ist unter den gemachten Annahmen und bei der unterschiedlichen Proben vorbereitung für beide Methoden eine sehr gute Näherung. Auch die Richtung der Abweichung stimmt. Für den Vergleich mit den eigenen Werten musste die Austauschrate mit einem Faktor von 41 multipliziert werden. Eine mögliche Ursache für diese Abweichung wäre, dass die NMR

nicht alle Platzwechsel sieht, da auch Sprünge zu magnetisch äquivalenten Gitterplätzen zum Selbstdiffusionskoeffizienten D^{sd} beitragen.

Eine deutlich einfachere Erklärung für die Abweichungen von der Literatur^[2] und innerhalb der eigenen Messungen, ist die Reinheit der verwendeten Proben. Hellstrom et al. haben ihre Probe selbst synthetisiert, das Material von Alfa Aesar enthält bis zu 6 % Nebenphasen. Diese haben auf die 2D-Austauschexperimente keine Auswirkungen (siehe, *Figure 3 b*) in P1), die Leitfähigkeitsmessungen können dadurch jedoch stark beeinflusst sein.

3.1.3 1D/2D $^{7,6}\text{Li}$ MAS NMR an paramagnetischen Kathodenmaterialien

P2 und P3: ^6Li -MAS-NMR-Arbeiten an paramagnetischen Materialien, die z. B. als positive Elektrodenmaterialien Verwendung finden könnten, sind auf Grund der deutlich kürzeren Zeit für die Experimente wesentlich zahlreicher, als Studien an diamagnetischen Materialien. Zu den interessanten Materialklassen gehören die Nickelfluoride (P2) und Vanadiumfluoride (P3). Die großen Fermi-Kontakt-Wechselwirkungen führen zu deutlichen paramagnetischen Verschiebungen der NMR-Linien. Um die Linienverbreiterung durch paramagnetische Einflüsse klein zu halten, werden die Experimente vorzugsweise bei niedrigem externen Magnetfeld durchgeführt. Die kurzen Spin-Gitter-Relaxationszeiten verkürzen die Messzeit gegenüber diamagnetischen Materialien (siehe P1) deutlich, selbst wenn die Auflösung der indirekten Ebene für 2D-Experimente höher gewählt wird. Andererseits wird dadurch aber auch das zugängliche dynamische Zeitfenster eingeschränkt.

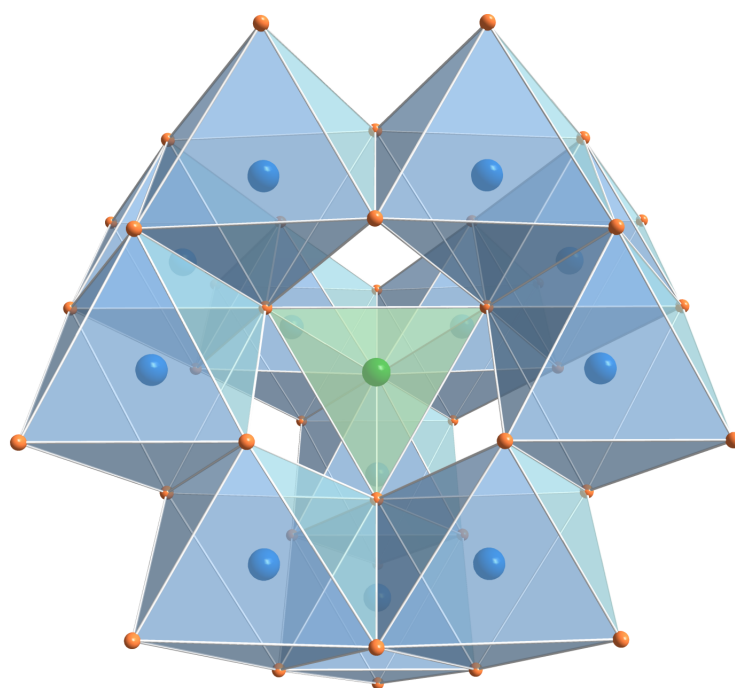
Erste NMR-Messungen an Li_2NiF_4 offenbaren die Komplexität von $^{7,6}\text{Li}$ MAS NMR-Spektren, die eine Vielzahl von magnetisch inequivalenten Li-Spins in der Fluorid-Struktur zeigt (P2). Die insgesamt neun verschiedenen Li Positionen konnten nur mittels *ultrafast* MAS (60 kHz Rotationsfrequenz) von den zahlreichen Seitenbanden getrennt werden.

Am Beispiel von Li_3VF_6 , das in der α ^[51]- und β^* -Modifikation vorliegen kann, konnten relative platzspezifische Li-Sprungraten erfasst werden. Über die Auswertung der Spektren, d. h. die Zuordnung der NMR-Linien zu den einzelnen Li-Positionen, gelang es, die bevorzugten Wanderungspfade nachzuvollziehen und die Diffusionseigenschaften auf atomarer Skala verstehen zu lernen.

1D ^7Li MAS NMR-Spektren der beiden Modifikationen bestätigen die Anzahl der jeweiligen kristallographischen Plätze (siehe P3). Für die α -Modifikation konnten 3 Li Plätze aufgelöst werden, die β -Modifikation hat sogar 5 verschiedene Li Positionen, wovon 3 *peaks* selbst bei 60 kHz teilweise überlagert waren.

Als Zusatz zu der Publikation 3 werden $^{7,6}\text{Li}$ -2D-Austauschexperimente an β - Li_3VF_6 gezeigt (ab Seite 72). Mit weiteren Informationen aus der Kristallstruktur war so die Zuordnung der NMR-Linien zu den Gitterplätzen möglich.

* Die Daten wurden bisher nur als Poster „veröffentlicht“.

P2 Low-Temperature Synthesis, Characterization, and Stability of Spinel-Type Li_2NiF_4 and Solid-Solutions $\text{Li}_2\text{Ni}_{1-x}\text{Co}_x\text{F}_4$ 

Li^+ (green), LiNi (blue) and F^- (orange)

ARTICLE

DOI: 10.1002/zaac.201200455

Low-Temperature Synthesis, Characterization, and Stability of Spinel-Type Li_2NiF_4 and Solid-Solutions $\text{Li}_2\text{Ni}_{1-x}\text{Co}_x\text{F}_4$

Julia Kohl,^[a] Suliman Nakhal,^[a] Noel Ferro,^[b] Patrick Bottke,^[c] Martin Wilkening,^[c]
Thomas Bredow,^[b] Paul Heitjans,^[d] and Martin Lerch^{*[a]}

Dedicated to Professor Hartmut Bärnighausen on the Occasion of His 80th Birthday

Keywords: Synthesis; Nickel; Cobalt; NMR spectroscopy; X-ray diffraction

Abstract. A new synthesis route to Li_2NiF_4 based on a fluorolytic process using $\text{Ni}(\text{acac})_2$ or $\text{Ni}(\text{OAc})_2 \cdot 4\text{H}_2\text{O}$ as precursor is presented. Variation of the synthesis conditions allows crystallite size control of the obtained powders. ^6Li and ^7Li MAS NMR experiments were carried out to study local environments of the lithium ions. Several attempts were made to synthesize Li_2CoF_4 , which are, unfortunately,

hitherto not successful. Nevertheless, our studies clearly reveal that solid solutions Li_2NiF_4 – Li_2CoF_4 are stable up to ca. 30% cobalt. High-temperature X-ray diffraction measurements also show no evidence for the existence of pure Li_2CoF_4 . These findings are supported by quantum chemical calculations.

Introduction

In the last years fluorides have attracted increasing attention as cathode materials for lithium-ion batteries. Compounds of the Li_xMF_y -type, where M represents a transition metal, are distinguished by a high amount of lithium together with a variety of structural features and possible oxidation states of M . Some exponents of this class of materials, such as monoclinic Li_3FeF_6 ^[1] and Li_3VF_6 ,^[2] have already been electrochemically investigated. From a crystal chemistry point of view Li_2NiF_4 may also be considered to serve as a cathode material in lithium-ion batteries. Li_2NiF_4 crystallizes in the well-known inverse spinel-type structure (space group $Fd\bar{3}m$).^[3,4] Usually, it is prepared by solid-state reaction of LiF and NiF_2 at $680\text{ }^\circ\text{C}$ ^[3] or by high-pressure solvothermal synthesis carried out at $625\text{ }^\circ\text{C}$,^[4] or by fluorination of $\text{Li}_2[\text{Ni}(\text{CN})_4]$ with an additional heating procedure in vacuo.^[5]

So far, this particular fluoride has also been in the focus of some electrochemical investigations. In 1999, the properties of an electrode made from Li_2NiF_4 , graphite, and polyvinyl-difluoride were investigated; the voltage (vs. Li metal) was reported to be 5.1 V.^[6] Moreover, mixed spinels such as $\text{Li}_2\text{Ni}_{1-x}\text{Co}_x\text{F}_4$ are also of interest: As an example, a cathode utilizing $\text{Li}_2\text{Ni}_{0.8}\text{Co}_{0.2}\text{F}_4$ shows a voltage of 5.2 V (vs. lithium metal).^[6] In contrast to Li_2NiF_4 , only little information can be found in the literature concerning the existence of the cobalt counterpart Li_2CoF_4 . To the best of our knowledge, there is only one single reference mentioning this compound; the possible phase formation of Li_2CoF_4 in the quasi binary system LiF – CoF_2 was investigated by means of X-ray powder diffraction and thermoanalytical methods (using Ni-containers!).^[7] The authors observed a diffraction pattern being similar to that of the nickel analogue and concluded that Li_2CoF_4 had been formed. However, apart from that work the formation of Li_2CoF_4 has never been reported again.

Keeping in mind the potential use of these spinels as cathode materials, the high synthesis temperature reported ($> 600\text{ }^\circ\text{C}$ for Li_2NiF_4) is far away from being optimally suited to control the morphology. Unfortunately, large crystallite sizes, which unavoidably form at such high temperatures, turn out to be disadvantageous for electrochemical applications. This is because of the resulting large Li^+ and e^- diffusion lengths as well as the poor electronic conductivity of lithium transition metal fluorides, which calls for additives enhancing e^- transport. The present work aims at developing a new, low-temperature synthesis route for Li_2NiF_4 based on precursors synthesized from corresponding organic salts such as acetylacetonates and acetates, respectively. As mentioned above, Li_2NiF_4 is formed at $680\text{ }^\circ\text{C}$; it is only stable in a narrow temperature range, i.e.,

* Prof. Dr. M. Lerch
Fax: +49-30-31479656
E-Mail: martin.lerch@tu-berlin.de

[a] Technische Universität Berlin
Institut für Chemie, Sekr. C2
Straße des 17. Juni 135
10623 Berlin, Germany

[b] Mulliken Center for Theoretical Chemistry
Institut für Physikalische and Theoretische Chemie,
Universität Bonn
Berlingstr. 4
53115 Bonn, Germany

[c] Institut für Chemische Technologie von Materialien
Technische Universität Graz
Stremayrgasse 9
8010 Graz, Austria

[d] Institut für Physikalische Chemie und Elektrochemie
Leibniz Universität Hannover
Callinstraße 3a
30167 Hannover, Germany

the reaction is incomplete below 680 °C and the product decomposes to the binary fluorides above this temperature. Recently we showed that, for example, Li_3VF_6 can be successfully prepared at low temperatures from LiOtBu , $\text{V}(\text{acac})_3$, and HF/EtOH by heating the precursor up to 300 °C only. This method is based on the fluorolytic sol-gel process described by Kemnitz et al.^[8] The applicability of this route on fluoro-metalates has also been demonstrated by the same group.^[9] The mean crystallite size of the powders could be modified by varying the decomposition temperature of the precursor.^[10] In respect to this work, the intention of the presented study is to synthesize Li_2NiF_4 from LiOtBu , $\text{Ni}(\text{acac})_2/\text{Ni}(\text{OAc})_2$, and various HF solutions with subsequent heating procedures of the precursors. Herein, main emphasis will be put on the decrease of the synthesis temperature as well as on the variation of the particle size. Additionally, our attempts on the preparation of pure Li_2CoF_4 and the solid solutions of the Ni- and Co-spinels ($\text{Li}_2\text{Ni}_{1-x}\text{Co}_x\text{F}_4$) will be presented as well.

Results and Discussion

Synthesis of Li_2NiF_4

Li_2NiF_4 can be synthesized via a two-step route. During the first step, $\text{Ni}(\text{OAc})_2 \cdot 4\text{H}_2\text{O}$ or $\text{Ni}(\text{acac})_2$ reacts with LiOtBu and HF in an organic solvent. The precursor is obtained after the solvent was removed and the mixture was dried in vacuo. Heating the precursor in nitrogen atmosphere yields the desired spinel phase. The corresponding X-ray powder diffraction patterns of the precursors, which turned out to be mainly X-ray amorphous, only show broad reflections of LiF . Depending on the kind of organic solvent and the Ni-educt used, some samples contain traces of $\text{NiSiF}_6 \cdot 6\text{H}_2\text{O}$ and/or Li_2SiF_6 originating from the reaction of HF with the Schlenk tube. Only the use of ethanol results in powders free of crystalline silicon compounds.

In the following section the preparation of the spinel-type phase of Li_2NiF_4 is described, while main emphasis is put on the attempt to lower the synthesis temperature as compared to the routes described in the literature so far. $\text{Ni}(\text{acac})_2$ precursors as well as $\text{Ni}(\text{OAc})_2$ -derived precursors were dried at 120 °C for 2 h and afterwards heated for 10 h at various temperatures ranging from 400 °C to 750 °C. Some significant differences are observed: the decomposition of the $\text{Ni}(\text{acac})_2$ precursor led to the formation of Li_2NiF_4 as main phase even at 400 °C. Ni and LiF are detected as side phases (see Figure 1a).

In contrast to this observation, heating $\text{Ni}(\text{OAc})_2$ -derived precursors in the same way led to LiF/NiF_2 mixtures rather than to the formation of the spinel phase (Figure 2a). Increasing the decomposition temperature, the ratio $\text{Li}_2\text{NiF}_4/\text{LiF}/\text{Ni}$ remains constant for the $\text{Ni}(\text{acac})_2$ precursor between 500 °C and 680 °C. Finally, at 750 °C no nickel metal can be observed any longer. Again, the behavior of the $\text{Ni}(\text{OAc})_2$ precursor is different: together with a small amount of LiF , the desired main phase Li_2NiF_4 forms at temperatures ranging from 500 °C to 750 °C (Figure 2). In addition, it was found that the formation of the spinel phase depends on the kind of organic solvent used for the preparation of the precursor (Figure 3). In

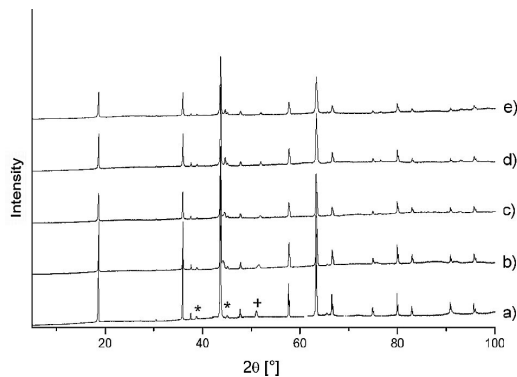


Figure 1. X-ray diffraction patterns of the powders obtained by heating $\text{Ni}(\text{acac})_2$ -based precursors for 10 h at different temperatures: (a) 400 °C: mixture of Li_2NiF_4 , LiF , Ni ; (b) 500 °C; (c) 600 °C; (d) 680 °C; (e) 750 °C: Li_2NiF_4 with small amounts of LiF (* mark the characteristic reflections of LiF , + marks nickel metal).

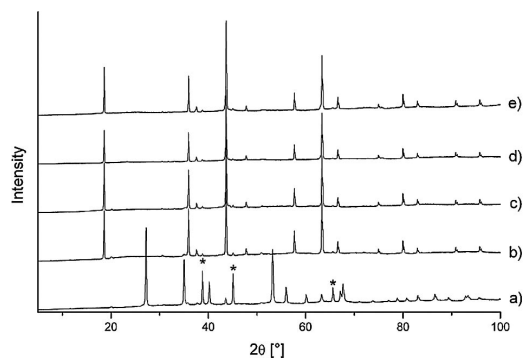


Figure 2. X-ray diffraction patterns of the powders obtained by heating $\text{Ni}(\text{OAc})_2$ -based precursors for 10 h at different temperatures: (a) 400 °C: mixture of NiF_2 and LiF ; (b) 500 °C; (c) 600 °C; (d) 680 °C; (e) 750 °C: Li_2NiF_4 with small amounts of LiF (* mark the characteristic reflections of LiF).

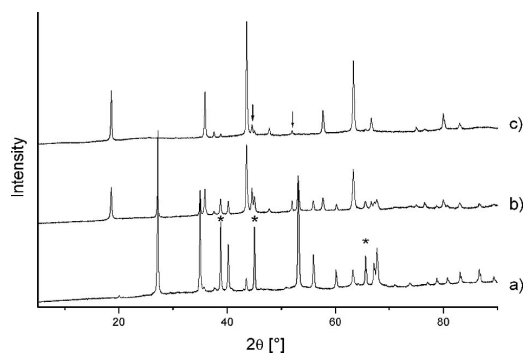


Figure 3. X-ray diffraction patterns of finally obtained powders using different organic solvents for precursor synthesis (decomposition for 10 h at 400 °C): (a) $\text{Ni}(\text{OAc})_2/\text{EtOH}$: mixture of LiF and NiF_2 ; (b) $\text{Ni}(\text{acac})_2/\text{Et}_2\text{O}$: Li_2NiF_4 with LiF , NiF_2 , and Ni ; (c) $\text{Ni}(\text{acac})_2/\text{EtOH}$: Li_2NiF_4 with small amounts of LiF and Ni (* mark the reflections of LiF , arrows (↓) mark the reflections of Ni).

ARTICLE

M. Lerch et al.

general, Ni(acac)₂/ethanol must be considered as first choice, only with ethanol as solvent Li₂NiF₄ is formed even at 400 °C.

The formation of Li₂NiF₄ was also investigated as function of the precursor decomposition time. Both the Ni(OAc)₂ precursor and the Ni(acac)₂-derived precursor were heated for 4 h, 40 h, and 100 h at 400 °C and 680 °C, respectively. It is worth noting that no significant differences of the ratio spinel phase / LiF were observed.

Bearing the properties of powerful cathode materials in mind, it might be crucial to control the crystallite size by, e.g., the variation of the decomposition temperature of the precursor. As an example, the effect of decomposition time on the resulting crystallite sizes was explicitly investigated at several temperatures (400 °C, 500 °C, 600 °C). Mean crystallite sizes were estimated from broadening of the X-ray powder reflections by using the formula introduced by Scherrer.^[11] The results are summarized in the following. The mean crystallite sizes of Li₂NiF₄, synthesized by decomposition (*t*_d = 10 h) of the Ni(acac)₂ precursor, are 66 nm (400 °C), 98 nm (500 °C), and 106 nm (600 °C), respectively. Reducing the decomposition time *t*_d to 4 h led to a mean crystallite size of 55 nm at 400 °C. Further decrease of *t*_d (2 h) resulted in crystallites with a mean diameter of ca. 22 nm. REM measurements of powders prepared from Ni(acac)₂/EtOH at 400 °C (*t*_d = 2 h) exhibit

particle sizes in a range of 150–200 nm. Such small nanoparticles are definitely of interest for cathode active materials in lithium ion batteries.^[12,13]

Besides the characterization by X-ray powder diffraction, first ⁷Li and ⁶Li MAS NMR spectra were recorded to probe local environments of the Li spins in Li₂NiF₄.

To optimize phase purity of the samples and avoid the presence of amorphous phases the solid state route described in the literature^[3] was chosen. The sample used for NMR investigations contains 98% Li₂NiF₄ and approximately 2% LiF. The crystal structure of Li₂NiF₄ can be described as inverse spinel type. This means a nominal distribution of Li in the following way: lithium ions fully occupy the tetrahedral 8*a* sites and share the octahedral sites 16*d* with Ni presumably in an irregular manner. Thus, half of the 16*d* sites are occupied by Ni according to the formula Li[Li,Ni]F₄. The 8*a* sites are surrounded by twelve 16*d* sites and are connected to these sites by corner sharing. Apart from the 8*a* sites in the direct neighborhood, each Li/Ni site is connected to six 16*d* sites by sharing a common edge of the surrounding 16*d* octahedra.^[3,4] As a result of our Rietveld refinements, the used Li₂NiF₄ is not a real inverse spinel: ca. 10% of the tetrahedral sites are occupied by nickel ions. This is also observed for the samples prepared by the fluorolytic route.

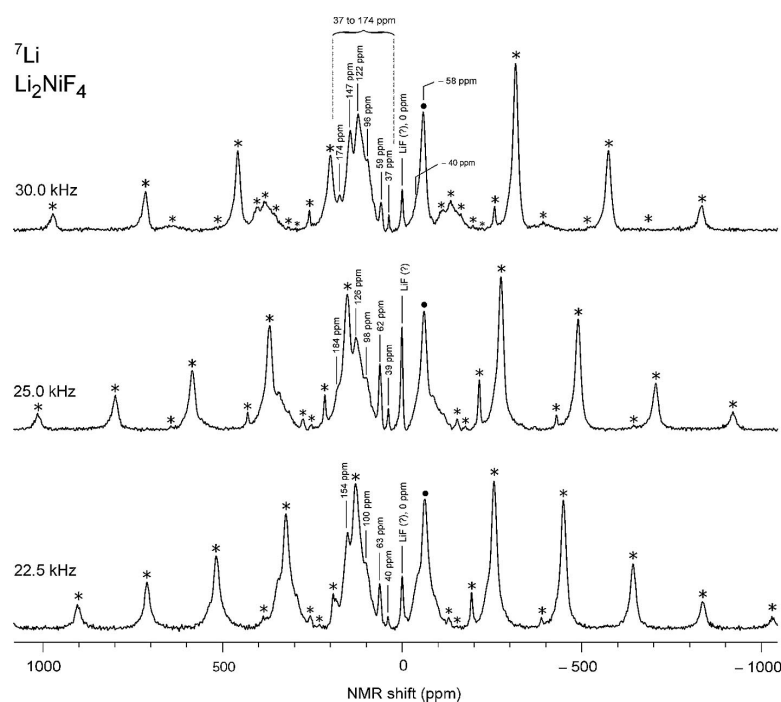


Figure 4. ⁷Li MAS NMR spectra of Li₂NiF₄ recorded at 116 MHz and the rotation frequencies indicated. Although bearing gas at ambient temperature was used, spinning causes an increase of the temperature inside the NMR rotor. Thus, the Li NMR signals expectedly shift towards smaller ppm values due to Curie-Weiss behavior. Most of the spinning sidebands are marked with asterisks. As an example, at a rotation frequency of 30 kHz, the Li NMR signals range from 174 ppm to 37 ppm. Interestingly, an intense and rather broad NMR signal also shows up at negative ppm values. The isotropic line, marked by a circle (●), is located at -58 ppm (see also Figure 5) at a spinning frequency of 30 kHz and ambient bearing gas pressure.

Spinel-Type Li_2NiF_4 and Solid-Solutions $\text{Li}_2\text{Ni}_{1-x}\text{Co}_x\text{F}_4$

Zeitschrift für
anorganische
und allgemeine
Chemie

ZAAC Journal of
Inorganic and
General
Chemistry

In general, the Li NMR (paramagnetic) shift is influenced by the extent and kind of electron spin-density transferred from the nickel ions to the central lithium atoms.^[14]

Due to the presumably irregular number of nickel ions residing in the neighborhood of the Li spins, the corresponding ${}^7\text{Li}$ MAS NMR spectrum is expected to show a distribution of NMR signals reflecting the various Fermi-contact hyperfine interactions of the Li spins with the paramagnetic central Ni^{2+} ions. Since the contact shift is additive, the NMR lines are expected to directly reflect the various numbers of Ni^{2+} ions in the neighborhood (first and second nearest neighbors) of the Li spins (see for example Refs [15,16]).

In Figure 4 some of the ${}^7\text{Li}$ MAS NMR spectra of Li_2NiF_4 are shown. The spectra were recorded at different spinning frequencies in order to differentiate between spinning sidebands, shifting with the rotation frequency, and the (isotropic) NMR lines being of interest. While the signal near 0 ppm most likely represents a diamagnetic impurity such as LiF (vide supra), at a rotation speed of 30 kHz distinct NMR lines show up whose shifts range from 174 ppm to 37 ppm. In contrast to the signal near 0 ppm, they shift towards larger ppm values the smaller the spinning frequency is chosen. Such a dependence reflects Curie-Weiss behavior because the larger the spinning frequency the higher the temperature inside the NMR rotor, which simply stems from the effect of friction (MAS effect). It is worth mentioning that the NMR lines appear in an almost equidistant manner. Probably, this directly reflects the number of central nickel atoms in the coordination sphere of lithium (see also Refs [15,16]).

Interestingly, besides these NMR intensities a relatively broad Li NMR signal shows up, which is characterized by a negative contact shift. By using ${}^6\text{Li}$ MAS NMR, carried out at a spinning speed of 65 kHz, we were able to identify the associated isotropic line being located at approximately -60 ppm (see Figure 5).

In general, ${}^6\text{Li}$ NMR measurements^[16] take advantage of the small magnetogyric ratio $\gamma({}^6\text{Li})$; moreover, the ${}^6\text{Li}$ nucleus is exposed to rather small second order quadrupole interactions, which might additionally affect the shape of ${}^7\text{Li}$ MAS NMR spectra. In the case of ${}^7\text{Li}$ (and at a spinning speed of 30 kHz, Figure 4) the isotropic signal of the broad NMR intensity is located at -58(2) ppm; it shifts only slightly with temperature.

The intensity near -40 ppm (see, for example the ${}^7\text{Li}$ NMR spectra recorded at 30 kHz and 22.5 kHz, respectively, of Figure 4) might indicate an additional NMR signal of very low intensity being also characterized by a negative contact shift. It also shows up in the corresponding ${}^6\text{Li}$ MAS NMR spectrum recorded at 65 kHz (Figure 5). It is worth mentioning that the NMR line at 0 ppm is characterized by a ${}^6\text{Li}$ NMR spin-lattice relaxation time, $T_1 > 200$ ms, which is much larger than those of the other NMR lines ($T_1 < 3$ ms). This further supports the assumption that the line at 0 ppm belongs to a diamagnetic impurity rather than to lithium ions in Li_2NiF_4 .

In the most general sense, the transfer of positive electron spin density to the 2s orbital of the lithium ions will lead to an additive local field resulting in a shift towards positive ppm values. On the other hand, the transfer of negative spin density will lead to

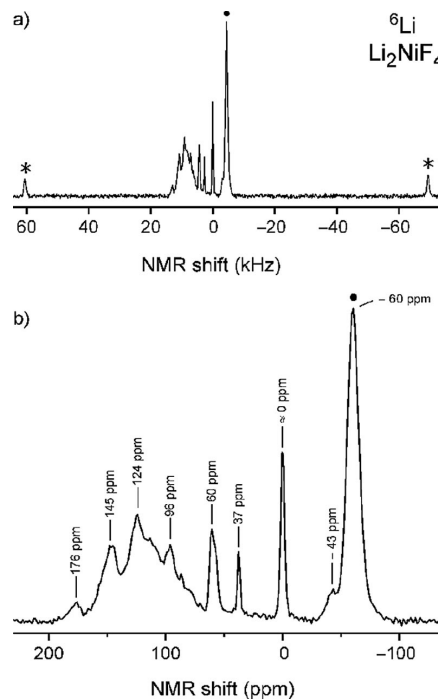


Figure 5. (a) ${}^6\text{Li}$ MAS NMR spectrum of Li_2NiF_4 recorded at 65 kHz (ambient bearing gas temperature) using a 1.3-mm rotor. Due to the high spinning frequency the sideband manifold (asterisks) is largely reduced. (b) Magnification of the spectrum shown in (a). The ppm values of the most intense NMR lines are indicated. Whereas the intensity at ≈ 0 ppm is characterized by a spin-lattice relaxation time T_1 of approximately 200 ms, for the other signals, $T_1 < 3$ ms is found indicating that the signal at 0 ppm most likely represents a diamagnetic impurity. See text for further explanation.

negative shifts as indeed observed in the present case.^[14,17] The final (total) Fermi contact shift is either dominated by a specific transfer mechanism or represents the result of a combination of different spin transfer effects such as delocalization of spin density or polarization of spin orbitals.^[14,17-22] Considering the spin configuration of $\text{Ni}^{2+}(\text{d}8)$, which is $t_{2g}{}^6e_g{}^2$, the unpaired electrons might polarize the doubly occupied t_{2g} crystalline orbitals. In the case of a 90° $M\text{-F-Li}$ interaction this would lead to an increase of positive spin density at the transition metal, while negative spin density is induced on the fluorine (p) and lithium (s) orbitals (polarization of the $t_{2g}\text{-p}\pi\text{-s}$ orbitals).^[14] The transfer of positive spin density can occur via an 180° $M\text{-F-Li}$ interaction involving the p_σ fluorine orbitals. However, there are no 180° $M\text{-F-Li}$ angles in Li_2NiF_4 , which also seems to rule out other transfer mechanisms^[14] needing such arrangements and involving e_g orbitals. Here, the transfer of negative spin density might indeed be possible via 90° $M\text{-F-Li}$ interactions in Li_2NiF_4 . Nickel ions residing on tetrahedral sites, as indicated above, might also be responsible for negative ppm shifts because the loops of the t_2 orbitals present in tetrahedral coordination of a Ni^{2+} ion roughly point into the direction of a lithium ion in an adjacent octahedral site.^[23]

ARTICLE

M. Lerch et al.

Attempts to Synthesize Li_2CoF_4

In this part various attempts to synthesize Li_2CoF_4 are presented, following the successful routes to Li_2NiF_4 .

(1) Precursor Decomposition as Described above for Li_2NiF_4

$\text{Co}(\text{OAc})_2 \cdot 4\text{H}_2\text{O}$ was used as starting material. The obtained precursor was heated under various conditions in analogy to the successful nickel spinel routes. Unfortunately, in all experiments mixtures of LiF and CoF_2 were obtained. No indications for the formation of Li_2CoF_4 are observed, not even smallest reflections of this phase are found in the X-ray diffraction patterns. In addition, the possibility to form solid solutions $\text{Li}_2\text{Ni}_{1-x}\text{Co}_x\text{F}_4$ was evaluated by the precursor route. To summarize the results, up to approximately 25% cobalt can be incorporated into the spinel phase, resulting in $\sim\text{Li}_2\text{Ni}_{0.75}\text{Co}_{0.25}\text{F}_4$.

(2) Reaction of Hydrofluoric Acid with Carbonates

It has long been known that metal fluorides can be synthesized by the reaction of metal carbonates with hydrofluoric acid.^[24] Thus, Li_2CO_3 , NiCO_3 , CoCO_3 , and overstoichiometric amounts of HF (40 wt%) were used to prepare various compounds of $\text{Li}_2\text{Ni}_{1-x}\text{Co}_x\text{F}_4$ with $0 < x < 1$. After removing the liquid components, mixtures of LiF and $(\text{Ni},\text{Co})\text{F}_2 \cdot 4\text{H}_2\text{O}$ were obtained. These mixtures were heated for 10 h at 640 °C and 680 °C, respectively. Apparently, for $0 < x < 0.3$, cobalt is incorporated in the spinel phase (see Table 1). This is reflected by the variation of the lattice parameter a , which increases with the amount of cobalt incorporated (see Table 2). For all samples Rietveld refinements reveal significant amounts of LiF as side phase. Besides that also small contents of $(\text{Ni},\text{Co})\text{F}_2$, nickel cobalt oxide $(\text{Ni},\text{Co})\text{O}$ and a Ni-type phase (Ni/Co) were formed. Surprisingly, the reduction to metal and the formation of monoxides (from the presence of hydrate water) occurs.

The lattice parameters of the difluorides show the same tendency as for the $\text{Li}_2\text{Ni}_{1-x}\text{Co}_x\text{F}_4$ phases. The parameters a and c steadily increase with increasing amounts of cobalt. For comparison, the refined values are listed in Table 2. For $0.4 < x < 0.6$ and also higher contents of cobalt the amount of the spinel phase decreases drastically leading to the main presence of $(\text{Ni},\text{Co})\text{F}_2$ and LiF. No spinel phase is formed at $x \geq 0.7$. In good agreement with the results of the precursor route, the maximum amount of cobalt, which can be incorporated in the spinel phase is approximately $x = 0.3$, leading to $\sim\text{Li}_2\text{Ni}_{0.7}\text{Co}_{0.3}\text{F}_4$.

(3) Solid-State Route using LiF/ CoF_2 Mixtures

As mentioned in the introduction, the formation of Li_2CoF_4 by heating mixtures of LiF and CoF_2 up to approximately 650 °C was reported.^[7] The authors investigated the phase diagram of the quasi binary LiF– CoF_2 system by using thermoanalytical methods combined with *ex situ* X-ray powder diffraction

Table 1. Observed phases for the carbonate route used to prepare $\text{Li}_2\text{Ni}_{1-x}\text{Co}_x\text{F}_4$.

Theoretical composition $\text{Li}_2\text{Ni}_{1-x}\text{Co}_x\text{F}_4$	Phases obtained after drying	Phases obtained after the heating procedure at 640 °C
$x = 0$	$\text{NiF}_2 \cdot 4\text{H}_2\text{O}$, LiF	Li_2NiF_4 (81%), LiF (9%), NiO (8%), NiF_2 (2%)
$x = 0.1$	$(\text{Ni},\text{Co})\text{F}_2 \cdot 4\text{H}_2\text{O}$, LiF	$\sim\text{Li}_2\text{Ni}_{0.9}\text{Co}_{0.1}\text{F}_4$ (87%), LiF (6%), $(\text{Ni},\text{Co})\text{O}$ (6%), $(\text{Ni},\text{Co})\text{F}_2$ (1%)
$x = 0.2$	$(\text{Ni},\text{Co})\text{F}_2 \cdot 4\text{H}_2\text{O}$, LiF	$\sim\text{Li}_2\text{Ni}_{0.8}\text{Co}_{0.2}\text{F}_4$ (92%), LiF (3%), Ni,Co (3%), $(\text{Ni},\text{Co})\text{F}_2$ (2%)
$x = 0.3$	$(\text{Ni},\text{Co})\text{F}_2 \cdot 4\text{H}_2\text{O}$, LiF	$\sim\text{Li}_2\text{Ni}_{0.7}\text{Co}_{0.3}\text{F}_4$ (73%), LiF (17%), Ni,Co (1%), $(\text{Ni},\text{Co})\text{F}_2$ (9%)
$x = 0.4$	$(\text{Ni},\text{Co})\text{F}_2 \cdot 4\text{H}_2\text{O}$, LiF	$\sim\text{Li}_2\text{Ni}_{0.72}\text{Co}_{0.28}\text{F}_4$ (14%), LiF (37%), $(\text{Ni},\text{Co})\text{F}_2$ (49%)
$0.5 < x < 0.6$	$(\text{Ni},\text{Co})\text{F}_2 \cdot 4\text{H}_2\text{O}$, LiF	$\text{Li}_2\text{Ni}_{1-x}\text{Co}_x\text{F}_4$ (traces), $(\text{Ni},\text{Co})\text{F}_2$, LiF
$0.7 < x < 0.9$	$(\text{Ni},\text{Co})\text{F}_2 \cdot 4\text{H}_2\text{O}$, LiF	$(\text{Ni},\text{Co})\text{F}_2$, LiF
$x = 1$	$\text{CoF}_2 \cdot 4\text{H}_2\text{O}$, LiF	CoF_2 , LiF

a) Stoichiometry calculated from the determined lattice parameter.

Table 2. Lattice parameters of solid solutions $\text{Li}_2\text{Ni}_{1-x}\text{Co}_x\text{F}_4$ and $(\text{Ni},\text{Co})\text{F}_2$ phases with $0 < x < 0.4$.

Theoretical composition $\text{Li}_2\text{Ni}_{1-x}\text{Co}_x\text{F}_4$	Spinel phases	Rutile-type difluorides
$x = 0$	Li_2NiF_4 : $a = 831,76(1)$	NiF_2 : $a = 465,58(4)$, $c = 308,40(3)$
$x = 0.1$	$\sim\text{Li}_2\text{Ni}_{0.9}\text{Co}_{0.1}\text{F}_4$: $a = 832,24(1)$	$(\text{Ni},\text{Co})\text{F}_2$: $a = 466,05(3)$, $c = 309,69(5)$
$x = 0.2$	$\sim\text{Li}_2\text{Ni}_{0.8}\text{Co}_{0.2}\text{F}_4$: $a = 833,23(1)$	$(\text{Ni},\text{Co})\text{F}_2$: $a = 466,46(4)$, $c = 310,99(5)$
$x = 0.3$	$\sim\text{Li}_2\text{Ni}_{0.7}\text{Co}_{0.3}\text{F}_4$: $a = 833,96(2)$	$(\text{Ni},\text{Co})\text{F}_2$: $a = 467,16(2)$, $c = 312,20(2)$
$x = 0.4$	$\text{Li}_2\text{Ni}_{1-x}\text{Co}_x\text{F}_4$: $a = 833,78(5)$	$(\text{Ni},\text{Co})\text{F}_2$: $a = 467,52(2)$, $c = 312,83(1)$

measurements carried out after cooling the samples. In the presented phase diagram the stability range of the spinel-type phase ranges from 606 °C to 670 °C. This phase was also observed by the authors when a mixture of 10 mol-% CoF_2 and 90 mol-% LiF was used. Following these results, four different mixtures of CoF_2 and LiF were reacted in the temperature range between 600 °C and 700 °C. The amount of CoF_2 was chosen to be 10, 25, 33.3, and 50 mol-%, respectively. A content of 33.3 mol-% CoF_2 represents the “spinel-type” mixture $\text{LiF}:\text{CoF}_2 = 2:1$. Independent of composition, temperature, and heating time, our experiments show that no spinel phase does form. In all experiments only mixtures of LiF and CoF_2 were

obtained – even when heating times as long as 120 h were chosen. For a more detailed investigation and for comparison with the results obtained for the LiF-NiF_2 system, in situ high-temperature X-ray diffraction measurements were carried out at temperatures up to $750\text{ }^\circ\text{C}$ using “spinel-type” mixtures of LiF/NiF_2 and LiF/CoF_2 ($\text{LiF:MF}_2 = 2:1$). In addition, also the LiF/CoF_2 mixture containing 10 mol-% CoF_2 , emphasized in the literature,^[7] was investigated. In Figure 6 the results obtained for the LiF/NiF_2 mixture are depicted. At approximately $500\text{ }^\circ\text{C}$ reflections of spinel-type Li_2NiF_4 are clearly observed. Above $700\text{ }^\circ\text{C}$ an almost single spinel phase is present. This result is in good agreement with that presented in the literature.^[3] A completely different behavior is observed for the corresponding Co-containing mixtures (see Figure 7). Independent of temperature, the experiments reveal no indications pointing to the formation of a spinel phase. The reflections of LiF strongly shift towards lower 2θ values at $\sim 600\text{ }^\circ\text{C}$, indicating a significant solubility of CoF_2 in LiF at elevated temperatures. In the temperature range from $680\text{ }^\circ\text{C}$ to $700\text{ }^\circ\text{C}$ the intensities of the CoF_2 reflections decrease dramatically. At higher temperatures the formation of Co_2SiO_4 starts, which originates from the reaction of Co-containing phases with the SiO_2 capillary. Similar results were obtained for the mixture containing 10 mol-% CoF_2 .

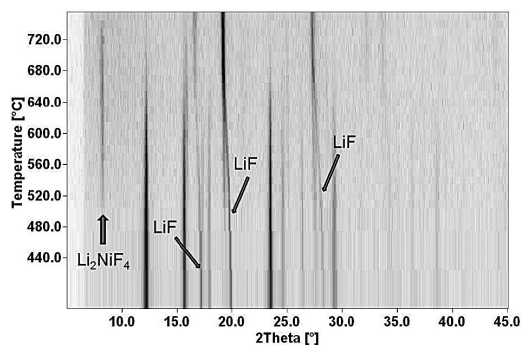


Figure 6. In situ high-temperature X-ray diffraction measurements of a mixture of LiF and NiF_2 ($\text{LiF:NiF}_2 = 2:1$). Up to $520\text{ }^\circ\text{C}$, LiF and NiF_2 exist. At approximately $500\text{ }^\circ\text{C}$ the formation of Li_2NiF_4 starts. At ca. $700\text{ }^\circ\text{C}$ mainly Li_2NiF_4 is observed.

Quantum-Chemical Calculations

The thermodynamic stability of $\text{Li}_2\text{Ni}_{1-x}\text{Co}_x\text{F}_4$ ($x = 0, 0.125, 0.25, 0.5, 1$) was studied theoretically at density-functional theory (DFT) level. Based on our experience with open-shell transition metal compounds^[25] we used the DFT-Hartree-Fock hybrid functional PWIPW.^[26] The calculations were performed with the crystalline-orbital program package CRYSTAL09.^[27] Atomic basis sets of triple-zeta quality for the elements Li, Ni, Co, and F were taken from the CRYSTAL homepage^[28] and augmented with diffuse shells and polarization functions. A detailed description of the optimized solid-state basis sets will be given elsewhere.^[29] The cobalt mole fraction x was varied by changing the size of the unit cell correspond-

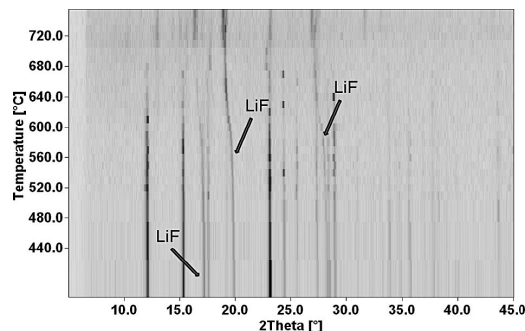


Figure 7. In situ high-temperature X-ray diffraction measurements of a “spinel-type” mixture of LiF and CoF_2 ($\text{LiF:CoF}_2 = 2:1$). At ca. $700\text{ }^\circ\text{C}$ the formation of Co_2SiO_4 is observed.

ingly. In the mixed phases we started with composition Li_2NiF_4 and replaced one Ni by Co. In this way only highly ordered Ni/Co distributions were considered in order to reduce the computational effort. Possible clustering effects were ignored, which can affect the calculated reaction energies. The presented results should therefore only be regarded as semi-quantitative, but are expected to reproduce qualitative trends. Cell parameters and atomic positions of all cells were fully optimized. The thermodynamic functions at 300 K and 1000 K were calculated from the phonon frequencies obtained within the quasi-harmonic approximation.^[30] In Table 3 the calculated free energies for the decomposition of the pure compounds Li_2NiF_4 and Li_2CoF_4 into the binary fluorides are presented. Under standard conditions (here we used 300 K instead of 298.15 K) Li_2NiF_4 is stable with respect to decomposition, while Li_2CoF_4 is not. This is in line with the experimental results of the presented study (vide supra). At elevated temperatures (we used 1000 K to approximate the experimental conditions) both Li_2MF_4 compounds are stabilized due to entropy effects. Li_2CoF_4 may be formed in a solid-state reaction at 1000 K and above, but will decompose during cooling.

Table 3. Calculated free energies $\Delta G/\text{kJ}\cdot\text{mol}^{-1}$ for the reaction $2\text{LiF} + \text{MF}_2 \rightarrow \text{Li}_2\text{MF}_4$ ($M = \text{Ni, Co}$) as a function of temperature T/K .

T/K	300	1000
$\Delta G/\text{kJ}\cdot\text{mol}^{-1}$		
Li_2NiF_4	-11	-32
Li_2CoF_4	+5	-3

With the unit cells and the theoretical approach described above we calculated the free energy of the reaction



for $x = 0.125, 0.25$, and 0.5 . In Figure 8 the results are shown for $T = 1000\text{ K}$. At this temperature incorporation of up to 25% cobalt leads to stable compounds with ΔG between $-32\text{ kJ}\cdot\text{mol}^{-1}$ ($x = 0$) and $-20\text{ kJ}\cdot\text{mol}^{-1}$ ($x = 0.25$). At $x = 0.5$ the situation has changed drastically, ΔG being highly positive ($+60\text{ kJ}\cdot\text{mol}^{-1}$).

ARTICLE

M. Lerch et al.

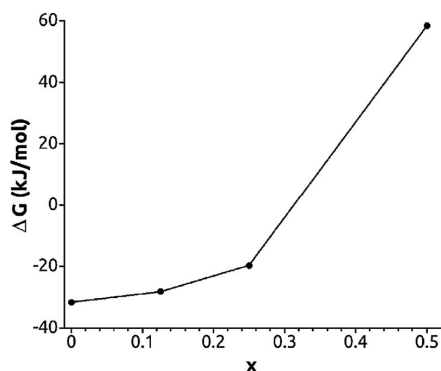


Figure 8. Calculated free energy ΔG /kJ·mol⁻¹ at 1000 K for the formation of $\text{Li}_2\text{Ni}_{1-x}\text{Co}_x\text{F}_4$ from the binary fluorides as a function of x .

A simple linear interpolation indicates that ΔG changes sign for $x = 0.3$ to $x = 0.4$. Again, this is in line with the experimental findings of the presented study.

From our experimental findings and the presented calculations the reported existence of Li_2CoF_4 ^[7] must be called into question. Unfortunately, the authors of reference^[7] have not presented refined lattice parameters. This leads to severe problems taking into account the container material used for the thermoanalytical measurements, which was nickel. Only a careful chemical analysis or determination of the lattice parameter of the spinel phase can avoid confusion. However, concerning this point no data is presented. If some nickel of the container material was involved in the reaction, the formation of a mixed spinel phase $\text{Li}_2\text{Ni}_{1-x}\text{Co}_x\text{F}_4$ is not astonishing.

Conclusions

A new precursor route being highly useful to prepare spinel-type Li_2NiF_4 was developed. The thermal decomposition of the precursors, synthesized from $\text{Ni}(\text{acac})_2$, $\text{LiO}t\text{Bu}$, and HF in ethanol, for example, allows the decrease of the preparation temperature down to 400 °C. By variation of the temperature and the synthesis time the crystallite size can easily be optimized so that even nm-sized crystallites are obtainable. Expectedly, the preliminary ⁷Li and ⁶Li MAS NMR results reveal rather complex spectra, which is due to the various environments the lithium spins are exposed to in $\text{Li}[\text{Li},\text{Ni}]\text{F}_4$. Additional 2D ⁶Li MAS NMR spectra might be helpful to interpret the NMR paramagnetic shifts observed. The synthesis of the corresponding cobalt spinel phase Li_2CoF_4 turned out to be not successful. This result is independent from the particular route chosen, i.e., preparation via acetylacetonates/alcoholates, by employing carbonates, or by solid-state reaction. So far, our experimental studies do not give any indication for the existence of Li_2CoF_4 . This is supported by quantum-chemical calculations of the corresponding free energies at density-functional level. However, on the other hand cobalt can be present in spinel-type solid solutions up to the composition of $\sim\text{Li}_2\text{Ni}_{0.7}\text{Co}_{0.3}\text{F}_4$, which is in excellent agreement with the calculations presented.

Experimental Section

Materials and Methods: $\text{Ni}(\text{acac})_2$, CoF_2 (ABCR), CoCO_3 , NiCO_3 , Li_2CO_3 (Alfa Aesar), $\text{Ni}(\text{OAc})_2 \cdot 4\text{H}_2\text{O}$, $\text{Co}(\text{OAc})_2 \cdot 4\text{H}_2\text{O}$, $\text{LiO}t\text{Bu}$, hydrofluoric acid (40 wt-%), and LiF (Sigma-Aldrich) were used as received. HF solutions in ethanol, THF, and Et_2O were prepared by feeding gaseous HF into the solvent under cooling. The solvents were dried using standard literature procedures. All reactions were carried out by using standard Schlenk techniques. Reagents and samples were stored in a glove box in an argon atmosphere.

General Synthesis

Synthesis of the Li_2NiF_4 -Precursor: $\text{Ni}(\text{acac})_2$ (1 g, 3.89×10^{-3} mol) (alternatively $\text{Ni}(\text{OAc})_2 \cdot 4\text{H}_2\text{O}$) and $\text{LiO}t\text{Bu}$ (0.6232 g, 7.79×10^{-3} mol) (Li:Ni = 2:1) were weighed into a Schlenk tube and suspended in absolute ethanol (30 mL) at room temperature. To the resultant suspension HF-EtOH solution (6.25 mL, 12.50 M) was added, leading to a light green solution (Ni:HF = 1:20). Alternatively, a HF- Et_2O (6.76 M) or a HF-THF (0.68 M) solution was used. The solutions were stirred 2 h at room temperature. Afterwards, the solvent was removed in a vacuum and the fine green powder was dried for 2 h at 80 °C.

Synthesis of Li_2MF_4 : All syntheses were carried out in sealed copper capsules in a nitrogen atmosphere. The respective precursor (ca. 100–200 mg) was filled into a one-side mechanically sealed capsule, which was afterwards completely closed. If not described else wise, all samples were slowly cooled down to ambient temperature.

Elemental Analysis: The carbon and hydrogen contents were determined by combustion analysis (Thermo Finnigan FlashEA 1112 NC analyzer), the oxygen contents with a LECO EF-TC 300 N_2/O_2 analyzer (hot gas extraction). The carbon, hydrogen, and oxygen contents of the precursor samples and of the Li_2NiF_4 samples vary with the Ni-educt and solvent used for precursor synthesis. The following amounts (wt-%) of C, H, and O were detected: $\text{Ni}(\text{OAc})_2/\text{Et}_2\text{O}$: C 1.9, H 2.6, O 22%; $\text{Ni}(\text{OAc})_2/\text{EtOH}$: C 4.0, H 2.3, O 16%. For Li_2NiF_4 -precursors based on $\text{Ni}(\text{acac})_2$, the values of C and H are considerably higher: $\text{Ni}(\text{acac})_2/\text{Et}_2\text{O}$: C 7.3, H 2.4, O 13%. Precursors based on $\text{Ni}(\text{acac})_2/\text{EtOH}$ exhibit the highest carbon contents, oxygen contents are the same as for the system with Et_2O : C 9.5, H 2.6, O 12%. Li_2NiF_4 samples prepared by decomposition of $\text{Ni}(\text{OAc})_2/\text{EtOH}$ precursors contain 0.2–0.3% carbon and 0–0.1% hydrogen. After decomposition at 400 °C, 1.4% oxygen were measured. At higher temperatures, e.g. 680 °C, samples contained 0.7% oxygen. Carbon contents of samples prepared from $\text{Ni}(\text{acac})_2/\text{EtOH}$ -precursors range between 0.4–0.7%, hydrogen contents range between 0–0.05%. Samples prepared by decomposition at 400 °C contained 0.9–1.3% oxygen, at 680 °C 0.2–0.3% oxygen are contained. Samples synthesized for MAS NMR measurements by the solid state route contained < 0.06% oxygen.

X-ray Powder Diffraction: X-ray powder diffraction measurements were performed with $\text{Cu-}K_\alpha$ radiation over a 2θ range from 5 to 120° (40 kV / 40 mA, Bragg-Brentano geometry, θ - θ arrangement). A PANalytical X'Pert PRO MPD diffractometer with PIXcel detector (Si-Li-semiconductor with 255 measuring channels) was used. Samples were prepared on small Si-cavity mounts. The program package FULLPROF 2009^[31] was used for Rietveld refinements; peak profiles were fitted with a pseudo-Voigt function. In situ high-temperature XRD measurements were carried out with a STOE STADI-P diffractometer equipped with a graphite-heated resistance furnace ($\text{Mo-}K_\alpha$ radiation, $\lambda = 70.93$ pm, imaging plate detector, samples in SiO_2 -glass capillaries in a nitrogen atmosphere).

Spinel-Type Li_2NiF_4 and Solid-Solutions $\text{Li}_2\text{Ni}_{1-x}\text{Co}_x\text{F}_4$

Zeitschrift für
anorganische
und allgemeine
Chemie **ZAAC** Journal of
Inorganic and
General
Chemistry

${}^7\text{Li}$ Solid-State NMR: High-resolution solid-state NMR spectra were recorded with Avance III spectrometers (Bruker) connected to shimmed 7 Tesla and 11.4 Tesla cryomagnets. The resonance frequency was 116 MHz (${}^7\text{Li}$) and 73 MHz (${}^6\text{Li}$), respectively. Standard magic angle spinning (MAS) NMR probes (Bruker) in combination with 2.5-mm rotors (${}^7\text{Li}$) and 1.3-mm rotors (${}^6\text{Li}$) were used. The maximum spinning frequency accessible was 30 kHz (${}^7\text{Li}$) and 65 kHz (${}^6\text{Li}$), respectively. Spectra were acquired at ambient bearing gas temperature using a single pulse experiment; the excitation pulse length ranged from 1 to 2.15 μs . Fourier transformation, phasing and baseline correction of the data were carried out using Mnova software (Mestrelab Research). Line specific NMR spin-lattice relaxation times (T_1) were measured using the conventional saturation recovery pulse sequence.

Acknowledgements

We thank the German Ministry of Education and Research (BMBF) for financial support within the LIB 2015 initiative, project HE-Lion. M. W. and P. H. also acknowledge financial support by the DFG within the Research Unit 1277 "molife". We further thank Prof. Erhard Kemnitz, Humboldt University Berlin, Germany, for supplying the HF solutions.

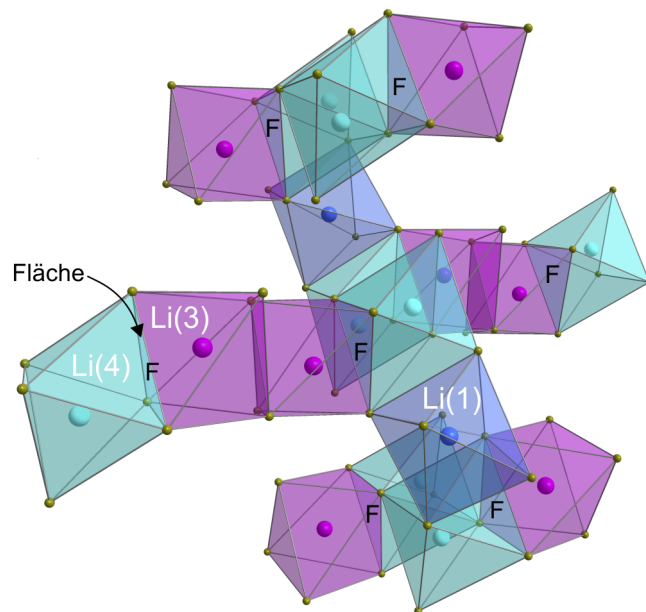
References

- [1] E. Gonzalo, A. Kuhn, F. Garcia-Alvarado, *J. Power Sources* **2010**, *195*, 4990.
- [2] I. Gocheva, K. Chihara, S. Okada, J. Yamaki, Lithium Batteries Discussion 2011 – Electrode Materials – Arcachon, France (extended abstract).
- [3] W. Rüdorff, J. Kändler, D. Babel, *Z. Anorg. Allg. Chem.* **1962**, *317*, 261.
- [4] J.-L. Fourquet, H. Duroy, M. Leblanc, G. Ferey, *J. Solid State Chem.* **1989**, *78*, 184.
- [5] W. Rüdorff, J. Kandler, *Naturwissenschaften* **1957**, *44*, 418.
- [6] Komiya, Hirokazu; Nitta, Yoshiaki; Okamura, Kazuhiro, Secondary Nonaqueous Electrolyte Batteries, *Jpn. Kokai Tokkyo Koho* **1999**, JP 11339800 A 19991210 (Patent).
- [7] L. A. Ol'khovaya, M. B. Ikrami, T. A. Nikolaeva, I. Y. Gracheva, *Russ. J. Inorg. Chem.* **1989**, *34*, 566.
- [8] E. Kemnitz, U. Groß, S. Rüdiger, C. S. Shekar, *Angew. Chem. Int. Ed.* **2003**, *42*, 4251.
- [9] M. Ahrens, G. Scholz, M. Feist, E. Kemnitz, *Solid State Sci.* **2006**, *8*, 798–806.
- [10] J. Kohl, D. Wiedemann, S. Nakhal, P. Bottke, N. Ferro, T. Bredow, E. Kemnitz, M. Wilkening, P. Heitjans, M. Lerch, *J. Mater. Chem.* **2012**, *22*, 15819.
- [11] T. Ressler, *WINXAS v3.1* **2011**.
- [12] P. G. Bruce, B. Scrosati, J.-M. Tarascon, *Angew. Chem. Int. Ed.* **2008**, *47*, 2930.
- [13] A. S. Aricò, P. Bruce, B. Scrosati, J.-M. Tarascon, W. V. Schalkwijk, *Nat. Mater.* **2005**, *4*, 366.
- [14] D. Carlier, M. Ménétrier, C. P. Grey, C. Delmas, G. Ceder, *Phys. Rev. B* **2003**, *67*, 174103.
- [15] C. Marichal, J. Hirschinger, P. Granger, M. Ménétrier, A. Rougier, C. Delmas, *Inorg. Chem.* **1995**, *34*, 1773.
- [16] D. Carlier, M. Ménétrier, C. Delmas, *J. Mater. Chem.* **2001**, *11*, 594.
- [17] C. Chazel, M. Ménétrier, L. Croguennec, C. Delmas, *Magn. Reson. Chem.* **2005**, *43*, 849.
- [18] M. Wilkening, E. Romanova, S. Nakhal, D. Weber, M. Lerch, P. Heitjans, *J. Phys. Chem. C* **2010**, *114*, 19083.
- [19] C. P. Grey, N. Dupré, *Chem. Rev.* **2004**, *104*, 4493.
- [20] L. S. Cahill, R. P. Chapman, J. F. Britten, G. R. J. Goward, *J. Phys. Chem. B* **2006**, *110*, 7171.
- [21] L. J. M. Davis, I. Heinmaa, G. R. Goward, *Chem. Mater.* **2010**, *22*, 769.
- [22] L. S. Cahill, Y. Iriyama, L. F. Nazar, G. R. Goward, *J. Mater. Chem.* **2010**, *20*, 4340.
- [23] A. R. Armstrong, C. Lyness, M. Ménétrier, P. G. Bruce, *Chem. Mater.* **2010**, *22*, 1892.
- [24] A. Kurtenacker, W. Finger, F. Hey, *Z. Anorg. Allg. Chem.* **1933**, *211*, 83.
- [25] M. M. Islam, T. Bredow, A. Gerson, *ChemPhysChem* **2011**, *12*, 3467.
- [26] T. Bredow, A. R. Gerson, *Phys. Rev. B* **2000**, *61*, 5194.
- [27] R. Dovesi, R. Orlando, B. Civalleri, C. Roetti, V. R. Saunders, C. M. Zicovich Wilson, *Z. Kristallogr.* **2005**, *220*, 571.
- [28] http://www.crystal.unito.it/Basis_Sets.
- [29] N. Ferro, C. Reimann, T. Bredow, in preparation.
- [30] F. Pascale, C. M. Zicovich-Wilson, F. Lopez Gejo, B. Civalleri, R. Orlando, R. Dovesi, *J. Comput. Chem.* **2004**, *25*, 888.
- [31] T. Roisnel, J. Rodriguez-Carvajal, *Mater. Sci. Forum* **2001**, *378–381*, 118.

Received: October 10, 2012
Published Online: December 18, 2012

P3 Synthesis of ternary transition metal Fluorides Li_3MF_6 via a sol-gel route as candidates for cathode materials in lithium-ion batteries

Strukturausschnitt von $\beta\text{-Li}_3\text{VF}_6$...



... zeigt bevorzugte Diffusionspfade über 3 von 5 Li-Positionen

Cite this: *J. Mater. Chem.*, 2012, **22**, 15819

www.rsc.org/materials

PAPER

Synthesis of ternary transition metal fluorides Li_3MF_6 via a sol–gel route as candidates for cathode materials in lithium-ion batteries†Julia Kohl,^a Dennis Wiedemann,^a Suliman Nakhla,^a Patrick Bottke,^b Noel Ferro,^c Thomas Bredow,^c Erhard Kemnitz,^d Martin Wilkening,^b Paul Heitjans^e and Martin Lerch^{*a}

Received 5th April 2012, Accepted 8th June 2012

DOI: 10.1039/c2jm32133e

A sol–gel route for ternary lithium fluorides of transition metals (M) is presented allowing the synthesis of Li_3MF_6 -type and Li_2MF_5 -type compounds. It is based on a fluorolytic process using transition metal acetylacetonates as precursors. The domain size of the obtained powders can be controlled by modifying the conditions of synthesis. ${}^6\text{Li}$ and ${}^7\text{Li}$ magic angle spinning (MAS) nuclear magnetic resonance (NMR) spectroscopy is used to study local environments of the Li ions in orthorhombic and monoclinic Li_3VF_6 as well as Li_2MnF_5 . The number of magnetically inequivalent Li sites found by MAS NMR is in agreement with the respective crystal structure of the compounds studied. Quantum chemical calculations show that all materials have high de-lithiation energies making them suitable candidates to be used as high-voltage battery cathode materials.

Introduction

The search for new cathode materials as part of lithium-ion batteries is an important objective today.^{1–5} Currently, oxides such as LiCoO_2 , layered Li–Mn–spinel as well as olivine-type structures such as LiFePO_4 are in the focus of interest.^{6,7} Modern cathode materials need to fulfil many different requirements. Promising compounds are supposed to exhibit high concentrations of lithium in order to achieve high energy densities and capacities. In addition, besides a good electronic conductivity, sufficiently high lithium-ion diffusivity is one of the prerequisites for facile lithium insertion and removal. Finally, chemical and thermal stability of the components directly affect the cyclability of the lithium-ion battery and thus its lifetime.

Until recently, various oxide materials have been in the focus of research.^{6,7} Interestingly, theoretical calculations indicate a

large increase of the redox potential by substituting fluorine for oxygen.⁸ Consequently, ternary lithium fluorides are increasingly considered for advanced electrochemical characterization. In particular, the Li_3MF_6 (M = transition metal) family exhibits high lithium contents combined with variable oxidation numbers. Recently, Gonzalo *et al.* reported Li_3FeF_6 to be a promising cathode material for lithium-ion batteries.⁹ Furthermore, the electrochemical properties of Li_3VF_6 prepared by microwave synthesis have been studied quite recently.^{10a} In addition, Li_3VF_6 is also in the focus of a low-temperature precipitation route in aqueous solution using alcohols recently reported by Basa *et al.*^{10b} The relatively low capacity of the compounds is assumed to increase with decreasing particle size. Therefore, the preparation of Li_3MF_6 phases with particle sizes less than 50 nm, as successfully shown by Basa *et al.*,^{10b} is of great interest to improve the associated electrochemical performance. The compounds Li_3MF_6 (M = V, Cr, Fe) are known to exist in two polymorphs. Whereas the monoclinic form (space group *C2/c*) crystallizes isotypically with $\beta\text{-Li}_3\text{AlF}_6$, the orthorhombic modification crystallizes with the space group *Pna2₁* being identical to that of the corresponding α -form of Li_3AlF_6 . The two polymorphs are structurally related to the cryolite type.^{11,12}

Usually, the monoclinic polymorph is obtained by slow cooling down of a stoichiometric mixture of the binary fluorides to room temperature, while the orthorhombic form can only be prepared by quenching the samples from an elevated ($T > 600$ K) to ambient temperature. Due to the poor electronic conductivity of transition metal fluorides the design of particle morphology is of great importance for potential electrochemical applications. Since ternary transition metal fluorides are usually synthesized by solid-state reactions at high temperatures and/or high pressures, the obtained particles show diameters in the micrometer

^aTechnische Universität Berlin, Department of Chemistry, Straße des 17. Juni 135, 10623 Berlin, Germany. E-mail: martin.lerch@tu-berlin.de; Fax: +49 030 314 22740; Tel: +49 030 314 22603

^bTechnische Universität Graz, Institut für Chemische Technologie von Materialien, Stremayrgasse 9, 8010 Graz, Austria. E-mail: wilkening@tugraz.at; Fax: +43 316 873 32332; Tel: +43 316 873 32330

^cUniversität Bonn, Mulliken Center for Theoretical Chemistry, Department of Physical and Theoretical Chemistry, Beringstr. 4, 53115 Bonn, Germany. E-mail: bredow@thch.uni-bonn.de; Fax: +49 0228 73 9064; Tel: +49 0228 73 3839

^dHumboldt-Universität zu Berlin, Department of Chemistry, Brook-Taylor-Straße 2, 12489 Berlin, Germany. E-mail: erhard.kemnitz@chemie.hu-berlin.de; Fax: +49 030 2093 7277; Tel: +49 030 2093 7555

^eLeibnitz Universität Hannover, Institute of Physical Chemistry and Electrochemistry, Callinstr. 3 – 3a, 30167 Hannover, Germany. E-mail: heitjans@pci.uni-hannover.de; Tel: +49 511 762 3187

† CCDC 868968. For crystallographic data in CIF or other electronic format see DOI: 10.1039/c2jm32133e

range. Generally, nm-sized particles can be easily prepared by high-energy ball milling of the coarse grained materials.^{13–15} Besides activation, mechanochemistry has also successfully been used for the synthesis of a variety of materials from precursors at room temperature including oxides and fluorides.^{16–18} However, in contrast to such a top-down approach, the preparation of nanostructured particles by precipitation from aqueous solution is much more beneficial when the shape and surface morphology of the crystallites have also to be controlled. By following such a route, the corresponding salts, for example nitrates or oxides, are reacted with hydrofluoric acid and subsequent dehydration is carried out by annealing at elevated temperatures. In general, solution-based syntheses offer many advantages. For instance, low temperatures and good mixing of the precursors allow the preparation of highly homogeneous compounds with a large surface area. In contrast to aqueous routes, syntheses carried out in organic solvents provide a large range of different media with versatile characteristics. When HF is dissolved directly in an organic solvent, competing reactions between HF and H₂O with the transition metal can be eliminated. When, for example, alcoholates or acetylacetonates are used as starting materials the corresponding alcohols or acetylacetone is formed which can easily be removed under vacuum. Moreover, due to very fast crystallization materials consisting of very small particle diameters (low nm-range) can be obtained.

To our knowledge only few reports can be found in the literature which report on the synthesis of ternary fluorides from these starting materials. Kemnitz *et al.* presented the synthesis of aluminum and magnesium fluorides with high surface areas by a fluorolytic sol-gel process.^{19,20} These studies illustrate the synthetic potential of organic hydrogen fluoride solutions. Aluminum compounds crystallizing in the cryolite or elpasolite type were prepared from the corresponding alcoholates. For example, Li₃AlF₆ can be obtained *via* the reaction of LiOrBu and Al(O*Pr*)₃ with HF in isopropanol.²¹ This method allows one to work under water-free conditions. Concerning transition metal fluorides only acetylacetonates, acetates and, in the case of iron, alcoholates are obtainable as starting materials. The aim of our present work is to develop a nonaqueous sol-gel route for the preparation of Li₃MF₆ compounds (M = V, Cr, Fe, Mn, Co) and to elucidate the possibilities of controlling the size of the particles synthesized.

Experimental section

X-ray powder diffraction

X-ray powder diffraction experiments were performed using a PANalytical X'Pert PRO MPD diffractometer (CuK_α-radiation, 2θ range 5 to 120°, Bragg-Brentano (θ-θ) geometry) with PIXcel detector (Si-Li-semiconductor with 255 measuring channels). All samples were prepared on small Si-cavity mounts.

X-ray fluorescence

For X-ray fluorescence analysis, a PANalytical Axios PW4400/24 X-ray fluorescence spectrometer with an Rh-tube and wavelength-dispersive detection was used. Depending on the analyzed elements a LiF single crystal (crystallographic orientation (220) and (200)), a Ge single crystal (orientation (111)), a PE single

crystal (orientation (002)) and a PX1 multi-layer monochromator were used together with an Si(Li) scintillation detector.

NMR

Liquid-phase ¹H, ¹³C, ⁵¹V, and ¹⁹F NMR spectra were recorded on a Bruker Avance 200 and a Bruker Avance 400 NMR spectrometer. TMS, CFC₃ and VOCl₃ served as references. Solid-state high-resolution, *i.e.*, magic angle spinning (MAS), ⁶Li and ⁷Li NMR spectra were acquired using Avance III NMR (Bruker BioSpin) spectrometers connected to cryomagnets with nominal fields of 7 T and 14.1 T. This results in ⁶Li resonance frequencies of 44 and 88 MHz and ⁷Li resonance frequencies of 117 and 233 MHz, respectively. We used a standard (double-resonance) 2.5 mm-probe (Bruker) which can be operated at spinning speeds of up to 30 kHz. Additionally, some ⁶Li MAS NMR spectra were recorded with an Avance NMR spectrometer being connected to a cryomagnet with a nominal magnetic field of 17.6 T. The spectrometer can be used in combination with an MAS NMR probe allowing a maximum spinning speed of 15 kHz. The Li MAS NMR spectra shown were referenced to LiCl (aq). They were recorded using a single excitation pulse and recycling delays of up to several seconds. ⁶Li and ⁷Li NMR spin-lattice relaxation times *T*₁ of the paramagnetic Li₃MF₆ and Li₂MnF₅ samples were measured with a conventional saturation recovery experiment using up to 12 different delay times. As expected, the *T*₁ values associated with the paramagnetic shifts do not exceed 100 ms. Preliminary 2D exchange MAS NMR spectra of Li₂MnF₅ were recorded using a conventional NOESY pulse sequence. Time domains of 512 data points in both *f*₁ and *f*₂ directions were used. Processing of the data was carried out using TopSpin 3.1 software (Bruker) and Mnova7 (Mestrelab research).

FTIR

FTIR spectra were measured on a Varian 640IR FTIR spectrometer equipped with a Pike GladiATR device for measurements in attenuated total reflectance mode. FTIR spectra of KBr pellets and CsI pellets were measured with a Nicolet Series II Magna-IR System 750 FTIR spectrometer in transmission mode.

Elemental analysis

The carbon and hydrogen contents were determined by combustion analysis (Thermo Finnigan FlashEA 1112 NC analyzer), the oxygen contents using a LECO EF-TC 300 N₂/O₂ analyzer (hot gas extraction).

Materials and methods

V(acac)₃ (ABCR), Fe(acac)₃, Cr(acac)₃, Mn(acac)₃, Mn(OAc)₃·2H₂O, Co(acac)₃ and LiOrBu (Sigma-Aldrich) were used as received. Solutions of HF in ethanol, THF and Et₂O were prepared by feeding gaseous HF into the solvent under cooling. The solvents were dried according to standard literature procedures. All reactions were carried out using standard Schlenk techniques. Reagents and samples were stored in an Ar-filled glove box.

General synthesis

Precursor synthesis, Li_3VF_6 as example: 1 g (2.87×10^{-3} mol) of $\text{V}(\text{acac})_3$ and 0.6895 g (8.61×10^{-3} mol) of LiOtBu ($\text{Li} : \text{V} = 3 : 1$) were weighed into a Schlenk tube and suspended in 20 ml of absolute ethanol at room temperature for 30 min. To the resultant suspension 8.40 ml of a 10.25 M HF-EtOH solution was added leading to a green solution ($\text{V} : \text{HF} = 1 : 30$). Alternatively, a 6.89 M $\text{HF-Et}_2\text{O}$ or a 10.68 M HF-THF solution was used. The solution was stirred for 2 h at room temperature. Afterwards, the solvent was removed under vacuum and the resultant fine green powder was dried at 80°C for 2 h.

Synthesis of the Li_3MF_6 samples: all syntheses were carried out in sealed copper or monel capsules under nitrogen atmosphere. 100 to 200 mg of the precursor were filled into a one-side sealed capsule. If not stated otherwise, all samples were slowly cooled down to room temperature. In Table 1, the synthesis conditions of the fluorides prepared are listed.

$\text{V}(\text{acac})_2(\text{CH}_3\text{CN})_2\text{BF}_4$: a saturated solution of the Li_3VF_6 precursor was prepared in 10 ml of absolute CH_3CN and stirred overnight at 50°C . The resulting green-brown solution was filled in small glass tubes. These glass tubes were positioned in a Schlenk tube filled with 20 ml of absolute Et_2O . After approximately 20 days dark red crystals were formed.

Results and discussion

Monoclinic and orthorhombic Li_3VF_6

As described in the Experimental section, Li_3VF_6 can be prepared by a two-step synthesis. During the first step the so-called precursor is synthesized. LiOtBu and $\text{V}(\text{acac})_3$ react with hydrogen fluoride in a dry solvent ($\text{Li} : \text{V} : \text{HF} = 3 : 1 : 30$). After evaporating the solvent and drying, the obtained Li_3VF_6 precursor is calcined at 300 to 800°C to form Li_3VF_6 . The precursor can be described as a fine, green and mainly X-ray amorphous powder. The corresponding X-ray powder pattern shows that the precursor also contains poorly crystalline LiF and Li_2SiF_6 . The latter phase results from the reaction of HF with the glassware used. However, Li_2SiF_6 does not affect the subsequent reactions because it decomposes into LiF and SiF_4 at temperatures above 250°C .²² As determined by X-ray fluorescence analysis, all samples contain approximately 3 to 4.5% Si. Interestingly, small amounts of Li_2SiF_6 were also formed when the synthesis was carried out in a glass Schlenk tube equipped with a closed PTFE insert inside (Fig. 1b and c). This insert was opened after synthesis for removing the solvent under vacuum.

Table 1 Synthesis conditions for the Li_3MF_6 compounds (orth. = orthorhombic and mon. = monoclinic)

Compound	Dwell time	Temperature	Further conditions
Li_3VF_6 , orth.	2 h	700°C	Quenching to room temperature after 2 h
Li_3VF_6 , mon.	4 h	150 to 600°C	
Li_3FeF_6 , orth.	2 h	800°C	Quenching to room temperature after 1 h
Li_3FeF_6 , mon.	4 h	400 to 600°C	
Li_3CrF_6 , mon.	4 h	500°C	
Li_2MnF_5	4 h	400°C	30% Li_2MnF_5

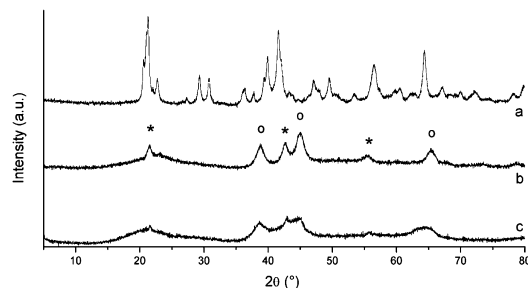


Fig. 1 X-ray powder diffraction patterns of different Li_3VF_6 precursors: (a) precursor decomposition at 300°C (Li_2SiF_6 has been completely decomposed), (b) synthesis in glassware, (c) synthesis with PTFE insert (o = LiF , * = Li_2SiF_6).

Surprisingly, remaining HF seems to react immediately with the glassware in which the PTFE tube is inserted. Note that from X-ray diffraction no information on the nature of the vanadium species can be obtained.

Li_3VF_6 , which was prepared by decomposition of the precursor, was also analyzed by X-ray powder diffraction. Heating to 300°C leads to the formation of Li_3VF_6 . Li_2SiF_6 seems to be completely decomposed (see also Fig. 1a). From the XRD patterns there are only vague indications of very small amounts of remaining LiF not reacted with vanadium species of the precursor. When the samples were cooled down to room temperature slowly, monoclinic Li_3VF_6 was observed. Heating the precursor to 700°C and quenching the sample to room temperature results in the formation of orthorhombic Li_3VF_6 as described in the literature (see Fig. 2). Both polymorphs were obtained with more than 98% purity. Elemental analysis resulted in a residual carbon content of approximately 2%.

Besides the successful preparation of highly pure α - Li_3VF_6 and β - Li_3VF_6 , it is also possible to modify the domain size of the samples prepared. For example, this can easily be achieved by

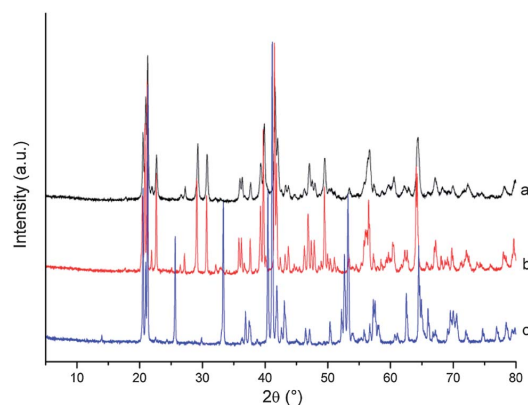


Fig. 2 X-ray powder diffraction patterns of monoclinic β - Li_3VF_6 synthesized at (a) 300°C and (b) 600°C . (c) Corresponding X-ray powder pattern of orthorhombic α - Li_3VF_6 which has been synthesized at 700°C and by subsequent quenching to room temperature.

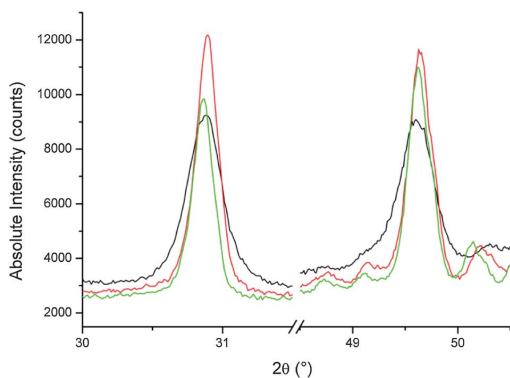


Fig. 3 Temperature-dependent broadening of the reflections at $2\theta = 30.72^\circ$ and $2\theta = 49.45^\circ$ of monoclinic Li_3VF_6 (400 °C (black), 500 °C (red), 600 °C (green)). All samples were slowly cooled down to room temperature.

varying the synthesis temperature as presented in the following. The precursors were heated for 4 h at 400, 500 and 600 °C, respectively. As shown in Fig. 3, the full width at half maximum of the diffraction reflections decreases with increasing temperature. The domain sizes were calculated by methods based on the Scherrer formula.²⁶ The results are depicted in Table 2. Here, the domain size can be varied from approximately 30 to 200 nm which is the range of interest for electrochemical applications. In general, the domain size increases with increasing temperature. For different solvents the absolute values as well as the temperature dependence of the sizes differs significantly. The reason for this is unclear. First investigations of the samples by means of standard SEM resulted in an average particle size of ~ 200 nm for the samples synthesized at 400 °C.

Typical ^6Li MAS NMR spectra of polycrystalline $\alpha\text{-Li}_3\text{VF}_6$ and $\beta\text{-Li}_3\text{VF}_6$ are shown in Fig. 4. In agreement with the crystal structure of the orthorhombic modification the NMR spectrum of $\alpha\text{-Li}_3\text{VF}_6$ reveals three distinct lines which can be attributed to the Li positions Li(1), Li(2), and Li(3) as shown recently by some of us.²³ The NMR shifts result from the Fermi-contact interaction which is related to the extent of electron spin density transferred from the $\text{V}^{3+} t_{2g}$ orbital to the 2s orbital Li ion. In ref. 23 the assignment of the NMR lines presented has been based on (i) results from temperature-variable 1D and 2D exchange NMR experiments, (ii) the considerations of different mechanisms to

Table 2 Calculated domain sizes for monoclinic Li_3VF_6 prepared at different temperatures. The values listed were calculated with LaB_6 as standard. The respective precursors were synthesized in different solvents

	Decomposition temperatures and corresponding domain sizes		
	400 °C	500 °C	600 °C
Li_3VF_6 , precursor synthesized in THF	37 nm	107 nm	127 nm
Li_3VF_6 , precursor synthesized in Et_2O	33 nm	84 nm	160 nm
Li_3VF_6 , precursor synthesized in EtOH	44 nm	80 nm	155 nm

transfer electron spin density, and (iii) the connectivities of the VF_6 and LiF_6 polyhedra in $\alpha\text{-Li}_3\text{VF}_6$. Note that with increasing temperature the lines first broaden and finally coalesce because of Li ion exchange taking place on the timescale determined by the distance of the NMR lines (see Fig. 1 in ref. 23). The beginning of this process can already be recognized when the spectrum shown in Fig. 4c is considered. At lower temperatures, note that NMR spectra down to 277 K were recorded, no additional lines show up indicating that the three lines observed are not affected by any coalescence phenomena occurring at lower temperatures. The three lines detected show approximately the same intensity which is expected from the crystal structure where the three crystallographically inequivalent Li sites, residing on the same Wyckoff position 4a, are fully occupied.

Interestingly, the individual paramagnetic NMR shifts δ depend on temperature. A linear relationship between δ and $1/T$ is expected for the Curie-Weiss behavior quantifying the dependence of the magnetic susceptibility on temperature. The larger the paramagnetic shift the steeper the slope of the corresponding δ ($1/T$) line: see, e.g., the recent study by Spencer *et al.*²⁴ This effect can be clearly seen in Fig. 4d-f showing the ^6Li MAS NMR spectra of the monoclinic counterpart of Li_3VF_6 . Up to 353 K no coalescence of the NMR lines is observed.

In $\beta\text{-Li}_3\text{VF}_6$ the Li ions occupy five crystallographically inequivalent sites whereby Li(2), Li(3), Li(4) and Li(5) reside on the Wyckoff position 8f and Li(1) on 4e. Since all the sites are fully occupied one might ascribe the NMR signal with the lowest intensity and the largest paramagnetic shift (76 ppm at 333 K) to the Li(1) ions. The asymmetric shape of this NMR peak might indicate that the signal is composed of more than one line, *i.e.*, the ions residing on the position 4e are crystallographically equivalent but not magnetically so. The assignment of the other NMR peaks, which do not differ in intensity as expected from the crystal structure, requires mixing time dependent 2D exchange NMR experiments and a careful analysis of the relevant transfer mechanisms of electron spin density. Such a study is beyond the scope of the present contribution and will be published elsewhere together with an investigation of the Li hopping processes taking place in $\beta\text{-Li}_3\text{VF}_6$. First results were shown in ref. 25. Comparing the 1D ^6Li MAS NMR spectra shown in ref. 23 with those obtained from $\alpha\text{-Li}_3\text{VF}_6$ and presented in Fig. 4, it is already evident that Li jump diffusion in the monoclinic modification is slower than that in the orthorhombic form. Interestingly, our quantum-chemical calculations show (*vide infra*) that the monoclinic modification is found to be more stable than the orthorhombic one which reveals rapid Li exchange among the three regularly occupied crystallographic positions (in particular, see Fig. 2 in ref. 23).

Li_3MF_6 (M = Cr, Fe, Co) and Li_2MnF_5

The preparation of the corresponding compounds containing chromium, iron, and manganese was performed in analogy to that of Li_3VF_6 . Unfortunately, and in contrast to Li_3VF_6 , which can be synthesized with high yields, the designated products could not be prepared as single-phase powders. During the synthesis of the precursor, the formation of larger quantities of the corresponding difluorides occurs. For the preparation of a Li_3FeF_6 -precursor, $\text{Fe}(\text{acac})_3$ and $\text{Fe}(\text{OEt})_3$ were tested in

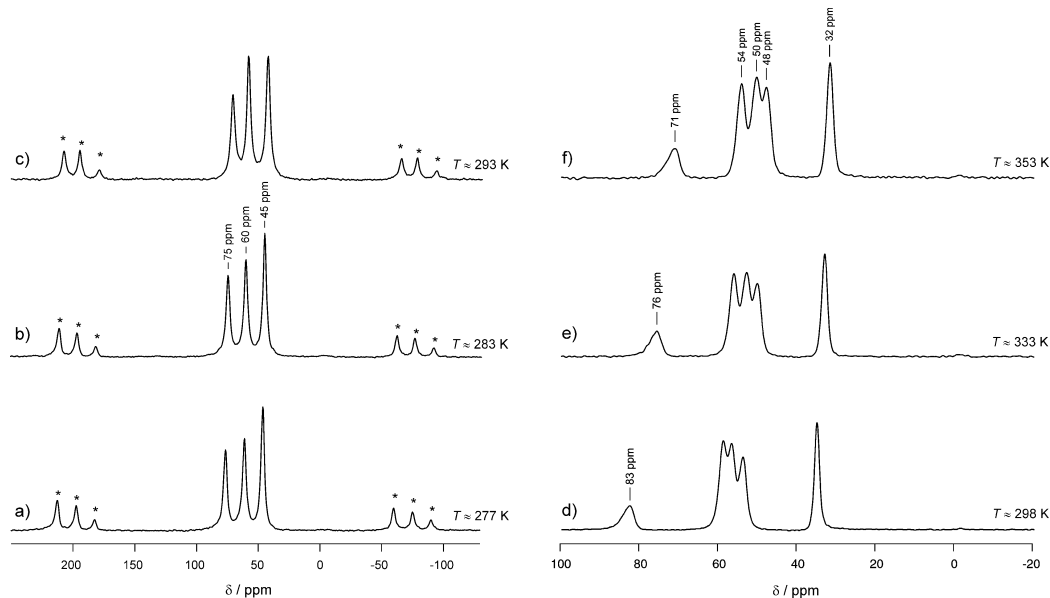


Fig. 4 ${}^6\text{Li}$ MAS NMR spectra of $\alpha\text{-Li}_3\text{VF}_6$ (a–c), 12 kHz spinning speed and $\beta\text{-Li}_3\text{VF}_6$ (d–f), 30 kHz spinning speed recorded at the temperatures indicated. Spectra have been referenced to aqueous LiCl. Note that in each case the number of NMR signals detected is in agreement with the crystallographic data of the two polymorphs. The temperature dependence of the NMR shifts points to Curie–Weiss behaviour as expected.

different solvents. Tempering of the obtained orange powder at $400\text{ }^\circ\text{C}$ always resulted in a mixture of monoclinic Li_3FeF_6 as well as LiF and FeF_2 . The orthorhombic modification of Li_3FeF_6 was also obtained with only a 50% yield. In the case of $\text{M} = \text{Cr}$, monoclinic Li_3CrF_6 could be obtained with approximately 85% purity. The precursor was prepared from LiOtBu , $\text{Cr}(\text{acac})_3$ and a HF–EtOH solution (see Fig. 5). Unfortunately, by using $\text{LiOtBu}/\text{Co}(\text{acac})_3/\text{HF}$, Co^{3+} was completely reduced to Co^{2+} and only LiF and CoF_2 were formed. Surprisingly, in the system Li–Mn–F the formation of Li_2MnF_5 was observed. $\text{Mn}(\text{acac})_3$ and $\text{Mn}(\text{OAc})_3 \cdot 2\text{H}_2\text{O}$ were used as starting materials. MnF_2 was

already formed during the synthesis of the precursor. The variation of the reaction time to prepare the precursor turned out to have no effect on the amount of MnF_2 formed. Interestingly, Li_2MnF_5 with a maximum yield of 30% was only formed by decomposing the precursor synthesized from $\text{Mn}(\text{OAc})_3 \cdot 2\text{H}_2\text{O}$ (Fig. 6). Precursors synthesized from $\text{Mn}(\text{acac})_3$ yielded only MnF_2 and LiF after decomposition. Compared to conventional solid-state routes reported in the literature, which require temperatures ranging from 700 to $800\text{ }^\circ\text{C}$,²⁷ the two-step synthesis route followed here allows the preparation of Li_2MnF_5 at temperatures as low as $400\text{ }^\circ\text{C}$.

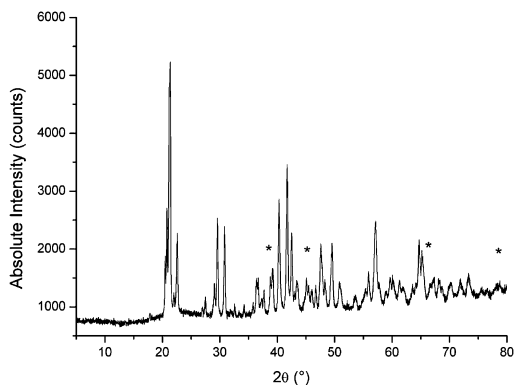


Fig. 5 X-ray powder diffraction pattern of monoclinic Li_3CrF_6 prepared at $500\text{ }^\circ\text{C}$. The sample was slowly cooled down to room temperature (* = LiF).

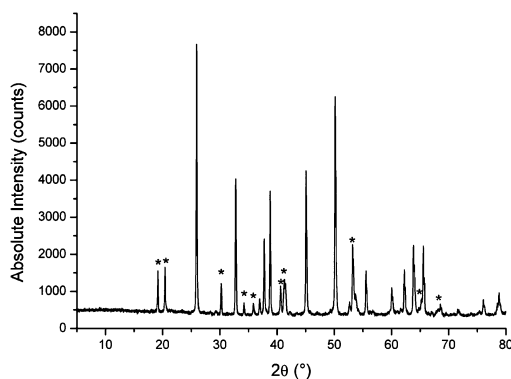


Fig. 6 X-ray powder pattern of Li_2MnF_5 (*). The sample was prepared at $400\text{ }^\circ\text{C}$ from $\text{Mn}(\text{OAc})_3 \cdot 2\text{H}_2\text{O}$. Other products found are LiF and MnF_2 .

Note that the procedure described in ref. 27 is useful to prepare single crystals. However, no information on the yields is given by the authors although preliminary experiments carried out by our group resulted in a maximum yield of 95% when a stoichiometric mixture of LiF and MnF₃ was used in a solid state route (60 h, 480 °C, monel capsule) to obtain Li₂MnF₅.

Preliminary ⁷Li MAS NMR spectra of Li₂MnF₅, synthesised via the above-mentioned solid state route (95% yield), recorded at spinning speeds ranging from 15 to 35 kHz (ambient bearing gas temperature) comprise rather broad resonance lines. The MAS NMR spectrum recorded at 15 kHz (see Fig. 7) reveals an intense line (A) at approximately 180 ppm and another one of lower intensity (B) at 0 ppm (the dashed line is to guide the eye), both with spinning sidebands. The intense line spreads over a range of some hundreds of ppm. The isotropic resonance can be distinguished from the spinning sidebands by recording MAS spectra at different rotation frequencies (see Fig. 7b). As can be clearly seen in Fig. 7b, the heat development, which increases with increasing spinning speed when ambient bearing gas pressure is used, is directly reflected by the shift of the isotropic resonance. As an example, using room temperature bearing gas the isotropic resonance of the main signal shows up at 172 ppm. Reducing the spinning speed by 5 kHz shifts the line towards positive ppm values. Additional heating of the bearing gas causes the line to show up at 162 ppm, as expected.

Thus, the main line clearly reveals a temperature-dependent NMR shift (see the corresponding MAS NMR spectra labeled (ii) and (iii) in Fig. 7b); the associated spin–lattice relaxation time *T*₁ turns out to be of the order of 2 ms only. This is in contrast to

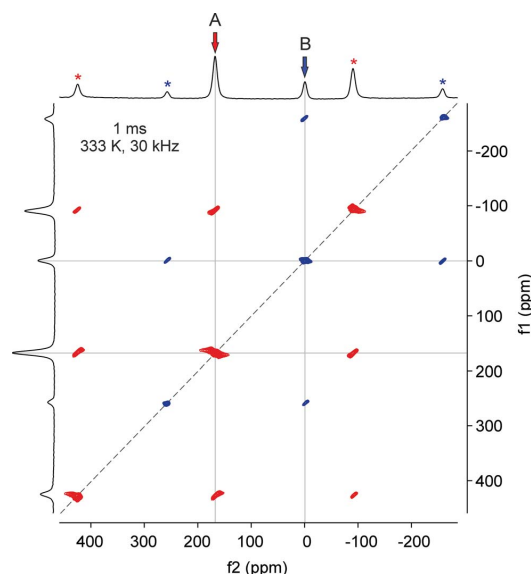


Fig. 8 2D ⁷Li exchange MAS NMR spectrum (116 MHz) of polycrystalline Li₂MnF₅ recorded at a spinning speed of 30 kHz and heated bearing gas pressure. The mixing time (1 ms) was chosen to be as large as possible; note that the corresponding NMR spin–lattice relaxation time of the main component (A) is approximately 2 ms. No off-diagonal intensities show up in the areas where the solid lines do cross. The dashed line simply connects the diagonal intensities.

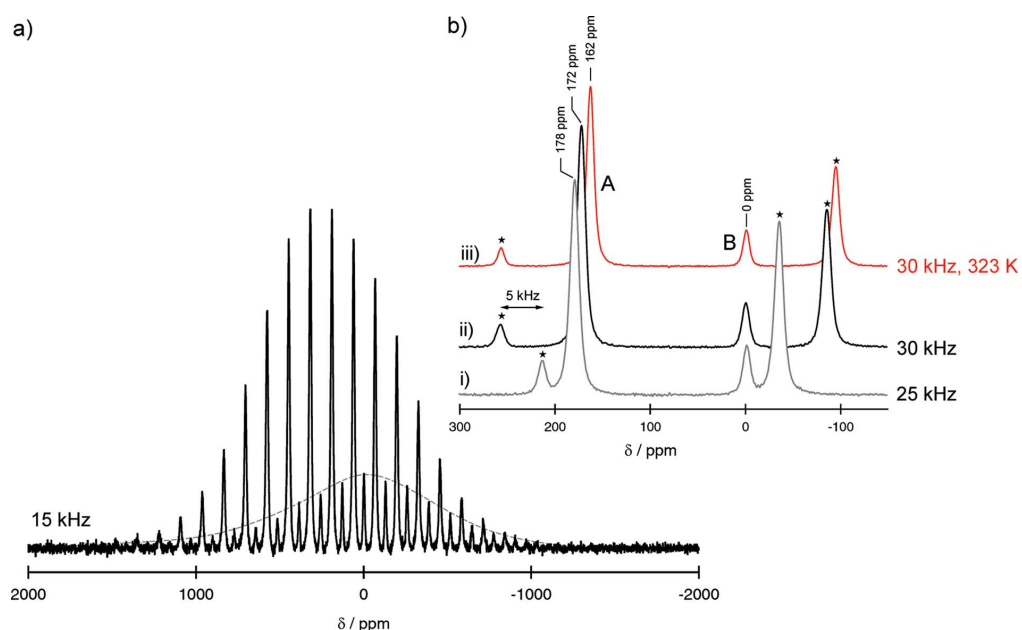


Fig. 7 ⁷Li MAS NMR spectra of Li₂MnF₅ recorded at (a) 15 kHz spinning speed and (b) at 25 and 35 kHz, respectively. The resonance frequency used was 116 MHz. Except for the spectrum labeled with (iii) ambient bearing gas temperature has been used. The dashed line is to guide the eye. Spinning sidebands, clearly shifting with rotation frequency, are marked with stars.

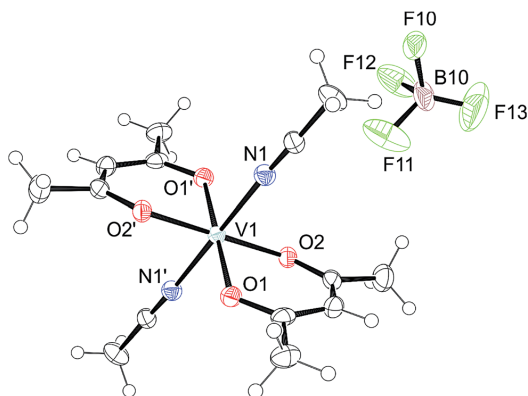


Fig. 9 Crystal structure of $[\text{V}(\text{acac})_2(\text{CH}_3\text{CN})_2]\text{BF}_4$ as derived from X-ray diffraction (ORTEP representation with 50% probability ellipsoids).^{37,38}

the line at 0 ppm which is characterized by $T_1 = 1.9$ s. Furthermore, no temperature dependence of this minor NMR component could be observed as shown in Fig. 7b. These findings indicate that the two spin ensembles seem to be magnetically decoupled.

This is supported by the observation that no cross-peaks show up between the isotropic resonances in a 2D exchange MAS NMR experiment (see the signals labeled A and B in Fig. 8), which was carried out at 116 MHz, with a heated bearing gas temperature of 333 K and a mixing time of 1 ms. Off-diagonal intensities are expected to be caused by, *e.g.*, chemical exchange or spin-diffusion between Li sites in the same lattice. The absence of any cross-peaks might indicate that the two signals simply stem from two different phases present whereby the signal at 0 ppm might reflect a (diamagnetic) impurity formed during synthesis (see above) and/or NMR sample preparation, see also ref. 28. In conclusion, at least at ambient temperature and above, the 1D MAS NMR spectra of Li_2MnF_5 reveal a single resonance. This is in good agreement with the crystal structure reported for Li_2MnF_5 showing only one Li site. Further measurements, which are intended to be performed at much lower temperatures, might help in finding out whether the main resonance detected is a coalesced one being the result of fast Li exchange processes between magnetically slightly differing Li positions. Previously, this was reported for Li intercalated $\text{Cr}_2\text{Ti}_3\text{Se}_8$ studied by Wontcheu *et al.*²⁸

Crystal structure determination of the Li_3VF_6 precursor

As already described above, X-ray powder diffraction gave no satisfying information on the crystal structure and the species the Li_3VF_6 precursor is composed of. Therefore, further analyses were performed to collect information on the vanadium species and to answer the question of whether Li_3VF_6 is already formed during the synthesis of the precursor or is generated during the annealing step. Such information helps optimize the synthesis conditions of the related precursors used to prepare Li_3FeF_6 and Li_2MnF_5 , for example. The Li_3VF_6 precursor described above was complementarily investigated by NMR and FTIR

spectroscopy. ^1H and ^{13}C NMR spectra of the removed solvents clearly show the signal of acetylacetonate which indicates that acetylacetonate was abstracted. Samples of the Li_3VF_6 precursor were measured in MeOH-d_4 and D_2O , respectively. ^1H NMR signals of acetylacetonate bonded to V^{3+} were observed at 44 ppm. The NMR signals are very broad and have a pronounced low-field shift which is caused by the V^{3+} ion (*vide infra*). The chemical shift corresponds to the values known for $\text{V}(\text{acac})_3$.^{29,30} The ^{19}F NMR spectra reveal intensities in the range from -124 ppm up to -145 ppm (D_2O). When the samples have been solved in MeOD-d_4 NMR signals at -132 and at -154 ppm show up. NMR lines with chemical shifts ranging from -124 to -135 ppm can be ascribed to Li_2SiF_6 .³¹ Note that the ^{19}F NMR shifts of $[\text{SiF}_6]^{2-}$ depend on the pH-value.³² Because of exchange reactions they shift to lower fields with increasing pH-value. In the ^{51}V NMR spectra signals at -657 and -896 ppm were observed. The ^{51}V shift for $\text{V}(\text{acac})_3$ in MeOD-d_4 shows up at -899 ppm.

FTIR experiments were carried out in transmission mode (50 to 4000 cm^{-1}) and by using an ATR-module (400 to 4000 cm^{-1} , attenuated total reflectance mode). We used samples which were prepared as KBr and CsI pellets. First, let us discuss the far IR range (50 to 400 cm^{-1}). The transmission spectrum shows one band at 295 cm^{-1} which is in good agreement with the ν_4 -band of $[\text{VF}_6]^{3-}$.³³ Further bands are visible in the organic fingerprint range.³⁴ The C=O- and C=C combination modes of acetylacetonate appear at 933 , 1532 and 1586 cm^{-1} . Further bands can be found at 1033 cm^{-1} ($\rho_r(\text{CH}_3)$), $1366 + 1388\text{ cm}^{-1}$ ($\delta_s(\text{CH}_3)$) and at 1290 cm^{-1} ($\nu(\text{C}-\text{CH}_3) + \nu(\text{C}::\text{C})$). Depending on the preparation conditions of the sample, the IR spectra show a broad band in the range from 714 to 741 cm^{-1} which agrees with the ν_3 -band of $[\text{SiF}_6]^{2-}$.³⁵ In summary, it might be concluded that the Li_3VF_6 -precursor contains several vanadium species including acetylacetonate as well as $[\text{VF}_6]^{3-}$.

In addition to the spectroscopic analyses, attempts were made to prepare single crystals. Saturated solutions of the precursor in CH_3CN or MeOH were filled into small glass tubes. These glass

Table 3 Crystal data of $[\text{V}(\text{acac})_2(\text{CH}_3\text{CN})_2]\text{BF}_4$

Chemical formula	$\text{C}_{14}\text{H}_{20}\text{BF}_4\text{N}_2\text{O}_4\text{V}$
Formula mass	418.07
Crystal system	Monoclinic
$a/\text{\AA}$	11.9556(10)
$b/\text{\AA}$	5.7003(4)
$c/\text{\AA}$	15.8568(19)
$\alpha/\text{^\circ}$	90.00
$\beta/\text{^\circ}$	119.774(7)
$\gamma/\text{^\circ}$	90.00
Unit cell volume/ \AA^3	937.99(17)
Temperature/K	150(2)
Space group	$P2_1/c$
Number of formula units per unit cell, Z	2
Radiation type	$\text{MoK}\alpha$
Number of reflections measured	3866
Number of reflections observed	1372
R_σ	0.0635
Number of independent reflections	1832
R_{int}	0.0390
Final R_1 values ($I > 2\sigma(I)$)	0.0450
Final $wR(F^2)$ values ($I > 2\sigma(I)$)	0.1044
Final R_1 values (all data)	0.0633
Final $wR(F^2)$ values (all data)	0.1093

Table 4 Calculated lattice parameters a , b , c , β and de-lithiation energy E_d of the compounds Li_3MF_6 and Li_2MnF_5 (method PWIPW). Values in parentheses correspond to measured lattice parameters (orth. = orthorhombic, mon. = monoclinic)

Compound	$a/\text{\AA}$	$b/\text{\AA}$	$c/\text{\AA}$	$\beta/^\circ$	E_d/eV
Li_3VF_6 , orth.	9.53 (9.59)	8.45 (8.49)	5.03 (5.04)		
Li_3VF_6 , mon.	14.30 (14.39)	8.68 (8.69)	10.05 (10.06)	96.4 (95.9)	4.73
Li_3FeF_6 , orth.	9.58 (9.53)	8.43 (8.24)	5.01 (4.88)		
Li_3FeF_6 , mon.	14.34 (14.41)	8.64 (8.67)	10.02 (10.05)	95.6 (95.3)	6.69
Li_3CrF_6 , mon.	14.32 (14.43)	8.59 (8.61)	10.02 (10.04)	94.9 (94.6)	6.18
Li_2MnF_5	10.02 (10.02)	4.97 (4.95)	7.39 (7.41)	112.4 (112.2)	5.88

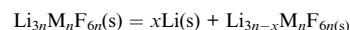
tubes were placed inside a Schlenk tube filled with Et_2O or pentane. From the CH_3CN solutions, dark red crystals of the compound $[\text{V}(\text{acac})_2(\text{CH}_3\text{CN})_2]\text{BF}_4$ were obtained (Fig. 9). This compound shows the existence of acac-containing vanadium species in the precursor. The current work of our group indicates that the here-presented species is just the first one in a sequence of more and more fluorinated species. More details will be given in a forthcoming contribution.³⁶ BF_4^- is formed by the reaction of HF with the borosilicate glassware during the synthesis of the precursor. V^{3+} is coordinated octahedrally by two acetylacetonate ions and two molecules of CH_3CN . The BF_4^- ion is severely disordered over a center of inversion. Crystal data for $[\text{V}(\text{acac})_2(\text{CH}_3\text{CN})_2]\text{BF}_4$ are given in Table 3.

Quantum-chemical calculations

In order to investigate the suitability of the synthesized Li_3MF_6 compounds as potential cathode materials in lithium-ion batteries, we calculated the corresponding de-lithiation energies at density-functional theory (DFT) level. Based on our experience with open-shell transition metal systems³⁹ we chose the DFT/Hartree–Fock hybrid functional PWIPW.⁴⁰ The calculations were performed with the crystalline-orbital program package CRYSTAL09.⁴¹ The standard atomic basis sets for the elements Li, O, V, Cr, Mn and Fe were taken from the CRYSTAL homepage⁴² and augmented where possible with diffuse shells and polarization functions. A detailed description of the optimized solid-state basis sets will be given elsewhere.⁴³ The computational accuracy parameters were set to rather strict values as described previously.³⁹ In Table 4 the calculated lattice parameters are compared with our measured values obtained from X-ray powder diffraction where available (*vide supra*). The agreement found between theory and experiment for the structure parameters is encouragingly good. In all cases the deviations are below 1% except the b and c lattice vectors of orthorhombic Li_3FeF_6 . This indicates that our theoretical approach is sufficiently accurate to describe the transition metal fluorides. For Li_3VF_6 and Li_3FeF_6 we computed the relative stability of the orthorhombic and monoclinic phases. In both cases the monoclinic polymorph was more stable so that only this phase was considered for the calculation of the de-lithiation energy E_d . For all compounds we also investigated the magnetic structure. Ferromagnetic and antiferromagnetic couplings were considered. For example, for Li_2MnF_5 the previously reported antiferromagnetic chains of Mn^{3+} ions were considered.⁴⁴

The de-lithiation energy was computed by removing all Li atoms occupying a certain Wyckoff position. As discussed above there are five crystallographically inequivalent Li atoms in the

asymmetric unit of monoclinic Li_3MF_6 . In Li_2MnF_5 the two Li atoms of the primitive unit cell are crystallographically equivalent. In the antiferromagnetic ground state they are not electronically equivalent anymore. However, the differences between local electrostatic potentials and electric field gradients are rather small. In Table 3 we only report the smallest values of the de-lithiation energies for each compound according to the following equation:



with lithium metal as reference according to the electrochemical reference. x corresponds to the number of Li ions occupying the particular Wyckoff position. E_d is then normalized to one Li atom. Since only one electron is transferred in this process, E_d in eV directly corresponds to a battery voltage in V (for approximations see below). It has to be noted that in the present lithium-ion batteries graphite is used as the counter anode rather than metallic lithium, but the potential differences are rather small. The present values can only be regarded as zero-order approximations since we did not take into account possible phase transitions after Li removal. The change in Li concentration is rather large in our models due to the small unit cell size. This means that we calculate an average value of the potential for the corresponding x range rather than $E_d(x)$ as in electrochemical measurements. Furthermore, enthalpy and entropy are not taken into account due to the high computational effort. Nevertheless, we have shown in a parallel study that the simplistic approach described here can indeed reproduce measured cell potentials of a wide range of battery materials with surprisingly high accuracy.⁴⁵ The resulting E_d values presented in Table 3 may therefore have some significance. As they range from 4.7 to 6.7 eV, not too far from the initially discussed theoretical result (6 eV) for LiCaCoF_6 or LiCdCoF_6 ,⁸ all materials synthesized in this work can be regarded as promising high-voltage cathode materials provided that stability issues are resolved.

Conclusions

Ternary lithium fluorides of transition metals were synthesized *via* a sol–gel route from transition metal acetylacetonates as precursors and hydrogen fluoride in organic solvents. The two polymorphs of Li_3VF_6 were obtained with approximately 98% purity. Local environments probed by high-resolution solid-state ^6Li and ^7Li NMR are in very good agreement with expectations from the crystal structure of the compounds. The synthesis of the monoclinic phase is already possible at temperatures as low as 300 °C. Its domain size can be controlled by modifying the temperature used for the synthesis. This may be of importance in

the preparation of cathode materials for lithium-ion batteries. Monoclinic Li_3CrF_6 was also prepared with a phase purity of approximately 85%. For manganese, iron and cobalt the corresponding difluorides were formed in addition to the ternary fluorides. Quantum chemical calculations show that all materials have high de-lithiation energies making them suitable candidates to be used as high-voltage battery cathode materials.

Acknowledgements

We thank the German Ministry of Education and Research (BMBF) for financial support within the LIB 2015 initiative, project HE-Lion. We thank D. Freude and E. Romanova (Leipzig) for recording of some of the NMR measurements presented. M.W. gratefully acknowledges financial support by the Deutsche Forschungsgemeinschaft (DFG). We would also like to thank Mr Manfred Detlaff (NMR service group, TU Berlin) and Ms Paula Nixdorf (XRD service group, TU Berlin) for their experimental help.

Notes and references

- J. M. Tarascon and M. Armand, *Nature*, 2001, **414**, 359.
- L. F. Nazar, G. Goward, F. Leroux, M. Duncan, H. Huang, T. Kerr and J. Gaubicher, *Int. J. Inorg. Mater.*, 2001, **3**, 191.
- M. S. Whittingham, *Chem. Rev.*, 2004, **104**, 4271.
- A. S. Arico, P. Bruce, B. Scrosati, J.-M. Tarascon and W. V. Schalkwijk, *Nat. Mater.*, 2005, **4**, 366.
- P. G. Bruce, B. Scrosati and J.-M. Tarascon, *Angew. Chem., Int. Ed.*, 2008, **47**, 2930.
- B. L. Ellis, K. T. Lee and L. F. Nazar, *Chem. Mater.*, 2010, **22**, 691–714.
- J. B. Goodenough and Y. Kim, *Chem. Mater.*, 2010, **22**, 587.
- Y. Koyama, I. Tanaka and H. Adachi, *J. Electrochem. Soc.*, 2000, **147**, 3633.
- E. Gonzalo, A. Kuhn and F. Garcia-Alvarado, *J. Power Sources*, 2010, **195**, 4990–4996.
- (a) I. Gocheva, K. Chihara, S. Okada and J. Yamaki, *Lithium Batteries Discussion 2011 – Electrode Materials – Archacon, France (extended abstract)*; (b) A. Basa, E. Gonzalo, A. Kuhn and F. Garcia-Alvarado, *J. Power Sources*, 2012, **207**, 160–165.
- W. Massa, *Z. Kristallogr.*, 1980, **153**, 201–210.
- W. Massa and W. Ruedorff, *Z. Naturforsch., B*, 1971, **26**, 1216–1218.
- P. Heitjans and S. Indris, *J. Mater. Sci.*, 2004, **39**, 5091–5096.
- M. Wilkening, V. Epp, A. Feldhoff and P. Heitjans, *J. Phys. Chem. C*, 2008, **112**, 9291.
- P. Heitjans, M. Masoud, A. Feldhoff and M. Wilkening, *Faraday Discuss.*, 2007, **134**, 67.
- E. Avvakumov, M. Senna and N. Kosova, *Soft Mechanochemical Synthesis: A Basis for New Chemical Technologies*, Kluwer Academic Publishers, Boston, 2001.
- K. L. Da Silva, D. Menzel, A. Feldhoff, C. Kübel, M. Bruns, A. Paesano, A. Düvel, M. Wilkening, M. Ghafari, H. Hahn, F. J. Litterst, P. Heitjans, K. D. Becker and V. Šepelák, *J. Phys. Chem. C*, 2011, **115**, 7209–7217.
- A. Düvel, M. Wilkening, R. Uecker, S. Wegner, V. Šepelák and P. Heitjans, *Phys. Chem. Chem. Phys.*, 2010, **12**, 11251–11262.
- E. Kemnitz, U. Groß, S. Rüdiger and C. S. Shekar, *Angew. Chem.*, 2003, **115**, 4383–4386.
- St. Wuttke, A. Vimont, J.-C. Lavaley, M. Daturi and E. Kemnitz, *J. Phys. Chem. C*, 2010, **114**, 5113–5120.
- M. Ahrens, G. Scholz, M. Feist and E. Kemnitz, *Solid State Sci.*, 2006, **8**, 798–806.
- (a) D. L. Deadmore, J. S. Machin and A. W. Allen, *J. Am. Ceram. Soc.*, 1962, **45**, 120–122; (b) Yu. N. Moskvich, B. I. Cherkasov and G. I. Dotsenko, *Zh. Strukt. Khim.*, 1979, **20**, 348–357.
- M. Wilkening, E. Romanova, S. Nakhal, D. Weber, M. Lerch and P. Heitjans, *J. Phys. Chem. C*, 2010, **114**, 19083.
- T. L. Spencer, A. Ramzy, V. Thangadurai and G. R. Goward, *Chem. Mater.*, 2011, **23**, 3105–3113.
- P. Bottke, S. Nakhal, M. Lerch, M. Wilkening and P. Heitjans, *Diff. Fundam.*, 2011, **16**, 40.
- T. Ressler, *WINXAS v3.1* 2011.
- J. Pebler, W. Massa, H. Lass and B. Ziegler, *J. Solid State Chem.*, 1987, **71**, 87–94.
- J. Wontcheu, W. Bensch, M. Wilkening, P. Heitjans, S. Indris, P. Sideris and C. P. Grey, *J. Am. Chem. Soc.*, 2008, **130**, 288.
- A. Johnson and G. W. Everett, *J. Am. Chem. Soc.*, 1972, **94**, 1419–1425.
- D. R. Eaton, *J. Am. Chem. Soc.*, 1965, **87**, 3087–3102.
- P. M. Borodin and N. Kim Zao, *Russ. J. Inorg. Chem.*, 1972, **16**, 1720–1722.
- W. F. Finney, E. Wilson, A. Callender, M. D. Morris and L. W. Beck, *Environ. Sci. Technol.*, 2006, **40**, 2572–2577.
- R. Becker and W. Sawodny, *Z. Naturforsch.*, 1973, **28b**, 360.
- M. Mikami, I. Nakagawa and T. Shiraanouchi, *Spectrochim. Acta*, 1967, **23A**, 1037.
- C. Naulin and R. Bougon, *J. Chem. Phys.*, 1976, **64**, 4155.
- J. Kohl, D. Wiedemann, S. Troyanov and M. Lerch, in preparation.
- Crystal data for $[\text{V}(\text{acac})_2(\text{CH}_3\text{CN})_2]\text{BF}_4$ were collected on an Oxford Diffraction Xcalibur S diffractometer equipped with an Enhance Mo- K_α source (graphite monochromated, $\lambda = 0.71073 \text{ \AA}$) and a Sapphire 3 detector at $T = 150 \text{ K}$. The structure was solved with SHELXS-97 and refined against all F^2 data using the full-matrix least-squares method of SHELXL-97. The tetrafluoroborate moiety is disordered over an inversion centre. The positional disorder was not further resolved resulting in somewhat higher displacement parameters.†
- G. M. Sheldrick, *Acta Crystallogr., Sect. A: Found. Crystallogr.*, 2008, **64**, 112–122.
- M. M. Islam, T. Bredow and A. Gerson, *ChemPhysChem*, 2011, **12**, 3467–3473.
- T. Bredow and A. R. Gerson, *Phys. Rev. B: Condens. Matter*, 2000, **61**, 5194–5201.
- R. Dovesi, R. Orlando, B. Civalleri, C. Roetti, V. R. Saunders and C. M. Zicovich-Wilson, *Z. Kristallogr.*, 2005, **220**, 571–573.
- http://www.crystal.unito.it/Basis_Sets.
- N. Ferro, C. Reimann and T. Bredow, in preparation.
- T. Roisnel, P. Nuñez, W. Massa and A. Tressaud, *Phys. B*, 1997, **234–236**, 579–581.
- N. Ferro, M. Lerch, R. Glaum, H. Ehrenberg and T. Bredow, in preparation.

3.1.6 2D ^6Li MAS EXSY NMR an $\beta\text{-Li}_3\text{VF}_6$

Die fünf NMR-Linien (A – E, alphabetisch von kleinen zu großen ppm-Werten geordnet) des $\beta\text{-Li}_3\text{VF}_6$ konnten den fünf unterschiedlichen Li-Positionen Li(1) – Li(5) im Kristallgitter zugeordnet werden. Dies gelang durch die kombinierte Analyse der Kristallstruktur (Daten aus Neutronenbeugung), den chemischen Verschiebungen der einzelnen NMR-Linien und den Austauschraten aus 2D ^6Li MAS EXSY NMR-Experimenten. Diese weisen generell auf eine geringere Diffusivität hin, als sie in der α -Modifikation vorliegt. Da dort alle drei Oktaeder, die von Li besetzt sind, eine Flächenverknüpfung aufweisen und in der β -Modifikation nur zwei der fünf Li-Positionen über Flächen verknüpft sind, war dieses Ergebnis zu erwarten. Sprünge durch Oktaederflächen bilden im Gegensatz zur α -Modifikation nur einen Teil des bevorzugten Diffusionspfads und es gibt „Sackgassen“, die nur von deutlich höher aktivierten Li-Ionen passiert werden können.

Der ^6Li -Kern wird aufgrund seiner geringen natürlichen Häufigkeit für das Experiment genutzt, da bei der Verwendung von ^7Li falsch-positive *cross peaks* durch *spin*-Diffusion auftauchen. Außerdem ist die Linienbreite wegen des kleineren Kernquadrupolmoments geringer, was die Auflösung bei überlagerten Linien deutlich verbessert.

In P3 wurde schon auf die Wyckoff Position 8f von Li(2), Li(3), Li(4) und Li(5) hingewiesen. Li(1) „sitzt“ auf Position 4e und kann somit nur der NMR-Linie E entsprechen, da alle Li-Plätze voll besetzt sind und diese Linie die halbe Intensität der anderen Linien im NMR-Spektrum zeigt (siehe Abb. 4 d–f in P3).

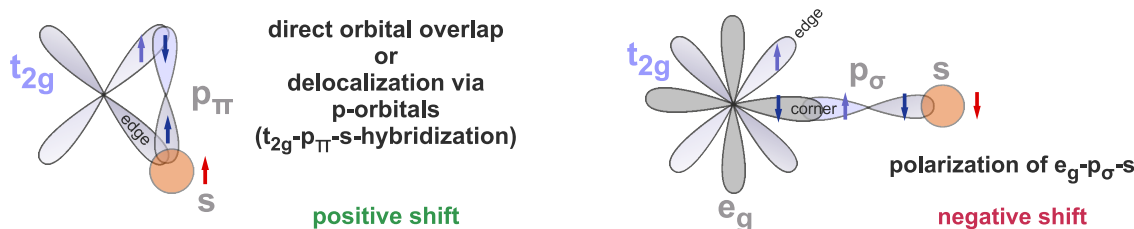


Abbildung 3.3: Gezeigt sind die beiden entscheidenden Spindichte-Transfermechanismen (von V^{3+} auf Li^+) für die chemische Verschiebung des Lithiumsignals im NMR-Spektrum. Überlappen die Orbitale wie links, entspricht dies einem Winkel von 90° für V-F-Li und das Signal wird positiv verschoben. Die rechte Darstellung entspricht einem 180° Winkel und verschiebt die Li-Signale zu negativen ppm-Werten. Für jede Li-Position im Gitter müssen mehrere Winkel (abhängig von der Koordinationszahl) betrachtet werden, um auf die absolute Verschiebung schließen zu können.

Die Winkel von Vanadium–Fluor–Lithium können aus den kristallographischen Daten für jede einzelne Position ausgemessen werden. Vier oktaedrische und ein tetraedrischer Polyeder liefern insgesamt 28 Winkel. Die chemische Verschiebung der zugehörigen Linien kann mit Hilfe der Spindichte-Transfermechanismen^[51,52] (Abb. 3.3) abgeschätzt werden. Je nach Polyederverknüpfung, d.h. der Überlappung der beteiligten Orbitale t_{2g} der Vanadi-

umzentren, p_π der Fluor-Anionen und des s-Orbitals der Li-Ionen, kann entweder positive oder negative Spindichte auf den Li-Kernort übertragen werden. Dies kann über direkte Orbitalüberlappung, den Delokalisierungsmechanismus oder den Polarisationsmechanismus geschehen.

Im Falle der β -Modifikation des Lithiumvanadiumfluorids ist eine Tabelle erstellt worden, in der auch noch die Anzahl der nächsten Li-Nachbarn (Li(1) und Li(5) haben jeweils 8 und Li(2) – Li(4) besitzen jeweils 7), sowie die Verknüpfungen der Polyeder untereinander und deren Anzahl notiert wurden. Sprunglängen und Sprungpfade wurden für die Zuordnung ebenso mit in Betracht gezogen. Durch die Bestätigung der erwarteten Austauschraten im 2D ${}^6\text{Li}$ MAS EXSY NMR-Experiment (Abb. 3.5), erfolgte die Zuordnung der Kristallpositionen zu den NMR-Linien wie in Abb. 3.6 gezeigt.

${}^7\text{Li}$ -Austauschmessungen Das 2D ${}^7\text{Li}$ EXSY NMR-Experiment (Abb. 3.4) am $\beta\text{-Li}_3\text{VF}_6$ zeigt bei einer Mischzeit von nur 3 ms und einer Proben temperatur von ca. 100°C (VT gas plus Rotationswärme) bereits deutliche Hinweise auf den Austausch von Li^+ zwischen den Plätzen B und C sowie zwischen C und D. Wird t_m auf 12 ms erhöht, nimmt die Intensität der *cross peaks* zu und es tauchen weitere auf, wie es zu erwarten war.

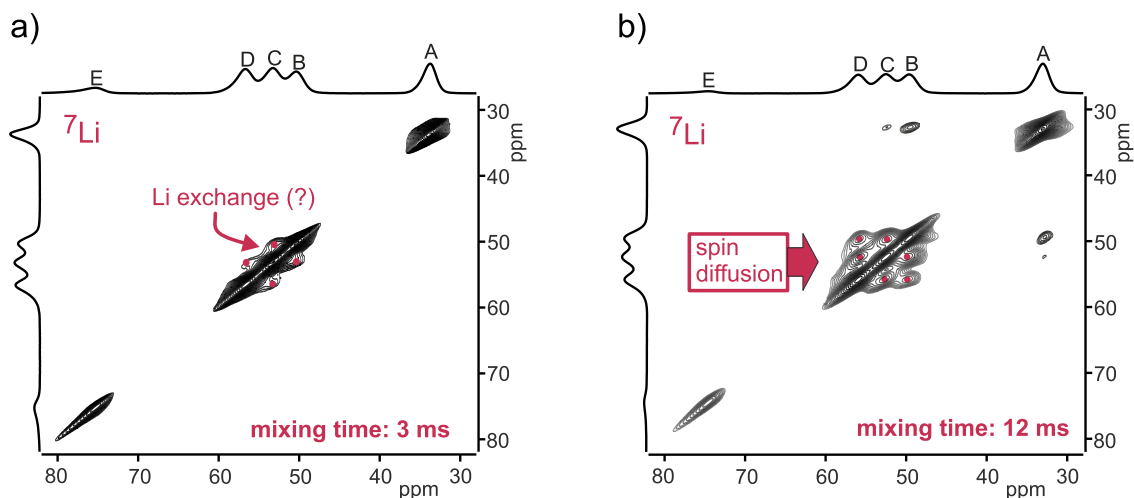


Abbildung 3.4: 2D- ${}^7\text{Li}$ -EXSY-NMR-Spektren; 233 MHz Resonanzfrequenz; 338 K und 60 kHz MAS-Rotationsgeschwindigkeit. a) $t_m = 3$ ms; 4 *cross peaks* (rote Punkte) b) $t_m = 12$ ms; mehr und intensivere *cross peaks*; rot markierte jedoch zeigen jedoch keinen Austausch an. Details siehe Text.

Nach den Vorüberlegungen (Analyse der Kristallstruktur zur Abschätzung der chemischen Verschiebungen und energetisch bevorzugten Sprungprozessen) sollten diese NMR-Linien jedoch nicht als erstes Austausch anzeigen. Erwartet wurde ein *cross peak* zwischen Linie A, die aufgrund der „negativsten“ chemischen Verschiebung zu Li(4) gehören sollte und

Li(3). Die beiden Positionen sind die einzigen, deren Polyeder (hier Oktaeder) über eine gemeinsame Fläche verknüpft sind. Alle anderen Diffusionspfade führen über Kantenverknüpfungen oder im Falle der Tetraeder von Li(2) auch über Ecken. Da die temporäre Besetzung von Zwischengitterplätzen bei niedrigeren Temperaturen „einfrieren“ müsste, dieses Verhalten aber nicht beobachtet werden konnte, kann ein solcher Diffusionspfad als bevorzugt ausgeschlossen werden.

^6Li -Austauschmessungen Das gleiche Experiment am ^6Li -Kern offenbart, welche *cross peaks* bei der Beobachtung von ^7Li nicht durch Li^+ -Platzwechsel hervorgerufen wurden. Die 2D-Austauschexperimente zeigen im gesamten zur Verfügung stehenden Temperaturbereich sehr ähnliche Spektren.

Eine Reihe zur temperaturabhängigen Bestimmung der Austauschraten für alle Positionen untereinander ist aus folgenden Gründen nicht möglich gewesen: a) die T_1 -Zeiten allgemein und insbesondere von Linie E sind sehr kurz (ca. 50 ms); b) der Temperaturbereich des MAS-Probenkopfes ist zu limitiert für eine systematische Analyse. Somit hatten die Hauptintensitäten bei langen Mischzeiten teilweise schon an Intensität durch Relaxation verloren. Das Berechnen der Verweilzeiten auf den einzelnen Gitterpositionen wäre dadurch auch ohne die Komplexität, die ein Material mit fünf Positionen mit sich bringt, nicht quantitativ möglich gewesen.

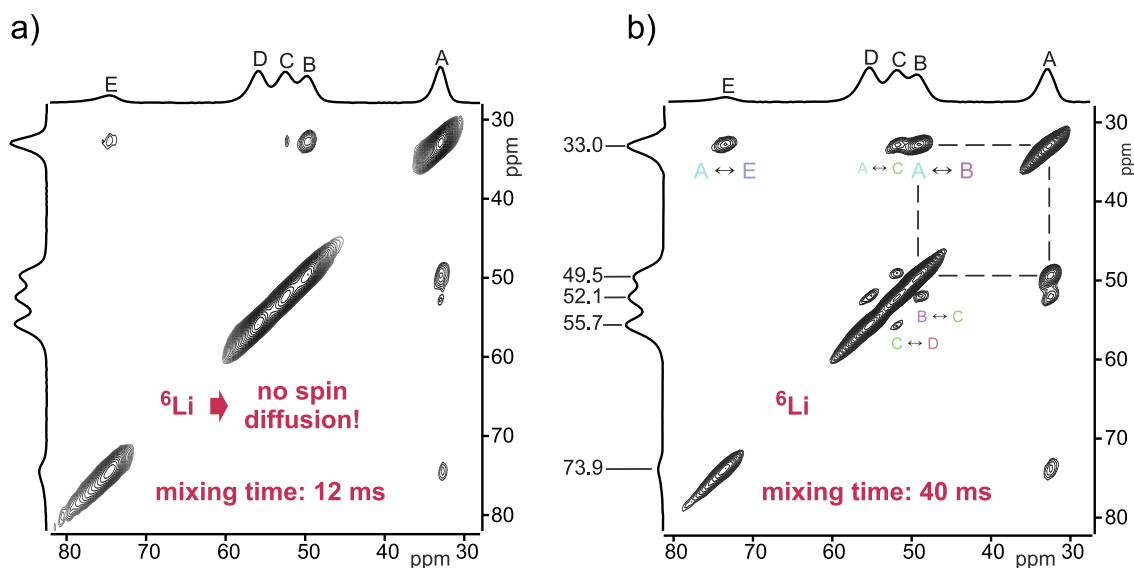


Abbildung 3.5: 2D- ^6Li -EXSY-NMR-Spektren; 233 MHz Resonanzfrequenz; aufgenommen bei 338 K und 60 kHz MAS-Rotationsgeschwindigkeit. a) $t_m = 12$ ms; b) $t_m = 40$ ms; bei eliminiertes Spin-Diffusion wird der „echte“ Li-Austausch sichtbar.

Für eine strukturelle Interpretation der 1D Spektren haben die 2D-Messungen jedoch wertvolle Hinweise gegeben und die komplette Zuordnung ermöglicht; dies ist in Abb. 3.6 illustriert.

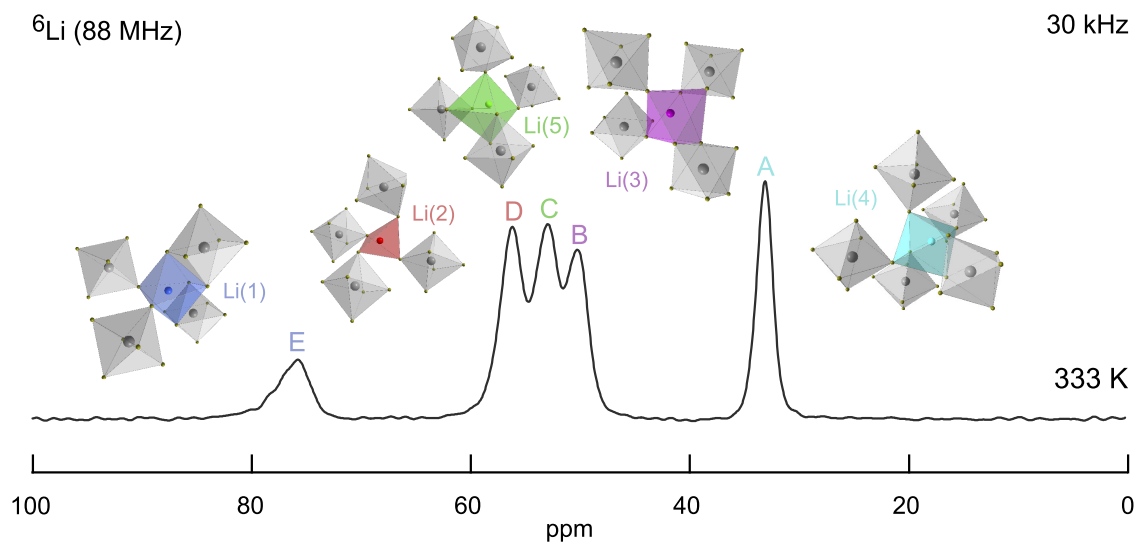


Abbildung 3.6: Zuordnung der Li-Plätze Li(1)–Li(5) im Kristallgitter zu den NMR-Linien im 1D ${}^6\text{Li}$ -Spektrum. Details siehe Text.

3.2 Li-Diffusion in Titandioxiden und Titanaten

Titandioxide und Titanate sind vielversprechende Anodenmaterialien. Ihre Leistungsfähigkeit ist gekoppelt an die Li-Diffusion in der Kristallstruktur, aber auch an die Zugänglichkeit einzelner Kristallite. D. h. die Oberfläche der Materialien hat einen entscheidenden Einfluss auf Ein- und Ausbau von Lithium. Drei Modellsysteme mit anwendungsorientiertem Charakter wurden ausgewählt, um die Spungprozesse auf atomarer Ebene dem makroskopischen Ladungstransport in einem Batteriesystem gegenüber zu stellen. Dabei wurden auch verschiedene Morphologien und Modifikationen studiert.

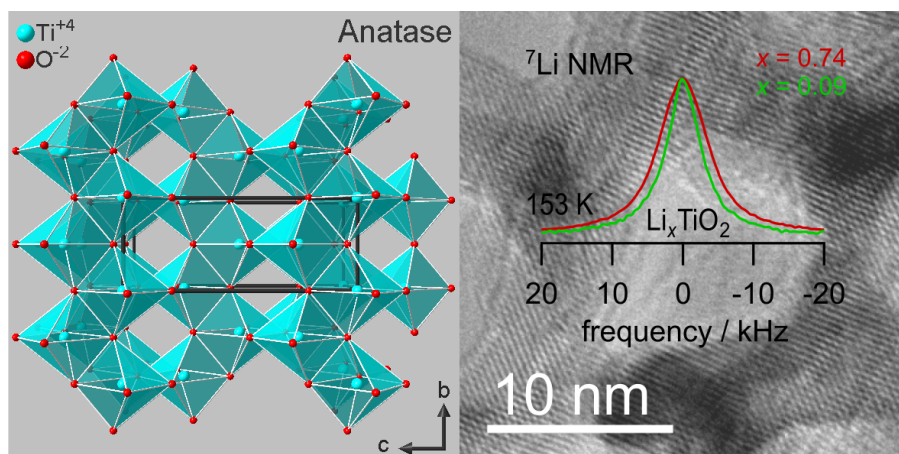
Die Interkalation von Li^+ in TiO_2 (Publikation 4 und Abschnitt 3.2.2) und in $\text{Li}_4\text{Ti}_5\text{O}_{12}$ (Publikation 5) erfolgt bei den untersuchten Materialien nur bis zu einem bestimmten Lithiumgehalt ohne strukturelle Änderungen des Wirtsgitters. All diese Anoden müssen daher als Insertionsmaterialien bezeichnet werden.

Bei den untersuchten Titandioxiden handelt es sich um nanostrukturierte Materialien mit entsprechenden Poren- bzw. Röhrendurchmessern. Das mesoporöse- TiO_2 wurde als Anatas hergestellt^[53] und dann elektrochemisch auf die Beladungsgrade $x = 0.09$, $x = 0.35$ und $x = 0.74$ (Li_xTiO_2) gebracht. Wobei die Probe mit dem höchsten Li-Gehalt vollständig die Struktur von orthorhombischem Titandioxid angenommen hat. Interessanterweise erhöht sich die Li-Diffusivität dadurch und ermöglicht so die schnelle Einlagerung von Lithium bis zur vollständigen Beladung. Die durchgeführten NMR-Messungen (Publikation 4) konnten die strukturelle Umwandlung in *ex situ* Experimenten verfolgen, wobei es gelang, die sehr gute Zyklenstabilität des Materials mittels Aktivierungsenergien aus $T_{1\rho}$ - und SAE-Messungen zu erklären.

Abschnitt 3.2.2 präsentiert Ergebnisse von Untersuchungen, die an TiO_2 Nanoröhren durchgeführt wurden. Die Präparation und die elektrochemischen Charakterisierungen wurden in Schottland durchgeführt. Die NMR-Ergebnisse sind teilweise in Hannover und teilweise in Graz entstanden. Weitere Details folgen ab Seite 86.

Das Li-Titanat LTO (Publikation 5) bietet die Möglichkeit, zusätzlich drei weitere Li-Ionen in die Struktur ($\text{Li}_{4+x}\text{Ti}_5\text{O}_{12}$) einzulagern. Die dadurch praxistauglichen Kapazitäten und die hohe Lebensdauer unter realen Bedingungen sind zwei Gründe für die Verwendung als Anodenmaterial in *battery packs* für *electric vehicles* (EV) wie z. B. den Modellen von Tesla Motors, Inc. Über die mikroskopischen Vorgänge, besonders beim ersten Beladen mit zusätzlichem Lithium bzw. bei Beladungszuständen $0 < x \ll 1$, gab es nicht genügend Informationen, um die flachen Insertionspotentiale zu erklären. Es hat sich gezeigt, dass die Li-Diffusivität gegenüber $x = 0$ zunächst drastisch ansteigt (max. bei $x = 0.3$) und während der steten Umwandlung vom Spinell-Typ zur Kochsalz-Struktur bei $x = 3$ wieder abnimmt. Der Verlauf deutet dabei auf die Bildung von Mischkristallen hin.

P4 Li ion dynamics in TiO_2 anode materials with an ordered hierarchical pore structure – insights from *ex situ* NMR



PCCP



PAPER

[View Article Online](#)
[View Journal](#) | [View Issue](#)

Li ion dynamics in TiO₂ anode materials with an ordered hierarchical pore structure – insights from *ex situ* NMR

Cite this: *Phys. Chem. Chem. Phys.*, 2014, 16, 1894

Patrick Bottke,^{*a} Yu Ren,^b Ilie Hanzu,^a Peter G. Bruce^b and Martin Wilkening^a

Ex situ Nuclear Magnetic Resonance (NMR) measurements were carried out to study lithium ion dynamics in lithium intercalated mesoporous anatase (Li_xTiO₂) serving as an anode material for rechargeable lithium-ion batteries. As has been shown recently, hierarchically ordered TiO₂ shows excellent cycling performance and ensures a high lithium storage capacity. ⁷Li spin–lattice relaxation NMR and stimulated echo NMR serve as a powerful combination to shed light on the Li hopping processes from an atomic-scale point of view. To determine atomic Li jump rates and microscopic activation energies temperature-variable SLR NMR measurements, in both the laboratory and rotating frame of reference, as well as mixing-time dependent spin-alignment echo NMR measurements were carried out. The results point to moderate Li diffusivities; however, in a lithium-ion cell this is compensated for by taking advantage of nm-structured materials with greatly reduced diffusion lengths. Importantly, although a phase transition from tetragonal symmetry to orthorhombic symmetry takes place at increased states of charge, the diffusion parameters and activation energies probed (0.4 to 0.5 eV) do depend weaker on Li content *x* than expected. Thus, despite the increased value of *x*, the evolution of the orthorhombic phase seems to support Li diffusivity rather than to affect the transport properties in a negative way. This interesting feature might be highly beneficial for the excellent cycling behavior observed recently.

Received 31st October 2013,
Accepted 18th November 2013

DOI: 10.1039/c3cp54586e

www.rsc.org/pccp

1 Introduction

The development of new electrode materials for lithium-ion batteries is a vital topic in materials science.^{1–6} Currently, materials with nm-sized dimensions,⁷ *i.e.*, those being characterized by large surface areas, are strongly considered to act as powerful anode and cathode materials significantly improving the performance of today's lithium ion batteries.^{1,8–13} Combined with an ordered 3D pore structure¹⁴ such materials ensure high storage capacities and facile Li insertion and removal. This is *inter alia* related to short diffusion lengths of the nm-sized materials¹ as well as to the involvement of Li surface storage⁸ (or even pseudo-capacitive faradaic processes^{15,16}) due to the large volume fraction of interfacial regions.

Quite recently, excellent cycling behavior of a lithium-ion battery was achieved when mesoporous TiO₂ with a 3D hierarchical pore structure served as an anode material.¹⁴ Even after extensive charging and discharging of the battery, the hierarchical

pore structure is preserved throughout clearly illustrating the high stability of the anode material.¹⁴ Initially, TiO₂ crystallizes with tetragonal symmetry. However, upon Li insertion the crystal structure transforms into an orthorhombic one,¹⁴ see also analogous studies where NMR has been used to monitor these changes.^{17–19} Besides kinetic effects also Li diffusion properties are anticipated to govern the insertion and removal rates. So far, only a few studies can be found in the literature being concerned with the atomic-scale measurement of Li self-diffusion parameters of TiO₂-based anode materials with different states of charges.^{17,20–23} The present study aims at the question if and to which extent Li *self-diffusion* changes as a function of Li content *x* in Li_xTiO₂. Since Li_xTiO₂ is a mixed conductor, that is, electrons *and* lithium ions contribute to the overall conductivity, those methods which are able to solely probe Li ion dynamics, such as NMR, represent favorable techniques for this purpose.^{17,20,22}

Therefore, we used complementary ⁷Li NMR techniques^{20,24,25} to study the Li⁺ self-diffusion parameters such as microscopic activation energies and jump rates. The techniques applied are sensitive to Li motional processes on quite different time scales.²⁶ In particular, while ⁷Li spin-alignment echo (SAE) NMR^{27–30} is useful to probe rather slow Li motions with correlation rates lower than 10⁴ Hz, ⁷Li NMR spin-lattice relaxation (SLR)

^a DFG Research Unit 1277 “Mobility of Lithium Ions in Solids” (TP 7), and Institute for Chemistry and Technology of Materials, Graz University of Technology Stremayrgasse 9, A-8010, Graz, Österreich. E-mail: bottke@tugraz.at

^b School of Chemistry, University of St Andrews The Purdie Building, North Haugh, St Andrews, Fife KY16 9ST, UK

measurements, in both the laboratory (SLR_L) and rotating frame of reference (SLR_P),^{26,31,32} are applicable to detect hopping processes with rates ranging from 10⁵ Hz to 10⁹ Hz. Interestingly, considering x and the reversible phase transformation mentioned above, the dynamic parameters deduced from NMR, if identified with bulk processes, turned out to be less influenced by the Li content than expected,³³ see also ref. 34. In contrast, the orthorhombic structure seems to facilitate Li migration which seems to be beneficial for the performance of the battery.

2 Experimental

Synthesis and characterization of mesoporous anatase are described elsewhere in detail, see ref. 14. Mesoporous anatase was prepared using the silica KIT-6 as a hard template¹⁴ and lithium intercalation was carried out electrochemically at a rate of 10 mA g⁻¹. Electrochemical cells were constructed by mixing the active material and Super S carbon (MMM) in the weight ratio of 8:1 and pressed into a pellet. After drying at 80 °C under vacuum for 8 hours, the electrodes were assembled into cells with a Li anode and an LP 30 electrolyte (Merck; 1 M LiPF₆ in 1:1 v/v ethylene carbonate/dimethyl carbonate).

The cells were constructed and handled in an Ar-filled MBraun glovebox. The cells were cycled at 10 mA g⁻¹ (C/33). The first discharge was used to prepare the three different samples with overall capacities of 30 mA h g⁻¹, 117 mA h g⁻¹, and 248 mA h g⁻¹ at certain cut-off potentials. This corresponds to Li_{x=0.09}TiO₂, Li_{0.35}TiO₂, and Li_{0.74}TiO₂ respectively (see Fig. 1). After that the electrodes were rinsed with a small amount of dry solvent (dimethyl carbonate) to remove the residual electrolyte. They were then left under dynamic vacuum overnight to ensure that all solvent had evaporated. Prior to the temperature-variable NMR measurements, the samples were fire-sealed in glass ampoules to protect them permanently from any traces of moisture.

⁷Li NMR data were recorded at temperatures ranging from 153 K to 453 K on MSL 100 and MSL 400 solid-state NMR spectrometers (Bruker). While the MSL 100 (Bruker) is connected to a Kalmus amplifier (400 W) and a field-variable Oxford cryo-magnet with 4.7 T, the MSL 400 (in standard configuration, Bruker) was used in combination with a shimmed Oxford cryo-magnet with

a nominal magnetic field of 9.4 T. The corresponding resonance frequencies $\omega_0/2\pi$ were 78 and 155 MHz, respectively. Mostly, commercial probes were used to record static NMR line shapes, SLR rates and SAE NMR decay rates as a function of temperature. Typically, 90° pulse lengths were in the order of 4 to 6 μ s. The temperature in the sample chamber was monitored using a Ni–CrNi thermocouple connected to an Oxford ITC. The accuracy of temperature adjustment was approximately ± 2 K. Temperatures below room temperature were reached by heating a stream of freshly evaporated nitrogen gas. Above room temperature heated air was used to achieve the desired temperatures.

NMR spectra, recorded at 155 MHz, were used to determine the line width (fwhm, full widths at half maximum) for the analysis of so-called motional narrowing curves. The corresponding free induction decays were recorded with the help of a single pulse sequence using a delay of $5 \times T_1$ between each scan to ensure full longitudinal relaxation; T_1 denotes the spin–lattice relaxation time. In the case of Li_{x=0.09}TiO₂ up to 64 scans were accumulated to compensate for the weak signal-to-noise ratio.

The classical saturation recovery pulse sequence³⁵ has served to determine ⁷Li SLR_L NMR rates. We used a comb of 10 closely spaced 90° pulses to destroy any longitudinal magnetization $M_z(t)$. The subsequent recovery of $M_z(t)$ was then recorded with a 90° detection pulse as a function of delay time and temperature. The transients follow non-exponential time behavior and have been parameterized with stretched exponentials.

Slower Li diffusion processes were measured *via* the spin-lock technique introduced by Ailion and Slichter:^{36–38} 90°–spin-lock pulse–acquisition (acq.) at angular locking frequencies $\omega_1/2\pi$ in the kHz range. Our locking pulses varied from $t_{\text{lock}} = 1 \mu\text{s}$ to $t_{\text{lock}} = 100 \text{ ms}$. As in the case of SLR_L the transients $M_p(t_{\text{lock}})$ of SLR_P NMR can only be described by stretched exponentials. Finally, mixing-time (t_m) dependent SAE NMR decay curves were recorded with the help of the Jeener–Broekaert^{39,40} three-pulse sequence: (90°)_x – t_p – (45°)_y – t_m – 45° – acq. We used a fixed preparation time t_p of 10 μ s to acquire two-time single-spin (sin–sin) correlation functions. The mixing time was varied from 100 μ s up to several seconds, *i.e.*, spanning a time window of many decades. A 32-fold phase cycle^{39,41} was employed to suppress unwanted coherences and to eliminate dipolar contributions to the echo showing up after the reading pulse. Fourier transformation of the spin-alignment echo, starting from the top of the signal, results in SAE NMR spectra useful to highlight quadrupole intensities due to the interaction of the quadrupole moment of ⁷Li (spin-3/2 nucleus) and non-vanishing electric field gradients (see below).

3 Results and discussion

Temperature-variable NMR line shape measurements give first insights into the microscopic jump processes of Li ions in solids.⁴² At low temperature (see Fig. 2), that is, at temperatures for which the mean Li jump rate is much lower than the spectral line width, both the shape and the width of an NMR line are determined by rigid dipolar interactions of the Li spins.

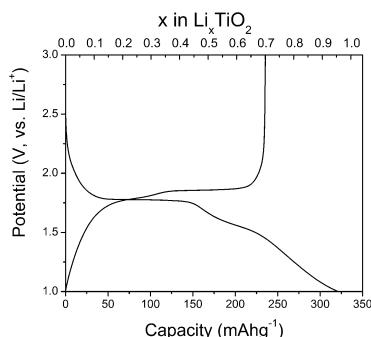


Fig. 1 First cycle load curve of mesoporous anatase at a rate of 10 mA g⁻¹.

PCCP

Paper

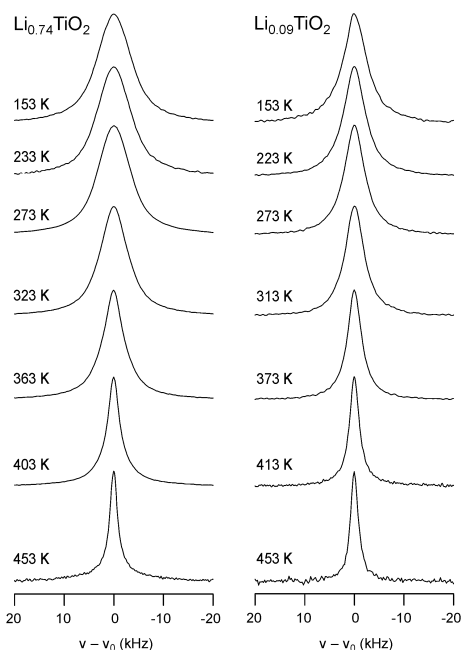


Fig. 2 Selected ${}^7\text{Li}$ NMR spectra of Li_xTiO_2 recorded at the temperatures indicated. Data were recorded at 155 MHz; $x = 0.74$ (fully orthorhombic) and $x = 0.09$ (crystallizing predominantly with the anatase structure). The lines were each centred to their individual resonance frequency ν_0 in order to better illustrate the shape and the widths of the selected lines.

With increasing T , however, homonuclear dipole–dipole interactions predominantly governing the line width are increasingly averaged due to Li translational motion on a sufficiently large length scale.⁴³ As a result, the NMR line undergoes a pronounced narrowing process. In many cases, the initial Gaussian shape of the NMR central line turns into a Lorentzian one determining the spectra in the regime of extreme narrowing. This is also observed for the sample with $x = 0.74$. The spectra shown in Fig. 2 were obtained by analyzing free induction decays. Thus, quadrupolar intensities are largely suppressed. These can be made visible by the use of spin-alignment echo NMR, for example. The technique is briefly described at the end of this section when SAE NMR decay curves are discussed. With SAE NMR, and with the solid echo technique as well, it is possible to overcome receiver dead-time effects and to increase the intensity of electric quadrupolar contributions to the overall NMR spectrum. A typical one is shown in Fig. 3 for $x = 0.74$, *i.e.*, the orthorhombic form. Besides the central transition, a broad quadrupole powder pattern is visible which can be approximated with a Gaussian line. The full width at half maximum is approximately 62 kHz. Assuming an axially oriented electric field gradient, this corresponds to a coupling constant of 124 kHz. For comparison, this value is smaller than that roughly calculated and probed for microcrystalline lithium titanate (160 kHz) by Wagemaker *et al.*¹⁷ For $x = 0.09$ a coupling

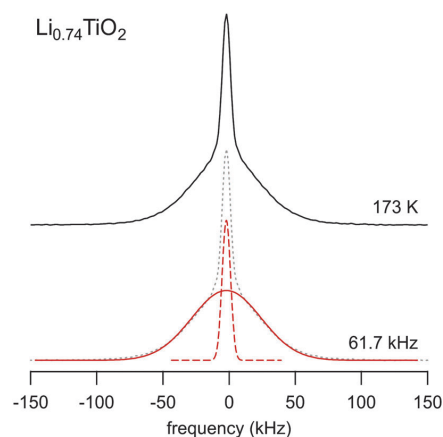


Fig. 3 ${}^7\text{Li}$ spin-alignment echo NMR spectrum recorded at 155 MHz (top). The spectrum can be deconvoluted into a broad Gaussian-shaped quadrupolar part with a full width of half maximum of ca. 62 kHz. The dashed line represents the central transition, see also Fig. 2.

constant of 140 kHz can be estimated in the rigid lattice regime of mesoporous Li_xTiO_2 .

Coming back to the NMR central lines shown in Fig. 2, it is worth mentioning that in the present case, no indications could be found which would significantly point to a so-called heterogeneous line narrowing, that is, the emergence of a pronounced two-component line shape with a broad and narrow contribution to the overall signal. Such a feature is thought to be diagnostic for a heterogeneous dynamics owing to two magnetically decoupled (and spatially separated) spin reservoirs of fast and slowly diffusing spins.^{44,45}

In Fig. 4 the ${}^7\text{Li}$ NMR line width, deduced from the central transition, is plotted *vs.* temperature for the three different samples studied. Starting with a rigid line width $\Delta\nu_{\text{rl}}$ of 5.8 kHz for the sample with $x = 0.09$, $\Delta\nu_{\text{rl}}$ increases to 6.7 kHz ($x = 0.35$) until, for the sample with $x = 0.74$, a significantly broadened line characterized by $\Delta\nu_{\text{rl}} = 7.9$ kHz is detected (see also Fig. 2). Generally, the rigid-lattice line width is directly proportional to the intensity of dipolar homonuclear Li–Li interactions; those scale with the mean interatomic Li–Li distance r which, for simple geometries, can be calculated *via* van Vleck's formula.⁴³ An estimation of large x values, taking into account Li–Li coupling only, leads to approximately 8 kHz.¹⁷ Note that this estimation disregards the coupling of Li spins with strictly paramagnetic Ti^{3+} centers expected to be generated during Li insertion.

The beginning of motional narrowing is expected when the mean correlation time, that is approximately the residence time between two successful Li jumps, reaches the order of the inverse rigid lattice line width $\Delta\nu_{\text{rl}}$. For example, at $x = 0.09$ line narrowing starts well below room temperature. The corresponding jump rate is then expected to range from 10^3 to 10^4 jumps per second. Most interestingly, although x has been increased from 0.09 to 0.74, that is, by a factor of eight, no drastic shift of the onset of motional narrowing towards higher temperatures is observed.

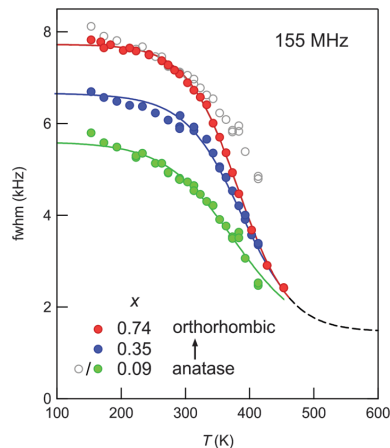


Fig. 4 ${}^7\text{Li}$ NMR line widths (fwhm: full width at half maximum) of Li_xTiO_2 as a function of temperature. Data were recorded at 155 MHz. x was varied from 0.09 to 0.74. Note that the data points of the sample with $x = 0.09$ are shown twice. For a better comparison with the data of sample $\text{Li}_{0.74}\text{TiO}_2$, the circles in grey were offset by 2.32 kHz.

At first glance, one would expect that the $\Delta\nu_{\text{H}}$ becomes larger and the more the lithium ions occupy sites within the TiO_2 matrix, the more the Li diffusion is slowed down. In the present case, however, something seems to (over-)compensate for the decrease expected. To our opinion, the reason should be looked for in the anatase-to-orthorhombic phase transition the TiO_2 anode material undergoes during Li uptake. Recently, this phase transition has been studied by *ex situ* X-ray powder diffraction and *in situ* Raman microscopy.¹⁴ It has also been reported by ${}^7\text{Li}$ magic angle spinning (MAS) NMR spectroscopy.^{17,18}

By analyzing ${}^7\text{Li}$ NMR spin–spin relaxation rates of a μm -sized powder sample showing a two-phase morphology Wagemaker *et al.* deduced that Li diffusivity in orthorhombic lithium titanate is enhanced compared to ion mobility in anatase. The NMR signal of Li in microcrystalline anatase ($\text{Li}_{0.12}\text{TiO}_2$) is reported to be 1.35 kHz in the rigid lattice while that of Li in lithium titanate is given by 11.8 kHz. Considering the shape of the rigid-lattice NMR spectrum of mesoporous $\text{Li}_{0.09}\text{TiO}_2$ shown in Fig. 2, which tends to be more peaked even at lower T compared to the situation in $\text{Li}_{0.74}\text{TiO}_2$, one might speculate that whether this sample is already a mixture of anatase and orthorhombic TiO_2 . While X-ray diffraction, which is being more sensitive to long-range order, does not reveal a distinct sign of a second phase in mesoporous Li_xTiO_2 until the composition of $x = 0.25$.¹⁴ Raman microscopy, instead, points to the formation of nuclei of the orthorhombic phase already at $x = 0.05$.¹⁴ However, as powder X-ray diffraction has shown,¹⁴ up to $x = 0.1$ Li intercalation into the tetragonal phase continues. Regarding the spectra shown in Fig. 2, in the case of nanostructured TiO_2 a deconvolution is hardly possible. Since Li ions are also expected to reside in the interfacial regions, the spectra may also be understood as a complex distribution of NMR intensities rather than a scenario of only two structurally distinct phases. Moreover, even for Li ions diffusing in a structurally well-defined single phase, a complex,

heterogeneous motional narrowing may be found. Therefore, the static (*ex situ*) NMR measurements presented here reflect the *overall* Li diffusivity in Li_xTiO_2 . Interestingly, even preliminary ${}^6\text{Li}$ MAS NMR measurements recorded at spinning frequencies of up to 30 kHz did not allow a reliable deconvolution of the NMR signals. Further high-resolution NMR measurements are currently underway in our lab.

To prove the above-mentioned assumption of an increase of ion diffusivity in Li-rich Li_xTiO_2 (with $x = 0.35$ and 0.74) against $\text{Li}_{x=0.09}\text{TiO}_2$ the application of diffusion-induced SLR NMR^{46–48} and SAE NMR^{25,28,30} as well is helpful to quantify Li dynamics in terms of decay rates and microscopic activation energies. As a preliminary point, it is important to note that ${}^7\text{Li}$ NMR relaxation transients, especially those recorded in the rotating frame of reference, may show a strongly non-exponential decay behavior even in those cases where a single spin reservoir is present. This is due to the spin-3/2 nature of ${}^7\text{Li}$ which is exposed to both dipolar and quadrupolar interactions. From the outset, this hinders a separation of the transients into, *e.g.*, two sub-transients. Additionally, in our case spin-relaxation phenomena taking place in the bulk may largely be different from those in the relatively large volume fraction of interfacial regions. Therefore, we analyzed the underlying magnetization transients in terms of stretched exponentials (as illustrated below) yielding a single relaxation rate which reflects the *overall* NMR spin relaxation.

In the lower part of Fig. 5 the temperature dependence of the ${}^7\text{Li}$ NMR SLR rates measured is illustrated. Below 300 K the rates are governed by non-diffusive background relaxation due

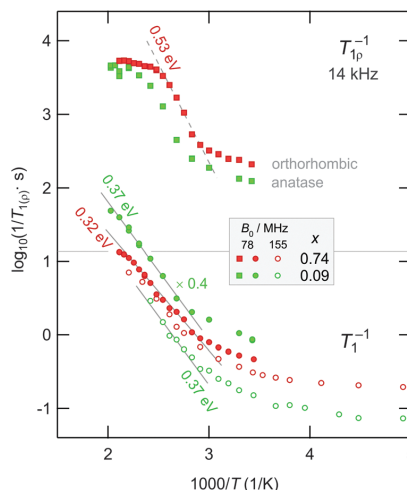


Fig. 5 Arrhenius plot of the ${}^7\text{Li}$ NMR SLR rates measured in the laboratory and rotating frame of reference. If not stated otherwise, data were recorded at 78 MHz. The rates $1/T_1$ and $1/T_{1p}$ are shown as a function of inverse temperature $1/T$. Note that, for a better comparison, the rates $1/T_1$ of $\text{Li}_{0.09}\text{TiO}_2$ are multiplied with a factor of 4. As in the case of $\text{Li}_{0.74}\text{TiO}_2$ the diffusion-induced rates on the low- T flank reveal a relatively weak frequency (sub-linear) dependence and show non-BPP behaviour for which $1/T_1 \propto \omega^{-2}$ is expected.⁴⁹

to coupling of the Li spins with the Ti^{3+} centers, lattice vibrations and/or other paramagnetic impurities. Expectedly, the absolute value of the background rates increases with increasing x pointing, *e.g.*, to a larger number of Ti^{3+} centers generated or to an increased coupling of Li spins with electrons in the conduction band, see the rates measured at a Larmor frequency of 155 MHz (Fig. 5). Sometimes these interactions can be extremely large hindering the detection of diffusion-induced contributions. In such cases other NMR techniques, as for instance mixing-time dependent SAE NMR (see below), can alternatively be used to study Li dynamics in solids.

Fortunately, above room temperature the $1/T_1$ NMR rates shown in Fig. 5 are increasingly influenced by diffusive Li^+ hopping. This is in contrast to the study reported by Wagemaker *et al.*, who did not observe a dependence of $1/T_1$ on temperature for μm -sized crystallites up to *ca.* 500 K.¹⁷ Here, the rates increase with temperature and follow the low- T flank of a diffusion-induced NMR relaxation rate peak. At even higher temperatures the rates are expected to pass through the maximum on a $\log(1/T_1)$ vs. $1/T$ plot. However, to prevent grain growth and to conserve the nanostructure of the materials, we restricted our measurements to 500 K. Therefore, the analysis of SLR NMR data is limited to the low-temperature limit characterized by $\omega_0\tau \gg 1$, which means that the mean correlation rate accessible is smaller than the Larmor frequency applied. In the case of $\text{Li}_{0.74}\text{TiO}_2$ the rates recorded at 78 MHz and at the highest temperature already indicate the appearance of a relatively broad $1/T_1$ peak. Note that at the rate maximum of such a peak the correlation time is expected to be in the order of the inverse Larmor frequency, *i.e.*, the relation $\omega_0\tau \approx 1$ holds. This corresponds to Li jump rates with values in the MHz range. In the present case this is expected to be fulfilled at *ca.* 500 K.

The solid lines in the lower part of Fig. 5 represent fits with an Arrhenius law. The fits include only those data points recorded well above 330 K. From the slope the activation energy for short-range Li hopping can be deduced. As in the case of line narrowing, very similar activation energies are found. Interestingly, for $x = 0.74$ the value of $E_a = 0.32(2)$ eV is somewhat smaller (0.37(2) eV) than that found for the sample with $x = 0.09$. This underpins the results from motional narrowing presented above. It is worth noting that correction procedures, taking into account the non-diffusive background rates, do not change those results much since the background rates turn out to be almost independent of temperature below $T = 220$ K (see also Fig. 5). Let us note that the activation energies probed here are much larger than those reported by Wagemaker *et al.* (0.2 eV and 0.09 eV)¹⁷ for Li diffusion in anatase and lithium titanate on the basis of spin-spin-relaxation NMR measurements.

In a more striking way the differences between the three samples probed here are illustrated by the rotating-frame SLR NMR rates of $\text{Li}_{0.09}\text{TiO}_2$ and $\text{Li}_{0.74}\text{TiO}_2$, which are exemplarily shown in the upper part of Fig. 5. The underlying magnetization transients M_p are shown in Fig. 6; their analysis with stretched exponentials (see above) leads to the rates plotted in Fig. 5. Starting with a weaker-than-activated background relaxation, the NMR relaxation rates of $\text{Li}_{0.74}\text{TiO}_2$ pass into

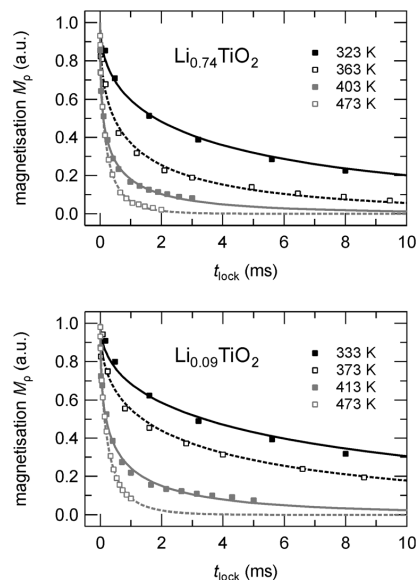


Fig. 6 ^7Li NMR magnetization transients $M_p(t_{\text{lock}})$ of $\text{Li}_{0.74}\text{TiO}_2$ and $\text{Li}_{0.09}\text{TiO}_2$ recorded at the temperatures indicated and at $\omega_0/2\pi = 78$ MHz and $\omega_1/2\pi = 14$ kHz. Dashed and solid lines represent fits according to stretched exponentials $M_p(t_{\text{lock}}) \propto \exp(-(t_{\text{lock}}/T_1)^\gamma)$ where the stretching exponent γ ranges from 0.45 at the lowest temperatures to 0.65 at the highest T .

the low- T flank at a slightly lower temperature than it is the case for the sample with $x = 0.09$. This also holds when the background rates were approximated with a power-law function, extrapolated to higher T and subtracted from the overall rates measured. At high temperatures the rates measured at a locking frequency of 14 kHz do not follow a simply shaped rate peak. Instead, they merge into a relatively broad plateau which is an indication of complex, non-BPP⁴⁹ lithium ion dynamics presumably additionally owing to the interplay with binders and carbon black present. Irrespective of that, the deviation of the SLR rates from the Arrhenius line drawn, which takes place at 420 K, points to correlation rates ranging from 10^5 to 10^6 jumps per second.

Lastly, the activation energy obtained from rotating-frame NMR data (*ca.* 0.53 eV (Fig. 4)), note that a similar value is found for the sample with $x = 0.09$ is clearly larger than that deduced from NMR measurements performed in the laboratory frame of reference. In contrast to SLR NMR in the lab frame, being sensitive to jump processes in the MHz range, data recorded with the spin-locking technique are able to probe ion motions on a longer length and time scale being defined by locking frequencies $\omega_1/2\pi$ in the kHz range. Additionally, the rather large activation energy probed is comparable with those usually found for long-range ion transport probed *via* dc conductivity. Thus, the SLR_p NMR rates on the low- T flank seem to be less influenced by correlation effects^{50–52} usually affecting SLR_l NMR rates in this limit characterized by $\omega_0\tau \gg 1$. Such effects may arise from repulsive Coulomb interactions and irregular formed energy landscapes the ions are subjected to, *i.e.*, structural disorder.⁵²

They are known to reduce the slope on the low- T flank of SLR NMR rate peaks.

Since the maxima of the SLR_p NMR rate peaks could not be resolved, we used Jeener–Broekaert⁴⁰ echoes to study spin-alignment echo (SAE) decay rates by recording single-spin motional correlation functions. Such measurements turned out to be useful to confirm the long-range nature of the activation energies probed *via* SLR_p NMR. Echo damping was recorded by using a three-pulse sequence; echo amplitudes were measured as a function of mixing time t_m but fixed preparation time of 10 μ s. The principle of SAE NMR is very similar to that of exchange NMR.^{25,30,53} The intensity of the echo generated after the first two pulses decreases if the jumping ions visit sites characterized by different electric field gradients (EFGs); other effects caused by (quadrupolar) spin–lattice relaxation or spin-diffusion may also contribute to the damping. A non-vanishing EFG is produced by the electric charge distribution in the direct neighborhood of the nucleus under investigation.⁴³ The interaction of the quadrupole moment of the nucleus with an EFG alters the Zeeman levels by a certain amount of energy which is determined by the quadrupole frequency ω_q . Thus, in the ideal case SAE NMR is directly sensitive to temporal changes of the site-specific quadrupole frequencies $\omega_{q,i}$ ($i = 1 \dots n$) the ions sense during hopping. Then, the decay curve represents a correlation function reflecting the probability to find an ion initially marked by $\omega_{q,1}$ at a site with the same $\omega_{q,1}$ at a later time.

In Fig. 7 typical two-time ⁷Li SAE NMR decay curves are shown for the samples with $x = 0.09$ and $x = 0.74$. Such curves are obtained when the intensity of the echo S_2 is plotted vs. t_m using a logarithmic abscissa. At very low temperatures the curves depend only weakly on temperature; presumably, in this T range echo damping is caused by spin-diffusion rather than by translational diffusion.⁵⁴ Stretched exponentials with a stretching factor γ ranging from 0.32 to 0.49 are best suited to describe the dependency on mixing time t_m in this non-diffusive temperature regime. In general, stretching factors

deviating from $\gamma = 1$ reveal a non-Debye motional process. For example, such deviations can arise from motions in confined dimensions⁵⁵ leading to a motional correlation function whose decay slows down with increasing time.

It is common to all samples that with increasing T the inflexion point of the echo decay curves shifts towards shorter t_m . Concomitantly, γ steadily decreases until values of, for example, 0.32 ($x = 0.09$) are reached. Moreover, at a sufficiently long mixing time the curves $S_2(t_p = \text{const.}, t_m)$ reach $S_{2,\infty} = 0$ which either indicates a rather large number of quadrupole frequencies involved or which points to the influence of dipolarly coupled spins, see ref. 41 for details of spin-alignment final state amplitudes $S_{2,\infty}$.

The decay rates $1/\tau_{\text{SAE}}$ of the fitting functions, which were used to describe the two-time correlation functions $S_2(t_p = \text{const.}, t_m)$, are exemplarily shown for $x = 0.35$ in Fig. 8 (grey squares). At temperatures below 200 K the rate $1/\tau_{\text{SAE}}$ amounts to about 10 s^{-1} and can be identified with $1/\tau_{\text{SAE,SD}}$ which is primarily influenced by spin diffusion (SD);^{20,54} the dashed line in Fig. 8 is to guide the eye. Above 250 K the SAE NMR rates increase due to translational Li hopping. To correct the rates $1/\tau_{\text{SAE}}$ for any non-diffusive background contribution, we calculated the difference $1/\tau'_{\text{SAE}} = 1/\tau_{\text{SAE}} - 1/\tau_{\text{SAE,SD}}$. The resulting rates $1/\tau'_{\text{SAE}}$ ($x = 0.35$) follow an Arrhenius law with an activation energy of $E_{a,\text{SAE}} = 0.44(2) \text{ eV}$ (see Fig. 8). The same procedure is applied to those data obtained for $x = 0.09$ and $x = 0.74$. Starting from $x = 0.09$, the activation energy decreases from 0.46 eV to 0.41 eV (see Fig. 8). This is consistent with the fact that the lowest rates were obtained for the sample with $x = 0.09$. Activation energies from SAE NMR are somewhat lower than those determined from SLR NMR in the rotating frame of reference, while the lowest values were found by SLR NMR performed in the laboratory frame of reference. These differences illustrate that there are different types of hopping motion that each experiment type is sensitive to. Usually, the low- T flank of SLR NMR in the lab frame is sensitive to short-range Li dynamics rather than to long-range ion motion. The latter seems to be better probed by rotating

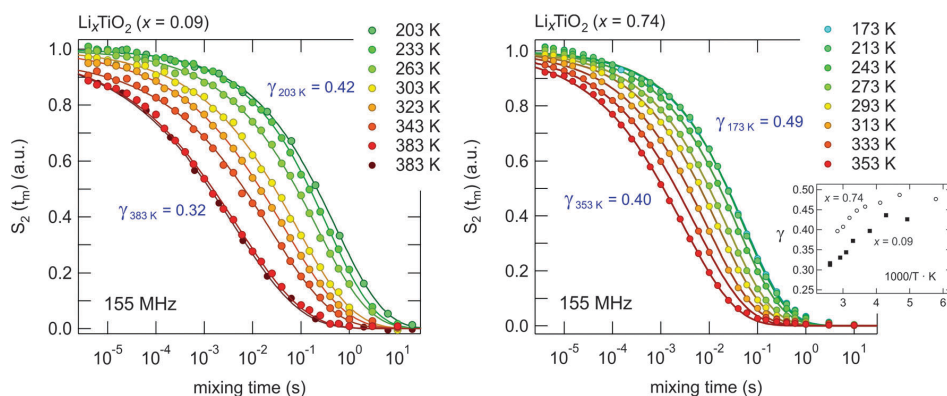


Fig. 7 ⁷Li SAE NMR decay curves of Li_xTiO_2 samples with $x = 0.09$ (left) and $x = 0.74$ (right). Decay curves follow stretched exponentials ($0.3 < \gamma < 0.5$) which are shown as solid lines. Data have been recorded at a Larmor frequency of 155 MHz. See the text for further details. The inset shows the T dependence of the stretching factors.

PCCP

Paper

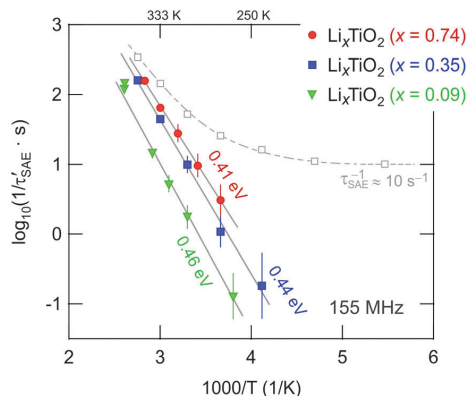


Fig. 8 Arrhenius plot of the ${}^7\text{Li}$ SAE NMR decay rates $1/\tau'_{\text{SAE}}$, which have been corrected for any non-diffusive background contributions to S_2 (see dotted line). Solid lines represent linear fits; the values given indicate the activation energies obtained for each sample.

frame methods carried out at much lower (effective) resonance frequencies (14 kHz, see above).

Although the differences in $1/\tau'_{\text{SAE}}$ (and $E_{\text{a,SAE}}$) found are small for the three samples investigated, they particularly underpin the trend obtained from SLR_p NMR. Thus, with the increase of x , which initiates the above mentioned phase transformation, Li diffusion is slightly increased rather than decreased. Besides other advantages of the mesoporous anode material this effect is highly desirable because it is expected to contribute to the excellent rate performance documented.¹⁴

4 Summary and outlook

The present study represents one of the very first examples that takes advantage of solid-state NMR to keep track of Li dynamics during charging a (mixed conducting) TiO_2 -based anode in a lithium-ion battery. The diffusion parameters extracted from the various NMR methods applied point to Li dynamics being almost independent of the amount of Li inserted into the transition metal oxide. In fact, Li bulk diffusivity, which might also be influenced by surface diffusivity, seems to increase rather than to decrease with increasing x in Li_xTiO_2 . This behavior might directly be related to the phase transformation which takes place during charging. The anode material, which initially crystallizes mainly with the anatase structure, gradually transforms into orthorhombic Li_xTiO_2 upon Li insertion.

In particular, results from SAE NMR, being sensitive to relatively slow but long-range, translational ion dynamics underline this behavior. The corresponding activation energies obtained from relaxation NMR in the rotating frame of reference and SAE NMR, respectively, range from 0.41 eV to 0.53 eV. Such relatively large values are expected for Li^+ ion transport proceeding on a longer length scale within the TiO_2 matrix. Besides NMR and a few other techniques, in the case of lithium such values are otherwise only obtainable by dc conductivity measurements.

However, when dealing with mixed conductors, impedance spectroscopy needs special setups and careful sample preparation to separate ionic from electronic contributions. NMR, however, is a contactless method with no requirement for special sample (post-)preparation.

Finally, both the stretching of the two-time SAE NMR correlation functions and the lower activation energy found by SLR NMR performed in the laboratory frame of reference point to a complex Li dynamics present. This manifests in activation energies which depend on the time scale the method applied is sensitive to. Further experiments, especially those using ${}^6\text{Li}$ (SAE) NMR techniques might be useful to shed light on the deviation from simple Debye behavior observed.

Further notes

The authors declare no competing financial interest.

Acknowledgements

Financial support from the Deutsche Forschungsgemeinschaft (DFG FOR 1277, project 7 “Li diffusion in nanostructured materials”) is highly appreciated. M.W. thanks the Leibniz University Hannover for further financial support (grant “Wege in die Forschung II”). P.G. Bruce is grateful to the EPSRC including SUPERGEN and the program grant “Nanoionics” for financial support.

References

- 1 P. G. Bruce, B. Scrosati and J.-M. Tarascon, *Angew. Chem., Int. Ed.*, 2008, **47**, 2930.
- 2 J. M. Tarascon and M. Armand, *Nature*, 2001, **414**, 359.
- 3 M. S. Whittingham, *Chem. Rev.*, 2004, **104**, 4271.
- 4 J. B. Goodenough and Y. Kim, *Chem. Mater.*, 2010, **22**, 587.
- 5 M. V. Reddy, G. V. Subba Rao and B. V. R. Chowdari, *Chem. Rev.*, 2013, **113**, 5364.
- 6 R. Marom, S. F. Amalraj, N. Leifer, D. Jacob and D. Aurbach, *J. Mater. Chem.*, 2011, **21**, 9938.
- 7 J. Maier, *Nat. Mater.*, 2005, **4**, 805.
- 8 M. Wagemaker and F. M. Mulder, *Acc. Chem. Res.*, 2012, **46**, 1206.
- 9 Y. Wang and G. Cao, *Adv. Mater.*, 2008, **20**, 2251.
- 10 D. Deng, M. G. Kim, J. Y. Lee and J. Cho, *Energy Environ. Sci.*, 2009, **2**, 818.
- 11 H.-K. Song, K. Lee, M. G. Kim, L. F. Nazar and J. Cho, *Adv. Funct. Mater.*, 2010, **20**, 3818.
- 12 A. Vu, Y. Qian and A. Stein, *Adv. Energy Mater.*, 2012, **2**, 1056.
- 13 Y. Ren, Z. Ma and P. G. Bruce, *Chem. Soc. Rev.*, 2012, **41**, 4909.
- 14 Y. Ren, L. J. Hardwick and P. G. Bruce, *Angew. Chem., Int. Ed.*, 2010, **49**, 2570.
- 15 M. Zukalová, M. Kalbáč, L. Kavan, I. Exnar and M. Graetzel, *Chem. Mater.*, 2005, **17**, 1248.
- 16 G. Sudan, E. Baudrin, D. Larcher and J.-M. Tarascon, *J. Mater. Chem.*, 2005, **15**, 1263.

- 17 M. Wagemaker, R. van de Krol, A. P. M. Kentgens, A. A. van Well and F. M. Mulder, *J. Am. Chem. Soc.*, 2001, **123**, 11454.
- 18 V. Luca, L. Hanley, N. K. Robers and R. F. Howe, *Chem. Mater.*, 1999, **11**, 2089.
- 19 M. Vijayakumar, S. Kerisi, C. Wang, Z. Nie, K. M. Rosso, Z. Yang, G. Graff, J. Liu and J. Hu, *J. Phys. Chem. C*, 2009, **113**, 14567.
- 20 M. Wilkening, C. Lyness, A. R. Armstrong and P. G. Bruce, *J. Phys. Chem. C*, 2009, **113**, 4741.
- 21 M. Wilkening, R. Amade, W. Iwaniak and P. Heitjans, *Phys. Chem. Chem. Phys.*, 2007, **9**, 1239.
- 22 M. Wagemaker, A. P. M. Kentgens and F. M. Mulder, *Nature*, 2002, **418**, 397.
- 23 M. Wagemaker, W. J. H. Borghols, E. R. H. van Eck, A. P. M. Kentgens, G. J. Kearley and F. M. Mulder, *Chem.-Eur. J.*, 2007, **13**, 2023.
- 24 M. Wilkening, W. Küchler and P. Heitjans, *Phys. Rev. Lett.*, 2006, **97**, 065901.
- 25 M. Wilkening and P. Heitjans, *ChemPhysChem*, 2012, **13**, 53.
- 26 M. Wilkening, A. Kuhn and P. Heitjans, *Phys. Rev. B: Condens. Matter Mater. Phys.*, 2008, **78**, 054303.
- 27 F. Qi, G. Hinze, R. Böhmer, H. Sillescu and H. Zimmermann, *Chem. Phys. Lett.*, 2000, **328**, 257.
- 28 R. Böhmer and F. Qi, *Solid State Nucl. Magn. Reson.*, 2007, **31**, 28.
- 29 M. Wilkening and P. Heitjans, *J. Phys.: Condens. Matter*, 2006, **18**, 9849.
- 30 R. Böhmer, K. Jeffrey and M. Vogel, *Prog. Nucl. Magn. Reson. Spectrosc.*, 2007, **50**, 87.
- 31 M. Wilkening, W. Iwaniak, J. Heine, V. Epp, A. Kleiner, M. Behrens, G. Nusspl, W. Bensch and P. Heitjans, *Phys. Chem. Chem. Phys.*, 2007, **9**, 6199.
- 32 V. Epp, S. Nakhil, M. Lerch and M. Wilkening, *J. Phys.: Condens. Matter*, 2013, **25**, 195402.
- 33 A. Van der Ven, J. Bhattacharya and A. A. Belak, *Acc. Chem. Res.*, 2013, **46**, 1216.
- 34 M. Wilkening, J. Heine, C. Lyness, A. Armstrong and P. Bruce, *Phys. Rev. B: Condens. Matter Mater. Phys.*, 2009, **80**, 064302.
- 35 E. Fukushima and S. B. W. Roeder, *Experimental Pulse NMR: A Nuts and Bolts Approach*, New Ed., Westview Press, Boulder, 1993.
- 36 D. Ailion and C. Slichter, *Phys. Rev. Lett.*, 1964, **12**, 168.
- 37 C. Slichter and D. Ailion, *Phys. Rev. A: At., Mol., Opt. Phys.*, 1964, **135**, 1099.
- 38 D. Ailion and C. Slichter, *Phys. Rev. A: At., Mol., Opt. Phys.*, 1965, **137**, 235.
- 39 R. Böhmer, *J. Magn. Reson.*, 2000, **147**, 78.
- 40 J. Jeener and P. Broekaert, *Phys. Rev.*, 1967, **157**, 232.
- 41 F. Qi, G. Diezemann, H. Böhm, J. Lamber and R. Böhmer, *J. Magn. Reson.*, 2004, **169**, 225.
- 42 M. Wilkening, V. Epp, A. Feldhoff and P. Heitjans, *J. Phys. Chem. C*, 2008, **112**, 9291.
- 43 A. Abragam, *The Principles of Nuclear Magnetism*, Clarendon, Oxford, 1961.
- 44 S. Indris and P. Heitjans, *J. Non-Cryst. Solids*, 2002, **307–310**, 555.
- 45 M. Wilkening, S. Indris and P. Heitjans, *Phys. Chem. Chem. Phys.*, 2003, **5**, 2225.
- 46 H. Buschmann, J. Dölle, S. Berendts, A. Kuhn, P. Bottke, M. Wilkening, P. Heitjans, A. Senyshyn, H. Ehrenberg, A. Lotnyk, V. Duppel, L. Kienle and J. Janek, *Phys. Chem. Chem. Phys.*, 2011, **13**, 19378.
- 47 A. Kuhn, M. Kunze, P. Sreeraj, H. D. Wiemhöfer, V. Thangadurai, M. Wilkening and P. Heitjans, *Solid State Nucl. Magn. Reson.*, 2012, **42**, 2.
- 48 A. Kuhn, P. Sreeraj, R. Pöttgen, H.-D. Wiemhöfer, M. Wilkening and P. Heitjans, *J. Am. Chem. Soc.*, 2011, **133**, 11018.
- 49 N. Bloembergen, E. M. Purcell and R. V. Pound, *Phys. Rev.*, 1948, **73**, 679.
- 50 K. Funke, *Prog. Solid State Chem.*, 1993, **22**, 111.
- 51 M. Meyer, P. Maass and A. Bunde, *Phys. Rev. Lett.*, 1993, **71**, 573.
- 52 A. Bunde, W. Dieterich, P. Maass and M. Meyer, in *Diffus. Condens. Matter – Methods, Mater. Model*, ed. P. Heitjans and J. Kärgel, Springer, Berlin, 2005, p. 813.
- 53 B. Koch and M. Vogel, *Solid State Nucl. Magn. Reson.*, 2008, **34**, 37.
- 54 C. Brinkmann, S. Faske, B. Koch and M. Vogel, *Z. Phys. Chem.*, 2010, **224**, 1535.
- 55 M. Wilkening and P. Heitjans, *Phys. Rev. B: Condens. Matter Mater. Phys.*, 2008, **77**, 24311.

3.2.2 TiO₂ Anatas Nanoröhren – Synthese, Zyklenstabilität als Anode und NMR-Messungen zur Dynamik

Die Synthese aus Abschnitt 2.3 lieferte hochkristalline Anatas-Nanoröhren (siehe Abb. 3.7). Die Proben für die NMR-Messungen sind sowohl chemisch mit *n*-BuLi/Hexan und elektrochemisch mit Li insertiert worden. Die Charakterisierung hinsichtlich Li-Einbau und Li-Ausbau erfolgte mit Hilfe der *coin-cell*-Technik (Abb. 3.8 c)), die in der AG Bruce etabliert ist. Die Präparation der Nanoröhren, die Li-Halbzellentechnik und z. B. Cyclovoltammetrie sowie weitere elektrochemische Charakterisierungsverfahren wurden während eines Forschungsaufenthalts in St. Andrews durchgeführt.

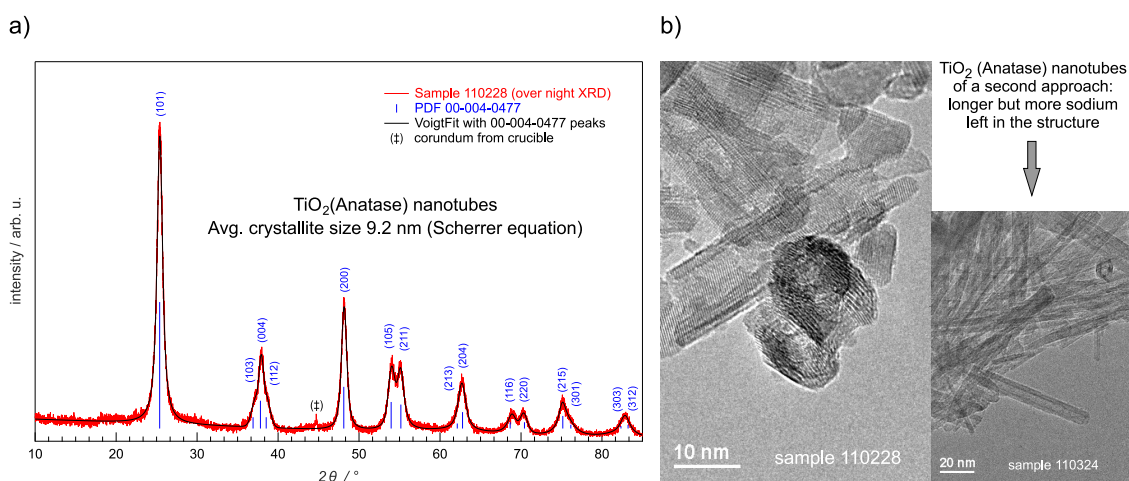


Abbildung 3.7: a) XRD der NMR-spektroskopisch untersuchten TiO₂-Nanoröhren 110228, die über Hydrothermalsynthese (Ausgangsmaterial Anatas-Partikel (99.8 %, Aldrich), 160 °C, 10 M Natronlauge, 72 Std. und Kalzinierung bei 380 °C (2 Std.)) in St. Andrews präpariert worden sind. b) HR-TEM-Aufnahmen der agglomerierten, hochkristallinen 4-wändigen Nanoröhren mit 40–50 nm Länge und ca. 10 nm Durchmesser (linkes Bild). Optimierte Reaktionsbedingungen (150 °C, 12 M Natronlauge, 72 Std. und Kalzinierung bei 380 °C (2 Std.)) führen zu längeren, perfekteren Nanoröhren (rechtes Bild). Das XRD (hier nicht gezeigt) offenbart aber trotz doppelter Aufreinigung einen deutlich höheren Natrium-Anteil im Produkt 110324.

Die Analyse der entsprechenden Röntgenprofile deutet auf Nanoröhren mit einem mittleren Durchmesser von knapp 10 nm hin. Hochoflösende TEM-Aufnahmen bestätigen diese Dimensionen und zeigen hochgeordnete, kristalline Wände. Im Einklang damit offenbaren ⁷Li-NMR-Spektren gut ausgebildete (typische) Quadrupolsatellitenintensitäten einer Pulverprobe.

Die komplexe Quadrupolstruktur (Abb. 3.8) der elektrochemisch interkalierten Probe E1 mit $x = 0.6$ zeigt an, dass die Li-Ionen verschiedenen elektrischen Feldgradienten in der TiO₂-Struktur ausgesetzt sind, die z. B. auch unterschiedliche (nm-große) Li_xTiO₂-Phasen widerspiegeln können (s. u.), welche mit XRD-Methoden nur schwer aufzulösen sind.

Die Leistungsfähigkeit der TiO_2 -Anoden, d. h. das Li-Ein- und Ausbauverhalten in die Kristallstruktur, ist in *coin*-Zellen mit Li-Metall als Gegenelektrode untersucht worden. Auch bei hohen Ladeströmen zeigen die Nanoröhren eine unerwartet* gute Zyklenstabilität bei relativ hoher Speicherkapazität. Ob die hervorragenden elektrochemischen Eigenschaften auf eine hohe Li-Selbstdiffusivität zurückzuführen ist, sollten u. a. die ^7Li -NMR-Messungen klären.

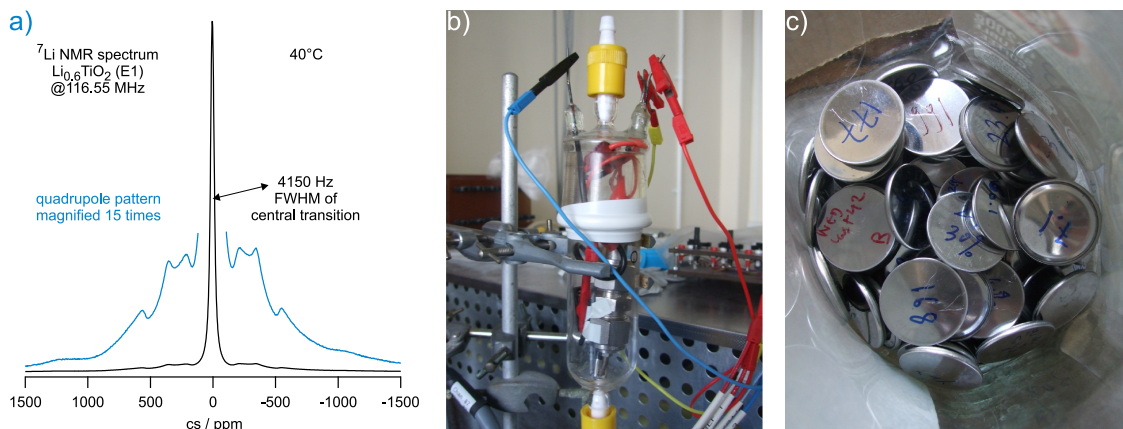


Abbildung 3.8: a) ^7Li -NMR-Spektrum der in Abb. 3.7 gezeigten mit Lithium elektrochemisch interkalierten TiO_2 -Nanoröhren. (116 MHz, ^7Li , *quadrupole-echo*-Pulsfolge); b) Typischer Versuchsaufbau zur elektrochemischen Li-Insertion der Nanoröhren. Swagelok-Zelle unter Argon als Schutzgas; c) *coin*-Zellen nach elektrochemischer Charakterisierung.

Temperaturabhängige ^7Li -NMR-Messungen der Spin-Gitter- und Spin-Spin-Relaxationsraten weisen auf eine unerwartet geringe Li-Diffusivität hin. Während die $1/T_1$ -Raten im bisher untersuchten T -Bereich unabhängig von der Temperatur sind, zeigen analoge NMR-Messungen, die mit einer weniger hohen Datendichte und *Scan*-Anzahl aufgezeichnet wurden, im rotierenden Koordinatensystem bei *locking*-Feldern zwischen 16 und 45 kHz scheinbar[†] eine deutliche T -Abhängigkeit. Lineare Regression führt auf unerwartet hohe Aktivierungsenergien von ca. 1 eV. Die zugehörigen Streckfaktoren γ , die erhalten werden, wenn die $M_\rho(t')$ -Transienten mit geeigneten Exponentialfunktionen $M_\rho(t') = A + B \exp(-(t'/T_{1\rho})^\gamma)$ angepasst werden, fallen äußerst klein aus und deuten auf einen Übergang vom Kohlrausch-Verhalten zu einem *quasi*-logarithmischen Zerfall von $M_\rho(t')$ hin. Ein solches Zeitverhalten kann im Sinne einer räumlich stark eingeschränkten Li-Beweglichkeit gedeutet werden und stünde in gutem Einklang mit den Dimensionen und der Wandstärke (3-4 Netzebenen) der untersuchten Nanoröhren (s. o.).

* Das Rohmaterial wurde nicht sehr lange getrocknet und auch die Herstellung des Elektroden slurries (70% TiO_2 -Nanoröhren (Aktivmaterial), 15% *cabon black* (Leitruß) und 15% Kynar Flex PPA 2801 (Binder) mit Aceton als Lösungsmittel und das Rakeln selbst erfolgte nicht auf dem Level, wie es zur Sicherung der Reproduzierbarkeit erforderlich ist. Es war ein erster Versuch.

† Mehr dazu am Ende dieses Abschnitts in einer kurzen Zusammenfassung.

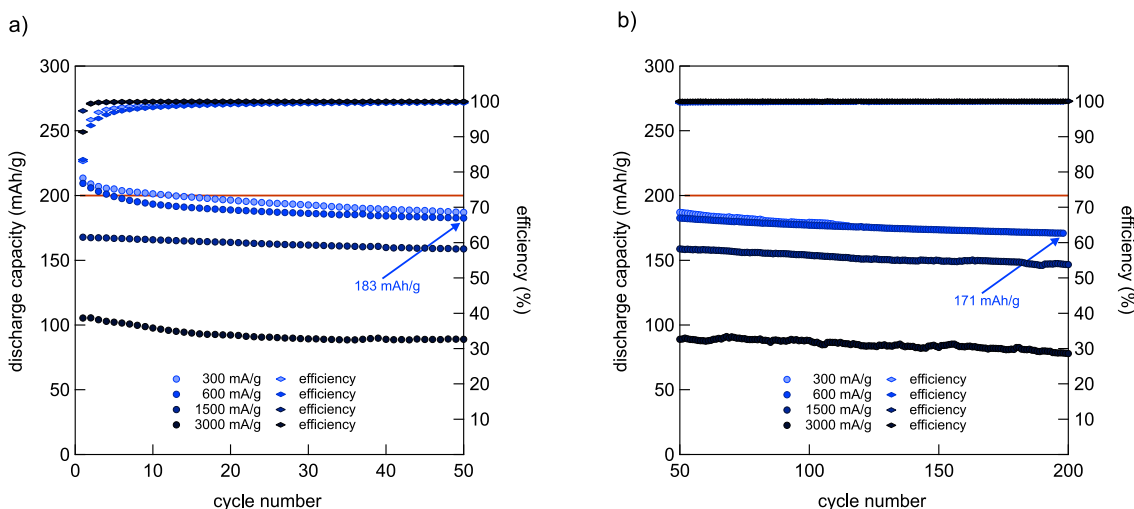


Abbildung 3.9: Konstantstromzyklisierung von Knopfzellen mit TiO_2 -Nanoröhren (110228) als Arbeitselektroden. a) die ersten 50 Zyklen aufgetragen gegen die Entladekapazität und die Effektivität von Lade- zu Entladestrom. b) Zyklen 50 bis 200. Die verwendeten Ladeströme (300 mA/g bis 3000 mA/g) entsprechen Laderaten von ca. 1,5 C bis 15 C. Die relativ späte Stabilisierung der Coulomb-Effizienz bei niedrigen Ladeströmen kann auf die Bauweise der *coin*-Zelle mit Li-Metall als Gegenelektrode zurückgeführt werden. Insgesamt zeigen alle Zellen eine Effizienz von 99,9 % und damit eine sehr gute Zyklenstabilität, bei relativ hoher Speicherkapazität.

Insbesondere die $1/T_{1\rho}$ -Transienten bei hohen Temperaturen und langen *locking*-Pulsen, die an einer leicht getemperten Probe (vorausgegangene NMR-Messungen) aufgezeichnet wurden, deuten jedoch auf ein zweistufiges Zeitverhalten hin. NMR-Messungen mit einer erhöhten Anzahldichte von *locking*-Zeiten und einer höheren Anzahl akkumulierter Transienten bestätigten diesen Verdacht (siehe Abb. 3.10 b)). Unerwarteterweise sind die zugehörigen Zeitkonstanten $1/T_{1\rho,\text{fast}}$ und $1/T_{1\rho,\text{fast}}$ kaum abhängig von T . Die Anfangsamplituden der beiden Transienten ändern sich mit der Temperatur. Es zeigen sich demnach zwei sehr langsame Spin-Reservoirs, die offenbar nicht miteinander durch schnellen Spin-Austausch koppeln. Interessanterweise berichtet die Gruppe um A. Kentgens (Delft) ^[54,55] über zwei strukturell unterschiedliche kristallographische Phasen (Anatas vs. orthorhombisches TiO_2), die sich während der Li-Insertion ausbilden sollen. Werden die oben gemachten Beobachtungen diesem Zwei-Phasen-Reaktionsverhalten zugeschrieben, verschieben sich die Phasenanteile offenbar (reversibel) mit der Temperatur. Nichtsdestotrotz ist die Li-Diffusivität innerhalb der kristallographisch unterschiedlichen Bereiche (oder Domänen) äußerst gering.

$2\text{D-}^6\text{Li-MAS-NMR-Messungen}$ an zweiphasigem Li_xTiO_2 aus der Gruppe Kentgens ^[55] zeigen einen sehr langsamen Austauschprozess, der offenbar mit NMR- $1/T_{1\rho}$ und $1/T_2$ -Messungen nicht zu erfassen ist. Es gibt hochauflösende $^6\text{Li-MAS-Austauschmessungen}$, ^[55]

um magnetisch nicht äquivalente Li-Ionen sichtbar zu machen und den Li-Austausch zwischen den möglichen Li-Spin-Reservoirs zu beschreiben. An diesen Proben sind solche Messungen bisher nicht möglich gewesen, da nur eine Linie aufgelöst werden kann.

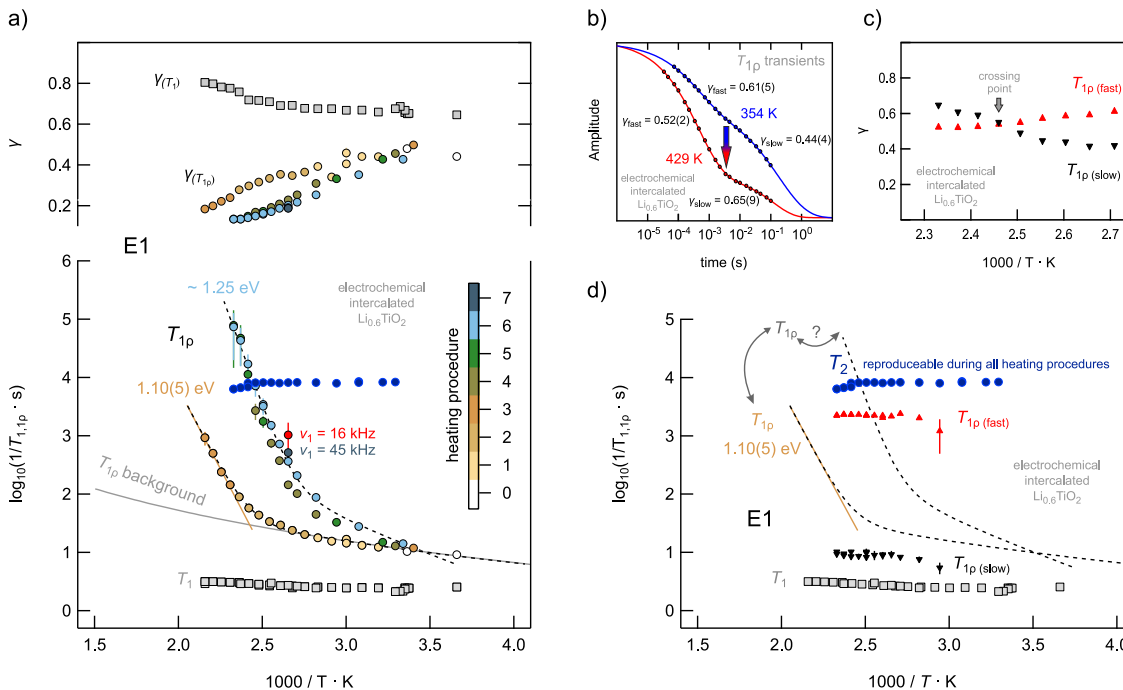


Abbildung 3.10: a) Arrhenius-Plot der $1/T_1$ - und $1/T_{1\rho}$ -Raten einer elektrochemisch interkalierten Li_xTiO_2 -Probe E1 mit ($x = 0.6$). Die Chronologie der NMR-Messungen ist farblich hervorgehoben (Durchläufe 0 bis 7 jeweils ohne zwischenzeitiges Abkühlen auf Raumtemperatur). Die (scheinbare) NMR-Flanke verschiebt sich mit zunehmendem Temperatureinfluss zu höheren $1/T$ -Werten. b) Werden die Transienten mit einer deutlich erhöhten Anzahl Scans aufgezeichnet, offenbart sich ein stufenweise Zerfall der transversalen Magnetisierung (kleines Bild, links oben). Die entsprechenden Transienten sind mit einer doppelt-exponentiellen Funktion angepasst worden, d. h. einer Summe aus zwei gestreckt exponentiellen Funktionen. Interessanterweise sind die erhaltenen NMR-Raten $T_{1\rho,fast}$ und $T_{1\rho,slow}$ dann unabhängig von der Temperatur. In b) sind beispielhaft zwei Transienten inklusive Fit (81 °C blau und 156 °C rot) und in c) die Streckfaktoren der einzelnen Komponenten (fast und slow) über diesen gesamten Temperaturbereich gezeigt. d) Die entsprechenden T_2 -Zeiten stehen mit diesem Verhalten im Einklang. Die $1/T_2$ -Raten sind ebenfalls unabhängig von $1/T$. Die NMR-Raten werden höchstwahrscheinlich durch starke, paramagnetische Li-Ti³⁺-Kopplungen dominiert. $1/T_{1\rho}$ - und $1/T_2$ -Raten deuten auf eine extrem langsame Li-Selbstdiffusivität hin.

1D-⁶Li-MAS-NMR-Messungen zeigen nur eine Linie bei einer MAS Frequenz von 30 kHz. Die Linienbreite (*fwhm*) von nur ca. 45 Hz lässt wenig Spielraum für eine zweite verdeckte Linie. Die auf diese Art untersuchten Proben wurden chemisch interkaliert und hatten einen Lithiumgehalt von $x = 0.1$; 0.3 und 0.6. An einer über mehrere Jahre in der *Glovebox*

gelagerten Probe $\text{Li}_{0.3}\text{TiO}_2$ wurden diese Messungen auch für verschiedene Kontaminationsgrade mit Sauerstoff durchgeführt. Gelegentlicher Lufteintritt in die *Glovebox* hatte die Probe mit der Zeit teilweise oxidiert und ihr einen Farbverlauf von blass-blau (an der Oberfläche) über hellblau (in der Mitte) bis zum ursprünglichen blau (am Boden des Schraubdeckelglases) gegeben. Die beschriebenen Schichten konnten leicht mit einem Spatel separiert werden. Alle $1\text{D-}^6\text{Li-MAS-NMR}$ -Messungen zeigen Linien der gleichen Form und Breite. Ein Alterungseffekt kann also ausgeschlossen werden. Für die elektrochemisch interkalierten Nanoröhren wurden derartige Spektren bisher nicht aufgenommen, an mesoporösem- TiO_2 wurde eine solche Messreihe jedoch mit dem gleichen Resultat wie oben durchgeführt. Es konnte nur eine schmale Linie aufgelöst werden.

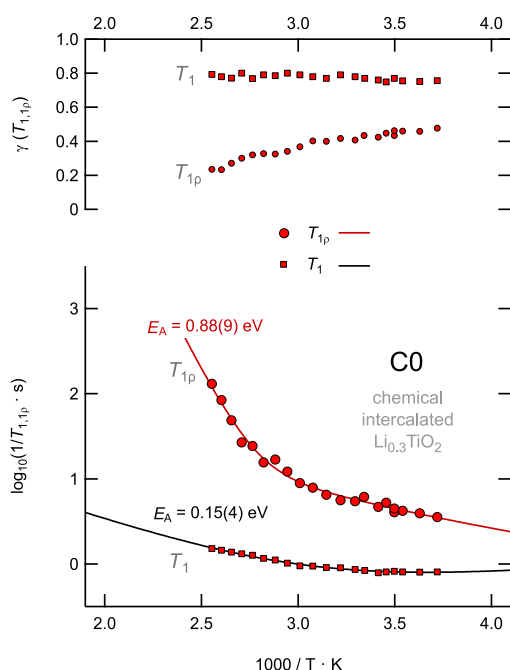


Abbildung 3.11: Arrheniusauftragung der $1/T_1$ - und $1/T_{1\rho}$ -Raten von Probe C0, d. h. chemisch mit Li interkalierte Li_xTiO_2 -Nanoröhren mit $x = 0.3$. Im oberen Teil sind auch die Streckfaktoren γ der Magnetisierungstransienten gezeigt. Die T -Abhängigkeit der Raten wurde mit einer Summe aus diffusionsinduziertem Anteil und Untergrundanteil angepasst. Das rechte Bild zeigt unterschiedlich interkalierte NMR-Proben von Li_xTiO_2 -Nanoröhren.

In Ergänzung zu den Messungen in Abb. 3.10 wurden TiO_2 -Nanoröhren derselben Herstellungsart auch chemisch mit Li interkaliert. Die Interkalation wurde in 20 mL trockenem Hexan (Sigma-Aldrich, ($\text{H}_2\text{O} \leq 0.01\%$), $\geq 99.0\%$) durch tropfenweise Zugabe von Butyllithium (Sigma-Aldrich, 1.6 M) und anschließendem Rühren (ca. 1.5 Stunden)

durchgeführt. Nach Abfiltrieren und Vortrocknen unter Argon-Schutzgas wurde die Probe in einem NMR-Röhrchen über Nacht unter Vakuum bei 100 °C getrocknet und anschließend abgeschmolzen. Die in Abb. 3.11 aufgetragenen ${}^7\text{Li}$ -NMR- $1/T_1$ - und $1/T_{1\rho}$ -Raten zeigen ein ähnliches Bild wie die Probe aus Abb. 3.10. Im Detail gibt es jedoch zwei wichtige Unterschiede. Die T_1 -Zeiten sind aufgrund des geringeren Li-Gehaltes nicht so stark durch $\text{Li}^+ \leftrightarrow \text{Ti}^{3+}$ -Wechselwirkungen beeinflusst, so dass sich bei höheren Temperaturen eine sehr schwach aktivierte Tieftemperaturflanke zeigt ($E_A = 0.15(4)$ eV). Aus $1/T_{1\rho}$ -Messungen, deren zugehörige Transienten sich ausschließlich mit einer gestreckten Exponentialfunktion anpassen lassen, kann eine Aktivierungsenergie von $E_A = 0.88(9)$ eV abgeleitet werden. Die bisher untersuchten chemisch interkalierten Li_xTiO_2 -Proben sind stark luftempfindlich. Dies mag ein Indiz dafür sein, dass im Falle dieser Proben, und im Gegensatz zu den elektrochemisch mit Li interkalierten Proben, Li vorwiegend auf der Oberfläche der Röhren lokalisiert ist und keine vollständige Insertion stattgefunden hat.

Anmerkungen: Die Temperaturen mussten teilweise durch eine Kalibrierung mit einem Referenzmaterial korrigiert werden, da der Hersteller ein falsches Thermoelement in einen Keramik-Probenkopf eingebaut hatte (Kalibrierung siehe 3.12). Messungen, die an einem anderen Probenkopf (Teflon) durch geführt wurden, lieferten die richtigen Temperaturen. Betroffen sind die Messungen an der Probe C0 (chemisch) und die $T_{1\rho}$ -Messungen an Probe E1 (elektrochemisch) ab Durchlauf 4 (zweite Flanke). Zuvor wurde mit dem Teflon-Probenkopf gemessen. Die Aktivierungsenergien sind dadurch jeweils gestiegen. Bei Probe E1 liegen die mehrfach gemessenen TT-Flanken deshalb nicht mehr alle „parallel“ zueinander, sondern liefern nach dem ersten Aufheizen bis 190 °C (Aktivierungsenergie 1.10(5) eV), nun einen Wert von ca. 1.25 eV. Dieses Verhalten ließ sich bei neuen Messungen auch Monate später reproduzieren. Abb. 3.12 d) veranschaulicht den Temperaturfehler, der um RT herum sehr klein war (bei ca. 30 °C kein Unterschied) und zu hohen sowie tiefen Temperaturen hin stetig größer wurde. Gezeigt sind die Temperaturen – 130 °C bis 300 °C in 10 °C Abständen. Die roten Striche stehen für die eingestellte Temperatur und die grünen Striche geben die wahre Temperatur an.

Die Auswertung der $T_{1\rho}$ -Transienten mit doppelt gestreckten Exponentialfunktionen liefert zwar „nur“ zwei scheinbar nicht diffusionsinduzierte Beiträge und ist nicht über den gesamten Temperaturbereich für beide Anteile möglich, wird aber durch neue Messungen an den selben Materialien bestätigt.

Neue Messungen: Die Probe E1 wurde zur Kontrolle nochmals vermessen und C1 wurde als chemisch interkalierte Probe mit wenig Lithium-Gehalt $x = 0.12$ gegenübergestellt (Abb. 3.12). Zur feineren Auswertung des Zweistufenzerfalls der $T_{1\rho}$ -Transienten wurden mehr Datenpunkte pro Temperatur aufgenommen und für das *locking* wurden kleinere Felder $B_1 = 20$ kHz verwendet.

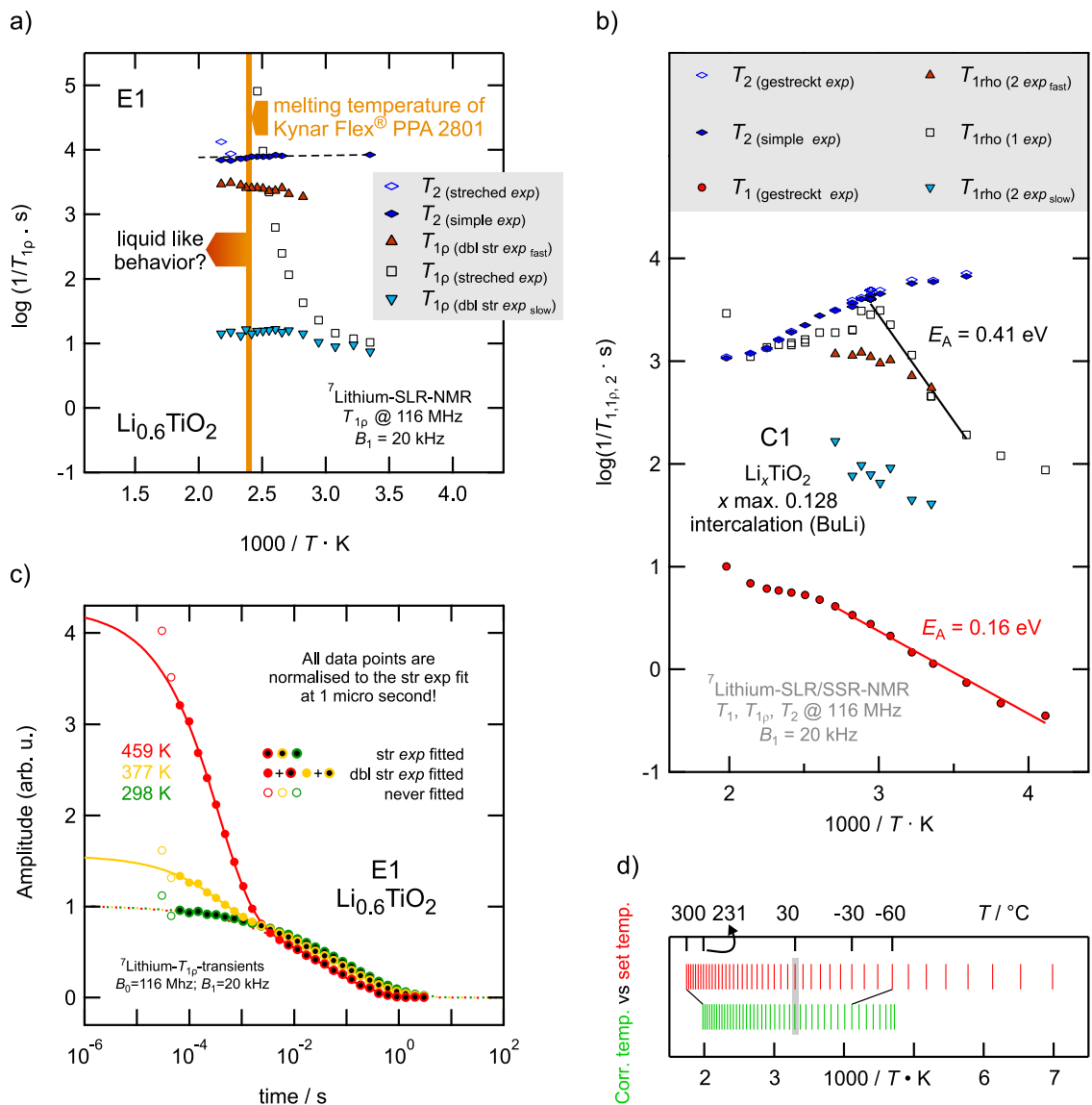


Abbildung 3.12: a) $T_{\max} = 459$ K; Probe E1 verhält sich noch immer gleich wie bei den Druckläufen 4 – 7. Scheinbar keine Materialveränderung mehr. Auswertung bei Temperaturen über 100 °C nur mit doppelt gestreckten Exponentialfunktionen möglich (siehe c). Die Werte des langsamen Prozesses deuten ein Ratenmaximum an. Der Schmelzpunkt des Binders (orangene Linie) hat wenig Einfluss. b) $T_{\max} = 504$ K; Probe C1 durchläuft ein Ratenmaximum ($1/T_{1\rho}$) bei einfach gestreckt exponentieller Anpassung der Transienten. E_A und Verlauf fragwürdig. c) Temperaturabhängigkeit des Ein- bzw. Zweistufenzerfalls der $T_{1\rho}$ -Transienten von E1. Die Daten wurden auf die erste Stufe normiert. d) Kalibrierung des Temperaturfehlers der durch den Einbau eines falschen Thermoelements auftrat. Die schwarzen Linien verbinden die Bereiche „eingestellte“ Temperatur (rot) und wahre Temperatur (grün). Details siehe Text.

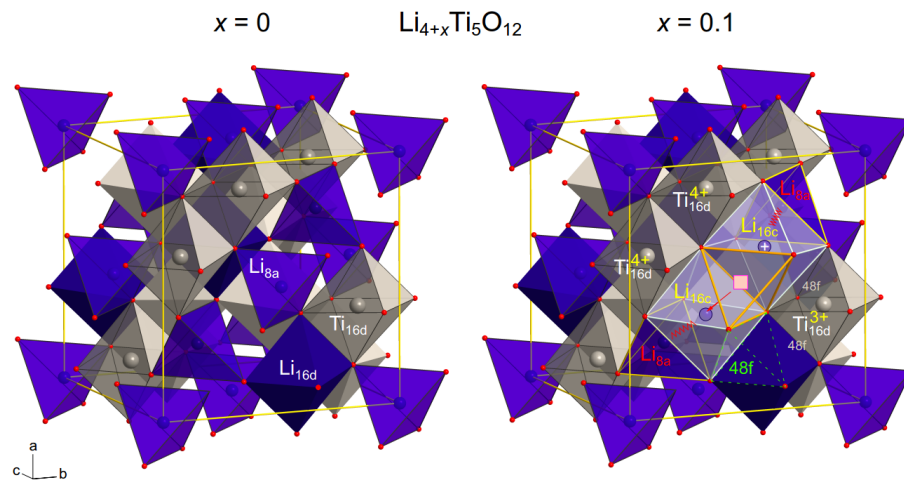
Zusammenfassung: Da der Temperaturfehler lange Zeit nicht bemerkt wurde sind noch keine Messungen bei höheren Temperaturen durchgeführt worden. Die hohen Aktivierungsenergien aus den $T_{1\rho}$ -Experimenten haben in ihren Absolutwerten wenig Aussagekraft. Die TT-Flanken einer einfach exponentiellen Auswertung der $T_{1\rho}$ -Transienten geben lediglich einen Hinweis auf die Veränderung des Materials durch die Temperierung. Die Auswertung zweier Anteile aus den Transienten ist nicht über den gesamten Temperaturbereich möglich. Sie bestätigt durch die Temperaturunabhängigkeit der Raten $1/T_{1\rho,fast}$ und $1/T_{1\rho,slow}$ jedoch die geringe Diffusivität im Material als solches und den beiden sichtbar gemachten Domänen.

$1/T_2$ -Raten, weitere *spin-lock*-Experimente bei höheren Temperaturen, sowie SAE-Messungen bei tiefen Temperaturen können hilfreich sein, um die Dynamik im Material besser zu verstehen. Es gibt aber jetzt schon einen deutlichen Trend. Je höher der Lithium-Gehalt in der Probe ist, desto stärker treten die zwei Anteile in den SGR-Messungen auf. Die Probe C1 (Li-Gehalt von $x = 0.1$) zeigt hier interessanterweise nicht nur die niedrigste Aktivierungsenergie, sondern auch ein „Ratenmaximum“, das die $1/T_2$ -Raten bis auf den Punkt bei der höchsten Temperatur nicht quert. Auch die Daten aus den T_1 -Messungen passen zu dem Verlauf der HT-Flanke von $1/T_2$.

Die Analyse der $T_{1\rho}$ -Transienten von Probe E1 deutet auf ein stetiges Anwachsen eines zweiten Prozesses oder die Auffüllung eines zweiten Spin-Reservoirs hin. Bei C0 (Li-Gehalt von $x = 0.3$) ist dieses Verhalten schon nicht mehr so ausgeprägt und nimmt bei C1 noch weiter ab. Dies kann eine Bestätigung für die Vermutung der Insertion von Lithium in das Kristallgitter durch die elektrochemische Lithiierung und die hauptsächlich „Anlagerung“ auf der Oberfläche durch die chemische Lithiierung sein.

Da die $\text{Li}_{0.6}\text{TiO}_2$ -Nanoröhren der Probe E1 in der $\text{TiO}_2(\text{B})$ -Modifikation vorliegen und die chemisch bis $x = 0.1$ bzw. $x = 0.3$ interkalierten Nanoröhren noch immer die Struktur von Anatas haben sollten, kann hier noch kein endgültiges Fazit gezogen werden.

P5 Small Change—Great Effect: Steep Increase of Li Ion Dynamics in $\text{Li}_4\text{Ti}_5\text{O}_{12}$ at the Early Stages of Chemical Li Insertion



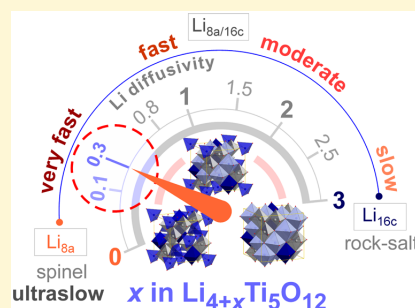
Small Change—Great Effect: Steep Increase of Li Ion Dynamics in $\text{Li}_4\text{Ti}_5\text{O}_{12}$ at the Early Stages of Chemical Li Insertion

Walter Schmidt,^{*,†,‡} Patrick Bottke,[†] Michael Stermad,^{†,‡} Peter Gollob,[§] Volker Hennige,[§] and Martin Wilkening^{*,†,‡}

[†]Institute for Chemistry and Technology of Materials, and [‡]Christian Doppler Laboratory for Lithium Batteries, Graz University of Technology (member of NAWI Graz), 8010 Graz, Austria

[§]AVL List GmbH, Hans-List-Platz 1, 8020 Graz, Austria

ABSTRACT: Lithium titanate (LTO) is one of the most promising anode materials for large-scale stationary electrochemical storage of energy produced from renewable sources. Besides many other aspects, such as negligible formation of passivation layers and no volume expansion during lithiation, the success of LTO is mainly based on its ability to easily accommodate and release Li ions in a fully reversible way. This feature is tightly connected with Li self-diffusion. As yet, little information is available about microscopic Li diffusion properties and elementary steps of Li hopping at low intercalation levels, i.e., at values of x being significantly smaller than 1. Here, we used ^7Li spin-locking NMR relaxometry to probe absolute hopping rates of LTO (homogeneous) solid solutions in quasi-thermodynamic equilibrium. As a result, the largest increase of Li diffusivity is observed when small amounts of Li are inserted. Strong Coulomb repulsions caused by the simultaneous occupation of neighboring 8a and 16c sites serve as an explanation for the enhanced Li diffusivity found. At even larger values of x , Li mobility slows down but is still much faster than in the host material with $x = 0$. Our results experimentally corroborate the outcome of recently published calculations on the DFT level focusing on both dynamic and structural aspects. The findings favor the formation of LTO solid solutions upon chemical lithiation; the steep increase in Li diffusivity found might also help with understanding the flat insertion potential observed.



1. INTRODUCTION

Li-bearing energy materials play a vital role in developing batteries that store electricity from renewable sources.^{1–3} Lithium titanate, $\text{Li}_{4+x}\text{Ti}_5\text{O}_{12}$ (LTO), is one of the most popular and abundant anode materials that offers facile and highly reversible Li insertion and deinsertion during charging and discharging lithium-ion batteries.^{6–10} It allows many charge–discharge cycles without losing significant performance; after thousands of cycles the retention is more than 90% of the original capacity making LTO a superior anode material for many applications.^{10–13}

LTO is well-known to be a so-called zero-strain material with negligible volume expansion and stress generated during lithiation up to $x = 3$. The insertion potential of approximately 1.55 V (vs Li metal) leads to both a lower overall battery voltage and, for many common electrolytes, to negligible solid electrolyte interphase (SEI) formation because the working potential is above that of electrolyte decomposition.^{7,11–13} Although its theoretical capacity is only 175 mAh/g, the titanate is, particularly in its mesoporous form as has been shown by Haetge et al.,⁹ a promising material for high rate thin-film applications as well as large-scale stationary energy storage for the grid. The latter is because of its nontoxicity as well as long-term cyclability, i.e., its inherent resistance to aging effects.^{10,13} For commercialization, of course, gas evolution^{16,17}

depending on the cathode materials used in a battery remains an issue that has to be carefully taken into account and brought under control in future studies, e.g., via carbon coating¹⁶ or the use of AlF_3 -modified LTO.¹⁸

Li insertion transforms the initially pure but poor¹⁵ ionic conductor LTO, showing ultraslow Li^+ exchange,¹⁹ into a mixed conducting oxide. During lithiation the originally colorless powder turns into a blue one; the darker the color, the larger the Li content x . In spinel-type LTO, crystallizing with the space group $Fd\bar{3}m$, the lithium ions occupy octahedral (16d) and tetrahedral (8a) sites according to the general formula (using Wyckoff notation) $[\text{Li}]_{8a}[\text{Li}_{1/3}\text{Ti}_{5/3}]_{16d}[\text{O}_4]_{32e}$ (see Figure 1). Wagemaker and co-workers have shown by thorough neutron diffraction measurements²⁰ that upon lithiation of LTO the Li^+ ions inserted occupy the initially empty (octahedral) 16c sites of the cubic structure. Simultaneously, the Li ions, originally residing on the 8a sites, are partly shifted to the 16c voids. Thus, during charging (discharging) an internal redistribution of the ionic charge carriers on the 16c and 8a sites takes place until at the composition of $x = 3$ rock-salt type $\text{Li}_7\text{Ti}_5\text{O}_{12}$

Received: December 12, 2014

Revised: February 3, 2015

Published: February 5, 2015

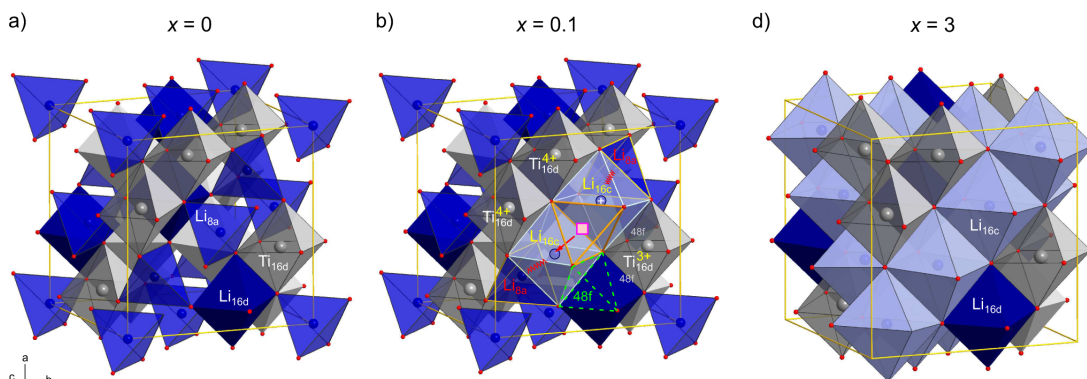


Figure 1. (a) Crystal structure of spinel-type $\text{Li}_4\text{Ti}_5\text{O}_{12}$ ($Fd\bar{3}m$); the Li ions occupy 16d and 8a positions; oxygen anions reside on 32e sites. (b) Inserting Li ions leads to a redistribution of the original Li ions nearby. The additional Li ions start to populate the 16c sites. In any case, Li–Li repulsions because of simultaneous occupation of neighbored (face-sharing) 16c and 8a polyhedra cannot be avoided at this insertion level even if some of the ions convert from 8a to 16c. This is because each 16c octahedron is connected to two 8a tetrahedra by face-sharing. At larger x levels the formation of nanometer-sized $\text{Li}_7\text{Ti}_3\text{O}_{12}$ domains may be energetically favored. During lithiation, titanium ions are partly reduced from Ti^{4+} to Ti^{3+} . (c) The crystal structure of $\text{Li}_7\text{Ti}_3\text{O}_{12}$ with all the 16c sites being fully occupied and the 8a sites being empty.

$([\text{Li}_2]_{16c}[\text{Li}_{1/3}\text{Ti}_{5/3}]_{16d}[\text{O}_4]_{32e})$ with empty 8a sites is formed via this topotactic reaction (see Figure 1). Rapid Li exchange between the 8a and 16c sites, sharing common faces, seems to be the relevant hopping mechanism in lithiated LTO.^{19,21} This might, to a certain degree, also include the involvement of Li ions on 16d sites and thus 48f sites acting as transition states. Oxygen vacancies (32e) are expected to affect the 8a–16c exchange further.^{22,23} More precisely, for nonlithiated LTO the pathway 8a–32e–32e–8a has also been discussed.^{22,24}

The flat insertion potential observed for LTO, when used as a negative electrode material in a lithium-ion battery, is frequently explained in terms of kinetically induced two-phase regions or domains being rich ($\text{Li}_7\text{Ti}_3\text{O}_{12}$) and poor ($\text{Li}_4\text{Ti}_5\text{O}_{12}$) in Li concentration. Recently, the coexistence of Li rich and Li poor regions in locally lithiated single crystals of LTO has been reported by Kitta et al.²⁵ For comparison, in electrochemistry, which deals with powder samples, the situation might be different. As has been demonstrated by Wagemaker et al. such domains are formed at high charging rates; with time, however, the two-phase structure relaxes toward a homogeneous distribution of Li ions, that is, a solid–solution-like structure.²⁰ This is what is expected to take place in a charged battery for longer periods of time when stored at room temperature or above. If, on the other hand, Li is inserted chemically, which is usually done by stirring a suspension of LTO in *n*-butyllithium (*n*-BuLi) over many days at ambient conditions, quasi solid solutions are expected to be formed in the first place rather than spatially extensive domains differing in Li content.²⁰ At room temperature the existence of nanometer-sized domains of Li rich and Li poor regions is assumed; these domains have recently been visualized via aberration-corrected scanning transmission electron microscopy (STEM).²⁶ Lu et al. have shown that nanodomains of $\text{Li}_7\text{Ti}_3\text{O}_{12}$ in a sample with about 0.15 mol of Li insertion per formula unit shows diameters of ca. 6–8 nm. Moreover, sharp phase boundaries have been detected.²⁶

Our investigation aims at understanding how Li diffusivity changes after very small amounts of Li have been inserted chemically into LTO that shows poor Li self-diffusivity.¹⁹ Since a mixed conductor is formed immediately after intercalation,

NMR was used in previous investigations to selectively study Li ion dynamics. The samples studied in the literature as yet are characterized by Li contents with x being larger or equal to 1. So far, little is known on how Li ion dynamics is influenced when x is kept well below $x = 0.5$. Such information is crucial if we are to overcome the limitations that face progress in electrochemical energy storage for both automotive and stationary applications.

Here, a series of samples has been prepared ($x = 0.1, 0.3, 1, 2, 3$) to unravel the change of Li diffusivity as a function of the degree of intercalation in thermodynamically stable solid solutions of LTO. NMR relaxometry, utilizing spin-lock fields in the kilohertz range,^{27–31} was employed to directly measure the elementary diffusion parameters such as migration barriers and absolute hopping rates of the lithium ions. Special emphasis is put on samples with $x = 0.1, 0.3$.

2. EXPERIMENTAL SECTION

Polycrystalline $\text{Li}_{4+x}\text{Ti}_5\text{O}_{12}$, which is available from SüdChemie AG (Germany), EXM 1037, was treated with appropriate amounts of *n*-butyllithium in hexane. Samples with the following stoichiometries, $x = 0.1, 0.3, 1, 2$ and $x = 3$, were prepared. The samples were rinsed with hexane and dried under vacuum at 333 K. The amount of Li inserted, i.e., the final Li content, was verified by inductively coupled plasma optical emission spectrometry (ICP-OES). It turned out that in each case the full amount of Li offered by the amount of *n*-butyllithium was inserted into LTO. *n*-Butyllithium reacts vigorously with LTO because it has a potential of 1 V vs Li. Note that all experiments were carried out in an Ar-filled glovebox ($\text{O}_2 < 1$ ppm, $\text{H}_2\text{O} < 1$ ppm, MBraun GmbH, Germany) to prevent any reaction with air or moisture. The final samples were fire-sealed in glass ampules under vacuum (2 cm in length and 4 mm in diameter).

NMR data were recorded using a Bruker 500 WB spectrometer operating at 11.7 T; this corresponds to a ^7Li Larmor frequency of 194.3 MHz. The 90° pulse lengths ranged from 3 to 5 μs in the temperature range from 223 to 448 K. Temperatures below room temperatures were reached with a flow of dry and cooled nitrogen gas; for temperatures above ambient, a stream of heated nitrogen gas was used.

To study Li ion dynamics, ^7Li NMR line shape studies and spin–lattice relaxation rate ($1/T_1$) measurements in both the laboratory frame and in the rotating frame ($1/T_{1\rho}$) were carried out.³² While the first were recorded with a single pulse sequence, the well-known

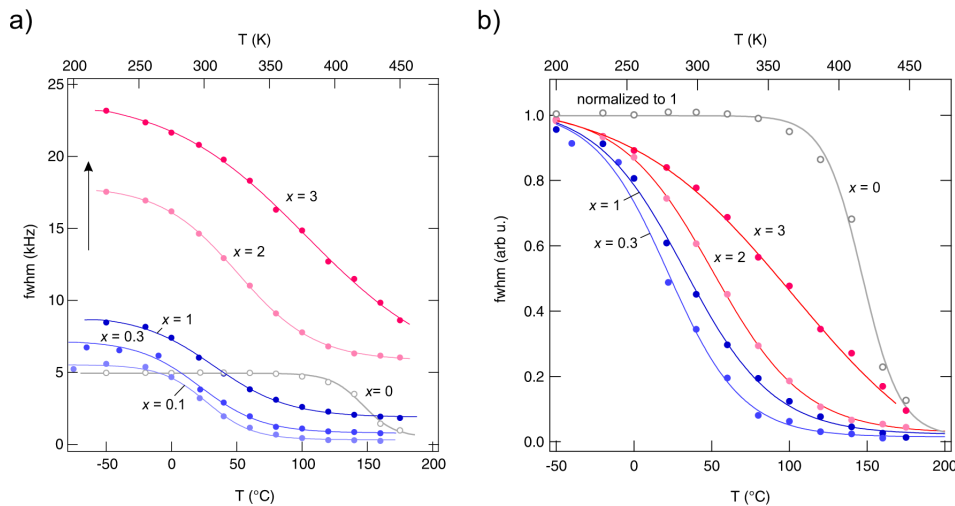


Figure 2. (a) Motional narrowing of the ${}^7\text{Li}$ NMR central lines of microcrystalline $\text{Li}_{4+x}\text{Ti}_5\text{O}_{12}$ with $x = 0, 0.1, 0.3, 1, 2, 3$. (b) Narrowing curves shown in (a) but scaled such that they are normalized to 1 at low temperatures. This scaling better illustrates the shape of the curves and locations of their inflection points. The lines are to guide the eye.

saturation recovery pulse sequence, $10 \times \pi/2 - t_d - \pi/2 - \text{acq.}$, was employed to record the rates $1/T_1$ as a function of temperature.³³ Here, the maximum value of t_d is chosen such that the transients well reached saturation of longitudinal magnetization ($t_d \approx 6T_1$); the curves obtained can be best approximated with single exponentials. For the $T_{1\rho}$ measurements we used the spin-lock technique, $\pi/2 p(t_{\text{lock}}) - \text{acq.}$, with a variable spin-lock pulse $p(t_{\text{lock}})$ as it was introduced by Ailion and Slichter.^{34–36} The spin-locking frequency was set to approximately 20 kHz; this value disregards additional contributions of local magnetic fields³⁰ of the samples. The transients recorded in the rotating frame were parametrized with stretched exponentials to extract the “transversal” relaxation rates.

In addition to temperature-variable, time-domain NMR data, being sensitive to ion dynamics on the Angström length scale, high-resolution ${}^6\text{Li}$ NMR lines were recorded under magic angle spinning (MAS) conditions with rotation frequencies of up to 30 kHz. For these measurements we employed a 2.5 mm MAS probe (Bruker); the spectra were recorded with ambient bearing gas pressure. If not stated otherwise, the corresponding ${}^7\text{Li}$ NMR spectra presented, which had been recorded under nonrotating conditions, were directly obtained by Fourier transformation of the free induction decays that were recorded with the saturation recovery sequence. Stimulated ${}^7\text{Li}$ NMR spectra,^{37–40} on the other hand, were acquired with the three-pulse Jeener–Broekaert⁴¹ pulse sequence, $\pi/2 - t_p - \pi/4 - t_m - \pi/4 - \text{acq.}$, optimized for spin-alignment echo (SAE) experiments on spin-3/2 nuclei such as ${}^7\text{Li}$;^{37,42} SAE NMR spectra were acquired with $t_p = 10 \mu\text{s}$ and $t_m = 100 \mu\text{s}$ to ensure negligible influence of Li diffusion on the shape of the lines.

3. RESULTS AND DISCUSSION

3.1. ${}^7\text{Li}$ NMR Line Shapes and Motional Narrowing.

The easiest way to collect first information on the extent of Li self-diffusivity in LTO having different amounts of Li inserted is to record ${}^7\text{Li}$ NMR line shapes as a function of temperature T . At low T the central line of a powder ${}^7\text{Li}$ (spin-3/2) NMR spectrum is dipolarly broadened due to the absence of any diffusive motions. Li hopping motion usually leads to an averaging of dipolar couplings.^{43–45} With increasing T , however, the Li jump rate $1/\tau$ increases and reaches the order of the rigid lattice line widths. As a consequence,

significant NMR motional line narrowing is observed (see Figure 2).^{43–45}

Starting our discussion with LTO ($x = 0$), diffusion-caused motional narrowing (MN) of the central line sets in at approximately $T_{\text{start}} = 350 \text{ K}$ (see Figure 2a). Temperatures T_{start} higher than room temperature roughly indicate very low Li diffusivity; this is particularly expected for crystal structures with the Li ions occupying tetrahedral sites connected by edge-sharing; LiAlO_2 may serve as an example here.⁴⁶ Below T_{start} the line width, i.e., the rigid-lattice line width of LTO, ν_0 ($x = 0$), is given by a full width at half-maximum (fwhm), ν_0 , of ca. 5 kHz; hence, below T_{start} the rate $1/\tau$ is estimated to be much smaller than 10^3 s^{-1} . This value illustrates the poor transport properties of nonlithiated LTO.²¹

With increasing Li content ν_0 increases from 5 to $\nu_0(0.1) = 5.5 \text{ kHz}$ and further to $\nu_0(0.3) = 7 \text{ kHz}$. As has been shown by several studies, the Li ions additionally inserted occupy the octahedrally coordinated 16c sites within the spinel structure; note that the 16c octahedra share common faces with the 8a tetrahedra; see above. The increase in ν_0 can be explained by two reasons: (i) the decreasing Li–Li distance (8a–16c) leads to an increase of dipolar interaction according to van Vleck and (ii) the generation of Ti^{3+} centers is related to paramagnetic interactions with the lithium spins. Recently, the electron energy-loss spectroscopy (EELS) analysis presented by Lu et al.²⁶ showed that the Ti ions adopt locally different valences (Ti^{4+} , Ti^{3+}) upon lithiation; the results point to strong $\text{Li}^+ - e^-$ associations; this picture of severe valence heterogeneities has also been verified by calculations using density functional theory (DFT). The latter interactions dominate the increase in ν_0 when going from $x = 0.3$ to $x = 1$ ($\nu_0 = 8.5 \text{ kHz}$) and further to $x = 2$ ($\nu_0 = 17.5 \text{ kHz}$), finally reaching ($\nu_0 = 23.5 \text{ kHz}$) at $x = 3$; see Figure 2a). For $x = 3$, and in terms of a simple structural picture, all of the 16c sites of rock-salt $\text{Li}_7\text{Ti}_5\text{O}_{12}$ are filled with Li ions and the formerly occupied 8a sites are empty. The increase in ν_0 does also hold for the increase in $\nu(T \rightarrow \infty)$, that is, the line width in the regime of extreme narrowing.

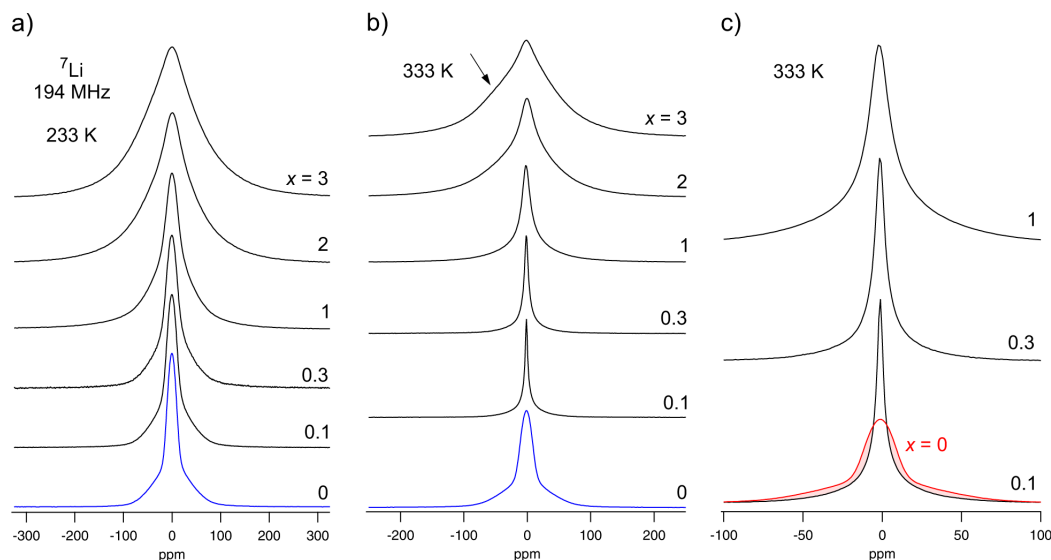


Figure 3. (a–c) ${}^7\text{Li}$ NMR spectra of $\text{Li}_{4+x}\text{Ti}_5\text{O}_{12}$ recorded at the temperatures and Li contents x indicated. In (c) a magnification of some of the spectra shown in (b) are shown. The small arrow in the spectrum of $\text{Li}_7\text{Ti}_5\text{O}_{12}$ recorded at 333 K indicates the NMR line that can be attributed to Li ions residing on 16c sites in the neighborhood of the Ti^{3+} centers. This component is clearly visible as a very broad but separated line in ${}^6\text{Li}$ MAS NMR centered at -9 ppm when referenced to $\text{LiCl}(\text{aq})$. See text for further explanation.

In Figure 2b, for a better comparison of onset temperatures and MN curve shapes, the line widths are scaled such that they range from 0 to 1, i.e., ν/ν_0 is plotted vs T . Increasing x from 0 to 0.1 (or 0.3), the onset temperature is drastically reduced to only 200 K, which is by approximately 150 K lower when compared to the sample with $x = 0$; see above ($T_{\text{start}}(x = 0) = 350$ K). This indicates a steep increase in Li diffusivity at the early stages of Li intercalation. Most likely, it can be traced back to increased 8a–16c Coulomb interactions as is illustrated in Figure 1. Spin–lattice relaxation NMR—see below—will allow a quantitative determination of the increase in diffusivity observed.

In addition to the shift of the MN curves found, we also observed that the larger the x the more stretched the curves become. This means, instead of a “homogeneous” diffusion process in the case of $x = 0$, complex Li dynamics is sensed—even for the sample with $x = 3$. Hence, one should expect multiple Li diffusion pathways and a distribution of energy barriers present in samples with $x > 0$. The stepwise activation of these pathways with increasing T leads to line narrowing that finally proceeds over a temperature range of almost $\Delta T \approx 200$ K. These assumptions should also be reflected by the NMR line shapes themselves from which the line widths were deduced; they are shown in Figure 3. The spectra shown in (a) have been recorded at 223 K, thus in the same dynamic state, viz., the rigid lattice regime. It can be clearly seen that the spectrum of LTO ($x = 0$) is composed of a central line (from both the ions on 8a and 16d sites) and a so-called quadrupole powder pattern. This pattern stems from the interaction of the quadrupole moment of the ${}^7\text{Li}$ spins (spin quantum number 3/2) with a nonvanishing electric field gradient (EFG) at the Li sites.^{37,40,43} The EFG is produced by the asymmetric electronic charge distribution in the direct neighborhood of the nucleus.

For comparison with this interpretation, Wagemaker et al. mentioned that the two contributions visible represent the

central lines of the two crystallographically inequivalent Li sites.⁴⁹ According to our static ${}^7\text{Li}$ NMR measurements, which particularly included (stimulated, here, spin-alignment) echo techniques, we tend to interpret the broad contribution as follows. It is likely that it represents the quadrupole intensities of the Li ions on 8a and 16d rather than a central line because the intensity can easily be influenced by (refocusing) echo techniques optimized for spin-3/2 nuclei (see Figure 4). Additionally, the quadrupole signals undergo motional averaging and lose intensity with increasing T (see Figure 5); this observation, which is shown exemplarily for the sample with $x = 0.3$ in Figure 5, underlines once more its origin from electric interactions. In particular, the effect of motional averaging is seen in NMR stimulated echo spectroscopy.

The “overall ${}^7\text{Li}$ central line”, on the other hand, cannot be separated into the two signals of Li ions on 8a and 16d sites. This is in contrast to ${}^6\text{Li}$ (MAS) NMR; compared to ${}^7\text{Li}$, for the ${}^6\text{Li}$ nucleus second order quadrupole interactions are much smaller enabling high-resolution NMR. Hence, ${}^6\text{Li}$ MAS NMR lines definitely reveal the magnetically inequivalent Li sites showing up as two partly overlapping lines with distinct chemical shifts of 0.08 ppm and -0.26 ppm. These values are in perfect agreement with previous results reported by Irvine and co-workers.⁵⁰ Moreover, the areas under the two ${}^6\text{Li}$ NMR lines nicely agree with those expected from the crystal structure (see Figure 4b).

As mentioned above, with increasing x the spectra of $\text{Li}_{4+x}\text{Ti}_5\text{O}_{12}$ broaden due to the formation of paramagnetic Ti^{3+} centers; finally, at $x = 3$ the paramagnetic interactions dominate the spectrum and the quadrupole intensities can hardly be distinguished from the central line(s) (cf. Figure 3). Paramagnetic broadening and the increase in dipolar interactions are in competition with averaging of dipole–dipole couplings due to diffusive motions. Despite these three effects working in opposite direction, the drastic decrease in line width (see Figure

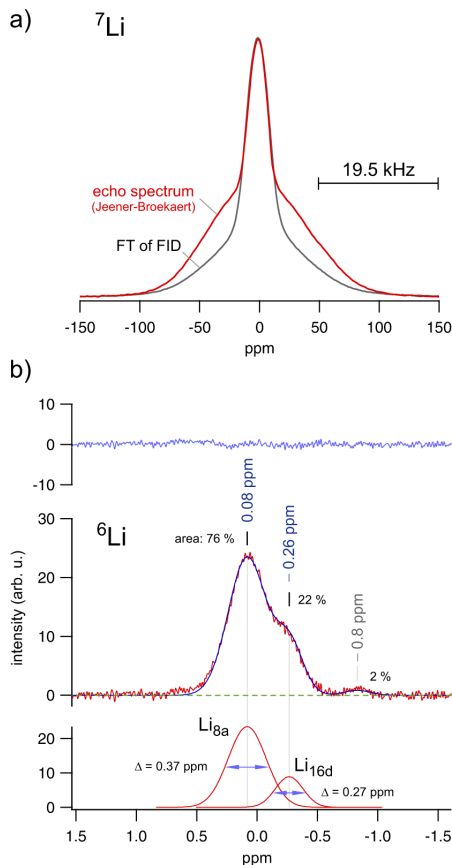


Figure 4. (a) ${}^7\text{Li}$ NMR spectrum of $\text{Li}_4\text{Ti}_5\text{O}_{12}$ obtained after Fourier transformation (FT) of an FID obtained via a single pulse experiment as well as obtained via FT of an Jeener-Broekaert echo with optimized phase cycling for spin-3/2 nuclei to enhance the intensity of quadrupole intensities. (b) ${}^6\text{Li}$ MAS NMR spectrum of $\text{Li}_4\text{Ti}_5\text{O}_{12}$ revealing the two magnetically different Li sites 8a and 16d; the whole spectrum, which is referenced to aqueous LiCl, can be deconvoluted with Gaussians that nicely reflect the population ratio expected for the two Li sites. The line at -0.8 ppm might be attributed to an (X-ray amorphous) impurity phase⁴⁷ such as Li_2TiO_3 , or to a small fraction of Li ions residing already on the 16c sites. Traces of Li_2CO_3 , which can build a thin film on the surface of the LTO particles, are hardly seen by NMR.⁴⁸ Δ denotes the MAS line width in ppm.

3b) that displays spectra recorded at 333 K) observed for $x = 0.1$ (and $x = 0.3$) can unequivocally be ascribed to a steep increase in Li ion dynamics setting in immediately after Li insertion. For the sake of completeness, in Figure 3c the shape of the ${}^7\text{Li}$ NMR spectrum LTO $x = 0$ is directly compared with those of the samples characterized by $x = 0.1$ and $x = 0.3$. Compared to the situation at $x = 0$, line narrowing of the central line and motional averaging of quadrupole intensities, as discussed above, can be observed for $x = 0.1$ and $x = 0.3$ (cf. also Figure 5). The averaging of EFGs can especially be recognized for the sample with $x = 0.1$; as is demonstrated via SLR NMR measurements presented below, at 333 K the mean Li jump rate (in Hz) becomes indeed comparable with the

quadrupole splitting (ca. 20 kHz) causing the motional averaging of the corresponding quadrupolar powder pattern.

Before we discuss our SLR NMR measurements (see Figure 6) giving precise quantitative insights into the ion dynamics of Li-inserted LTO, we should have a look on the NMR spectrum of the sample with $x = 2$ recorded at 333 K; see Figure 3b. It represents the spectrum at the inflection point of the corresponding MN curve (see Figure 2). The line shape cannot be approximated with a single line; rather, it reflects a superposition of a motionally narrowed signal superimposed on a dipolarly broadened line. The width of the broad line is due to homonuclear Li–Li couplings that have not been averaged by Li exchange processes at the temperature given. The line is additionally broadened by $\text{Li}^+ - \text{Ti}^{3+}$ interactions. The emergence of a narrowed line on top of the NMR signal points to a stepwise MN, which is in many cases a signature of heterogeneous Li ion dynamics. For $\text{Li}_{4+x}\text{Ti}_5\text{O}_{12}$, this has already been observed by Wagemaker et al. in their ${}^7\text{Li}$ NMR spin–spin relaxation ($1/T_2$) study.⁴⁹ Such a two-component feature, however, should not necessarily result in pronounced two-component SLR NMR transients if sufficiently fast ${}^7\text{Li} - {}^7\text{Li}$ spin-diffusion mediated through flip-flop processes is present. Spin-diffusion has been indicated by Hain et al.⁵¹ Indeed, our $T_{1\rho}$ transients, and particularly those of the T_1 measurements, can be best fitted with single or slightly stretched exponentials rather than by a sum of two (single) exponential functions.

As a last remark, a slight asymmetry of the static line shapes of the samples with $x = 2$ and $x = 3$ recorded at 333 K can be seen; this is indicated by the small arrow drawn in Figure 3b. The shoulder showing up at negative ppm values reflects those Li ions residing on 16c sites nearby the Ti^{3+} centers. This component can be clearly resolved via ${}^6\text{Li}$ (as well as ${}^7\text{Li}$) magic angle spinning NMR; it appears as a broad signal at NMR shifts ranging from -9 to -10 ppm when aqueous LiCl is used as a secondary reference; here, the primary reference was lithium acetate. Such a relatively large NMR shift can be understood as a direct consequence of the strong and localized $\text{Li}^+ - \text{e}^-$ associations described by Lu et al.²⁶

3.2. ${}^7\text{Li}$ NMR Spin–Lattice Relaxation Rates. In Figure 6 the ${}^7\text{Li}$ NMR SLR rates recorded in the laboratory (a) and rotating frame (b) of reference are plotted vs the inverse temperature. The rates of the host material $\text{Li}_4\text{Ti}_5\text{O}_{12}$, when measured at a ${}^7\text{Li}$ Larmor frequency of 194.3 MHz, follow classical temperature behavior. Below 300 K a nondiffusive, weaker-than-activated regime shows up. The corresponding rate $1/T_{1,\text{bgr}}$ shows a $T^{1+\beta}$ behavior with $\beta = 1.31(1)$; constant loss behavior, which refers to a frequency independent imaginary part of the complex permittivity $\hat{\epsilon}$, would lead to $\beta = 1$.⁵² Thus, besides strictly localized Li motions, lattice vibrations and coupling to paramagnetic impurities may give rise to a β larger than 1. Nevertheless, in this low- T region successful translational jump processes are rare.

This behavior changes when the rates above 300 K are considered. They increase with temperature and follow the flank of a diffusion-induced rate peak. The associated activation energy of only 0.35 eV is linked with local motions of the Li spins including, for example, forward–backward jumps between 8a and vacant 16c sites. Note that the slope is also affected by correlation effects due to, e.g., electric Coulomb interactions. Hence, it does not reflect long-range ion transport that would be probed via conductivity spectroscopy in the frequency limit $\omega \rightarrow 0$.

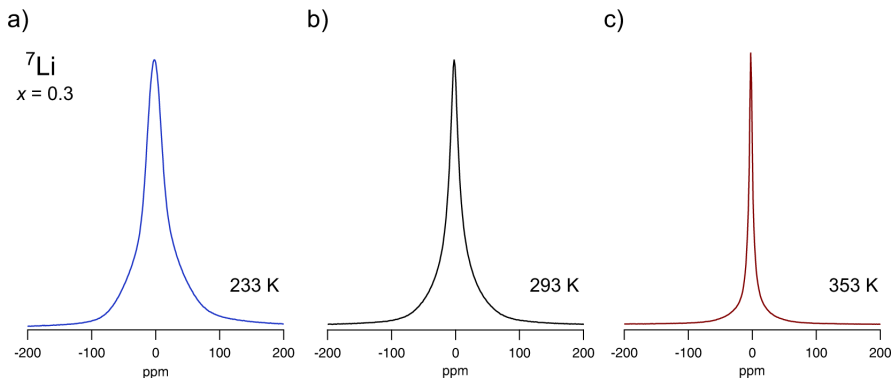


Figure 5. (a–c) ${}^7\text{Li}$ NMR spectra of $\text{Li}_{4+x}\text{Ti}_5\text{O}_{12}$ with $x = 0.3$ recorded at the temperatures indicated. With increasing T significant line narrowing sets in indicating rapid Li exchange at low Li contents. Noteworthy, the spectra have been recorded at extraordinary long recycle delays, $t_d = 100\text{ s}$ ($\gg 5T_1$), to reveal any slowly relaxing components. Since they coincide with those recorded at $t_d = 2\text{ s}$ ($\approx 5T_1$) shown in Figure 3, such components are evidently absent; see the discussion in section 3.2.3. Quadrupole intensities showing up at 233 K as a broad *foot* of the spectrum seem to be averaged due to rapid Li exchange at elevated temperatures; see section 3.2 for the quantification of the absolute Li jump rate via spin-lock NMR relaxometry.

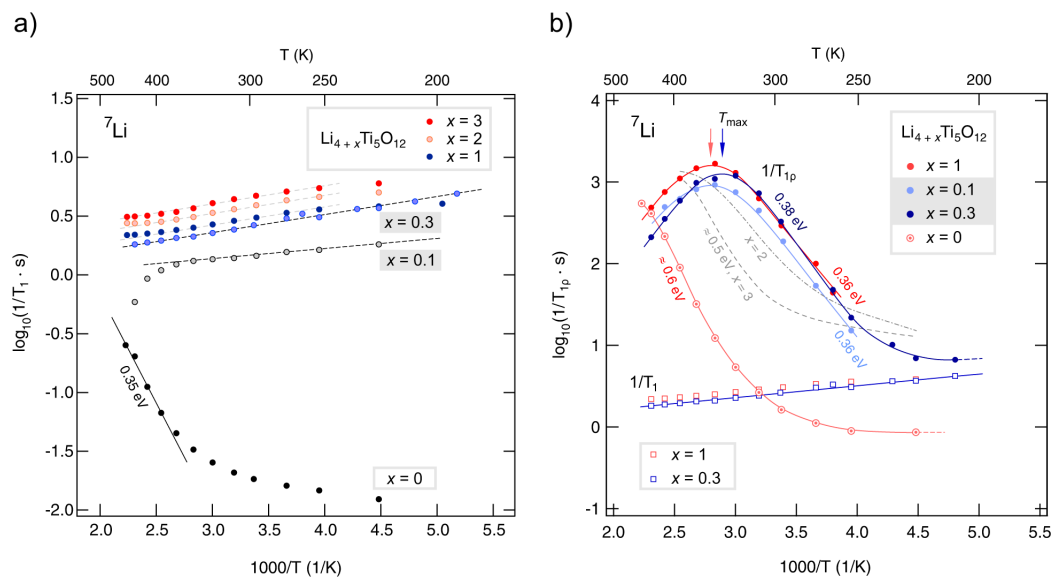


Figure 6. (a) ${}^7\text{Li}$ NMR relaxation rates of $\text{Li}_{4+x}\text{Ti}_5\text{O}_{12}$ that have been recorded in the laboratory frame of reference. Beginning with $x = 0$ they reveal the typical behavior seen for many ion conductors: a low- T nondiffusion induced background and an Arrhenius-activated flank (0.35 eV). This is in contrast to the samples with $x > 0$. Most likely they reveal Curie behavior and/or the segregation into a Li poor and Li rich phase well below room temperature as it was seen by neutron diffraction measurements.²⁰

In contrast to SLR NMR performed at frequencies in the MHz range, $1/T_{1Q}$ rates, which have been recorded at locking frequencies in the kHz regime, are sensitive to slower Li motions; concomitantly they trace ion dynamics on a longer length scale as compared to $1/T_1$. Consequently, if an irregular potential landscape is present, larger (mean) activation energies are expected to be probed via $1/T_{1Q}$ measurements. Indeed this is the case here; from the slope of the low- T flank of the rate peak $1/T_{1Q}(1/T)$ an activation energy E_a of ca. 0.62 eV is obtained; see also the analysis presented in Figure 7.

Contrary to the nonlithiated host material, the rates $1/T_1$ of the samples with Li contents of $x = 0.1$ and larger reveal

temperature dependencies that can be ascribed to paramagnetic relaxation according to Curie–Weiss behavior. One should keep in mind that additionally to the coupling of the Li spins with the Ti^{3+} centers generated, upon cooling, the solid solutions of $\text{Li}_{4+x}\text{Ti}_5\text{O}_{12}$ tend to segregate into Li rich ($\text{Li}_7\text{Ti}_5\text{O}_{12}$) and Li poor $\text{Li}_4\text{Ti}_5\text{O}_{12}$ regions. This has been verified by neutron diffraction as mentioned above.²⁰ Since for $\text{Li}_7\text{Ti}_5\text{O}_{12}$ a shorter T_1 is expected than for $\text{Li}_4\text{Ti}_5\text{O}_{12}$, with decreasing T the formation of $\text{Li}_7\text{Ti}_5\text{O}_{12}$ domains might cause an overall increase of $1/T_1$. Above 250 K, however, the segregation process should play a minor role.

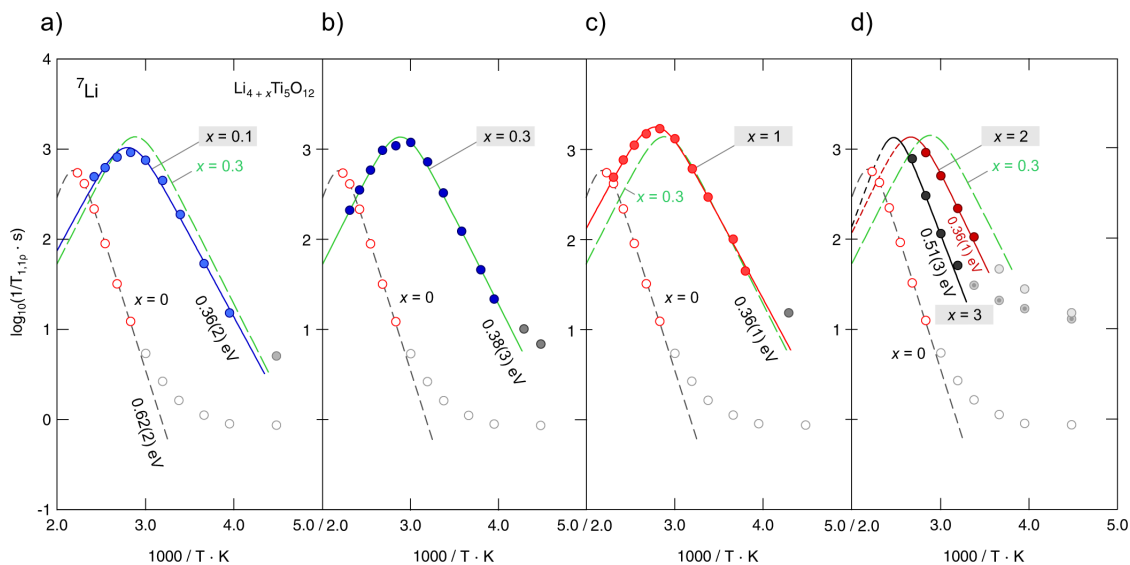


Figure 7. (a–d) ${}^7\text{Li}$ NMR SLR peaks of polycrystalline $\text{Li}_{4+x}\text{Ti}_5\text{O}_{12}$ recorded at a locking frequency of $\omega/2\pi = 20$ kHz using a Larmor frequency of 194.3 MHz. The solid lines show fits with a BPP-type spectral density function being based on a single exponential correlation function. This leads to symmetric rate peaks; thus, activation energies (0.62–0.36 eV) can be obtained from the slope of the low- T flank, i.e., in the limit $\omega_1\tau \gg 1$. The individual peaks are compared with the SLR NMR rates of the sample with $x = 0$. The green dashed line in (a, c, and d) reflects the position and shape of the peak for $x = 0.3$.

Due to the increasing number fraction of Ti^{3+} centers with increasing x , the rates $1/T_1$ steadily increase at fixed temperature (Figure 6a). This is consistent with the line broadening observed in the rigid lattice regime, as presented above.

Most importantly, when regarding the corresponding diffusion-induced rates $1/T_{1Q}$ shown in Figure 6b), a drastic increase in Li ion dynamics is already observed for the sample with $x = 0.1$. While for the nonlithiated sample only the low- T flank of the rate peak is accessible up to temperatures of 450 K, for $\text{Li}_{4.1}\text{Ti}_5\text{O}_{12}$ almost the complete rate peak could be recorded. In general, the maximum in $1/T_{1Q}(1/T)$ shows up if the (mean) Li jump rate $1/\tau$, which is within a factor of 2 identical with the mean correlation rate $1/\tau_c$ of the underlying hopping correlation function, becomes similar to the angular locking frequency ω_1 , i.e., $\omega_1\tau_c \approx 0.5$; in our case we have $\omega_1 = 125.7$ kHz. Hence, at the temperatures T_{max} (see Figure 6b) where the rate passes through the rate maximum, the correlation rate $1/\tau_c$ is in the order of 2.5×10^5 s $^{-1}$; this corresponds to a mean residence time τ of the Li ions of ca. 4 μs (at $T_{\text{max}} = 354(5)$ K for $x = 0.1$). Such a relatively high rate is capable to average EFGs at the nuclear site. In $\text{Li}_{4.1}\text{Ti}_5\text{O}_{12}$ the corresponding quadrupole splitting can be estimated to be in the order of 20 kHz (see above).

Increasing x to 0.3 shifts the rate peak toward even lower temperatures ($T_{\text{max}} = 336(5)$ K). Remarkably, at $x = 1$ a revised point has already been passed and the rate peak shifts back toward larger T values; for $x = 1$ we obtained $T_{\text{max}} = 360(5)$ K. This behavior is also seen for the samples with even larger Li contents; the low- T flanks appear at higher temperatures which directly reveals a slow down of Li diffusivity. Thus, starting from slow Li ion dynamics ($x = 0$), Li^+ diffusivity sharply increases at small x values reaching its maximum near $x = 0.3$; further lithiation, however, clearly slows down cation mobility

once again ($x = 1$) until at larger Li contents, see $x = 2$ and particularly $x = 3$, a significant reduction in Li ion mobility is observed. The Li diffusivity finally reached for rock-salt type $\text{Li}_7\text{Ti}_5\text{O}_{12}$ is, however, higher than that found for the starting material with $x = 0$. The latter finding has recently been pointed out by detailed DFT calculations of Ziebarth et al.,⁵³ moreover, it has been shown in a qualitative way via temperature-variable T_2 NMR measurements by Wagemaker et al.⁴⁹

The maximum passed through in Li diffusivity is also nicely reflected by the activation energies, which can be deduced by analyzing the rate peaks recorded. Whereas in Figure 6b the solid lines, comprising also the background rates, are simply drawn to guide the eye, in Figure 7 the $1/T_{1Q}(1/T)$ data have been analyzed with an NMR relaxation model according to Bloembergen, Purcell, and Pound (BPP). Here, a single-term fit, which is based on a Lorentzian shaped spectral density function $J(\omega_1) \propto 1/T_{1Q}$, served as a good approximation for our analysis: $1/T_{1Q} \propto \tau_c/[1 + (2\omega_1\tau_c)^\beta]$ with $1 < \beta \leq 2$. τ_c denotes the correlation time that is usually Arrhenius activated (see below). The best fits obtained are fully symmetric, i.e., β turned out to be 2. This points to an overall exponential (motional) correlation function $G(t)$ governing Li motion in $\text{Li}_{4+x}\text{Ti}_5\text{O}_{12}$ with $x = 0.1, 0.3$, and 1. Note that $J(\omega_1)$ is obtained from $G(t)$ via Fourier transformation.

Solid and dashed lines in Figure 7 show the BPP fits obtained; unfilled symbols or those in greyscale have been omitted for the analysis since they are not purely induced by Li jump diffusion. From $x = 0$ to $x = 0.1$ the BPP activation energy sharply decreases from $E_a = 0.62$ to 0.3 eV. For the samples with higher Li content ($x = 0.3, 1$) E_a takes similar values; upon further lithiation the flanks shift toward higher T and E_a increases again (0.51(3) eV for $x \rightarrow 3$). Thus, although Li diffusivity passes through a maximum, over a relatively large x range the mean value of E_a is almost constant. This is in

reasonable agreement with the results presented by Wagemaker and co-workers (0.31 eV, $x = 0.3, 1, 2$) deduced from T_2 measurements.⁴⁹ Consequently, the differences in Li hopping from $x = 1$ to $x = 2$ (and further to $x = 3$) have been looked for in the prefactor, τ_0^{-1} , of the underlying Arrhenius relation, $\tau^{-1} = \tau_0^{-1} \exp(-E_a/(k_B T))$. In particular, τ_0^{-1} is expected to increase from $x = 1$ to $x = 2$, and indeed this is observed (Table 1). Remarkably, the disordered samples with $0 < x < 3$

Table 1. Activation Energies and Pre-Factors Obtained from the BBP Fits Shown in Figure 7

$\text{Li}_{4+x}\text{Ti}_5\text{O}_{12}$	E_a , eV	τ_0 , s	T_{max} , K
$x = 0$	0.62(2)	7.3×10^{-13}	>450
0.1	0.36(2)	3.4×10^{-11}	354(5)
0.3	0.38(2)	1.0×10^{-11}	336(5)
1	0.36(1)	3.4×10^{-11}	360(5)
2	0.36(1)	6.6×10^{-12}	>370
3	0.51(3)	8.8×10^{-13}	>400

show rather small prefactors τ_0^{-1} , while for the end-members ($x = 0$ and $x = 3$) the factors are in the usual range of phonon frequencies (10^{13} – 10^{14} Hz).

3.2.1. Comparison with Results from Other NMR Studies Previously and Recently Published. Activation energies for $x = 1$ and $x = 2$ are in reasonable agreement with the value (0.43(2) eV) probed previously by our group on a $\text{Li}_{5.6}\text{Ti}_5\text{O}_{12}$ sample prepared in two different ways, viz., chemically with n -BuLi and electrochemically. Small differences in E_a have to be looked for in differences of the starting material such as crystallite size, crystallinity, morphology, and defect densities. Moreover, the value 0.43 eV was deduced from a complete peak $1/T_{1\rho}(1/T)$ recorded at 13.8 kHz; compared with 0.36 eV for $x = 1$, the somewhat larger value for $x = 1.6$ already points to an increase in E_a reaching ca. 0.51 eV at $x = 3$.

The activation energies reported by Hain et al.,⁵¹ who published a similar ^7Li NMR study, are 0.55(1) eV ($x = 0$), 0.39(1) eV ($x = 2$), and 0.45(1) eV ($x = 3$). The value for nonlithiated LTO turned out to be rather low; it is in contrast to what is usually found by $1/T_{1\rho}$ measurements and differs from results obtained by impedance spectroscopy in the low frequency limit. While E_a of $\text{Li}_6\text{Ti}_5\text{O}_{12}$ is similar to our result, we observed a steeper increase in activation energy for rock-salt $\text{Li}_7\text{Ti}_5\text{O}_{12}$.

Much more striking is another fact: Although Hain et al. also used LTO purchased from Süd-Chemie,⁵¹ as we have done here and in our previous study that appeared in 2007,²¹ the NMR relaxation rates presented by them are shifted toward much higher temperatures. They pass through peak maxima at temperatures as high as 570 K. For comparison, this is at 1.75 on the $1/T$ scale in Figure 7. In addition, the sample with $x = 3$ studied by Hain et al. suffers from interfering background relaxation while for the sample with $x = 0$ only four $1/T_{1\rho}$ NMR data points were measured over a temperature range from 300 to 660 K.⁵¹ Besides these peculiarities we should note that some of the samples of the investigation by Hain et al. were prepared electrochemically. Therefore, besides crystallinity, morphology, defect concentration (including also oxygen vacancies), and differences in NMR measurement procedures, at first the question arises whether the way Li is inserted in LTO can affect the final result. Let us keep in mind that samples prepared electrochemically may contain additives such as binders and conductive carbon. Since at sufficiently large

potentials the formation of an SEI (see above) is almost negligible—in many cases LTO is called an SEI-free anode material—we do not expect that a possible thin SEI layer influences the NMR result as large as the additives mentioned.

To answer this question, we would like to refer to our previous study²¹ focusing on a sample with $x = 1.6$ synthesized via both preparation routes—chemically and electrochemically. If properly prepared, bulk properties of $\text{Li}_{4+x}\text{Ti}_5\text{O}_{12}$ are available nonetheless. As we have shown previously, there was no difference observed in $1/T_{1\rho}(1/T)$ for the two samples. The assumption of Aldon et al.⁵⁴ anticipating the occupancy of 48f sites in the case of *chemically* lithiated LTO (see the 48f tetrahedra marked in Figure 1) seems to be not supported by the neutron diffraction study carefully carried out by Wagemaker et al.²⁰ Of course, this does not rule out the possibility, or necessity, that 48f sites^{19,54} are temporarily occupied or used as transition states when the Li ions jump from 16d to 16c sites and *vice versa* (see above).^{19,53}

3.2.2. Comparison with Results from Theory, Self-Diffusion Coefficients. Let us come back to the activation energies found here and compare them with those calculated in various studies. The studies published so far have also focused on possible Li diffusion pathways in the host material LTO and in the lithiated phases; particular attention was put on the $\text{Li}_7\text{Ti}_5\text{O}_{12}$ phase. As has been pointed out by Ziebarth et al.,⁵³ who did calculations based on DFT (referring to 0 K), the random occupancy of 16d sites by both Li and Ti results in a couple of energetically different diffusion pathways leading to a distribution of activation energies. Moreover, this also includes that the profiles of the migration pathways are asymmetric. Here, via spin–lattice relaxation NMR *only* mean values over the possible migration pathways can be probed. Nevertheless, the calculations predict activation barriers for $\text{Li}_4\text{Ti}_5\text{O}_{12}$ ranging from 0.3 to 0.48 eV when pathways are considered that involve hops between 8a and 16c sites. Most interestingly, Li^+ exchange from 16d toward an empty 8a position is reported to be governed by an activation energy of approximately 0.92 eV. Hence, a mean value larger than 0.48 eV can be expected for $x = 0$. Indeed this is the case here and in our previous study. Moreover, via ^7Li spin-alignment echo NMR we were able to trace extremely slow Li exchange processes; the associated activation energy, which could be precisely measured via SAE NMR two-time correlation functions, was 0.86 eV.¹⁹ Ziebarth et al. proposed that Li vacancies are trapped preferentially at 16d sites in the nonlithiated host material causing low Li diffusivity.⁵³ This is in contrast to the situation for $x = 3$ for which no trapping is reported; most of the activation energies calculated range from 0.2 to 0.51 eV. The involvement of 16d sites, however, leads to barriers between 0.56 and 0.94 eV.⁵³

The results by Chen et al.,⁵⁵ who did similar *ab initio* calculations, as well as that of van der Ven and co-workers,⁵⁶ point to the same direction. Although only few pathways have been studied by Chen et al.,⁵⁵ the activation energies calculated for several Li migration routes in spinel-type LTO ($x = 0$) turned out to be larger than those predicted for $\text{Li}_7\text{Ti}_5\text{O}_{12}$ crystallizing with the rock-salt structure. In particular, for the diffusion pathway 8a–16c–8a' in $\text{Li}_4\text{Ti}_5\text{O}_{12}$ the activation energy turned out to be 0.7 eV; for the pathway 16c–48f–16c' (see Figure 1) a value of 1.0 eV was given. This confirms the relatively high barriers found for the sample with $x = 0$ here and in our previous SAE NMR study; note that SAE NMR is sensitive to very slow Li diffusion processes. For comparison, the barriers from macroscopic ac impedance spectroscopy,

which may also be affected by grain boundary effects, point to values as high as 0.96 eV.^{9,19} Worth mentioning, the value calculated by Chen et al.⁵⁵ is, however, larger than those predicted by Ziebarth et al.⁵³ and by Bhattacharya et al.⁵⁶ Comparing the theoretical studies presented so far, there is still some disagreement about the existence and energetic level of metastable transition states.

Finally, the $1/T_{10}(1/T)$ peaks can be used to estimate self-diffusion coefficients from the hopping correlation rates directly determined (see above). With the value of $2.5 \times 10^5 \text{ s}^{-1}$, as it has been found at 354(S) K for $x = 0.1$ (see above), with the Einstein–Smoluchowski equation a diffusion coefficient in the order of $1.35 \times 10^{-15} \text{ m}^2 \text{ s}^{-1}$ can be estimated. The Einstein–Smoluchowski relation links τ with the self-diffusion coefficient D .⁵⁷ For 3D uncorrelated motion²⁴ we have $D = a^2/(6\tau)$; a denotes the (mean) jump distance.⁵⁷ Here, we have used $a = 1.8 \text{ \AA}$ that is a good approximation for the 8a–16c distance. Using the Nernst–Einstein equation to relate D with the ion conductivity σ_{ion} , this corresponds to $\sigma_{\text{ion}} \approx 10^{-6} \text{ S cm}^{-1}$ at 354 K ($\text{Li}_{4.1}\text{Ti}_5\text{O}_{12}$). For $x = 0.3$ the same value is reached at somewhat lower T ; see above. Values in the order of $10^{-6} \text{ S cm}^{-1}$ reflect transport properties that are characteristic for solids with modest ion conductivity.

3.2.3. Homogenous vs Nonhomogenous Spin-System. As a last remark, we recall the reader's attention to the nanodomain picture of $\text{Li}_{4+x}\text{Ti}_5\text{O}_{12}$. As has been shown by neutron diffraction,²⁰ the separation into $\text{Li}_4\text{Ti}_5\text{O}_{12}$ and $\text{Li}_7\text{Ti}_5\text{O}_{12}$ is kinetically driven by electrochemical lithiation (vide supra). As mentioned above, Lu et al. used STEM experiments to visualize the corresponding domain structure.²⁶ The phases, however, appear to be unstable at room temperature leading to a homogeneous solid solution.²⁰ In contrast, for chemical lithiation, usually carried out at ambient for several days, a morphology without a significant domain structure is expected. The vigorous reaction with $n\text{-BuLi}$ might cause significant local heating leading to homogenized samples. Significant phase segregation, however, is anticipated at 100 K and below;²⁰ such a T range has not been covered here. Interestingly, the ^7Li 2D MAS exchange measurements presented by Wagemaker et al. on chemically lithiated samples have been interpreted in terms of a *nano*-domain structure with domain sizes of less than approximately 10 nm at 373 K.⁴⁹ The rather long correlation times in the ms time regime (2.3 ms) as deduced from ^7Li NMR exchange spectroscopy experiments on $\text{Li}_6\text{Ti}_5\text{O}_{12}$ (373 K) lead to this conclusion. In the meantime, however, it has been shown by Indris and co-workers that ^7Li 2D MAS NMR is largely influenced by spin-diffusion, at least below 323 K; note that very similar correlation times have been reported (2.1 ms, $\text{Li}_6\text{Ti}_5\text{O}_{12}$ (323 K)) even for samples with different compositions ($x = 2, x = 4$).⁵¹

Hence, in our opinion the “NMR picture” of nanodomains, as it was claimed from 2D exchange experiments, rests on unsound footing at least for samples prepared via chemical lithiation. We have to ask what signature a domain structure would leave behind in NMR relaxation rates and line shapes. Even if we (generously) consider spin-diffusion effects with correlation rates in the microsecond range, nanometer-sized Li rich domains ($\text{Li}_7\text{Ti}_5\text{O}_{12}$) embedded in $\text{Li}_4\text{Ti}_5\text{O}_{12}$ should result in a two-reservoir spin-system with spatially separated ensembles of relatively fast ($x > 0$) and slow ($x = 0$) Li ions. In other words, the transients of T_1 and $1/T_{10}$ should be composed of two contributions with two distinct SLR rates. In the case of T_1 the two rates should differ by approximately 2

orders of magnitude when ambient conditions are regarded (see Figure 6).

To shed light on this issue we have to ask the following question: Did we overlook the missing slowly relaxing component in our SLR NMR measurements for the samples with $x > 0$? Or, in other words, did we selectively excite only those Li ions residing in the Li rich (mixed conducting) domains proposed? To check whether there is a hidden component M_{slow} that behaves like that of the end-member $\text{Li}_4\text{Ti}_5\text{O}_{12}$, we carried out further SLR measurements taking advantage of extremely long waiting times t_d (see Figure 8).

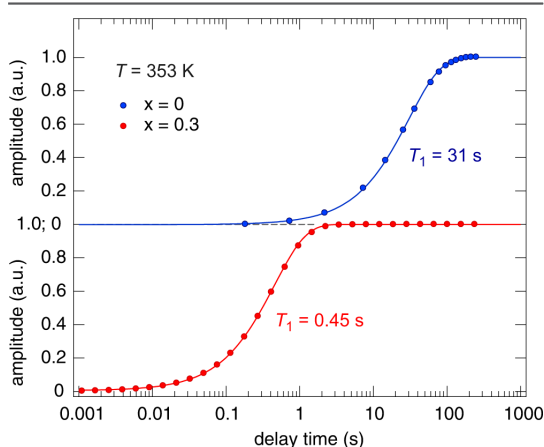


Figure 8. ^7Li NMR SLR magnetization transients of $\text{Li}_{4+x}\text{Ti}_5\text{O}_{12}$ with $x = 0$ and $x = 0.3$. Data have been recorded at 353 K for extraordinary long waiting times t_d of up to 250 s. The corresponding rates $1/T_1$ differ by approximately 2 orders of magnitude; see also Figure 6. Solid lines show fits with single exponential functions. Most importantly, the transient of the sample with $x = 0.3$, which was followed over six decades, already reached full saturation after 3 s. Any second contribution from a spatially separated $\text{Li}_{4+x}\text{Ti}_5\text{O}_{12}$ phase is missing. Such a contribution should significantly show up at delay times larger than 10 s. For $x = 0.3$, this Li poor phase would form the main volume of the sample. The transients shown here give evidence that all the 8a and 16c Li ions in $\text{Li}_{4.3}\text{Ti}_5\text{O}_{12}$ sense the Li^+e^- coupling because of localized but, most likely, homogeneously distributed Ti^{3+} centers.

Even if we extend t_d to be much larger than $6T_1$ (see section 2), exactly the same single exponentially decaying transients, M_{fast} were obtained as measured for $t_d = 6T_1$. As an example, the T_1 transients of $\text{Li}_{4.3}\text{Ti}_5\text{O}_{12}$ recorded at 293 and 353 K with t_d values of up to 100 s resulted in single exponentials with effective SLR rates in the order of $T_1 = 450 \text{ ms}$ only; see Figure 8. A magnetization component M_{slow} characterized by $T_1 = 31 \text{ s}$ (293 K), as expected for large domains of $\text{Li}_4\text{Ti}_5\text{O}_{12}$ completely free of Ti^{3+} centers, is most certainly absent. Note that one cannot distinguish between differently mobile Li ions residing regularly on 8a and 16c sites also. Most importantly, the comparison of the two transients proved that within our NMR relaxometry measurements, particularly including the $1/T_{10}$ data, the *entire* Li ensemble has been nonselectively excited. Note that the introduction of paramagnetic impurities during synthesis is a common practice to reduce T_1 . Here, this effect enables us to excite the whole spin system; therefore, the diffusion-induced rate peaks $1/T_{10}(1/T)$ seem to reflect all of the Li ions present in the oxide. This view is supported by the

observation of fully motionally narrowed NMR lines at 373 K and above. Spin-diffusion would not cause such line narrowing.

In summary, so far, we could not find any convincing indications from SLR NMR for two magnetically decoupled or even spatially separated spin ensembles that can be described by distinct Li ion dynamics. Quite the contrary, even at very low x values, see particularly the sample with $x = 0.3$, all of the 8a and 16c Li ions seem to be mobile on the NMR time scale as evidenced by $1/T_{1e}$ measurements. From a dynamic point of view, at least up to the composition of $x = 1$, a single and entirely homogeneous spin-system was detected. This strongly points to the formation of a solid solution with homogeneously distributed Li ions interstitially occupying the empty 16c sites in the spinel structure (Figure 1). Differently speaking, the Ti^{3+} centers generated during lithiation are expected to be distributed over the whole crystalline areas.

For larger Li contents ($x = 2$ and $x = 3$), cf. the NMR lines in Figure 3 b, so-called heterogeneous motional line narrowing is seen. To assign this feature to a domain structure is a speculative interpretation. As mentioned above, many structurally uniform spin-systems reveal complex, heterogeneous ion dynamics. A distribution of jump rates does not necessarily need a two-phase or many-phase picture on a nanometer length scale to be explained. In such cases a nonexponential (non-Debye) motional correlation function might be expected; here, however, this is not observed. The “simple” (isotropic) BPP model being based on a single exponential correlation function is sufficient to fully describe the $1/T_{1e}$ peaks recorded. Moreover, we also checked the shape of the corresponding transients, as it was done for the $1/T_1$ magnetization curves of the sample with $x = 0.3$. Their shapes do not hint to a two-phase spin system. It is likely that the formation of Ti^{3+} centers affects the entire spin–lattice relaxation behavior in both the rotating and laboratory frame of reference. Hence, once again, all of the Li spins contribute to the diffusion-induced $1/T_{1e}$ peaks obtained for $x = 2$ and $x = 3$.

Of course, the view drawn by NMR relaxometry should not be mixed with (i) the phase segregation observed and proven by neutron diffraction carried out at temperatures being much lower than ambient²⁰ and (ii) the known kinetically induced phase separation via electrochemical lithiation.²⁰ We assume that Lu et al.²⁶ (see above) studied a sample that was electrochemically intercalated to make visible the Li poor and Li rich phases via STEM. Although it is declared differentially in the main text, it was stated in the Supporting Information of their recent paper²⁶ that they performed STEM investigations on electrochemically lithiated samples

As a last remark, let us note that during the analysis the samples are heated above 423 K. Starting with a two-phase system such heat-treatment could cause homogenization of the Li environment. Here, however, even at room temperature or below, we did not find any evidence for a distinct two-phase scenario. In other words, the measurement order did not influence our analysis. The reproducibility of the results has been checked by several consecutive heating and cooling runs.

4. SUMMARY AND CONCLUSION

$\text{Li}_{4+x}\text{Ti}_5\text{O}_{12}$ belongs to one of the most promising anode materials. Zero-strain and highly reversible Li insertion/deinsertion guarantees an extremely long cycle life of lithium-ion batteries with moderate capacities. While nonlithiated $\text{Li}_4\text{Ti}_5\text{O}_{12}$ is a rather poor ion conductor with negligible electronic conductivity, small amounts of Li inserted ($x = 0.1$,

$x = 0.3$) transform the material in a mixed conducting oxide that shows greatly improved Li ion diffusivities.

The steep increase in Li ion hopping rates, which is associated by a significant reduction of the mean activation barrier E_a from 0.62 to 0.36 eV ($x = 0.1$), was directly followed on the Ångström length scale by both ^7Li NMR line shape measurements and ^7Li NMR spin–lattice relaxation experiments. From the latter, activation energies and absolute hopping rates could be deduced. For the end-member, that is, rock-salt type $\text{Li}_7\text{Ti}_5\text{O}_{12}$, Li diffusivity slows down once again and E_a increases reaching approximately 0.51 eV.

We attribute the steep increase in Li diffusivity to the generation of strong repulsive Coulomb interactions because of the simultaneous occupation of (face-sharing) 8a and 16c sites within the spinel structure of LTO. Coupling of Li^+ and e^- migration is likely since upon lithiation LTO turns into a mixed conductor and both electronic and ionic conduction occur simultaneously. The significant reduction of the elementary Li ion jump barriers probed via NMR helps us understanding the superior insertion behavior of LTO at the early stages of Li insertion. Especially, it might be useful to consider also a solid-solution model if we want to understand the flat insertion potential observed in LTO.

Worth noting, the results from ^7Li NMR relaxometry and line shape analysis obtained refer to solid solutions of $\text{Li}_{4+x}\text{Ti}_5\text{O}_{12}$. Even if performed at sufficiently long delay times (or waiting times), our findings do not entail any evidence for the formation of a two-phase material with spatially extended and largely separated Li rich and Li poor regions. Excluding fast spin-diffusion being effective over large distances, there are no indications for the presence of two magnetically decoupled spin-ensembles in samples with $x \geq 0.1$; this is underlined by the observation of fully motionally narrowed NMR lines that appear upon Li intercalation; see $x = 0.1$ and $x = 0.3$.

The formation of a kinetically induced two-phase material, however, might be expected for samples that have been prepared electrochemically.^{20,26} In contrast, in the case of *chemically* lithiated LTO, which we have synthesized at ambient temperature by treatment with *n*-BuLi, it seems likely that a homogeneous distribution of Li ions among the 8a and 16c sites is present at sufficiently high temperatures; such a scenario fully agrees with previous results from neutron diffraction measurements.²⁰ Quite recently, Pang et al.²³ have even used the solid solution model to explain their results from *in situ* neutron diffraction on Li ion transport in LTO working as electrode material in electrochemical cells.

■ AUTHOR INFORMATION

Corresponding Authors

*(W.S.) E-mail: w.schmidt@tugraz.at.

*(M.W.) E-mail: wilkening@tugraz.at.

Notes

The authors declare no competing financial interest.

■ ACKNOWLEDGMENTS

We thank our colleagues at the TU Graz for valuable discussions. Moreover, we gratefully acknowledge SüdChemie for providing the EXM 1037 sample. Financial support by the Austrian Federal Ministry of Science, Research and Economy, and the National Foundation for Research, Technology and Development is gratefully acknowledged. Moreover, we thank

the Deutsche Forschungsgemeinschaft (DFG) (Research Unit 1277, Grant No. WI3600/2-2 and 4-2) for financial support.

REFERENCES

- (1) Whittingham, M. S. *Prog. Solid State Chem.* **1978**, *12*, 41–99.
- (2) Whittingham, M. S. *Chem. Rev.* **2004**, *104*, 4271–4301.
- (3) Aricó, A. S.; Bruce, P.; Scrosati, B.; Tarascon, J.-M.; Schalkwijk, W. V. *Nat. Mater.* **2005**, *4*, 366–377.
- (4) Armand, M.; Tarascon, J.-M. *Nature* **2008**, *451*, 652–657.
- (5) Palacín, M. R. *Chem. Soc. Rev.* **2009**, *38*, 2565–2575.
- (6) Colbow, K.; Dahn, J.; Haering, R. J. *Power Sources* **1989**, *26*, 397–402.
- (7) Ferg, E.; Gummow, R. J.; de Kock, A.; Thackeray, M. M. *J. Electrochem. Soc.* **1994**, *141*, L147–L149.
- (8) Ohzuku, T.; Ueda, A.; Yamamoto, N. *J. Electrochem. Soc.* **1995**, *142*, 1431–1435.
- (9) Haetge, J.; Hartmann, P.; Brezesinski, K.; Janek, J.; Brezesinski, T. *Chem. Mater.* **2011**, *23*, 4384–4393.
- (10) Zhu, G.-N.; Wang, Y.-G.; Xia, Y.-Y. *Energy Environ. Sci.* **2012**, *5*, 6652–6667.
- (11) Yi, T.-F.; Jiang, L.-J.; Shu, J.; Yue, C.-B.; Zhu, R.-S.; Qiao, H.-B. *J. Phys. Chem. Solids* **2010**, *71*, 1236–1242.
- (12) Xia, H.; Luo, Z.; Xie, J. *Nanotechnol. Rev.* **2014**, *3*, 161–175.
- (13) Chen, S.; Xin, Y.; Zhou, Y.; Ma, Y.; Zhou, H.; Qi, L. *Energy Environ. Sci.* **2014**, *7*, 1924–1930.
- (14) Thackeray, M. J. *Electrochem. Soc.* **1995**, *142*, 2558–2563.
- (15) Yonglong, Z.; Xuebu, H.; Yunlan, X.; Mingliang, D. *Acta Chim. Sinica* **2013**, *71*, 1341–1353.
- (16) He, Y.-B.; Li, B.; Liu, M.; Zhang, C.; Lv, W.; Yang, C.; Li, J.; Du, H.; Zhang, B.; Yang, Q.-H.; Kim, J.-K.; Kang, F. *Sci. Rep.* **2012**, *2*, 913–1–913–8.
- (17) Bernhard, R.; Meini, S.; Gasteiger, H. A. *J. Electrochem. Soc.* **2014**, *161*, A497–A505.
- (18) Li, W.; Li, X.; Chen, M.; Xie, Z.; Zhang, J.; Dong, S.; Qu, M. *Electrochim. Acta* **2014**, *139*, 104–110.
- (19) Wilkening, M.; Amade, R.; Iwaniak, W.; Heitjans, P. *Phys. Chem. Chem. Phys.* **2006**, *9*, 1239–1246.
- (20) Wagemaker, M.; Simon, D. R.; Kelder, E. M.; Schoonman, J.; Ringpfeil, C.; Haake, U.; Lützenkirchen-Hecht, D.; Frahm, R.; Mulder, F. *Adv. Mater.* **2006**, *18*, 3169–3173.
- (21) Wilkening, M.; Iwaniak, W.; Heine, J.; Epp, V.; Kleinert, A.; Behrens, M.; Nusspl, G.; Bensch, W.; Heitjans, P. *Phys. Chem. Chem. Phys.* **2007**, *9*, 6199–6202.
- (22) Laumann, A.; Boysen, H.; Bremholm, M.; Fehr, K. T.; Hoelzel, M.; Holzapfel, M. *Chem. Mater.* **2011**, *23*, 2753–2759.
- (23) Pang, W. K.; Peterson, V. K.; Sharma, N.; Shiu, J.-J.; Wu, S.-h. *Chem. Mater.* **2014**, *26*, 2318–2326.
- (24) Dolotko, O.; Senyshyn, A.; Mühlbauer, M. J.; Boysen, H.; Monchak, M.; Ehrenberg, H. *Solid State Sci.* **2014**, *36*, 101–106.
- (25) Kitta, M.; Akita, T.; Tanaka, S.; Kohyama, M. *J. Power Sources* **2014**, *257*, 120–125.
- (26) Lu, X.; Zhao, L.; He, X.; Xiao, R.; Gu, L.; Hu, Y.-S.; Li, H.; Wang, Z.; Duan, X.; Chen, L.; Maier, J.; Ikuhara, Y. *Adv. Mater.* **2012**, *24*, 3233–3238.
- (27) Epp, V.; Wilkening, M. *Phys. Rev. B* **2010**, *82*, 020301–1–020301–4.
- (28) Epp, V.; Gün, O.; Deiseroth, H.-J.; Wilkening, M. *Phys. Chem. Chem. Phys.* **2013**, *15*, 7123–7132.
- (29) Epp, V.; Nakhil, S.; Lerch, M.; Wilkening, M. *J. Phys.: Condens. Matter* **2013**, *25*, 195402–1–195402–7.
- (30) Kuhn, A.; Narayanan, S.; Spencer, L.; Goward, G.; Thangadurai, V.; Wilkening, M. *Phys. Rev. B* **2011**, *83*, 094302–1–094302–11.
- (31) Langer, J.; Epp, V.; Heitjans, P.; Mautner, F. A.; Wilkening, M. *Phys. Rev. B* **2013**, *88*, 094304–1–094304–9.
- (32) Heitjans, P.; Schirmer, A.; Indris, S. In *Diffusion in Condensed Matter – Methods, Materials, Models*, 2nd ed.; Heitjans, P., Kärger, J., Eds.; Springer: Berlin, 2005; Chapter 9, pp 369–415.
- (33) Fukushima, E.; Roeder, S. *Experimental Pulse NMR*; Addison-Wesley: Reading, 1981.
- (34) Ailion, D.; Slichter, C. P. *Phys. Rev. Lett.* **1964**, *12*, 168–171.
- (35) Slichter, C. P.; Ailion, D. *Phys. Rev.* **1964**, *135*, A1099–A1110.
- (36) Ailion, D. C.; Slichter, C. P. *Phys. Rev.* **1965**, *137*, A235–A245.
- (37) Böhmer, R.; Jeffrey, K.; Vogel, M. *Prog. Nucl. Magn. Reson. Spectrosc.* **2007**, *50*, 87–174.
- (38) Böhmer, R.; Jörg, T.; Qi, F.; Titze, A. *Chem. Phys. Lett.* **2000**, *316*, 419–424.
- (39) Qi, F.; Jörg, T.; Böhmer, R. *Solid State Nucl. Magn. Reson.* **2002**, *22*, 484–500.
- (40) Wilkening, M.; Heitjans, P. *Phys. Rev. B* **2008**, *77*, 024311–1–024311–13.
- (41) Jeener, J.; Broekaert, P. *Phys. Rev.* **1967**, *157*, 232–240.
- (42) Qi, F.; Diezemann, G.; Böhm, H.; Lambert, J.; Böhmer, R. *J. Magn. Reson.* **2004**, *169*, 225–239.
- (43) Abragam, A. *The Principles of Nuclear Magnetism*; Clarendon: Oxford, 1961.
- (44) Epp, V.; Gün, O.; Deiseroth, H.-J.; Wilkening, M. *J. Phys. Chem. Lett.* **2013**, *4*, 2118–2123.
- (45) Wilkening, M.; Epp, V.; Feldhoff, A.; Heitjans, P. *J. Phys. Chem. C* **2008**, *112*, 9291–9300.
- (46) Wohlmuth, D.; Epp, V.; Bottke, P.; Hanzu, I.; Bitschnau, B.; Letofsky-Papst, I.; Kriechbaum, M.; Amenitsch, H.; Hofer, F.; Wilkening, M. *J. Mater. Chem. A* **2014**, *2*, 20295–20306.
- (47) Stenina, I. A.; Il'in, A. B.; Yaroslavtsev, A. B. *Inorg. Mater.* **2015**, *51*, 62–67.
- (48) Gao, Y.; Wang, Z.; Chen, L. *J. Power Sources* **2014**, *245*, 684–690.
- (49) Wagemaker, M.; van Eck, E. R. H.; Kentgens, A. P. M.; Mulder, F. M. *J. Phys. Chem. B* **2009**, *113*, 224–230.
- (50) Kartha, J.; Tunstall, D.; Irvine, J. T. *J. Solid State Chem.* **2000**, *152*, 397–402.
- (51) Hain, H.; Scheuermann, M.; Heinzmann, R.; Wünsche, L.; Hahn, H.; Indris, S. *Solid State Nucl. Magn. Reson.* **2012**, *42*, 9–16.
- (52) Kanert, O.; Küchler, R.; Soares, P. C.; Jain, H. *J. Non-Cryst. Solids* **2002**, *307–310*, 1031–1038.
- (53) Ziebarth, B.; Klinsmann, M.; Eckl, T.; Elsässer, C. *Phys. Rev. B* **2014**, *89*, 174301–1–174301–7.
- (54) Aldon, L.; Kubiak, P.; Womes, M.; Jumas, J.; Olivier-Fourcade, J.; Tirado, J.; Corredor, J.; Vicente, C. *Chem. Mater.* **2004**, *16*, 5721–5725.
- (55) Chen, Y.; Ouyang, C.; Song, L.; Sun, Z. *Electrochim. Acta* **2011**, *56*, 6084–6088.
- (56) Bhattacharya, J.; van der Ven, A. *Phys. Rev. B* **2010**, *81*, 104304–1–104304–12.
- (57) Mehrer, H. *Diffusion in Solids*; Springer: Berlin, 2006.

3.3 Oxidische Granate als Festkörperelektrolyte für Lithium-Ionen-Batterien

In den handelsüblichen, wiederaufladbaren Lithium-Ionen-Batterien werden aktuell Interkalationsmaterialien, wie z. B. Graphit, $\text{Li}_4\text{Ti}_5\text{O}_{12}$ (P5) oder diverse Morphologien von Titandioxid (siehe P4 und Abschnitt 3.2.2), verwendet, obwohl reines Li-Metall eine deutlich höhere Kapazität pro Volumen und Gewicht bietet. Dieser Umstand ist der Tatsache geschuldet, dass elementares Lithium als Anode in Zellen mit flüssigem Elektrolyt ungeeignet ist. Einige Zyklen funktioniert eine solche Batterie tadellos. Es bilden sich jedoch mit der Zeit Dendriten aus, die auch durch verschiedenste Arten von Zellstoff- oder Glasfaserseparatoren nicht davon abgehalten werden können, mit jedem Laden der Batterie kontinuierlich in Richtung der Kathode zu wachsen. Dies führt zum Kurzschluss und die Zelle wird unnötig früh unbrauchbar. Ein Festkörper, der nicht porös ist, wie es die Separatoren für die Aufnahme von flüssigem Elektrolyt sind, und eine ausreichend hohe Li-Ionenleitfähigkeit aufweist, kann die Verwendung von Li-Metall als Anode ermöglichen. Festkörperelektrolyte steigern somit die Sicherheit (keine brennbaren organischen Lösungsmittel) und erhöhen die Kapazität. Als Schutzschichten in Lithium-Luft-Batterien und Lithium-Schwefelbatterien sind sie ebenso unerlässlich.^[56]

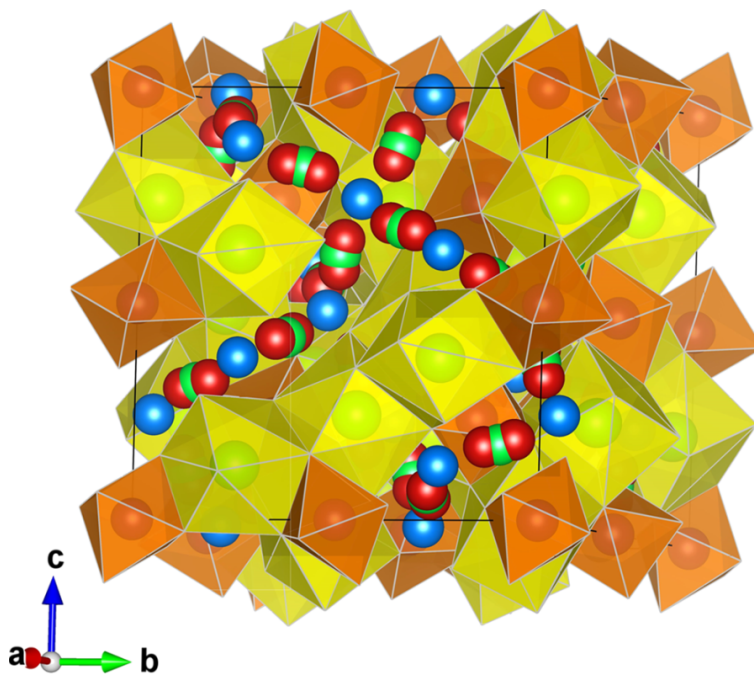
Die Anforderungen an Festkörperelektrolyte gehen jedoch weiter. Sie müssen genau wie ihre flüssigen Analoga elektrische Isolatoren sein und elektrochemische Stabilität gegenüber den Elektroden im gesamten Arbeitsbereich/Potentialfenster der Zelle aufweisen. Zusätzlich müssen sie jedoch auch noch mechanische Stabilität, gute Kontaktierbarkeit und eine hohe Reproduzierbarkeit in der Herstellung gewährleisten. Aus diesen Gründen haben Systeme mit flüssigem Elektrolyt für die meisten Anwendungen noch immer ein besseres Preis-/Leistungsverhältnis.

Im Fokus der weltweit intensiven Forschung stehen Granate. Die Veröffentlichung von Buschmann et al. (P6) war eine der ersten Untersuchungen zur Struktur und Dynamik von oxidischen Granaten des Typs LLZO " $\text{Li}_7\text{La}_3\text{Zr}_2\text{O}_{12}$ ". Dabei wurden die kubische und die tetragonale Modifikation hinsichtlich der Lithiumionenleitfähigkeit und der Strukturstabilität verglichen. Das thermodynamisch begünstigte tetragonale LLZO zeigt eine moderate Leitfähigkeit in der Größenordnung von $10^{-6} \text{ S cm}^{-1}$. Deutlich höhere Leitfähigkeiten (bis zu $4 \times 10^{-4} \text{ S cm}^{-1}$) werden durch die Stabilisierung der kubischen Modifikation mittels Aluminiumdotierung auf den 24 d Lithium-Plätzen im Kristallgitter erreicht. Dies konnte auch durch die ^{27}Al und ^7Li -NMR Ergebnisse belegt werden. Die in P6 gezeigte NMR-Linienformanalyse (P. Bottke) und die von A. Kuhn in Hannover durchgeführten NMR-Relaxationsmessungen deuten auf eine heterogene Li-Dynamik hin.

In den folgenden Jahren wurde LLZO mit verschiedenen anderen trivalenten Kationen wie z. B. Ga^{3+} oder Ge^{3+} stabilisiert. Dabei wurden ähnliche Leitfähigkeiten gefunden.

Durch die Dotierung mit Molybdän wird Zirkon substituiert und das Li-Untergitter bleibt intakt.^[57] $\text{Li}_{6,5}\text{La}_3\text{Zr}_{1,75}\text{Mo}_{0,25}\text{O}_{12}$ ist somit eine ideale Modellsubstanz mit Anwendungspotential, um die kubische Struktur von LLZO auf ihre Li-Dynamik hin zu untersuchen.

P6 Structure and dynamics of the fast lithium ion conductor
“ $\text{Li}_7\text{La}_3\text{Zr}_2\text{O}_{12}$ ”



Cite this: *Phys. Chem. Chem. Phys.*, 2011, **13**, 19378–19392

www.rsc.org/pccp

PAPER

Structure and dynamics of the fast lithium ion conductor “Li₇La₃Zr₂O₁₂”[†]

Henrik Buschmann,^a Janis Döle,^a Stefan Berendts,^a Alexander Kuhn,^b Patrick Bottke,^b Martin Wilkening,^b Paul Heitjans,^b Anatoliy Senyshyn,^c Helmut Ehrenberg,^d Andriy Lotnyk,^e Viola Duppel,^f Lorenz Kienle^e and Jürgen Janek^{*a}

Received 28th June 2011, Accepted 30th August 2011

DOI: 10.1039/c1cp22108f

The solid lithium-ion electrolyte “Li₇La₃Zr₂O₁₂” (LLZO) with a garnet-type structure has been prepared in the cubic and tetragonal modification following conventional ceramic syntheses routes. Without aluminium doping tetragonal LLZO was obtained, which shows a two orders of magnitude lower room temperature conductivity than the cubic modification. Small concentrations of Al in the order of 1 wt% were sufficient to stabilize the cubic phase, which is known as a fast lithium-ion conductor. The structure and ion dynamics of Al-doped cubic LLZO were studied by impedance spectroscopy, dc conductivity measurements, ⁶Li and ⁷Li NMR, XRD, neutron powder diffraction, and TEM precession electron diffraction. From the results we conclude that aluminium is incorporated in the garnet lattice on the tetrahedral 24d Li site, thus stabilizing the cubic LLZO modification. Simulations based on diffraction data show that even at the low temperature of 4 K the Li ions are blurred over various crystallographic sites. This strong Li ion disorder in cubic Al-stabilized LLZO contributes to the high conductivity observed. The Li jump rates and the activation energy probed by NMR are in very good agreement with the transport parameters obtained from electrical conductivity measurements. The activation energy E_a characterizing long-range ion transport in the Al-stabilized cubic LLZO amounts to 0.34 eV. Total electric conductivities determined by ac impedance and a four point dc technique also agree very well and range from $1 \times 10^{-4} \text{ Scm}^{-1}$ to $4 \times 10^{-4} \text{ Scm}^{-1}$ depending on the Al content of the samples. The room temperature conductivity of Al-free tetragonal LLZO is about two orders of magnitude lower ($2 \times 10^{-6} \text{ Scm}^{-1}$, $E_a = 0.49 \text{ eV}$ activation energy). The electronic partial conductivity of cubic LLZO was measured using the Hebb–Wagner polarization technique. The electronic transference number t_{e-} is of the order of 10^{-7} . Thus, cubic LLZO is an almost exclusive lithium ion conductor at ambient temperature.

^a *Physikalisch-Chemisches Institut, Justus Liebig Universität Giessen, Heinrich-Buff-Ring 58, 35392 Giessen, Germany.*

E-mail: juergen.janek@phys.chemie.uni-giessen.de

^b *Institut für Physikalische Chemie und Elektrochemie, Leibniz Universität Hannover, Callinstraße 3a, 30167 Hannover, Germany*

^c *Forschungsneutronenquelle Heinz Maier-Leibnitz (FRM II), Technische Universität München, Lichtenbergstrasse 1, 85747 Garching, Germany*

^d *Institute for Applied Materials (IAM), Karlsruhe Institute of Technology (KIT), Hermann-von-Helmholtz-Platz 1, 76344 Eggenstein-Leopoldshafen, Germany*

^e *Faculty of Engineering, Institute for Material Science, Synthesis and Real Structure, Christian Albrechts Universität zu Kiel, Kaiserstr. 2, D-24143 Kiel, Germany*

^f *Max Planck Institute for Solid State Research, Heisenbergstr. 1, D-70569 Stuttgart, Germany*

[†] Electronic supplementary information (ESI) available: TEM pictures. CCDC reference numbers 833727. For ESI and crystallographic data in CIF or other electronic format see DOI: 10.1039/c1cp22108f

Introduction

Today, state-of-the-art electrolytes in lithium (ion) batteries are composed of organic solvents or polymers with a dissolved Li-salt.¹ These are combustible in case of abuse, and they often react with electrode materials to form passivating films in the best case.^{2,3} This is on the one hand necessary and favourable, on the other hand proceeding film growth and electrolyte decomposition at elevated temperatures lead to degradation of the battery and shorter battery life times.⁴ In particular, new cell concepts based on high voltage cathodes or mobile non-metal cathode systems based on sulfur or oxygen require improved electrolytes, and it may well be that ion-conducting membranes become indispensable. Therefore, the search for stable and incombustible inorganic solid electrolytes with high lithium ion conductivity is currently an important issue in battery research.

Recently Li ion conducting garnet-type oxides are considered as promising electrolytes because of their high conductivity and stability vs. Li metal. Thangadurai *et al.* first reported about Li ion mobility in $\text{Li}_5\text{La}_3\text{M}_2\text{O}_{12}$ ($M = \text{Nb}, \text{Ta}$).⁵ After the report on cubic $\text{Li}_7\text{La}_3\text{Zr}_2\text{O}_{12}$ (LLZO) with the so far highest room temperature conductivity⁶ in 2007 these materials have attracted a lot of interest, but it was often found to be difficult to obtain highly conductive LLZO. Later Awaka *et al.* showed that the reason for this is the existence of a second, tetragonally distorted modification⁷ with a much lower conductivity than cubic LLZO. Although some groups reported about the successful preparation of cubic LLZO it is impossible to judge about the quality of the reported materials, due to missing experimental data like conductivities and/or X-ray diffractograms (XRD).^{8,9} Recently, some groups reported on aluminium impurities and the formation of cubic LLZO in combination with Al impurities or Al doping.^{10–13} None of these groups could clarify the exact effect of Al on the formation of cubic LLZO and the changes of the crystal structure caused by Al incorporation except the suggestion that Al might substitute Li in the garnet lattice. In order to indicate that it is in fact not pure $\text{Li}_7\text{La}_3\text{Zr}_2\text{O}_{12}$ which shows high Li ion conductivity, we will use the abbreviation LLZO or the formula in quotation marks throughout the paper.

Despite attempts to clarify the crystal structure of cubic LLZO by single crystal XRD^{8,10} not much is known about the lithium distribution in cubic LLZO, owing to the small scattering factors of lithium ions. It is the aim of this study to gain deeper insight into the structure and ion dynamics of cubic LLZO in order to better judge its potential as a battery electrolyte. In particular, we made a systematic study of the effect of aluminium doping on the formation of the tetragonal and the cubic LLZO modification. In order to obtain maximal structural information we combined XRD, neutron powder diffraction as well as transmission electron microscopy/precession electron diffraction (TEM-PED) and nuclear magnetic resonance (NMR) spectroscopy. We propose a structure model which takes the lithium ions properly into account as well as the aluminium dopant. In order to also obtain comprehensive information on the lithium ion dynamics we combined electrochemical measurements and ⁷Li NMR spin–spin as well as spin–lattice relaxation techniques. Very good agreement of the different results was found. Finally, we used the Hebb–Wagner method to determine the electronic transference number of cubic LLZO which has not been reported before so far.

Experimental

Synthesis

LLZO was prepared by a high temperature route using LiOH (Chempur, 99%, anhydrous), ZrO_2 (Chempur, 99.9%) and La_2O_3 (Chempur 99.99%, dried at 900 °C for 12 h). The starting materials were mixed in stoichiometric amounts (10 wt%–20 wt% LiOH excess was used) and milled for 8 h–12 h in 2-propanol in a planetary ball mill (Fritsch, Pulverisette 7 premium line or Fritsch, Pulverisette 5 classic line)

with zirconia balls and grinding bowls. We made use of three different procedures to prepare Al-free and Al-containing LLZO samples. Interestingly, although we followed the preparation route described in the literature⁶ to synthesize cubic LLZO, the second calcination step at 1130 °C led to the formation of the tetragonal modification⁷ of LLZO. The successful preparation of cubic LLZO turned out to depend on the number of calcination steps and the kind of crucibles used. The cubic phase of LLZO only formed when alumina crucibles were used and when the powder was annealed several times at 1130 °C for about 12 h with milling steps in between. As a result of the reaction between the crucible and the powder a thinning of the crucible after some preparation steps was observed. Several batches of cubic LLZO were prepared according to this procedure and investigated by ICP-OES (inductively coupled plasma optical emission spectroscopy). All of the cubic LLZO samples prepared showed an Al content of about 0.9 wt% (28 mol% Al per mol $\text{Li}_7\text{La}_3\text{Zr}_2\text{O}_{12}$). To verify the hypothesis that Al stabilizes the cubic modification we prepared LLZO samples intentionally doped with Al as well as free of Al. For this purpose crucibles free of any Al traces have been used. A small amount (corresponding to 0.5 wt% and 0.9 wt% in LLZO) of $\gamma\text{-Al}_2\text{O}_3$ (Merck, anhydrous) was added to the mixture of the starting materials. The Al-doped samples were otherwise prepared according to the procedure described above. After calcination at 900 °C and 1130 °C the powder was pressed to pellets, covered with mother powder, and sintered at 1230 °C for 30 h. For comparison, Al-free LLZO has been prepared without addition of $\gamma\text{-Al}_2\text{O}_3$ powder.

Phase characterization

Phase analysis along synthesis was carried out on a Siemens D500 Siemens AG, now Bruker AXS in Bragg-Bretano geometry with $\text{CuK}\alpha$ -radiation. Phase analysis and determination of cell parameters at room temperature in cubic LLZO were carried out using X-ray powder diffraction (XPD) with a STOE STADI P diffractometer either by using $\text{MoK}\alpha_1$ -radiation, $\lambda = 0.7093 \text{ \AA}$ or $\text{CoK}\alpha_1$ -radiation, $\lambda = 1.78897 \text{ \AA}$.

Elastic coherent neutron scattering experiments were performed on the high-resolution powder diffractometer SPODI at the research reactor FRM-II (Garching, Germany).¹⁴ Monochromatic neutrons ($\lambda = 1.5482 \text{ \AA}$) were obtained at a 155° take-off angle using the (551) reflection of a vertically-focused composite Ge monochromator. The vertical position-sensitive multidetector (300 mm effective height) consisting of 80 ³He tubes and covering an angular range of 160°. 2θ was used for data collection. Measurements were performed in Debye–Scherrer geometry. The powder sample was filled into a thin-wall (0.15 mm) vanadium can of 13 mm in diameter and then mounted in the top-loading closed-cycle refrigerator. Helium 4 was used as a heat transmitter. The instantaneous temperature was measured using two thin film resistance cryogenic temperature sensors Cernox and controlled by a temperature controller from LakeShore. Two-dimensional powder diffraction data were collected at 4 K and 300 K using two wavelengths and then corrected for geometrical aberrations and curvature of Debye–Scherrer rings.

The analysis of powder diffraction data was carried out using the Rietveld technique implemented into the software package FullProf.¹⁵ The peak profile was described by a modified pseudo-Voigt function (*Thompson–Cox–Hastings*). The background of the diffraction patterns was fitted using a linear interpolation between selected data points in non-overlapping regions. Cylindrical absorption correction with $\mu R = 0.7072$ has been applied to obtain neutron intensities. The scale factor, lattice parameter, fractional coordinates of atoms and their iso-/anisotropic displacement parameters, zero angular shift, profile shape parameters and half width (Caglioti) parameters were varied during the fitting. Prior to the Rietveld refinement route the lattice parameters, background and profile shape parameters were estimated using the full profile decomposition (Le-Bail) technique.

The maximum entropy method (MEM) implemented in the program PRIMA¹⁶ was used to determine the nuclear densities. MEM deals with the 3D densities in the way giving the maximum variance of structure factors $F_c(\text{MEM})$ within standard deviation of observed structure factors F_o , where structural information can effectively be extracted from the diffraction data and reflected on the resulting three-dimensional distribution of electron/nuclear densities. MEM analysis was conducted using either 189 (at 4 K) or 192 (at 300 K) structure factors obtained from the Rietveld analysis, with the unit cell divided into $128 \times 128 \times 128$ pixels.

TEM investigations

Transmission electron microscopy (TEM) was performed in a Philips CM 30 STwin microscope ($C_s = 1.15$ mm, 300 kV, LaB₆) equipped with a Spinning Star precession module (Nanomegas) and an EDX detector (Fa. Noran). Energy dispersive X-ray (EDX) analyses were performed in a Tecnai F30 STwin microscope ($C_s = 1.2$ mm, 300 kV, FEG) equipped with a Si/Li detector (EDAX system). The analyses were carried out in scanning transmission electron microscope (STEM) mode using the HAADF detector for image acquisition. The samples for TEM investigations were grinded and suspended in n-butanol. One drop of each suspension was placed on a TEM support (a lacey carbon film on a copper grid). All images were recorded with a Gatan Multi-scan CCD camera ($1 \text{ k} \times 1 \text{ k}$) and evaluated with a program Digital Micrograph (Gatan, Inc.). Identification of the crystal modification of LLZO was performed by comparing the diffracted intensities of simulated and experimental precession electron diffraction (PED) images. The precession angle was set to 3° for the PED experiments. The selected area electron diffraction (SAED) and PED patterns were recorded along different zone axes. Several zone axes were examined, however, in the present work we are focusing on [001] since this direction represents the most significant one for phase distinction. The software JEMS¹⁷ was used for the simulations of SAED and PED patterns (including multiple scattering events (dynamical calculations)) as well as for simulations of high-resolution TEM (HRTEM) images (using the multislice approach). The Weickenmeier–Kohl atomic form factor was used for the simulations. For PED calculations the sample thickness was set to 10 nm. For HRTEM simulations the

following microscope parameters were used: $C_s = 1.15$ mm, defocus spread 7 nm and illumination semiangle of 0.8 mrad. In order to reduce noise, all HRTEM images were filtered after Fast Fourier transformation using a band-pass mask, with no loss of essential structural information in the following. The structural data for PED simulations of tetragonal LLZO were taken from ref. 7.

NMR measurements

⁷Li (spin-quantum number $I = 3/2$) NMR spin–spin- and spin–lattice relaxation rates in both the laboratory and rotating frame of reference were recorded using a modified MSL 100 spectrometer and an MSL 400 spectrometer operating at 4.7 T (77.8 MHz) and 9.4 T (155.5 MHz), respectively. The spectrometers were connected to Oxford cryomagnets. Standard broadband probes (Bruker) as well as home-built high temperature probes were used for data acquisition. 90° pulse lengths ranged from 4 μs to 6 μs . The temperature in the sample chamber was monitored with the help of an Oxford ITC4 using Ni–CrNi thermocouples to within ± 2 K. Temperatures below room temperature were adjusted with the help of a flow of freshly evaporated nitrogen. Above 290 K the temperature in the sample chamber was controlled with a stream of heated air. ⁷Li NMR spin–lattice relaxation rates ($1/T_1 = R_1$) in the laboratory frame of reference were recorded using a saturation recovery pulse sequence: a 90° detection pulse is sent after a comb of closely spaced saturation pulses of the same duration. The corresponding transients $M_z(t)$ describing the recovery of longitudinal magnetization follow single exponential time behaviour. This is in contrast to the analogous measurements of $1/T_{1\rho} = R_{1\rho}$ in the rotating frame of reference performed using the spin-lock technique at frequencies of 11.5 kHz and 33.1 kHz. The transients $M_{(xy)}(t)$ can be well parameterized by stretched exponentials $M_{(xy)}(t) \propto \exp(-(t/T_{1\rho})^\gamma)$ with $0.4 < \gamma < 1$.

High-resolution ⁶Li and ²⁷Al NMR spectra under fast sample rotation were recorded using an Avance III spectrometer (Bruker) in combination with a shimmed cryomagnet of 14.1 T. Magic angle spinning (MAS) spectra were recorded with a 2.5-mm-probe at 88.4 MHz and 156.5 MHz, respectively. The spinning speed was 30 kHz.

Electrochemical characterization

Pellets of sintered LLZO samples were cut into pieces of different lengths and vacuum dried at 100 °C for at least 6 h. The dried pellets were then exclusively handled in an argon filled glove box (MBraun, Labmaster) with less than 0.1 ppm H₂O and O₂ in the gas. Lithium foil (Chemetall) was used as electrode material for conductivity measurements by two electrode ac impedance spectroscopy and four electrode dc techniques. The lithium foil was pressed on the sides of the LLZO pellets (Fig. 1a) and then annealed at 170 °C for some minutes on a heating plate to improve the contact between Li and LLZO. For the dc measurements two additional electrodes were placed in the flank of the pellet. Therefore, two 0.5 mm wide grooves were cut in the flank and filled with Li metal (Fig. 1b). For both ac and dc measurements the Li

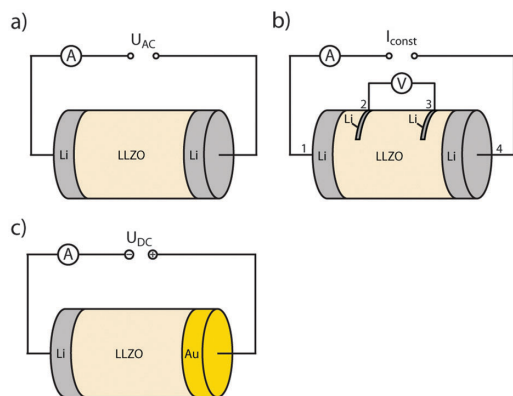


Fig. 1 Scheme of different electrode arrangements (a) for ac conductivity measurements with two lithium electrodes, (b) for dc conductivity measurements with four lithium electrodes and (c) for Hebb-Wagner type electronic conductivity measurements with one lithium and one Li ion blocking gold electrode.

electrodes were contacted with a silver or copper wire. These cells were sealed in gas-tight pouches of aluminized compound foil. Temperature dependent conductivity measurements were carried out in a temperature chamber (WTL 64 Weiss Technik) in the temperature range from $-40\text{ }^{\circ}\text{C}$ to $100\text{ }^{\circ}\text{C}$. A potentiostat/galvanostat (model SP-300 from Biologic Science Instruments) was employed for electrochemical characterization. The software package EC-Lab V10.02 was used for data acquisition and impedance data fitting. Impedance spectroscopy was carried out in the frequency range from 7 MHz to 1 Hz (amplitude of 20 mV).

Additionally, low-temperature impedance spectra down to $-148\text{ }^{\circ}\text{C}$ were recorded by employing a Novocontrol Concept 80 broadband dielectric spectrometer which is equipped with a BDS 1200 sample cell and a BETA analyzer. The latter is capable to measure impedances down to $10^{-14}\ \Omega$ at frequencies ranging from a few μHz to 20 MHz. Temperature regulation and controlling within an accuracy of about 0.5 K was carried out with a Quattro crysystem (Novocontrol) using dry nitrogen gas. The root mean square ac voltage was typically 0.1 V to 1.0 V. These data were mainly used to extract electrical relaxation rates from the corresponding modulus spectra.

The dc conductivity was measured by applying a constant current in the range from $1\ \mu\text{A}$ – $100\ \mu\text{A}$ between the electrodes 1 and 4 (Fig. 1b) and measuring the resulting voltage drop over the distance of the potential probes 2 and 3 (Fig. 1b). At each temperature a constant dc current was applied for 90 s. The voltage drop was simultaneously measured and remained constant over the measured time period.

The electronic partial conductivity of cubic LLZO was measured using the Hebb-Wagner technique.^{18,19} A gold blocking electrode of approximately $1\ \mu\text{m}$ thickness was deposited on one of the pellets surfaces by thermal Au evaporation. As mentioned above, Li foil was attached on the opposing surface as a reversible electrode for Li ions (Fig. 1c). Measurements were performed in potentiostatic

mode (Keithley 6430) in a home-built cell in the range from 2.5 V and 4.5 V vs. Li/Li^+ in an argon filled glove box with the Li electrode connected as cathode. Steady-state was assumed when the current remained constant within 10% over a period of several hours.

Results and discussion

Synthesis

Synthesis of cubic LLZO was only successful when an aluminium source was present during synthesis. Thus cubic LLZO formed either by working in Al_2O_3 crucibles, where the LLZO starting materials react with the crucible, or when intentionally using $\gamma\text{-Al}_2\text{O}_3$ powder as a dopant in the LLZO synthesis. Preparation of cubic LLZO in Al_2O_3 crucibles without further doping takes more than two calcination and milling steps due to the stepwise reaction of the powder at the crucible walls only. When the formation of phase pure cubic LLZO (by reaction with the wall) was completed the aluminium content of these samples was typically about 0.9 wt% as determined by ICP-OES. The Al free synthesis did not lead to pure cubic LLZO but rather to the tetragonal modification or a mixture of the cubic and tetragonal modifications of LLZO (Fig. 2a–b). Synthesis with 0.5 wt% Al_2O_3 led mainly to cubic LLZO, however, the corresponding reflexes are somewhat broader indicating that there might be some tetragonal LLZO present as well (Fig. 2c). Doping with 0.9 wt% Al_2O_3 in Al free crucibles as well as synthesis without doping but using Al_2O_3 crucibles led to cubic LLZO (Fig. 2d and e). These results clearly prove that the aluminium content plays a crucial role for the formation of phase pure cubic LLZO.

Structural information from MAS NMR

Structural features of Al-doped cubic LLZO were elucidated by ^{27}Al MAS NMR spectroscopy. In Fig. 3 the NMR spectra

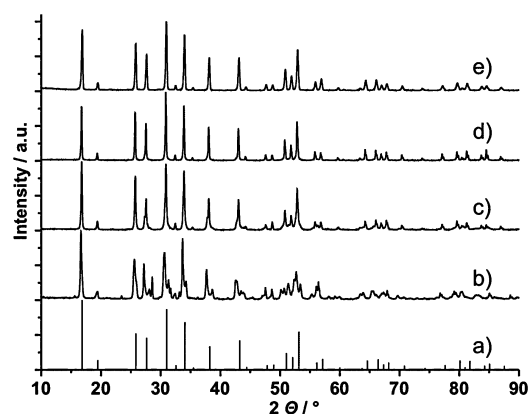


Fig. 2 XRD patterns of LLZO after the final calcination step (a) simulated pattern (JCPDS 80-0457), (b) Al-free synthesis in Al free crucible, (c) doping with 0.5 wt% $\gamma\text{-Al}_2\text{O}_3$ in Al free crucible, (d) doping with 0.9 wt% $\gamma\text{-Al}_2\text{O}_3$ in Al free crucible, (e) undoped sample prepared in Al_2O_3 crucible (0.9 wt% Al content measured by ICP-OES).

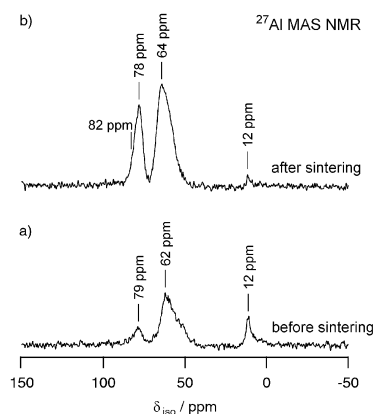


Fig. 3 ^{27}Al MAS NMR spectra of cubic LLZO before (a) and after sintering (b). The spectra were recorded at a magnetic field of 14.1 T and referenced to aqueous $\text{Al}(\text{NO}_3)_3$. The rotation frequency was 30 kHz.

of cubic LLZO before and after sintering at elevated temperatures (see above) are shown. The spectrum obtained after the sintering step is similar to that in ref. 10. Geiger *et al.* suggest that the signal showing up at a chemical shift of $\delta_{\text{iso}} = 12$ ppm reflects octahedrally coordinated Al in LaAlO_3 being an impurity phase.¹⁰ The δ_{iso} value of 64 ppm (see Fig. 3b) is characteristic of Al ions residing on lattice sites with tetrahedral coordination. Most probably the Al ions occupy the Li site $24d$ in the garnet structure according to the aliovalent doping mechanism $3 \text{Li}^+ \rightarrow \text{Al}^{3+}$. Multiple-quantum magic angle spinning (MQ-MAS) measurements of Geiger *et al.* have shown that the asymmetry parameter η of the corresponding electric field gradient EFG tensor is close to zero indicating axial symmetry.¹⁰ Preliminary ^{27}Al MAS measurements on samples with varying Li, La and Al contents indicate that the signal near 80 ppm in fact represents at least two NMR lines.²⁰ Obviously, at a sufficiently large Al content, Al^{3+} ions occupy various magnetically inequivalent sites in the cubic LLZO structure. NMR lines near 80 ppm, which most likely reflect Al ions also occupying sites with tetrahedral coordination, show up for samples of cubic LLZO which are characterized either by a deficit of La and/or Zr.²⁰

It is worth mentioning that the cubic LLZO sample obtained before the sintering step (see the ^{27}Al MAS NMR spectrum in Fig. 3a) is characterized by a Li ion conductivity which is by about two orders of magnitude lower than that reported for cubic LLZO. The low Li conductivity of the non-sintered sample, which is comparable to that of LLZO crystallizing in tetragonal symmetry, has been confirmed by ^7Li NMR spin-lattice relaxation measurements revealing a rather low Li diffusivity.²¹ Comparison of the two spectra reveals distinct differences which might help explain the high ion conductivity (see below) of the sintered material from an atomic-scale point of view. Firstly, the sintering step clearly enhances the Al content within LLZO. Secondly, the NMR line intensity at 12 ppm has decreased after the sintering step. Thus, LaAlO_3 seems to act as a kind of precursor for the incorporation of Al into LLZO.

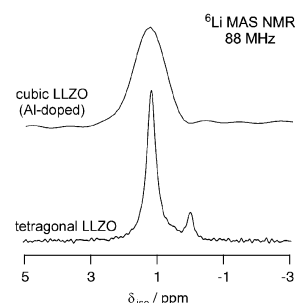


Fig. 4 ^6Li MAS NMR spectra of cubic and tetragonal LLZO. The latter was taken from ref. 21. A 1 M aqueous solution of LiCl served as reference. The spectrum of cubic LLZO refers to the sample which has been sintered at elevated temperatures; the corresponding ^{27}Al MAS NMR spectrum is shown in Fig. 8b. Note that the tetragonal Al-free sample and its Li dynamics have been investigated in detail by NMR spectroscopy in ref. 21.

Finally, in Fig. 4 (top) the ^6Li MAS spectrum of Al-doped cubic LLZO is shown. Even under MAS conditions with a spinning rate of 30 kHz, the ^6Li NMR line is comparably broad showing a line width (full width at half maximum, fwhm) of 1.1 ppm. This value should be compared with that one of the tetragonal Al-free counterparts (space group $I4_1/acd$)²¹ (see Fig. 4, bottom).

Crystal structure from neutron and X-ray diffraction

Our XRD results do not indicate any tetragonal distortion, but show some weak reflections, which can be attributed to a residue of lithium carbonate. These reflexes are more pronounced in the neutron data (Fig. 5) and the content of lithium carbonate can be quantified as 1.8(4) wt%. The comparison of neutron powder diffraction patterns collected at 4 K and 300 K indicates the isostructurality of LLZO at both temperatures. All reflexes originate either from cubic LLZO as the main phase or lithium carbonate as the residual phase. Different structure models were considered and simulated^{7,10,22} which, however, did not reveal a satisfactory description of the Bragg intensities mainly due to underestimated isotropic displacement parameters and differences in lithium occupations. After the adjustment of the models, the best results have been obtained with the model proposed by Geiger *et al.*¹⁰ Aluminium was not taken into account in their structure model, as its position in the lattice cannot easily be determined by X-ray diffraction. In fact, in the presence of relatively heavy lanthanum and zirconium atoms the location of “light” lithium and aluminium atoms is cumbersome. Moreover, the neutron scattering length b for aluminium is rather low and therefore small concentrations can be hardly quantified using neutron powder diffraction. However, the ^{27}Al MAS NMR spectra show that about 70% of the aluminium is located on the lithium sites with $24d$ symmetry which was included into our structure simulation. Placing Al on the $24d$ position did not improve the residual intensities in the difference between observed and calculated diffraction patterns, but affects the lithium occupation on the $24d$ site. Without aluminium $g_{\text{Li}(24d)}$ has been found to be 42(2)%, whilst $g_{\text{Li}(24d)} = 52(2)\%$ was

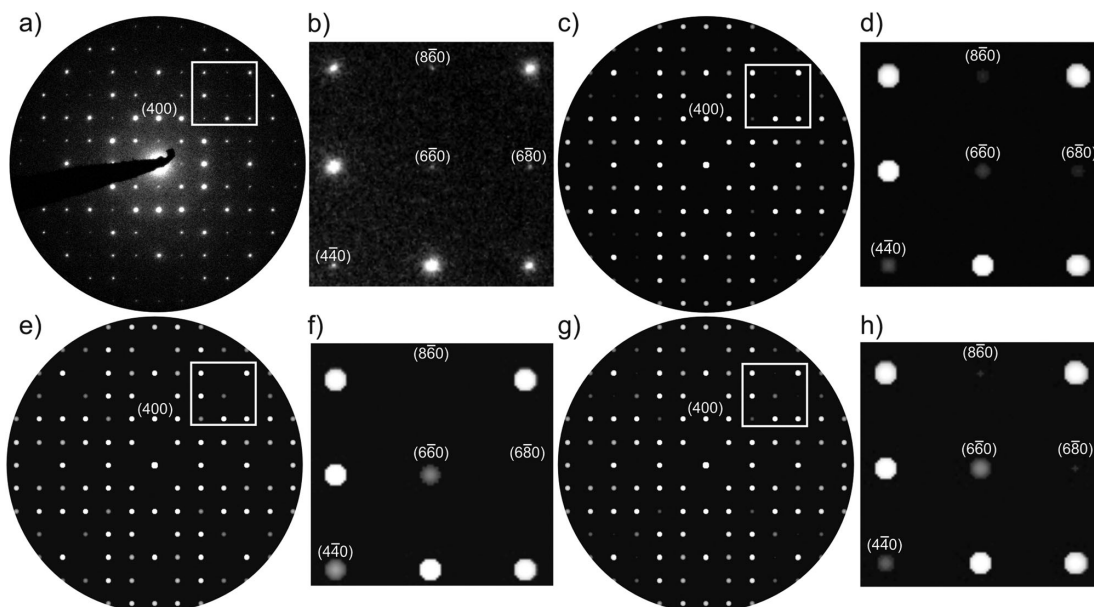


Fig. 5 (a) Experimental and (c) simulated PED patterns of LLZO along [001] assuming the cubic structural model from Table 1. (e) Simulated PED pattern of cubic LLZO according to ref. 9. (g) Simulated PED images of cubic LLZO using the structural model from ref. 10. (b), (d), (f) and (h) Enlarged areas of the marked regions in (a), (c), (e) and (g). The differences between the simulated and experimental PED patterns are clearly seen, with the experimental pattern most convincingly agreeing with the simulated image in (c) (our structure model from Table 1).

determined assuming the presence of Al with $g_{Al(24d)} = 6.53\%$. In the latter case the overall lithium content x in $Li_xLa_3Zr_2O_{12}$ has been determined to be 6.05 ± 0.25 , which agrees with the proposed heterovalent substitution mechanism $3Li^+ \leftrightarrow Al^{3+}$ (see above).¹⁰ The best fits to the neutron diffraction data collected at 4 K and 300 K were obtained with the parameters listed in Table 1 and the results of the Rietveld refinements are shown in Fig. 5. Anomalously large isotropic displacement parameters have been noticed for both lithium sites in LLZO already at low temperatures, which might be attributed to static lithium disorder. An application of the split site model to Li on the 24d atomic site did neither lead to a stable fit nor a significant improvement of the fit residuals. The comparison of results obtained at 4 K and 300 K indicates a minor influence of the temperature on the crystal structure of LLZO which is quite typical for garnet-like structures.^{23,24} Heating from 4 K to 300 K results in the elongation of the lattice parameter a by 0.223% with very small atomic movements involved. This means that only a small shift of Li2 in the a_1 direction of the cubic lattice takes place, whereas the coordinates for the other atoms in LLZO remain almost unchanged within the limits of their estimated standard deviations. Temperature increase causes a pronounced rise of displacement parameters on all atomic sites, but the major increase (ca. 50%) was observed for Li on the 96h atomic site and (ca. 30%) for Li on 24d. A strong increase of the displacement parameter indicates a development of dynamic lithium disorder on the background of the static one. The analysis of the temperature evolution of the anisotropic displacement parameters for lanthanum, zirconium and oxygen indicates their evolution from elliptic

towards spherical shape with nearly unchanged spatial orientation. This might correspond to a temperature stability of the framework built by these elements. A closer look on the disorder details by examination of differential Fourier maps indicates the presence of quite broad minima around Li (24d) with a stripe-like shape penetrating the garnet lattice. This anomaly can be related to the observed very high displacement parameters. However, details of such stripes with negative densities were sufficiently smeared out due to termination effects. Therefore, further examinations of the disorder have been performed using the maximum entropy method (MEM),²⁶ which can estimate non-zero structure factors for high-Q reflections (typically excluded in the analysis of the powder diffraction data). This feature makes the termination effect in MEM analysis less pronounced in comparison to Fourier synthesis, thus yielding less noisy three-dimensional distributions of electron/nuclear densities. Therefore, the MEM technique has been successfully used to a diversity of scientific problems either concerning disorder in $Sr_{9.3}Ni_{1.2}(PO_4)_7$ ²⁷ and in $Rb_4Cu_{16}I_{7.2}Cl_{12.3}$ ²⁸ or experimental visualization of lithium diffusion in Li_xFePO_4 ²⁹ and $La_{9.69}(Si_{5.70}Mg_{0.30})O_{26.24}$.³⁰

The negative nuclear densities obtained after the MEM analysis of datasets collected at 4 K and 300 K are shown in Fig. 6. They correspond to stripes observed in differential Fourier maps and might be related to the lithium diffusion pathway (as lithium is the only negative neutron scatterer in LLZO), where all lithium atoms take part in the diffusion process. Rise of the temperature from 4 K to 300 K unambiguously indicates an enhancement of Li-ion diffusivity, which corresponds to the increase of the ionic conductivity.

Table 1 Refined structural parameters of cubic LLZO at $T = 4$ K and $T = 300$ K as deduced from Rietveld refinement with FullProf. The space group is $Ia\bar{3}d$ (No. 230). Displacement parameters for lithium were modelled in isotropic approximation. Numbers in parentheses give the statistical deviations of the last significant digit

$T = 4$ K, Lattice parameter: $a = 12.9438(2)$ Å						
Atom site	x/a_1	y/a_2	z/a_3	$u_{\text{iso}} = u_{\text{eq}}/\text{Å}^2$	$u_{11}, u_{22}, u_{33}, u_{12}, u_{13}, u_{23}/\text{Å}^2$	Occ. g
Li1, 24d	1/8	0	1/4	0.041(6)	—	0.54(2)
Al1, 24d	1/8	0	1/4	0.041(6)	—	0.0653 ^a
Li2, 96h	0.0980(7)	0.6859(7)	0.5764(7)	0.020(4)	—	0.37(1)
La, 24c	0	1/4	1/8	0.0074(6)	0.0065(5), 0.0065(5), 0.0091(10), 0.0039(6), 0.00000, 0.00000	1.0
Zr, 16a	0	0	0	0.0067(3)	0.0067(3), 0.0067(3), 0.0067(3), 0.0006(5), 0.0006(5), 0.0006(5)	1.0
O, 96h	-0.03173(8)	0.05463(9)	0.14951(8)	0.0105(6)	0.0120(6), 0.0137(7), 0.0058(5), 0.0017(5), -0.0013(4), -0.0037(5)	1.0
Fit residuals: $R_p = 2.53\%$, $R_{wp} = 3.22\%$, $R_{exp} = 0.93\%$						
$T = 300$ K, Lattice parameter: $a = 12.9727(2)$ Å						
Atom site	x/a_1	y/a_2	z/a_3	$u_{\text{iso}} = u_{\text{eq}}/\text{Å}^2$	$u_{11}, u_{22}, u_{33}, u_{12}, u_{13}, u_{23}/\text{Å}^2$	Occ. g
Li1, 24d	1/8	0	1/4	0.054(5)	—	0.54 ^b
Al1, 24d	1/8	0	1/4	0.054(5)	—	0.0653
Li2, 96h	0.1004(8)	0.6853(8)	0.5769(8)	0.031(3)	—	0.37 ^b
La, 24c	0	1/4	1/8	0.0106(6)	0.0095(4), 0.0095(4), 0.0128(9), 0.0035(6), 0.00000, 0.00000	1.0
Zr, 16a	0	0	0	0.0095(3)	0.0095(3), 0.0095(3), 0.0095(3), 0.0005(5), 0.0005(5), 0.0005(5)	1.0
O, 96h	-0.03161(8)	0.05454(9)	0.14940(8)	0.0148(6)	0.0170(6), 0.0179(6), 0.0094(5), 0.0018(5), -0.0006(4), -0.0026(5)	1.0
Fit residuals: $R_p = 2.22\%$, $R_{wp} = 2.79\%$, $R_{exp} = 0.94\%$						
^a Taken from NMR experiments. ^b Fixed to the value obtained at 4 K.						

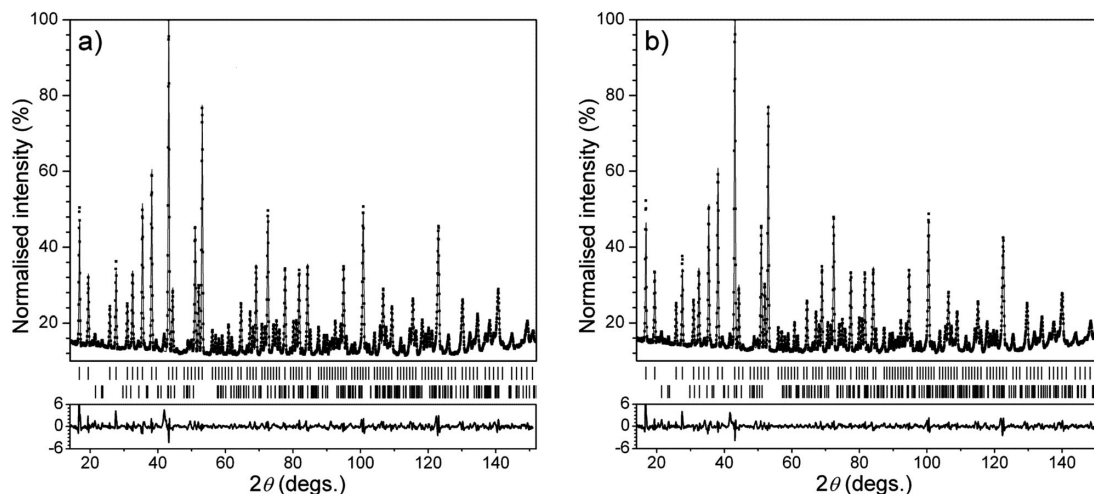


Fig. 6 Results of Rietveld refinements for neutron powder diffraction data at 4 K (a) and 300 K (b) for LLZO ($\lambda = 1.5482$ Å). Calculated positions of Bragg reflections are shown by vertical tick marks, where the top row of the tick marks corresponds to LLZO, whilst the lower ones describe the peak positions for lithium carbonate. Differences between observed and calculated pattern are shown below.

It is noteworthy that the structural investigations were carried out on the LLZO powder before sintering. Although the ^{27}Al NMR results show changes of the Al distribution on different crystallographic sites during sintering which seems to have a significant effect on the Li diffusivity we do not believe that this significantly changes the results of the diffraction investigations. As already mentioned it is quite cumbersome to

refine Al and Li positions with a high level of reliability. Therefore, from a crystallographic point of view, the small structural changes detected by NMR after sintering might only lead to an increase of the Li displacement parameters. The small changes in the occupations of La and Zr positions by Al will hardly be detectable by diffraction methods. As the disorder of Li atoms is already quite high, an additional

increase will be within the limit of reasonably refineable displacement parameters. Nevertheless, this will be a subject for further investigations.

PED and HRTEM results

In the last decade, PED has become a powerful technique for the advanced characterization of materials. The superior advantage of the PED method over the SAED technique is its ability to reduce dynamical effects arising due to multiple scattering in the transmission electron microscope. Dynamical effects in SAED patterns make the distinction between two phases difficult, particularly, if the phases are structurally and chemically related, as it is the case for cubic and tetragonal LLZO (see ESI†, Fig. SX1). In this case, the diffraction patterns differ only by the absolute values of diffracted intensity. Recently, PED was successfully applied for the distinction of polymorphs occurring in bulk materials and thin films, *e.g.* of quartz³¹ and Ag₂Se,³² respectively. In the present work, we compare our results from PED examinations on single microcrystals with those from neutron powder diffraction. Fig. 7a displays the experimental PED pattern of a LLZO sample containing 0.9 wt% of Al and the simulated PED patterns based on the cubic and tetragonal LLZO along zone axis [001] (Fig. 7b and c, respectively). The differences in the simulated intensities of the reflections $h00$ with $h = 2n$ are obvious.

For the cubic phase, the $h00$ reflections with $h \neq 4n$ are kinematically forbidden (Fig. 7b). However, since the PED only reduces dynamical effects, the serial reflection conditions based on the 4_1 screw axis can be violated by residual dynamical effects. Thus, the significant intensity of the (200) reflection in the experimental PED pattern (Fig. 7a) can be rationalized, even for the cubic structure. The dynamical effects decrease with increasing h , thus, the intensity of the reflections (600) and (10 0 0) are zero in the experimental and simulated patterns (Fig. 7a and b). In the case of the tetragonal LLZO, the integral reflection condition $h00$ with $h = 2n$ is consistent with the occurrence of strong reflections (600) and (10 0 0), *cf.* the simulated pattern in Fig. 7c. Simulated patterns based on the tetragonal and cubic polymorphs also

indicate differences in the intensities of (440) and (660) reflections, *cf.* line profiles in Fig. 7. Thus, the experimental PED pattern is better described by the cubic structure of LLZO. It should be noted that we have tested different structural models for PED simulations obtained from neutron powder diffraction. We found that calculated PED patterns using the structural model in Table 1 show the best match with our experimental PED data. In addition, the calculated PED patterns using the structural model for LLZO of Table 1 match even better as the PED images calculated based on the models for the cubic LLZO^{8,10} (see *e.g.* Fig. 8).

Even when adjusting low dose settings, the LLZO sample was extremely unstable under the imaging conditions used for HRTEM. Thus, a complete series of images with variable focus values could not be recorded without initiating considerable loss of structural ordering. Fig. 9a and b show experimental and Fourier-filtered HRTEM micrographs for the first overfocused image of a focus series, zone axis [111]. The simulated micrograph of Fig. 9c convincingly agrees confirming again our assignment to the cubic structure given in Table 1. However, after a few seconds the structure is completely amorphized, just leaving crystalline islands embedded within an amorphous matrix, *cf.* complete focus series in ESI†, Fig. SX2.

EDX investigations showed a homogeneous distribution of Al in the LLZO sample within the experimental errors. Particularly, no Al-rich regions were found in the LLZO specimen (see ESI†, Fig. SX3).

Electrochemical results

Electrochemical measurements were performed to determine the ionic and electronic conductivity of the cubic LLZO. The total conductivity was measured both by ac impedance spectroscopy and four electrode dc measurements. The electronic conductivity was determined by the Hebb–Wagner technique.^{18,19} Impedance measurements with Au electrodes on LLZO known from the literature show two semicircles and a low frequency tail. These were interpreted to be corresponding to the bulk, grain boundary and electrode contributions, respectively.⁶ Our impedance measurements performed with

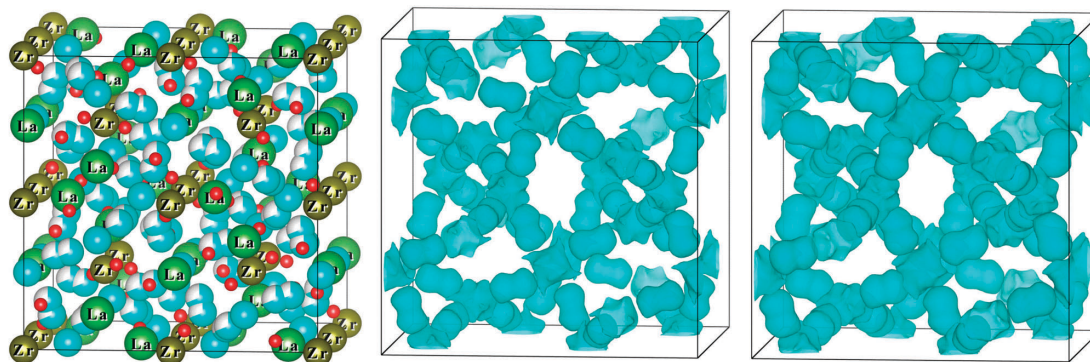


Fig. 7 Structural model of cubic LLZO (left, atoms shown by cyan and red correspond to lithium and oxygen, respectively) and negative scattering neutron density maps determined at 4 K (middle) and 300 K (right) by MEM. Negative scattering neutron density maps are shown with an equidensity level of $0.035 \text{ fm } \text{\AA}^{-3}$. Data visualization has been performed using the program VESTA.²⁵

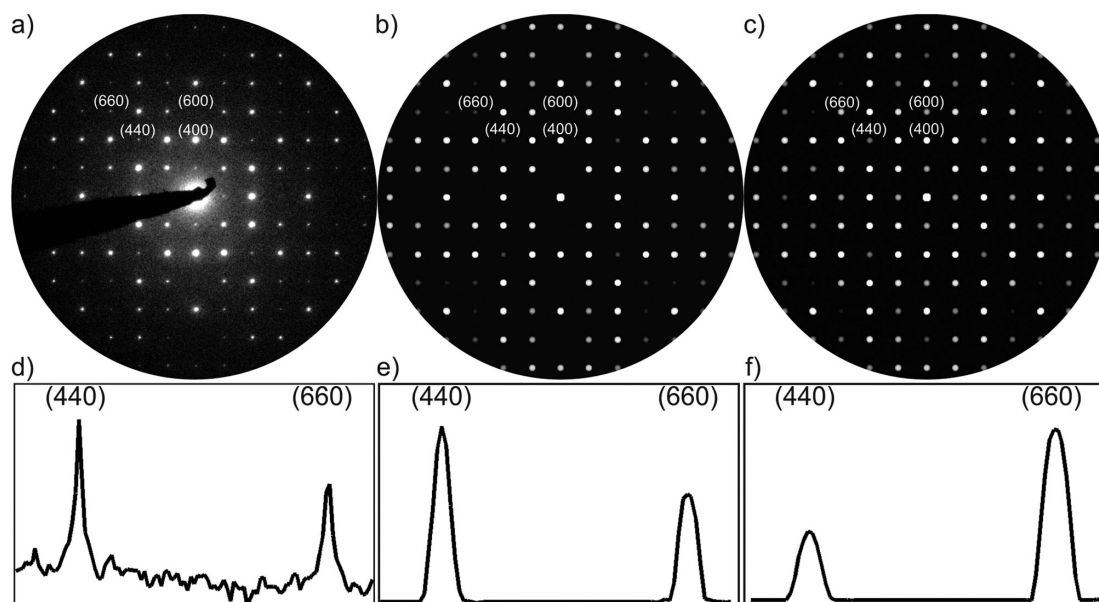


Fig. 8 (a) Experimental and (b) simulated PED patterns of LLZO along [001]. For the simulation of (b) we used the cubic structure model presented in Table 1. (c) Simulated PED images of tetragonal LLZO based on the structure model from ref. 7. (d)–(f) Line profiles taken from (440) and (660) reflections in (a)–(c). The differences in the intensities of (600), (440) and (660) reflections are clearly seen. The experimental pattern fits better to the cubic LLZO.

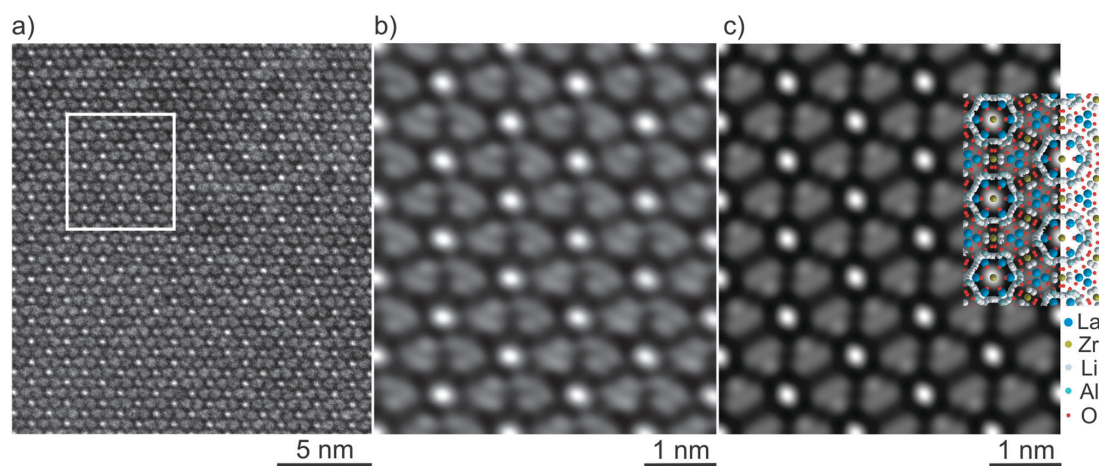


Fig. 9 (a) Experimental HRTEM micrograph of LLZO along [111] viewing direction. (b) Fourier-filtered HRTEM image of the region marked in (a). (c) Simulated HRTEM image (defocus 90 nm, $t = 9$ nm, 2-fold astigmatism estimated to 10 nm) based on the crystal structure model of LLZO from Table 1 (inserted).

Li electrodes show only one semicircle for the total resistivity of the LLZO pellet and a second semicircle instead of the tail. The appearance of an additional semicircle when using Li electrodes can be expected since Li electrodes can reversibly incorporate Li ions from the LLZO, so the charge transfer resistance and the electrode capacity should give rise to an additional semicircle in the impedance measurements explaining the appearance of a second semicircle instead of the low

frequency tail. Still it was surprising that our samples only showed one semicircle for the LLZO contribution so we took a detailed look into the impedance data to be sure that there was no misinterpretation. Fig. 10a shows an example of a typical Nyquist plot measured on a LLZO pellet between Li electrodes. Impedance data were fitted with an equivalent circuit (RC)(RQ) or (RQ)(RQ) depending on whether the respective sample showed a depressed high frequency semicircle or not.

From the fit to this measurement the first high frequency semicircle resistance and capacity were determined to be 20.4 k Ω and 0.38 nF, respectively. The second low frequency semicircle resistance and capacity result in 13.3 k Ω and 0.15 μ F, respectively. These relatively high capacity values are typical for grain boundaries or electrodes of polycrystalline ceramics.³³ As both semicircles yield to comparable resistances as supposed for the bulk and grain boundary contributions in cubic LLZO,⁶ some additional experiments were carried out to clarify the origin of the impedance contributions when using Li electrodes. Fig. 10b shows a Nyquist plot of a sample measured once with Au and once with reversible Li electrodes. The Au electrodes were gas phase deposited by thermal evaporation, whereas the Li electrodes were pressed

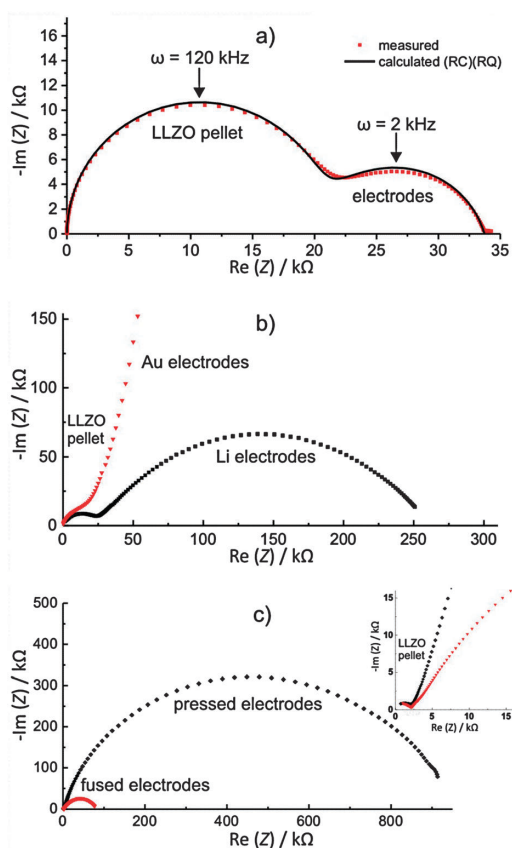


Fig. 10 Room temperature impedance spectra of different LLZO samples with various electrodes (a) impedance spectrum of a LLZO pellet doped with 0.9 wt% Al. The pellet size was 5.3 mm diameter and 16.2 mm length. The pellet was sandwiched between two Li electrodes (frequency range from 7 MHz to 50 mHz at 20 mV amplitude). An equivalent circuit (RC)(RQ) was used to fit the impedance data. (b) Impedance spectra of a LLZO pellet doped with 0.9 wt% Al measured with blocking Au and reversible Li electrodes in a frequency range 7 MHz to 1 Hz at 20 mV. (c) Impedance spectra of a LLZO pellet doped with 0.9 wt% Al measured with Li electrodes pressed and fused on the pellet (frequency range 7 MHz to 1 Hz at 20 mV).

mechanically on the pellet. The measurement with the Au electrodes shows a semicircle merging into a low frequency tail. The low frequency tail is caused by an almost solely capacitive behaviour of the Au electrodes indicating their blocking nature under the given experimental conditions. The measurement with Li electrodes leads to two semicircles proving that the second semicircle corresponds to the Li electrodes charge transfer resistance and capacity. This also clarifies that our samples only show one semicircle representing the total resistivity of the LLZO pellet. Murugan *et al.* reported that bulk and grain boundary contributions could only be resolved at low temperatures,⁶ *i.e.*, in their case room temperature and slightly above. In the present case even at -40 $^{\circ}$ C only one semicircle representing the total resistivity of the sample is observed. As shown in Fig. 10c the charge transfer resistance of the Li electrodes depends strongly on the preparation method of the Li electrodes. Two impedance measurements of the same sample, in one case with Li electrodes gently pressed on the pellet and in the second case with Li electrodes fused on the pellet, were performed. The different preparation methods change the charge transfer resistance almost by one order of magnitude while the pellet resistance remains unchanged as seen in the inset. We did not find any evidence for a reaction of the LLZO with Li metal which might have shown up as an additional impedance during our measurements. It has to be noted that the charge transfer resistance is not negligible and may play a role when LLZO is applied as a solid electrolyte in battery cells with Li metal electrodes. The total voltage drop across a cell is the sum of the charge transfer resistances at the electrode interfaces and the voltage drop along the electrolyte bulk itself. Therefore further investigations on the charge transfer resistances between different electrode materials and preparation procedures are in progress.

In addition to ac impedance we used four electrode dc measurements to determine the conductivity of the samples under continuous current load. By using the four electrode dc technique the bulk resistance of the sample (as a sum of grain and grain boundary contributions) can be determined without electrode overvoltages. The results of the dc conductivities are shown together with ac data in Fig. 11. Comparing the conductivities of samples with different aluminium contents it is clearly visible that the conductivity depends on the aluminium content in the samples. The highest conductivity of 3×10^{-4} Scm $^{-1}$ to 4×10^{-4} Scm $^{-1}$ at 25 $^{\circ}$ C were found for samples containing 0.9 wt% Al prepared either by synthesis in Al $_2$ O $_3$ crucibles or by intentional γ -Al $_2$ O $_3$ doping. The Arrhenius activation energy is determined to be 0.34 eV. The conductivity and activation energy data agree well with results from Murugan *et al.*⁶ who did not report on any aluminium in their samples and did not give information on the impurity level at all. The 0.5 wt% Al containing sample (γ -Al $_2$ O $_3$ doped) shows a slightly lower conductivity of 1×10^{-4} Scm $^{-1}$ but the same activation energy of $E_a = 0.34$ eV. The Al-free sample with tetragonal crystal structure is characterized by a two orders of magnitude lower conductivity of 2×10^{-6} Scm $^{-1}$ at 25 $^{\circ}$ C and an activation energy $E_a = 0.49$ eV. The latter value is in good agreement with that reported for a tetragonal sample which has recently been

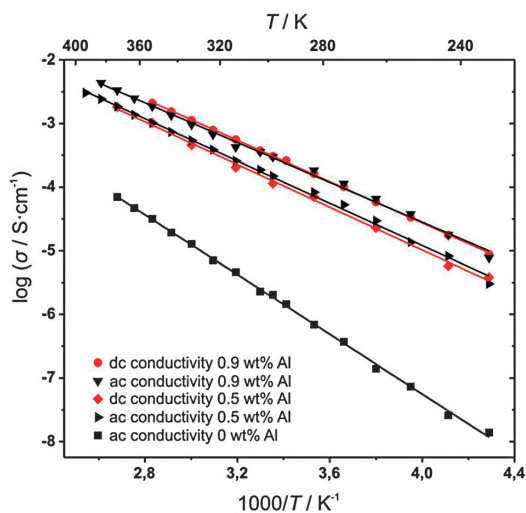


Fig. 11 Temperature dependence of the conductivity of LLZO samples with different Al contents. Al-containing samples have been studied by two electrode ac (impedance) as well as four electrode dc techniques. Note, for the sake of readability $\log \sigma$ vs. $1000/T$ is shown. The activation energies given in the text were calculated from the slope of $\ln(\sigma T)$ vs. $1000/T$ remembering that $\ln(\sigma T) = \ln \sigma_0 - E_a/RT$.

investigated by NMR spectroscopy.²¹ The electronic conductivity of cubic LLZO, which controls the self-discharge of a lithium battery and therefore is of great interest, was measured with a Hebb–Wagner type cell arrangement with one reversible and one blocking electrode (Fig. 1c). In optimal cases Hebb–Wagner measurements can be used to determine the individual electron hole and electron partial conductivities as a function of the Fermi level (*i.e.* as a function of the lithium metal content in the present case).

When the cell is polarized, as can be seen in Fig. 1c, a high mixed ionic and electronic transient current is rapidly decreasing and finally reaching a steady state electronic current. The steady state current under ion-blocking conditions can only be due to electron and hole conduction in the material as no Li ions can be delivered from the blocking gold electrode. Prior to the polarization experiments the open circuit voltage of the cell shown in Fig. 1c was approximately 2 V which is probably due to formation of a lithium gold alloy at the LLZO Au interface³⁴ prior to the measurement. Lithium activity gradients in the sample may also be a reason as well as capacitive effects of the high resistance cell. (Note that the low electronic conductivity leads to an electronic resistance in the order of $10^{10} \Omega$). Fig. 12 shows the potential dependent mean conductivities measured in the range of typical battery operating voltage. As described in detail in the literature on the Wagner–Hebb technique, the increasing voltage leads to a corresponding decrease of the chemical potential of Li at the Au electrode. This changes the electron and hole concentrations in LLZO. Therefore, the overall electronic partial conductivity increases with increasing polarization voltages. Over the potential range of 2.5 V–4.5 V the electronic conductivity takes values in the range from

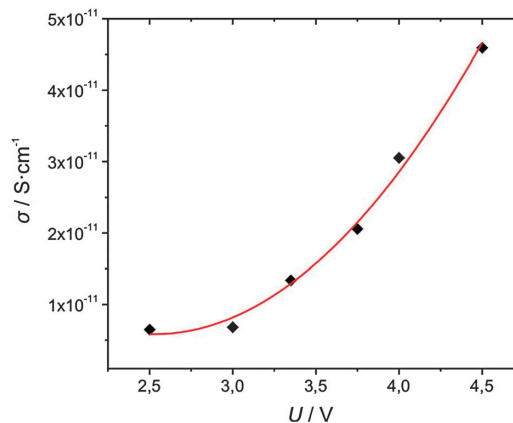


Fig. 12 Partial electronic conductivity of a cubic LLZO pellet vs. Hebb–Wagner cell voltage at room temperature. The solid line is only a guide to the eye.

$5 \times 10^{-12} \text{ Scm}^{-1}$ to $5 \times 10^{-11} \text{ Scm}^{-1}$. With the total conductivity of $3 \times 10^{-4} \text{ Scm}^{-1}$ the electronic and ionic transference numbers

$$t_{e^-} = \frac{\sigma_{e^-}}{\sigma_{\text{total}}} \quad \text{and} \quad t_{\text{Li}^+} = \frac{\sigma_{\text{Li}^+}}{\sigma_{\text{total}}} \quad (1)$$

result in values between 2×10^{-8} – 2×10^{-7} and 0.99999998 – 0.99999998 , respectively. This clearly shows that cubic Al-doped LLZO is an almost exclusive Li ion conducting material having great potential as an electrolyte for lithium-ion batteries. We note that the increase of the electronic conductivity with increasing potential is due to growing hole conduction.

Solid-state NMR measurements

In addition to impedance spectroscopy we used various NMR techniques to probe Li dynamics in a sintered sample of garnet-like LLZO crystallizing with cubic symmetry. In Fig. 13 the central transitions (see below) of a typical set of ^7Li NMR spectra of cubic LLZO doped with 0.9 wt% Al are shown. The corresponding ^{27}Al MAS NMR spectrum is shown in Fig. 3b. The ^7Li NMR spectra were recorded at various temperatures at a resonance frequency of 155.5 MHz. The broad NMR line, which is observed at the very low temperatures, can be well represented by a Gaussian reflecting the distribution of resonance frequencies due to non-averaged dipole–dipole interactions of the Li nuclei. Here, the associated line width δ (full width at half maximum) of this so-called rigid lattice regime is given by $\delta_{\text{rl}} = 9.7(2) \text{ kHz}$. In this temperature range the mean Li jump rate $1/\tau$ is much smaller than the spectral width δ_{rl} , *i.e.*, $1/\tau \ll 10^3 \text{ s}^{-1}$. With rising temperature $1/\tau$ increases resulting in an averaging of homonuclear dipolar interactions. Consequently, the NMR line increasingly narrows, finally reaching the width δ_{en} which is solely governed by inhomogeneities of the external magnetic field used (regime of extreme narrowing). Interestingly, in the case of cubic LLZO doped with Al a heterogeneous motional narrowing (MN) is observed. At intermediate temperatures

the NMR line partially narrows resulting in a two-component line shape, *i.e.*, the broad rigid-lattice line (see above) is superimposed by a motionally narrowed Lorentzian-shaped component.³⁵ Recently, the same behaviour has been observed by Koch *et al.* who studied the Li dynamics in the garnet $\text{Li}_5\text{La}_3\text{Nb}_2\text{O}_{12}$.³⁶ It is worth mentioning that the spectra shown in Fig. 13 were simply obtained by Fourier transformation of a free induction decay recorded after excitation with a 90° pulse. Thus, quadrupole intensities arising from the interaction of the spin-3/2 probe nucleus with electric field gradients produced by the electric charge distribution in the neighbourhood of the Li nuclei are largely suppressed. These can be made visible by using appropriate echo pulse sequences.^{35,37} Usually, when low temperatures are regarded, such interactions are represented by a broad Gaussian line of low intensity characterized by a width of some tens of kHz.^{21,36} As an example, a stimulated echo NMR spectrum is shown in Fig. 13e which has been recorded using the Jeener–Broekaert echo sequence.³⁸ In the present case, we will exclusively focus on the ^7Li NMR central transition of LLZO. In contrast to other garnet-like oxides, in the case of cubic LLZO two-phase NMR spectra show up at

temperatures as low as 200 K indicating a spin ensemble of rapidly diffusing Li ions (see Fig. 13). As an example, at 220 K the narrow Lorentzian-shaped component shows a line width of approximately 1.9 kHz while the broad one is characterized by $\delta = 8.7$ kHz. The area fraction A_f of the narrow line, which reflects the number fraction of fast Li ions with jump rates larger than about 10^4 s^{-1} , amounts to approximately 19% at this temperature. Values of A_f have been estimated by fitting the spectra with a combination of two Voigt functions. Interestingly, A_f steadily increases with increasing T reaching 28% at 233 K, 35% at 243 K, and 41% at 253 K. At a temperature of 263 K nearly 50% of the total number of Li ions participate in a very fast Li diffusion process. The corresponding line width of the sharp component became smaller than 1 kHz. Thus, with rising temperature the fractional amount of Li ions being highly mobile on the NMR time scale increase in an almost linear fashion (Fig. 13c), a similar behaviour has been found for nanocrystalline LiNbO_3 .³⁸ Let us note that at higher temperatures a separation of the two spin reservoirs with their distinct dynamics turns out to be difficult. This is due to the fact that the broad spectral component, representing rather

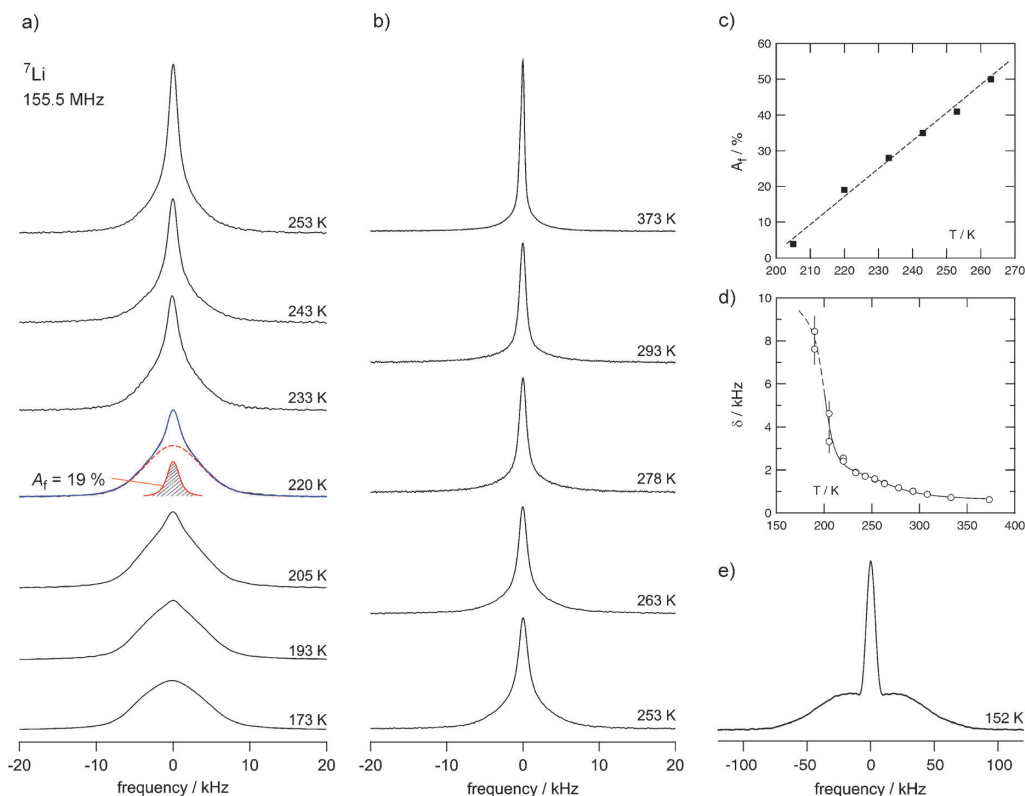


Fig. 13 (a) and (b) ^7Li NMR spectra of a non-rotating sample of cubic LLZO (0.9 wt% Al) recorded at 155.5 MHz in the temperature range from 173 K to 373 K. As an example, the two-component NMR line at 220 K is represented by a superposition of two Voigt functions, that is, a combination of a Gaussian and a Lorentzian. The area fraction $A_f = f(T)$ of the narrow contribution (solid line), representing very fast Li ions in LLZO, amounts to approximately 19%. The dashed line shows the dipolarly broadened component which reflects slow Li ions. See text for further details. (c) Temperature dependence of A_f , (d) NMR line width d of the narrow component highlighted in (a), (e) ^7Li stimulated echo NMR spectrum recorded at 152 K in order to reveal quadrupole intensities next to the Gaussian-shaped central transition.

slow Li ions in LLZO, steadily decreases in intensity. The heterogeneous MN observed at low T might reflect a large distribution of Li jump rates. Such a distribution is expected to be preserved even at temperatures larger than 300 K. Interestingly, even the line width of the sharp component reveals a stepwise narrowing reflecting a transition from partial to full averaging of dipolar interactions. Starting from 2 kHz at 263 K the line width is further decreased with increasing T finally reaching 800 Hz in the regime of extreme narrowing (see Fig. 13d). This is very similar to the behaviour observed by ^7Li NMR spin-spin-relaxation measurements discussed below (see Fig. 14).

In addition to NMR line shapes, ^7Li NMR spin-lattice relaxation (SLR) rates have been recorded in both, the laboratory and rotating frames of reference, see ref. 21, 37, and 39 for an introduction into these NMR techniques. It is worth mentioning that the two components of the NMR line are characterized by the same ^7Li SLR NMR rates R_1 and $R_{1\rho}$. Thus, a separation of the two, dynamically different spin reservoirs according to that shown previously for the nanocrystalline two-phase Li conductor $\text{Li}_2\text{O}:\text{Al}_2\text{O}_3$,^{35,40} is not possible. In contrast to the present work, in the previous study two spin ensembles, which seem to be unaffected by spin-diffusion effects, were anticipated to be also spatially separated.²⁹ The temperature dependence of the rates of the sintered sample of cubic LLZO, which have been recorded at different frequencies, are shown in Fig. 14 in an Arrhenius plot. Below 180 K, *i.e.*, in the rigid-lattice regime (see above), the rates are governed by non-diffusive background relaxation and reveal a weaker-than-activated temperature dependence. Presumably, the SLR NMR rates in this temperature range are influenced by lattice vibrations, interactions between the spins and paramagnetic impurities and/or by strictly localized, *i.e.*, caged ion dynamics which do not reflect translational jump processes. However, at higher temperatures the SLR

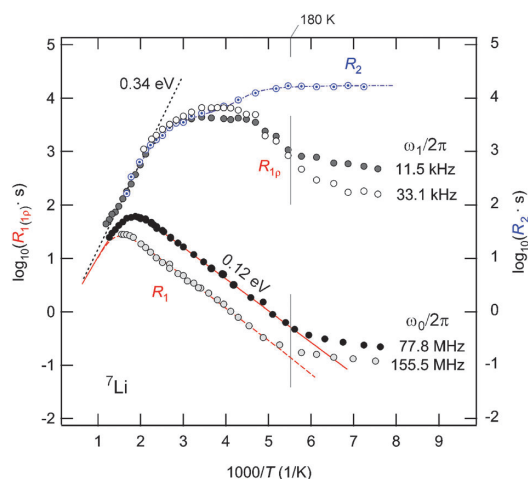


Fig. 14 Temperature dependence of the ^7Li NMR spin-spin (R_2) as well as spin-lattice relaxation rates (R_1 and $R_{1\rho}$) of cubic LLZO. The NMR spin-lattice relaxation rates were measured at the frequencies indicated. Spin-spin relaxation rates were recorded at a resonance frequency of 77.8 MHz. See text for further details.

NMR rates pass through characteristic diffusion-induced rate peaks from which Li jump rates $1/\tau$ and activation energies $E_{a,\text{NMR}}$ can be deduced. Interestingly, the rates recorded at 77.8 MHz reveal an asymmetric diffusion-induced peak $R_1(1/T)$. In general, the low-temperature flank, for which $\omega_0\tau \gg 1$ holds, is influenced by short-range Li motions which might be affected by correlation effects (see below).^{21,37,39,40} Compared with this, on the high-temperature side of the rate peak, *i.e.*, in the limit $\omega_0\tau \ll 1$, the SLR rate is governed by long-range Li transport.^{21,37,39,40}

The mean diffusion parameters characterizing the latter are directly comparable with the results obtained from dc conductivity measurements (see above). The solid line in Fig. 14 represents a fit according to the model introduced by Bloembergen, Purcell and Pound⁴¹ which was originally developed for isotropic uncorrelated diffusion: $R_1 \propto \tau/[1 + \omega_0\tau]^\beta$. Here, the asymmetry of the rate peak is taken into account by the parameter β , which can adopt values ranging from 1 to 2. $\beta = 2$, the so-called BPP-behaviour, is obtained for uncorrelated motion. $\beta < 2$ indicates that the underlying hopping correlation function $G(t)$ is represented by a non-exponential rather than an exponential function. Correlation effects such as structural disorder and/or Coulomb interactions are considered to be responsible for the deviation from exponential time behaviour of $G(t)$. In the present case, β amounts to about 1.4; the activation energy $E_{a,\text{NMR}}$ turns out to be approximately 0.31 eV. This value is in good agreement with that probed by impedance spectroscopy (see above). For comparison with $E_{a,\text{NMR}}$, the corresponding activation energy in the limit $\omega_0\tau \gg 1$ turns out to be about $E'_{a,\text{NMR}} = 0.12$ eV. In general, $E'_{a,\text{NMR}}$ and $E_{a,\text{NMR}}$ are linked with each other *via* $E'_{a,\text{NMR}} = (\beta - 1) E_{a,\text{NMR}}$.³⁷ In addition, β determines the frequency dependence of R_1 in the limit $\omega_0\tau \gg 1$ according to $R_1 \propto \omega_0^{-\beta}$. No frequency dependence is expected in the limit $\omega_0\tau \ll 1$ when 3D diffusion is regarded.³⁷ This is in contrast to ion conductors showing low-dimensional Li diffusion.^{37,42-44}

Owing to technical limitations of our NMR setup, temperatures higher than 800 K could not be reached. Thus, the high-temperature flank of the R_1 rate peak recorded at 77.8 MHz was only partly accessible. However, with the help of SLR NMR measurements performed in the rotating frame of reference and carried out at locking frequencies $\omega_1/2\pi$ in the kHz the complete high-temperature flank of the corresponding diffusion-induced rate peak can be probed. The dotted line in Fig. 14 represents an Arrhenius fit of some of the data points of the high- T flank of the $R_{1\rho}$ data recorded at $\omega_1/2\pi = 11.5$ kHz. The fit yields an activation energy of approximately 0.34 eV and is in good agreement with the trend of the ^7Li NMR spin-spin relaxation rates R_2 which are also included in Fig. 13. The $R_{1\rho}$ measurements are limited by R_2 leading to an apparently broad rate peak whose top is cut off. Nevertheless the temperature at which the rate maximum appears can be estimated to be approximately 300 K. In general, the diffusion-induced SLR rate maximum shows up when the Li correlation rate $1/\tau'$ reaches the order of the angular frequencies ω_0 and ω_1 , respectively.³⁷ $1/\tau'$ is expected to be identical with the mean jump rate $1/\tau$ within a factor of two. In Fig. 15 the Li

jump rates $1/\tau_{\text{NMR}}$ directly deduced from the rate maxima according to $\omega_0\tau_{\text{NMR}} = 1$ and $\omega_1\tau_{\text{NMR}} = 0.5$, see ref. 39, respectively, are shown in an Arrhenius plot. The additional vertical axis in Fig. 15 converts the rates $1/\tau_{\text{NMR}}$ into self-diffusion coefficients according to the Einstein–Smoluchowski equation: $D_{\text{NMR}} = a_j^2/(6\tau_{\text{NMR}})$. The mean jump distance a_j was estimated to be approximately 0.2 nm. In analogy to previous studies^{21,45,46} comparing results obtained from NMR with those from impedance spectroscopy, dc conductivity values σ_{DC} (Fig. 11) have been roughly converted into Li jump rates using both the Nernst–Einstein and Einstein–Smoluchowski equations. As is well-known, the combination of the two relations yields

$$\tau_{\sigma}^{-1} = H_{\text{R}} f_{\text{c}} \frac{6k_{\text{B}}T}{Nq^2a_j^2} \sigma_{\text{DC}} \quad (2)$$

where N denotes the number density of charge carriers and q the charge of the Li ions. The product of Haven ratio H_{R} and correlation factor f_{c} was assumed to be 1. Additionally, in Fig. 15 electrical relaxation rates $1/\tau_{\text{M}}$ are included which were obtained from the imaginary part of the electrical modulus M'' which has been analyzed as a function of frequency ν . Modulus spectra $M''(\nu)$ were recorded at various temperatures T (not shown here for the sake of brevity). The characteristic maxima show up when $1/\tau_{\text{M}}'$ is of the order of the angular frequency $\nu 2\pi$. The solid line in Fig. 15 represents a fit taking into account $1/\tau_{\text{M}}'$ and $1/\tau_{\sigma}$ yielding 0.34 eV (see above).

The jump rates $1/\tau_{\text{NMR}}$ obtained from NMR R_1 measurements are in fair agreement with the conductivity results. The agreement between $1/\tau_{\sigma}$ and $1/\tau_{\text{NMR}}$ probed via $R_{1\rho}$ turns out to be somewhat better which might be due to the fact that the two methods probe Li dynamics on a very similar time scale. For the sake of completeness, a Li jump rate is included in Fig. 15 which has been estimated from NMR line narrowing (Fig. 8). Slightly above 200 K the narrow

component shows up. At 225 K the corresponding line width is reduced to $\delta_{\text{H}}/2$ and the associated jump rate is given by $1/\tau_{\text{NMR}} = \delta_{\text{H}}/2\pi$. For comparison, at 205 K the rates R_2 start to deviate from their rigid-lattice value $R_{20} = 60 \mu\text{s}$ leading to $1/\tau_{\text{NMR}} \approx R_{20}$ at this temperature. This jump rate is also included in Fig. 15. Taken together, the jump rates probed by NMR spectroscopy corroborate the transport parameters of a sintered sample of cubic LLZO obtained from impedance spectroscopy. In agreement with line widths measurements (Fig. 13d), R_2 shows a two-step decrease with increasing temperature indicating that the Li ions get access to further diffusion pathways at elevated temperatures.

Conclusions

We have synthesized the two different structural modifications of LLZO and found a certain Al content to be necessary for the formation of cubic LLZO. One already could speculate from the patent by Yoshida⁴⁷ that Al is a necessary ingredient for the formation of cubic LLZO. As in the present work, the recently published papers^{10–13} state that cubic LLZO only forms when Al is present during synthesis but there was no definite knowledge about the role of Al. With the combination of XRD, TEM-PED and neutron scattering we are able to propose a structure model which takes both Al and Li ions into account. Neutron diffraction measurements show a high degree of Li disorder even at 4 K which becomes even more pronounced at 300 K. We regard this disorder as the reason for the high mobility of the Li ions in the cubic garnet-type lattice. As proved by ²⁷Al MAS NMR spectroscopy most of the Al ions are located on the 24d site. With the results of phase transformation during synthesis we regard the Al ions on the 24d site to stabilize the cubic garnet structure.

NMR was found to be a very sensitive probe for small structural changes in the garnet-type lattice. NMR shows that minor changes of the Al distribution during the sintering process cause the Li disorder to become even more pronounced than in the powder before sintering. The TEM-PED patterns agree very well with our proposed structure model and the corresponding pattern simulation; other structure models fit less well. The simulated structure image also fits well with the HRTEM image, confirming our cubic structure model.

Electrochemical measurements performed with different LLZO samples confirm that the conductivity depends on the Al content, *i.e.*, the degree of transformation from the tetragonal to the cubic crystal structure. Ac and dc conductivities show almost identical values approving the high conductivity also under current load. Li jump rates deduced from NMR spin-lattice relaxation measurements agree well with those calculated from electrical conductivity data. Moreover, the activation energies determined by both techniques agree very well. The electronic conductivity and the corresponding electronic transference number are very small, and LLZO was found to be stable against reaction with Li metal over the measured period of several days. Therefore, we suppose that Al-stabilized cubic LLZO is a suitable Li solid electrolyte. Tests of the compatibility of LLZO with various cathode materials and measurements of the overvoltages occurring

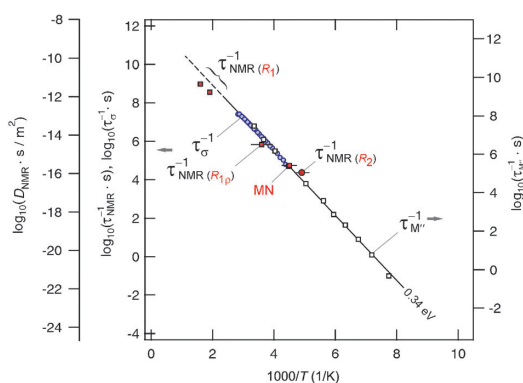


Fig. 15 Temperature dependence of the Li jump rates of cubic LLZO (0.9 wt% Al) obtained from NMR $1/\tau_{\text{NMR}}$ and impedance spectroscopy $1/\tau_{\sigma}$. For comparison, electrical relaxation rates $1/\tau_{\text{M}}'$ deduced from the peaks of various modulus spectra $M''(\nu)$ are also included. The solid line shows an Arrhenius fit yielding 0.34 eV. The jump rate marked with MN denotes a value deduced from NMR line narrowing. See text for further details.

in contact with these as well as Li metal under current load are in progress and will help further clarify the applicability of cubic LLZO as a solid state electrolyte for Li ion batteries.

Acknowledgements

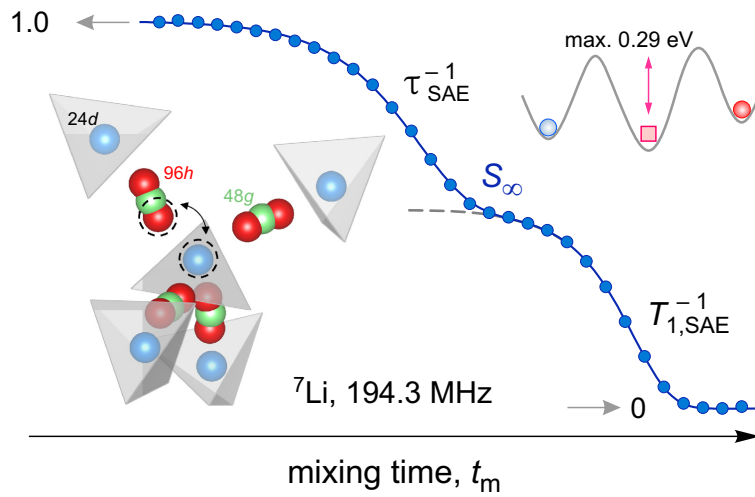
We acknowledge financial support by the German Research Foundation (DFG) within the project “High performance lithium batteries” (DFG JA 648/15-1 and 15-2). We also acknowledge helpful discussion within the BASF research network for Batteries and Electrochemistry. Furthermore financial support by the Federal Ministry of Education and Research (BMBF) within the projects “Competence in Electrochemistry for Electromobility” and “Lithium Ion Batteries LIB 2015” both for the Gießen and the Hannover teams is gratefully acknowledged.

The authors benefitted from discussions with Alan Logéat, Thomas Köhler and Ulrich Eisele from Robert Bosch GmbH and thank Christoph Essig for the ICP-OES analysis of the garnet samples.

Notes and references

- 1 K. Xu, *Chem. Rev.*, 2004, **104**, 4303–4417.
- 2 D. Aurbach, *J. Power Sources*, 2000, **89**, 206–218.
- 3 D. Aurbach, B. Markovsky, G. Salitra, E. Markevich, Y. Talyossef, M. Koltypin, L. Nazar, B. Ellis and D. Kovacheva, *J. Power Sources*, 2007, **165**, 491–499.
- 4 J. Vetter, P. Novak, M. R. Wagner, C. Veit, K. C. Moller, J. O. Besenhard, M. Winter, M. Wohlfahrt-Mehrens, C. Vogler and A. Hammouche, *J. Power Sources*, 2005, **147**, 269–281.
- 5 V. Thangadurai, H. Kaaack and W. J. F. Weppner, *J. Am. Ceram. Soc.*, 2003, **86**, 437–440.
- 6 R. Murugan, V. Thangadurai and W. Weppner, *Angew. Chem., Int. Ed.*, 2007, **46**, 7778–7781.
- 7 J. Awaka, N. Kijima, H. Hayakawa and J. Akimoto, *J. Solid State Chem.*, 2009, **182**, 2046–2052.
- 8 J. Awaka, A. Takashima, K. Kataoka, N. Kijima, Y. Idemoto and J. Akimoto, *Chem. Lett.*, 2011, 60–62.
- 9 K. H. Kim, Y. Iriyama, K. Yamamoto, S. Kumazaki, T. Asaka, K. Tanabe, C. A. J. Fisher, T. Hirayama, R. Murugan and Z. Ogumi, *J. Power Sources*, 2011, **196**, 764–767.
- 10 C. A. Geiger, E. Alekseev, B. Lazić, M. Fisch, T. Armbruster, R. Langner, M. Fechtelkord, N. Kim, T. Pettke and W. Weppner, *Inorg. Chem.*, 2011, **50**, 1089–1097.
- 11 S. Kumazaki, Y. Iriyama, K.-H. Kim, R. Murugan, K. Tanabe, K. Yamamoto, T. Hirayama and Z. Ogumi, *Electrochem. Commun.*, 2011, **13**, 509–512.
- 12 Y. Jin and P. J. McGinn, *J. Power Sources*, 2011, DOI: 10.1016/j.jpowsour.2011.05.065.
- 13 M. Kotobuki, K. Kanamura, Y. Sato and T. Yoshida, *J. Power Sources*, 2011, **196**, 7750–7754.
- 14 M. Hoelzel, A. Senyshyn, R. Gilles, H. Boysen and H. Fuess, *Neutron News*, 2008, **18**.
- 15 J. Rodriguez-Carvajal, *Commission on Powder Diffraction Newsletter*, 2001, **26**, 12–19.
- 16 F. Izumi and R. A. Dilanian, *Recent Research Developments in Physics*, Transworld Research Network, 2002.
- 17 P. A. Stadelmann, *Ultramicroscopy*, 1987, **21**, 131–145.
- 18 M. H. Hebb, *J. Chem. Phys.*, 1952, **20**, 185–190.
- 19 C. Wagner, *J. Chem. Phys.*, 1953, **21**, 1819–1827.
- 20 A. Kuhn, A. Düvel and P. Heitjans, 2011, unpublished results.
- 21 A. Kuhn, S. Narayanan, L. Spencer, G. Goward, V. Thangadurai and M. Wilkening, *Phys. Rev. B: Condens. Matter Mater. Phys.*, 2011, **83**, 094302.
- 22 E. J. Cussen, T. W. S. Yip, G. O'Neill and M. P. O'Callaghan, *J. Solid State Chem.*, 2011, **184**, 470–475.
- 23 L. Thieblot, J. Roux and P. Richet, *Eur. J. Mineral.*, 1998, **10**, 7–15.
- 24 A. Grzechnik, H. Kruger, V. Kahlenberg and K. Friese, *J. Phys.: Condens. Matter*, 2006, **18**, 8925–8934.
- 25 K. Momma and F. Izumi, *J. Appl. Crystallogr.*, 2008, **41**, 653–658.
- 26 F. Izumi, *Solid State Ionics*, 2004, **172**, 1–6.
- 27 A. A. Belik, F. Izumi, T. Ikeda, V. A. Morozov, R. A. Dilanian, S. Torii, E. M. Koppin, O. I. Lebedev, G. Van Tendeloo and B. I. Lazoryak, *Chem. Mater.*, 2002, **14**, 4464–4472.
- 28 K. Oikawa, T. Kamiyama, R. Kanno, F. Izumi, T. Ikeda and B. C. Chakoumakos, *Mater. Sci. Forum*, 2004, **443–444**, 337.
- 29 K. Takada, H. Sakurai, E. Takayama-Muromachi, F. Izumi, R. A. Dilanian and T. Sasaki, *Nature*, 2003, **422**, 53–55.
- 30 M. Yashima, *J. Ceram. Soc. Jpn.*, 2009, **117**, 1055–1059.
- 31 D. Jacob and P. Cordier, *Ultramicroscopy*, 2010, **110**, 1166–1177.
- 32 L. Kienle, V. Duppel, B. Mogwitz, J. Janek, M. v. Kreutzbruck, A. Leineweber and A. Simon, *Cryst. Growth Des.*, 2011, **11**, 2412–2421.
- 33 I. M. Hodge, M. D. Ingram and A. R. West, *J. Electroanal. Chem.*, 1976, **74**, 125–143.
- 34 A. D. Pelton, *Bull. Alloy Phase Diagrams*, 1986, **7**, 228–231.
- 35 M. Wilkening, S. Indris and P. Heitjans, *Phys. Chem. Chem. Phys.*, 2003, **5**, 2225–2231.
- 36 B. Koch and M. Vogel, *Solid State Nucl. Magn. Reson.*, 2008, **34**, 37–43.
- 37 P. Heitjans and J. Kärger, *Diffusion in Condensed Matter—Methods, Materials, Models*, Springer, Berlin, 2005.
- 38 P. Heitjans, M. Masoud, A. Feldhoff and M. Wilkening, *Faraday Discuss.*, 2007, **134**, 67–82.
- 39 W. Bensch, T. Bredow, H. Ebert, P. Heitjans, S. Indris, S. Mankovsky and M. Wilkening, *Prog. Solid State Chem.*, 2009, **37**, 206–225.
- 40 M. Wilkening and P. Heitjans, *Phys. Rev. B: Condens. Matter Mater. Phys.*, 2008, **77**, 024311.
- 41 N. Bloembergen, E. M. Purcell and R. V. Pound, *Phys. Rev.*, 1948, **73**, 679–712.
- 42 V. Epp and M. Wilkening, *Phys. Rev. B: Condens. Matter Mater. Phys.*, 2010, **82**, 020301.
- 43 W. Küchler, P. Heitjans, A. Payer and R. Schöllhorn, *Solid State Ionics*, 1994, **70**, 434–438.
- 44 A. Kuhn, P. Sreeraj, R. Pöttgen, H. D. Wiemhofer, M. Wilkening and P. Heitjans, *J. Am. Chem. Soc.*, 2011, **133**, 11018.
- 45 M. Wilkening, C. Mühle, M. Jansen and P. Heitjans, *J. Phys. Chem. B*, 2007, **111**, 8691–8694.
- 46 M. Wilkening, A. Kuhn and P. Heitjans, *Phys. Rev. B: Condens. Matter Mater. Phys.*, 2008, **78**, 054303.
- 47 *United States Pat.*, US 2010/0047696 A1, 2010.

P7 Ion dynamics in solid electrolytes: NMR reveals the elementary steps of Li^+ hopping in oxide garnets



Ion dynamics in solid electrolytes: NMR reveals the elementary steps of Li⁺ hopping in oxide garnets

Patrick Bottke,^{*,†,‡} Daniel Rettenwander,[¶] Georg Amthauer,[¶] and
Martin Wilkening^{*,†,‡}

[†]*Christian Doppler Laboratory for Lithium Batteries, Institute for Chemistry and Technology,
Graz University of Technology (NAWI Graz), 8010 Graz, Austria*

[‡]*DFG Research Unit 1277 'molife', Graz University of Technology, 8010 Graz*

[¶]*Department of Materials Research and Physics, University of Salzburg, 5020 Salzburg, Austria*

E-mail: bottke@tugraz.at; wilkening@tugraz.at

Abstract

Garnet-type oxides are considered to be the most attractive solid Li⁺ electrolytes. This is due to their wide electrochemical stability window as well as their superior ionic conductivity with a Li ion transference number being almost one. Usually ionic conductivities are studied via impedance spectroscopy on a macroscopic length scale. Time-domain NMR methods, however, have been used much less extensively to shed light on the elementary hopping processes in highly conducting oxide garnets. Here, we used NMR relaxometry and stimulated echo NMR to study Li⁺ self diffusion in Li_{6.5}La₃Zr_{1.75}Mo_{0.25}O₁₂ (LLZMO) serving as a model compound to collect information on the ⁷Li spin dynamics. It turned out that NMR spin-lattice relaxation (SLR) recorded in both the laboratory and rotating frame of reference shows features that seem to be a universal fingerprint for fast conducting garnets that have been stabilized in their cubic modification. In contrast to Al-doped garnet-type Li₇La₃Zr₂O₁₂ that modifies the Li sublattice, in LLZMO the Li sublattice remains intact offering the possibility to get to the bottom of Li ion dynamics in LLZO-based garnets. Most importantly, whereas NMR SLR rates measured at 194.3 MHz reflect an almost universal behavior of local hoppings being thermally activated by only 151(3) meV, the spin-lock technique (33.3 kHz) gives evidence of two separate, overlapping rate peaks with activation energies in the order of 0.29 eV for the elementary steps of Li ion hopping. This points to a less pronounced distribution of Li⁺ jump rates on the kHz time scale than it has been observed for the Al-stabilized LLZO samples. The NMR results obtained also entail information on both the Li⁺ diffusion coefficients and the shape of the underlying motional correlation functions. The latter has been provided by ⁷Li NMR spin-alignment echo correlation spectroscopy that also shows the involvement of 24*d* and 96*h* sites in Li⁺ diffusion.

1 Introduction

Clean energy storage is one of the most urgent issues that has to be solved if we are to stop our dependency on diminishing fossil fuels. There is general agreement about the need to cut CO₂ emissions by storing electricity generated from renewable sources via, *e.g.*, powerful and sustainable systems that store energy electrochemically.¹⁻⁵

Ionically conducting solid electrolytes⁶⁻⁸ are key to developing advanced all-solid-state batteries being based on Li⁺ as ionic charge carriers. In order to replace liquid electrolytes that are commonly used in lithium-ion batteries, Li-bearing sulfides and oxides are feverishly searched that fulfill the requirements put on solid electrolytes.⁷⁻¹⁸ Considering oxides, garnet-type electrolytes are currently in the spotlight of materials science and battery research.^{7,19}

In 2007, Weppner and co-workers reported on very high Li ion conductivity (10^{-3} to 10^{-4} S cm $^{-1}$) in garnet-type $\text{Li}_7\text{La}_3\text{Zr}_2\text{O}_{12}$ (LLZO) crystallizing with cubic symmetry (space group $Ia\bar{3}d$).⁹ Since then many papers have been published focussing on both synthesis and characterization of ion transport in Li-bearing garnets, an overview is given by Thangadurai and co-workers.¹⁹ The electrochemical stability of LLZO has been studied recently by the Sakamoto group.²⁰ Nowadays we know that aliovalent doping of LLZO with, e.g., Al, Ga or even Fe,^{21–26} is essential not only to stabilize the cubic modification^{21,27,28} against the tetragonal one²⁹ with its lower conductivity, but also to free the lithium ions from their fixed sites enabling them to quickly diffuse along various pathways in the complex oxide network.^{19,21}

While ionic transport properties in garnets are commonly studied by impedance spectroscopy,^{19,30} some of us reported on a comprehensive time-domain nuclear magnetic resonance (NMR) study on Al-doped LLZO in 2011.²¹ NMR relaxometry was used to corroborate the findings from impedance spectroscopy; moreover, it was helpful to deliver further insights on Li^+ self-diffusion from a microscopic point of view by taking advantage of methods that are sensitive to ion hopping on the Ångström scale.^{21,31} Such information are crucial if we are to understand the extraordinary dynamic properties of garnets. Until now, however, NMR relaxometry has only rarely been used to characterize doped Li-containing garnets.^{21,31,32}

In our preceding work²¹ we discovered some NMR anomalies that are anticipated to be tightly linked with the high Li ion diffusivity probed. For example, via spin-locking ^7Li NMR spin-lattice relaxation (SLR) rate measurements an extremely broad diffusion-induced rate peak was observed²¹ pointing to high-temperature activation energies (ca. 0.34 eV) being comparable with that from conductivity measurements. Unexpectedly, the shape of the corresponding peak in the lab frame turned out to be much different. Its so-called low- T flank followed Arrhenius behavior over a large temperature range characterized by an activation energy of only ca. 120 meV.²¹

The present study is aimed at answering the question whether this is a special feature of Al-doped LLZO or a universal one of fast Li ion conducting garnets with cubic structure. Here, $\text{Li}_{6.5}\text{La}_3\text{Zr}_{1.75}\text{Mo}_{0.25}\text{O}_{12}$ (LLZMO) turned out to be a promising model system to throw light on this aspect. Most importantly, as compared to Al (or Ga)-doped LLZO,^{21,25} for which the dopants on $24d$ sites might act as blocking ions for Li^+ transport, the cubic modification studied here is not stabi-

lized by manipulating the Li sublattice; *au contraire*, in LLZMO the La-Zr sublattice is modified leaving the Li sublattice untouched. To our opinion, this can be used to explain the differences found here when compared to the previous NMR relaxation studies on Al-doped LLZO.

Moreover, compared to the available investigations on LLZO in the literature, in the present study we go one step further and apply spin-alignment echo (SAE) NMR correlation spectroscopy^{33–40} to probe slow ion dynamics at temperatures well below ambient. ^7Li SAE NMR is able to provide more precise information on the nature of Li ion dynamics since it directly measures a single-spin two-time hopping correlation function;^{33,38,41–44} it takes advantage of the quadrupolar interaction of the Li spin with electric field gradients at the nuclear sites. From temperature-variable echo decay curves both Li activation energies, *i.e.*, hopping barriers, and correlation times can be deduced.^{39,45–48} In addition, SAE NMR contains information on the shape of the underlying average motional correlation function that is behind fast ion transport in LLZMO.

2 Experiment

Synthesis of $\text{Li}_{6.5}\text{La}_3\text{Zr}_{1.75}\text{Mo}_{0.25}^{6+}\text{O}_{12}$ was performed by high-temperature sintering methods as according to Wagner et al.⁴⁹ The starting materials were Li_2CO_3 (99%, Merck), La_2O_3 (99.99%, Aldrich), ZrO_2 (99.0%, Aldrich) and MoO_3 (99.98%, Aldrich). Li_2CO_3 was mixed with the various oxides in the necessary proportions; they were ground intimately together using a hand mortar, a pestle, and isopropanol. This mixture was pressed uniaxial to a pellet and afterwards calcined at 1123 K for 4 h with a heating rate of 5 K min $^{-1}$; then the mixture was allowed to cool down in the furnace to approximately 473 K. The sample was milled in isopropanol using planetary ball mill (Fritsch Pulverisette 7) for 2 h (12 times 550 rpm for 5 min with a break of 5 min between each milling period). Finally, the powder was isostatically pressed (15 kbar) to yield pellets. Afterwards the pellets were sintered at 1500 K for 4 h; the heating rate was 20.5 K min $^{-1}$; after the sintering period the pellets were allowed to cool down to room temperature. The phase purity was checked via X-ray powder diffraction and neutron diffraction;⁴⁹ the final Li content was verified by means of ICP-OES. The sample investigated here crystallizes with cubic symmetry, space group $Ia\bar{3}d$, see above.

A piece of the cylindrical pellet prepared was placed directly inside the NMR probe. A flow of dry ni-

trogen gas in combination with a heater inside the probe head was used to adjust temperatures inside the sample chamber. A preceding recuperator inserted in a dewar filled with liquid nitrogen was used to cool the sample below ambient conditions. We used an Avance 500 spectrometer (Bruker BioSpin, shimmed magnet with a magnetic field B_0 of 11.7 Tesla, ^7Li resonance frequency $\omega_0/2\pi = 194.3$ MHz) to record ^7Li NMR line shapes and SLR rates as a function of temperature. While spectra under non-rotating conditions were recorded with a single 90° pulse, the SLR rates (R_1 , $R_{1\rho}$) were acquired either with the saturation recovery pulse sequence^{50,51} or the spin-lock technique^{13,51–58} taking advantage of transversal relaxation in along a locked B_1 field. For the latter a locking frequency of $\gamma_m B_1 = \omega_1/2\pi = 33.3$ kHz was used; here γ_m denotes the magnetogyric ratio of ^7Li .

Additionally, spin-spin relaxation rates R_2 and Jeener-Broekaert⁵⁹ echo decay rates^{33,36} were measured. We used a two-pulse quadrupole echo pulse sequence optimized for spin-3/2 nuclei⁴¹ to record transversal echo damping. Jeener-Broekaert echoes were generated with a 45° pulse following a 90° pulse after a short preparation time t_p of $10 \mu\text{s}$.^{33,34,37} The damping of the spin-alignment (quadrupolar) echo was followed as a function of mixing time t_m . A 45° reading pulse was used to transfer magnetization back into in an observable signal. Optimized phase cycling⁴¹ served to suppress unwanted coherence pathways; in general, a short preparation time^{33,34,37} is necessary to eliminate dipolar contributions as effectively as possible.

3 Results and Discussion

3.1 Change of NMR line shapes

The garnet-type oxides studied so far by ^7Li NMR spectroscopy are characterized by a significant line narrowing that starts at temperatures much below room temperature. The same feature is seen for the new garnet $\text{Li}_{6.5}\text{La}_3\text{Zr}_{1.75}\text{Mo}_{0.25}\text{O}_{12}$ studied here. In Fig. 1 selected ^7Li NMR lines are shown; while 1 a) focus on the central transition, in b) the satellite transitions are shown. Since ^7Li is a spin-3/2 nucleus the corresponding NMR line is composed of a central line ($+1/2 \rightleftharpoons -1/2$) and satellite intensities that reflect the spin-transitions $+3/2 \rightleftharpoons -3/2$. The latter interaction is of electric quadrupolar nature; it reflects the interaction of the quadrupole moment of ^7Li with non-vanishing electric field gradients (EFGs) in the direct neighborhood of the nucleus.⁶⁰ This interaction alters the Zee-

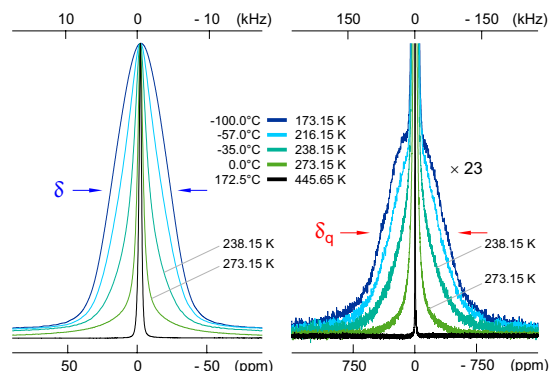


Figure 1: a) ^7Li NMR spectra of garnet-type, Mo-bearing $\text{Li}_{6.5}\text{La}_3\text{Zr}_{1.75}\text{Mo}_{0.25}\text{O}_{12}$ recorded at 194.3 MHz at the temperatures indicated. The heights of the spectra are normalized; in a) only the central line is shown. b) the same spectra as in a) but plotted with a magnification factor (23 times) to make the complete quadrupolar powder pattern visible.

man levels giving rise, in the case of a single crystal, to a central line flanked by two satellite transitions. For powder samples, on the other hand, the orientation dependence of the electric quadrupole interactions results in a broad quadrupolar powder pattern.⁶⁰ The more electrically inequivalent sites Li occupies, *i.e.*, the more EFGs are present, the more complex the resulting overall line shape at low temperature. At sufficiently low T , where ion dynamics do not affect the line shape – this is called the *rigid lattice* regime – the quadrupole intensities can usually be approximated with a Gaussian function. Similarly, in this T regime the central line, which reflects the magnetic dipolar interactions, shows in many cases Gaussian shape.

With increasing mobility of the Li spins, however, magnetic dipolar as well as electric quadrupolar interactions are continuously averaged. This manifests itself in pronounced line narrowing⁶¹ that is shown in 1 a). While at 173.15 K the line recorded is as expected for the rigid lattice regime, ion dynamics start to affect the line widths already at 183.15 K. Above 273 K the line is almost fully narrowed indicating very fast Li ion hopping processes. The ^7Li NMR line widths (FWHM, (overall) full width at half maximum) are shown in Fig. 2 as a function of temperature. Starting with a rigid lattice line width, δ_0 , of ca. 9 kHz, the line reaches half of its initial value at ca. 240 K. At the inflexion point of the motional narrowing curve the Li^+ jump rate τ^{-1} is approximately given by $\tau^{-1} = \delta_0 \times 2\pi \approx 5.6 \times 10^4 \text{ s}^{-1}$. At room temperature, being the normal operation temperature for solid state batteries, τ^{-1} is expected to be much larger (see below).

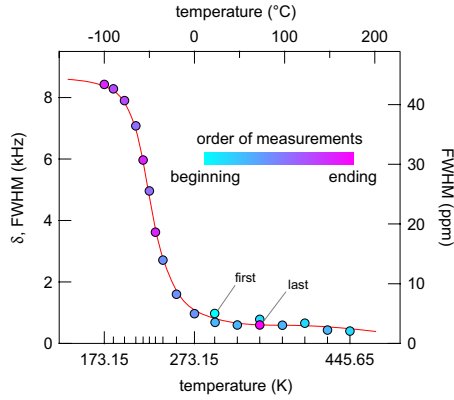


Figure 2: a) The ${}^7\text{Li}$ NMR line width of the central transition (FWHM, full width at half maximum) of $\text{Li}_{6.5}\text{La}_3\text{Zr}_{1.75}\text{Mo}_{0.25}\text{O}_{12}$ as a function of temperature. The color of the data points refer to the measuring order of the lines. It turned out that the powder sample, which was measured as a piece of the pellet in dry N_2 atmosphere, is stable over the whole T range investigated.

Interestingly, the ${}^7\text{Li}$ NMR line shapes, in contrast to what has been observed for Al-doped LLZO, undergo a relatively homogenous motional narrowing. This means that almost the whole line is affected by the narrowing process; for Al-doped LLZO we found a marked heterogeneous motional narrowing that points to mobile ions next to less mobile ions in the garnet structure. Here, the smooth transition from a Gaussian shape toward a Lorentzian line at elevated T indicates that the majority of Li ions take part in the diffusion process even at relatively low T . This is a noteworthy difference compared to Li-bearing garnets stabilized by aliovalent Al doping.

Line narrowing is sensitive to ion dynamics determined by the spectral width of the component. While δ_0 is in the order of 9 kHz, the quadrupole intensities (see Fig. 1 b)) span a spectral range of ca. 300 kHz. The width of the quadrupole foot, δ_q , is ca. 150 kHz. This is ten times larger than δ_0 . Hence, full averaging of the quadrupole intensities is expected if the jump rate reaches values (significantly) larger than δ_q . While at 273.15 K the satellite intensity has drastically lost in intensity, it has completely been vanished at 445.65 K. Already at 395.65 K (spectrum not shown) the mean jump rate has increased to values being much larger than 10^6 s^{-1} at least. The fact that averaging of quadrupole satellites sets in at relatively low temperatures and accompanies narrowing of the central line, which is sensitive to slower Li ion diffusion, points to a fraction of Li ions that are quite mobile on the timescale set by δ_q . This feature shows that we have not to deal

with a single diffusion process in LLZMO that governs ion transport. Our ${}^7\text{Li}$ NMR SLR measurements, see next section, will clearly underpin this view.

3.2 Diffusion-induced NMR spin-lattice relaxation rates

To quantify Li ion diffusion parameters in the crystalline garnet $\text{Li}_{6.5}\text{La}_3\text{Zr}_{1.75}\text{Mo}_{0.25}\text{O}_{12}$, we recorded both ${}^7\text{Li}$ NMR SLR rates (T_1^{-1}) in (i) the laboratory frame of reference ($\omega_0/2\pi = 194.3 \text{ MHz}$) and (ii) in the so-called rotating frame of reference^{56–58} ($T_{1\rho}^{-1}$) by utilizing an angular spin-lock frequency $\omega_0/2\pi$ that is much lower than the Larmor frequency $\omega_0/2\pi$ (Fig. 3). Hence, spin-lock NMR is sensitive to slower Li ion dynamics as compared to T_1^{-1} NMR experiments.^{39,40,62}

At first, we will present the T_1^{-1} results. The corresponding transients, which describe the recovery of longitudinal magnetization M_z as a function of delay time t_d can be best parameterized with single exponentials: $M_z(t_d) \propto 1 - \exp(-(t/T_1)^{\gamma_1})$, where γ_1 does only slightly deviate from 1. The rates T_1^{-1} and the corresponding stretching exponents γ_1 are shown in the Arrhenius plot of Fig. 3. At low temperatures T_1^{-1} deviates from Arrhenius behavior due to non-diffusive effects on $M_z(t_d)$. These can be lattice vibrations and coupling of the ${}^7\text{Li}$ spins to paramagnetic centers.⁶³ Above 250 K the rates T_1^{-1} follow an Arrhenius law that is given by $T_1^{-1} \propto \exp(-E_a/(k_B T))$. k_B denotes Boltzmann's constant and E_a is the activation energy. Here, we found $E_a = 151(3) \text{ meV}$. Although slightly larger, this value is comparable with previous results on Al-doped garnets (120 meV).²¹ Since E_a is smaller than the activation energy that is commonly found by conductivity spectroscopy, which is sensitive to long-range ion transport, the recovery of $M_z(t_d)$ is likely induced by short-range motions of the Li ions. These may also include unsuccessful, *i.e.*, forward-backward, Li jumps that are accompanied by correlation effects.^{64–66} The value of 151(3) meV might be closely related to the activation energy that represents the barrier of an elementary Li^+ jump process in LLZMO.

Taking the present result the rather shallow increase of T_1^{-1} seems to be a universal feature of the highly conducting garnets with cubic symmetry investigated by NMR so far. This is in stark contrast to what is seen for the tetragonal modification of LLZO whose ion conductivity is by two orders of magnitude lower.^{29,31} For tetragonal LLZO, which does not need stabilization via Al doping, the rates T_1^{-1} follow a low- T flank of a diffusion induced rate peak that is characterized

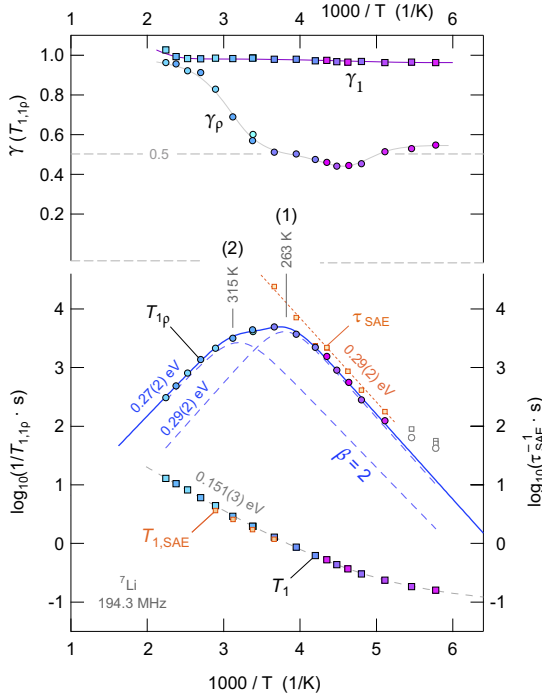


Figure 3: Arrhenius plot of the ${}^7\text{Li}$ SLR NMR rates T_1^{-1} and $T_{1\rho}$ of crystalline $\text{Li}_{6.5}\text{La}_3\text{Zr}_{1.75}\text{Mo}_{0.25}\text{O}_{12}$. The Larmor frequency was 194.3 MHz, we used a locking frequency of $\omega_1/2\pi$ of 33.3 kHz to record the $M_\rho(t_{\text{lock}})$ transients that are shown in Fig. 4. The continuous line represents the sum of two single rate peaks that are characterized by the dashed lines shown. The dashed line drawn through the T_1^{-1} data points is a combination of an Arrhenius fit with a power-law fit that takes into account background relaxation at low T . The solid lines in the upper part of the graph, which show the temperature dependence of γ_1 and γ_ρ , are just to guide the eye. For comparison, decay rates obtained from SAE NMR are also shown. The dotted line is an Arrhenius fit yielding 0.29 eV; the corresponding rates $T_{1,\text{SAE}}^{-1}$, which coincide with T_1^{-1} , are also included.

by 0.32 eV.³¹ The same low- T activation energy was found by $T_{1\rho}^{-1}$. Altogether, a joint fit of $T_{1\rho}^{-1}(1/T)$ and $T_1^{-1}(1/T)$ resulted in 0.48 eV.³¹ This value is directly comparable with activation energies deduced from conductivity spectroscopy (0.47 eV).

By formally replacing ω_0 by ω_1 we are able to shift the low- T SLR rate flank toward lower temperatures.³⁹ This enables us to record the complete diffusion-induced rate peak $T_{1\rho}^{-1}(1/T)$ as has been shown for tetragonal LLZO and Al-doped, cubic LLZO.^{21,31} In general, the peak maximum shows up at $\omega_{0(1)}\tau_c \approx 1$ where the correlation time τ_c is within a factor of 2 identical with the jump rate τ .⁵¹ The correspond-

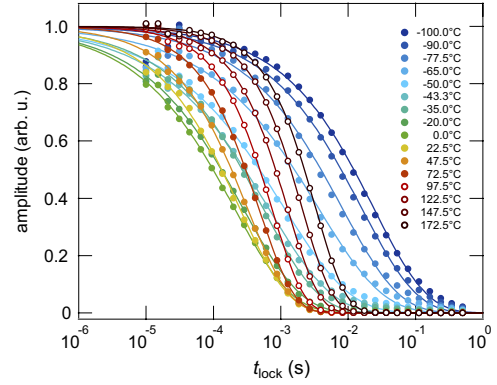


Figure 4: ${}^7\text{Li}$ NMR $T_{1\rho}$ transients, M_ρ amplitude vs locking time normalized to range between 0 and 1, that were recorded with the spin-lock technique. The solid lines represent fits according to $M_\rho(t_{\text{lock}}) \propto \exp(-(t/T_{1\rho})^{\gamma_\rho})$. The stretching exponents obtained, γ_ρ , are shown in Fig. 3. At the highest temperatures $M_\rho(t_{\text{lock}})$ follows a single exponential.

ing rates $T_{1\rho}^{-1}$ are included in Fig. 3. They have been extracted from transversal magnetization transients $M_\rho(t_{\text{lock}})$ by varying the spin-lock time t_{lock} from 10 μs up to 0.5 s. The transients obtained are presented in Fig. 4. Solid lines show fits with stretched exponentials according to $M_\rho(t_{\text{lock}}) \propto 1 - \exp(-(t/T_{1\rho})^{\gamma_\rho})$. The stretching factor γ_ρ strongly varies with temperature. It takes values of ca. 0.5 at low temperatures where $\omega_1\tau \gg 1$ holds. Such a $\sqrt{t_{\text{lock}}}$ decay behavior is expected for $T_{1\rho}$ transients that are governed by interactions of the Li spins with paramagnetic impurities.⁶⁷ At high temperatures, *i.e.*, in the regime $\omega_1\tau \ll 1$ the exponent γ_ρ strive toward $\gamma_\rho = 1$ that is reached at approximately 450 K. The increase of γ_ρ shows up when $T_{1\rho}^{-1}$ has passed through the peak maximum reaching the limit $\omega_1\tau \ll 1$. Likely, in this T range the shape of the underlying (averaged) motional correlation function resembles that of a pure exponential.

At first glance the shape of the rate peak $T_{1\rho}^{-1}(1/T)$ turns out to be rather broad. In the present case, however, it is much narrower than what has been observed for Al-doped (and Ga-doped) LLZO. For LLZO this has been interpreted as a large distribution of jump rates and activation energies leading to a superposition of many SLR rate peaks showing up at different temperatures. In the present case instead, the shape of $T_{1\rho}^{-1}(1/T)$ can be well reproduced with a combination of only two individual rate peaks. The two peaks are shown in Fig. 3 as dashed lines.

We used the SLR NMR model according to BPP theory that relies on a Lorentzian shaped spectral density

function $J(\omega_{0(1)})$ to which the rate $T_{1(1\varrho)}^{-1}$ is proportional to:⁶⁰

$$J(\alpha \cdot \omega_{0(1)})_{\alpha=1,2} = C_{0(1)}\tau_c / (1 + (\alpha \cdot \omega_{0(1)}\tau_c)^\beta). \quad (1)$$

The data $T_{1\varrho}^{-1}(1/T)$ can be approximated with the following expression for 3D motion

$$T_{1\varrho}^{-1} = C_\varrho \left(J(2\omega_1) + \frac{5}{3}J(\omega_0) + \frac{2}{3}J(2\omega_0) \right) \quad (2)$$

The parameter β in eq. 1 reflects deviations from the case of uncorrelated motion. τ_c is given by $\tau_c \approx \tau = \tau_0^{-1} \exp(-E_{a\varrho}/(k_B T))$. Here, the best fits were obtained with $\beta = 2$, *i.e.*, a simple BPP-type spectral density function is sufficient to reproduce the rate peaks. $\beta = 2$ leads to symmetric rate peaks.

Interestingly, the shape of the two peaks is rather similar. In the limit $\omega_1\tau \gg 1$ we obtain $E_{a\varrho}^{\text{low}} \approx 0.29$ eV; almost the same value governs the rates in the regime $\omega_1\tau \gg 1$ for which $E_{a\varrho}$ is given by 0.29(2) eV (peak 1) and 0.27(2) eV (peak 2), respectively. The latter value, which refers to the peak at lower T , is definitely smaller than the activation energy of tetragonal LLZO (0.42 eV). This suggests a high overall Li^+ diffusivity. The fact that peak 1 shows up at lower T is due to the larger pre-factor obtained. Here, we have $\tau_0^{-1}(1) = 1.6 \times 10^{11} \text{ s}^{-1}$ and a rather small value for $\tau_0^{-1}(2)$ *viz.* $8 \times 10^9 \text{ s}^{-1}$.

Considering the fitting results, it is obviously possible to probe two different, quite fast, diffusion processes in LLZMO. Note that the present case, such information is neither available by T_1 nor by line shape measurements, it is solely seen in $T_{1\varrho}^{-1}(1/T)$. The separation into two peaks enables us to determine the temperatures of the peak maxima and to estimate Li^+ self-diffusion coefficients. Here, the rate peaks $T_{1\varrho}^{-1}(1/T)$ show up at $T_{\text{max},1} = 263$ K and $T_{\text{max},2} = 315$ K. With $\omega_0\tau \approx 0.5$, which is valid for $T_{1\varrho}$ at the peak maximum, the jump rate $\tau^{-1}(T_{\text{max}})$ is given by $4.2 \times 10^5 \text{ s}^{-1}$. Using the Einstein-Smoluchowski equation, $D = a^2/(6\tau)$ this yields a self-diffusion coefficient D of ca. $1.9 \times 10^{-11} \text{ cm}^2 \text{ s}^{-1}$ at 263 K (and 313 K, respectively). Here, we choose the jump distance a to be equal to the distance between the Li^+ sites 24d and 96h ($a = 1.66 \text{ \AA}$, see below).

3.3 Li jumps in LLZMO as seen via stimulated echo NMR

In order to find out whether the activation energy of 0.29 eV can also be seen by other NMR techniques, we employed stimulated echo correlation spectroscopy to study Li ion hopping processes between electri-

cally inequivalent Li^+ sites in LLZMO. In detail, we used the Jeener Broecker three-pulse sequence⁵⁹ to record (sinus-sinus) two-time single-spin correlation functions³⁸ (see Figs. 5, 6).

3.3.1 SAE decay curves recorded at short preparation times

By using a short preparation time t_p of 10 μs between the first and the second pulse a spin state close to that of ideal spin-alignment can be reached as has been at first shown by Wu and co-workers.³³ The corresponding spin-alignment echo (SAE) that is recorded after a variable mixing time t_m ($10 \mu\text{s} \leq t_m \leq 10 \text{ s}$) shows up after the reading pulse. Its amplitude, $S_2(t_p = \text{const.}, t_m, t = t_p)$, decays either due to (i) slow Li^+ jump processes between sites with different EFGs, *i.e.*, $\tau_{\text{SAE}}^{-1} \approx \tau^{-1}$, or (ii) due to ordinary (quadrupolar) NMR spin-lattice relaxation ($T_{1,\text{SAE}}^{-1}$) or (iii) because of spin-diffusion effects ($T_{1,\text{sd}}^{-1}$):^{43,44}

$$S_2 \propto \exp[-(t_m/\tau_{\text{SAE}})^\gamma] \cdot A \quad (3)$$

with

$$A = \exp[-(t_m/T_{1,Q})^{\gamma'}] \exp[-(t_m/T_{1,\text{sd}})^{\gamma''}].$$

The pure SAE decay is given by $S_2' \propto \exp[-(t_m/\tau_{\text{SAE}})^\gamma]$. In many cases the Li^+ jump process proceeds on a shorter time scale than the latter two effects; hence it is possible to separate the term $S_2' \propto \exp[-(t_m/\tau_{\text{SAE}})^\gamma]$ from the non-diffusive ones. And indeed this is the case here; as we will show below a two-step decay shows up that can be attributed to S_2' and to the term $\exp[-(t_m/T_{1,Q})^{\gamma'}]$ where, in our case, $T_{1,Q}$ equals T_1 .^{44,48}

Another way of separation can be chosen if SAE curves have been recorded down to sufficiently low T . At low T the damping is mainly governed by $T_{1,Q}$ or $T_{1,\text{sd}}$; this helps estimate the influence of the two rates on the echo decay of interest.⁴³ Additionally, $T_{1,\text{sd}}^{-1}$ is expected to change only little with temperature. This is, however, in contrast to τ_{SAE}^{-1} which, in the ideal case, resembles the temperature dependence of ionic conductivities as has been shown for quite a large number of examples.^{39,45–47,68,69} Hence, via SAE NMR it is possible to access long-range (bulk) ion transport parameters with the help of a microscopic tool.³⁹ Moreover, in certain cases, it provides information on the geometry, that is, the diffusion pathways of Li ions.^{40,63}

The ^7Li SAE NMR curves recorded for the oxide garnet $\text{Li}_{6.5}\text{La}_3\text{Zr}_{1.75}\text{Mo}_{0.25}\text{O}_{12}$ are shown in Fig. 5. At the lowest temperatures a one-step echo decay is seen; the SAE curve obtained can be parameterized with a

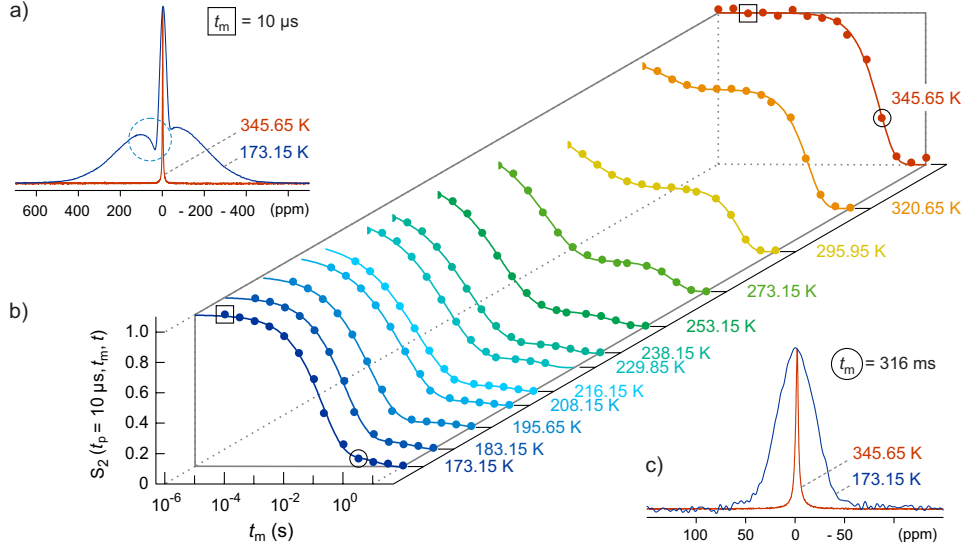


Figure 5: a) Fourier transforms (173.15 K, 345.65 K) of the ${}^7\text{Li}$ spin-alignment echoes of $\text{Li}_{6.5}\text{La}_3\text{Zr}_{1.75}\text{Mo}_{0.25}\text{O}_{12}$ which have been recorded at $t_p = 10 \mu\text{s}$ and short $t_m = 10 \mu\text{s}$, *i.e.*, before ion dynamics can have an effect on the echo amplitude; in c) the Fourier transforms at $t_m = 316 \text{ ms}$ are shown for comparison. b) Stacked plot of the ${}^7\text{Li}$ NMR SAE single-spin (sin-sin) two-time correlation functions recorded at $t_p = 10 \mu\text{s}$. From ca. 200 K to ca. 273 K the first decay step is visible that contains the rate τ_{SAE}^{-1} which can be identified with the Li^+ jump rate τ^{-1} . At 345.65 K echo damping is solely governed by spin-lattice relaxation characterized by $T_{1,\text{SAE}}^{-1}$; the two rates are shown in Fig. 3. See text for further details.

stretched exponential function. With increasing temperature the curves shift toward shorter mixing times indicating that Li jumps between electrically inequivalent sites increasingly cause echo damping. Simultaneously, at long mixing times a second decay process gains in intensity. While the first process is shifted out of the accessible time window, the latter process dominates the S_2 curves at elevated T . This is also illustrated in Fig. 6; the curve recorded at 273.15 K reveals the two-step decay behavior best. Note that for the curves recorded above 300 K the normalization is difficult, thus the data obtained at 320.65 K and 345.65 K has been chosen arbitrarily.

By plotting the two different rates resulting from the two-step decay curves in an Arrhenius plot (see Fig. 3) does clearly reveal their origins. At the highest temperatures, the rates of the second decay step coincide with the $T_{1,Q}^{-1}$ rates: $T_{1,Q}^{-1} = T_1^{-1}$. The rates of the first decay step follow Arrhenius behavior down to ca. 200 K. Below this temperature a deviation from Arrhenius behavior is seen that, most likely, can be ascribed to spin-diffusion effects now dominating echo decay. The fit shown in Fig. 3 does not take into account the last two data points. It yields an activation energy, $E_{a,\text{SAE}}$, of 0.29 eV which is consistent with that deduced from SLR NMR in the rotating frame of ref-

erence ($E_{a,Q}$). Moreover, this value also agrees with that from preliminary impedance spectroscopy measurements (ca. 0.3 eV) performed on the same sample.⁷⁰ In summary, the time-domain NMR methods applied tell us that at low temperatures (< 300 K) the bulk long-range lithium ion transport in LLZMO is characterized by an activation energy of ca. 0.30 eV. This value is even slightly smaller than that found for Al-doped LLZO (0.34 eV).²¹

Coming back to the two-step decay behavior of our S_2 curves that evolves with increasing temperature. We have to ask the question what can we learn about the spin system behind? As expected, the first decay step shifts toward shorter mixing times the faster the Li ions jump between the available non-equivalent Li^+ sites in LLZMO. We should keep in mind that only a limited number of crystallographic sites are regularly occupied in our LLZMO sample – the tetrahedral site 24d and the split-atom site 96h, see below. Because of this circumstance we have to consider, of course, the effect of final state amplitudes on echo decay, as will be discussed below.

Besides shifting of the first decay step toward shorter mixing times, extremely rapid Li exchange, on the other hand, might lead to complete or partial averaging of the quadrupole interactions. We have to con-

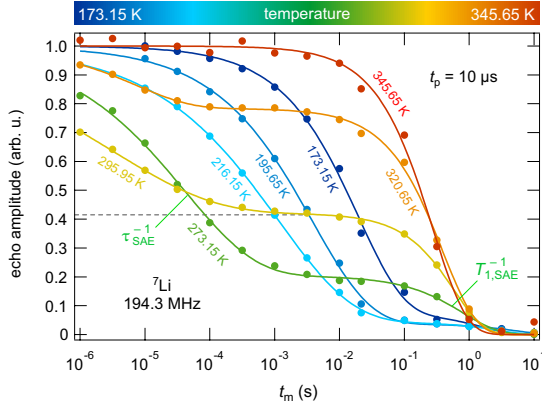


Figure 6: ${}^7\text{Li}$ SAE NMR two-time correlation functions $S_2(t_p = \text{const.}, t_m, t = t_p)$ recorded at $t_p = 10 \mu\text{s}$. The amplitude of the quadrupolar spin-alignment echo is plotted vs mixing time t_m . Data have been recorded at 194.3 MHz. The solid lines show fits being a sum of two exponential functions that contain the rates τ_{SAE}^{-1} and $T_{1,\text{SAE}}^{-1}$; the two-step decay feature is at best seen at 273.15 K. The emergence of the second decay step can have different origins, see text for further explanation.

consider this scenario as we study an ion conductor showing rapid Li diffusion at ambient temperature. Remember that SAE NMR is usually applied to study slow Li motions to which the sinus-sinus correlation function is sensitive. As we can infer from the ${}^7\text{Li}$ NMR spectra shown in Fig. 1 b) the quadrupole interactions are indeed significantly averaged due to sufficiently fast Li exchange between the available Li^+ sites. This process sets in at relatively low temperatures. If the Li spins “sense” a single, averaged EFG, no temporal fluctuations of the associated quadrupole frequency is given any longer during the time period t_m ; moreover, Li ions could have visited a number of sites during t_p if $\tau \lesssim t_p$, *i.e.*, the evolution times is not short as compared to the hopping correlation time (as discussed below).⁴² A similar situation would be present for Li ions that jump between electrically equivalent sites. It means that the pre-requirement that makes SAE NMR gets lost; consequently, there would be no SAE decay because the rate $\tau_{\text{SAE}}^{-1} \approx \tau^{-1}$ would be given by $\tau_{\text{SAE}}^{-1} \rightarrow 0$ (being equivalent to $\tau_{\text{SAE}} \rightarrow \infty$). Instead, the only reason for the decay of an echo formed would be because of (ordinary) spin-lattice relaxation.

The fact that, if we consider temperatures below ambient, the second step grows while the first, which is shifting, is still present could tell us that the spin-system appears to formally consist of two spin reservoirs: a subsystem with slow Li spins for which SAE NMR works, and a second one made up of very fast ions that already

see an averaged EFG. The higher the temperature the more ions convert into this fast reservoir, as a result the amplitude of the second decay step steadily increases with temperature. For example, at 295.15 K about 40% of the ions, see the amplitude of the plateau value (Fig. 6), would have access to a fast diffusion process that is invisible for SAE NMR. At 320.65 K and above a reliable normalization of the S_2 curves is no longer possible since the initial amplitude of the SAE echo is out of the time window at short preparation times.

Regarding the shape of the first decay step, there are indeed indications of heterogeneous dynamics although the ${}^7\text{Li}$ NMR spectra do not point to pronounced heterogeneous motional narrowing. For instance, only stretched exponentials are suitable to parameterize the first decay step, see, *e.g.*, the curve recorded at 216.15 K (Fig. 6) that do not follow single exponential decay behavior. Between 200 and 280 K a stretching exponent γ (see eq. 3) of 0.4 is best suited to describe echo damping of S_2' . Obviously, heterogeneous dynamics is only seen if we use the site-specific electric quadrupolar information to identify the ions rather than to rely on homonuclear dipole-dipole interactions. Of course, the distribution width of jump rates in LLZMO is assumed to be much narrower than that of Al-doped LLZO studied by ${}^7\text{Li}$ SLR NMR previously.²¹ Compared to Al-stabilized $\text{Li}_7\text{La}_3\text{Zr}_2\text{O}_{12}$ no additional disorder on the Li sublattice is introduced in the case of LLZMO. As noted above, in LLZMO the Mo ions share common sites with Zr residing on the Wyckoff position 16a; they do not influence the sites of the Li sublattice (24d, 96h) directly.⁷⁰

3.3.2 SAE decay curves recorded at long preparation times

Alternatively, one might think about another scenario that could explain the two-step S_2 decay: While at low T the Li ions could be exchanged over various inequivalent sites, at higher temperatures a diffusion pathway connecting only electrically equivalent sites may play the dominant role (see below). For instance, this could include direct jumps between 96h sites bypassing the 24d site as is illustrated below. Xu et al.,⁷¹ however, pointed out that such a diffusion pathway is characterized by a much higher activation energy ($> 0.8 \text{ eV}$) than found by rotating-frame SLR NMR here.

Thus, it seems to be more likely that echo damping is affected by the heterogeneous dynamics that lead to (partial) phase averaging. The plateau value reached at intermediate mixing times can also be interpreted as a final state amplitude, S_∞ . This means, if only a lim-

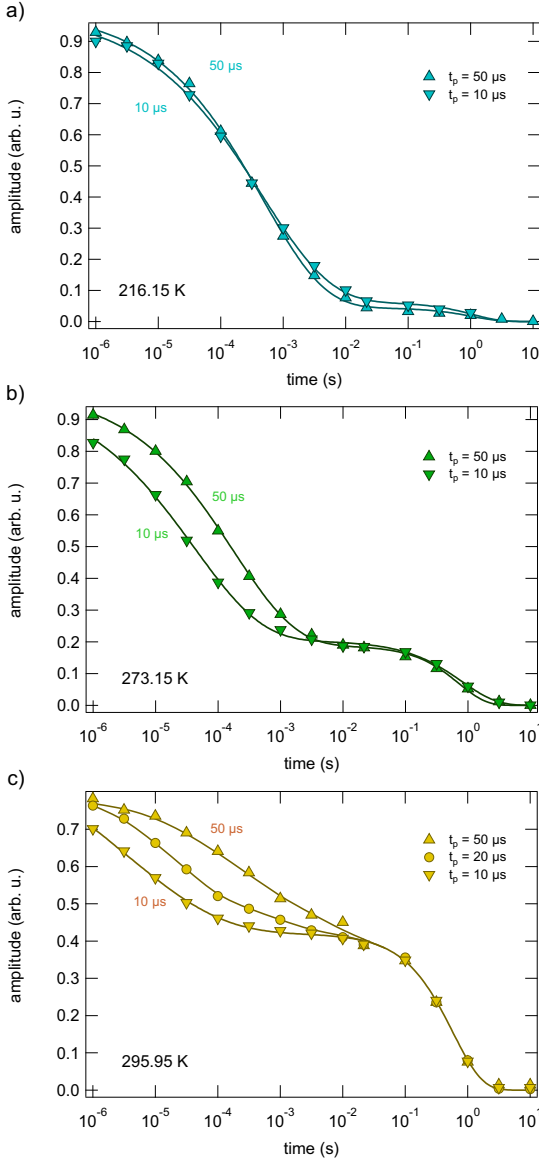


Figure 7: ${}^7\text{Li}$ SAE NMR echo decay curves, $S_2(t_p, t_m)$ vs t_m , that have been recorded at preparation times t_p being equal or larger than $10 \mu\text{s}$ but shorter than $50 \mu\text{s}$. With increasing t_p the first decay step shifts toward larger mixing times t_m . This is because of motional phase averaging that takes place during the evolution period t_p . The higher T the more pronounced the effect because Li diffusivity steadily increases with T .

ited number of electrically inequivalent sites participate in the Li ion diffusion process the loss of phase coherence is restricted. This would lead to a final amplitude S_∞ that is, if S_2 is properly normalized to range between 0 and 1, given by the inverse number $1/N$ of the

quadrupole frequencies ω_Q involved provided the available Li sites are equally populated. If this is not the case (see below), S_∞ is given by the summation over the squared weighing factors w_i : $S_\infty = \sum_{i=1}^N w_i^2$.³⁸ Considering a powder average ($\langle \dots \rangle$) the pure SAE NMR decay, see above, is given by^{38,43,44}

$$S'_2(t_m) \propto \langle (\sin[\omega_Q(0)t_p] \sin[\omega_Q(t_m)t_p]) \rangle \quad (4)$$

$$\propto \exp[-(t_m/\tau_{\text{SAE}})^\gamma] \quad (3')$$

relating the phase angles given by $\omega_Q(0)t_p$ and $\omega_Q(t_m)t_p$ (or their mean values $\bar{\omega}_Q$). The final value of $S_\infty(t_p \rightarrow \infty)$ is reached if large t_p times are used to sample the data. At shorter t_p it will vary around the final value. In general, S_2 will be of the form of

$$S'_2(t_m) = (A \cdot S'_2 + B) \cdot \exp[-(t_m/T_{1,Q})^{\gamma'}] \quad (5)$$

if we consider temperatures where $T_{1,\text{SAE}}$ equals $T_{1,Q}$, *i.e.*, the two-step decay regime. The final state amplitude is then given by $S_\infty = B/(A + B)$. Thus, to determine S_∞ echoes at large t_p have to be recorded. For ${}^7\text{Li}$, however, this will simultaneously create (unwanted) dipolar order. A disadvantage that is less important in ${}^2\text{H}$ SAE NMR because of the much larger quadrupole interaction in deuterium NMR. Therefore, SAE decay curves, and echoes as well, recorded at preparation times significantly larger than, *e.g.*, $10 \mu\text{s}$ will be affected by dipole-dipole interactions. Such interactions do also play a role at $t_p = 10 \mu\text{s}$ if we consider the Fourier transforms shown in Fig. 5 a). The apparent “central” line that shows up at low T and short t_p and t_m reflects dipolar coupling of the Li spins.⁴¹ Note that at short t_m the influence of ion dynamics is kept as low as possible. For comparison, the Fourier transforms of the second decay step (see Fig. 5 c)) is composed of a single line that does not contain the quadrupole intensities any longer.

Before discussing the results for S_∞ , we have to know the influence of large t_p values on the $S'_2(t_m)$ decay. If t_p is increased, *i.e.*, if t_p is (much) larger or equal to τ_{SAE} (as mentioned above) phase averaging during t_p might affect echo damping. This would shift the $S'_2(t_m)$ curve back toward longer mixing times, and indeed this is found here. The result is shown in Fig. 7 presenting the curves acquired at three different temperatures for t_p increased from 10 to $50 \mu\text{s}$. Whereas t_p has no effect on the term $\exp[-(t_m/T_{1,\text{SAE}})^{\gamma'}]$, as expected, the increase of preparation time affects τ_{SAE}^{-1} of the first decay step since the condition to determine τ_{SAE} times, *viz* $\tau_{\text{SAE}} \gg t_p$ is no longer valid. The higher the temperature the larger the influence because τ_{SAE} decreases

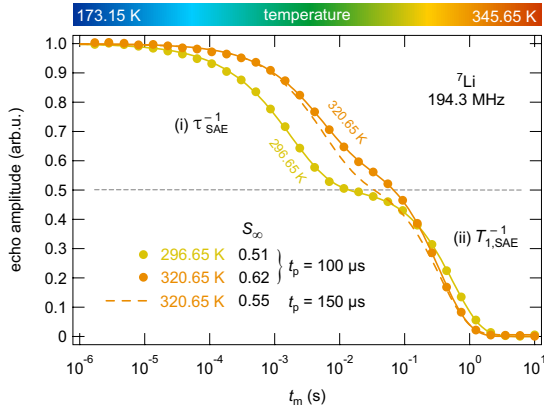


Figure 8: ${}^7\text{Li}$ SAE NMR decay curves, $S_2(t_p, t_m)$ vs t_m , recorded at large preparation times t_p of up to $150 \mu\text{s}$. As is evident from the normalization of S_2 final state amplitudes S_∞ between 0.5 and 0.6 show up. The slight increase of $T_{1,\text{SAE}}$ reflects the temperature dependence of T_1 . The data points refer to the amplitude of the quadrupolar spin-alignment echo. Note that at such large preparation times the whole echo is composed of both a quadrupolar and a dipolar part. The dipolar part, however, behaves very similar compared to the sharp alignment echo. Note that the slight temperature dependence of the second decay step reflects the diffusion-induced increase of R_1 with T (see Fig. 3).

with T . In the ideal case, during the short time period t_p no Li^+ exchange should occur guaranteeing the storage of all of the necessary phase information of the spins. Here, below 240 K overall Li exchange is slow and an increase of t_p has little effect on τ_{SAE}^{-1} (and on the amplitude S_∞) making sure that the rate is useful to derive a reliable activation energy, see Fig. 3. At 273 K and above the effect of t_p is apparent. Obviously, jumping of Li ions within the time scale set by t_p causes motional phase averaging⁴² that affects the inflexion point of the decay curves, *i.e.*, the mean time constant associated with S_2 . Because of this averaging, which is the more pronounced the higher T , not all of the Li^+ jump processes can be detected any longer. The effect is best seen at 295 K and above. From a quantitative point of view it definitely says that at ambient temperature τ_{SAE}^{-1} is in the order of 10^5 s^{-1} . This is in perfect agreement with the result derived from SLR NMR in the rotating frame. In particular, it reflects the jump rate ($4.2 \times 10^5 \text{ s}^{-1}$) estimated from the second rate peak showing up at 313 K (see above).

In this section, let us turn to the S_2 decay curves recorded at increased t_p and temperatures above ambient. Since $S_2'(t_m)$ is expected to shift toward longer mixing times the initial amplitudes of S_2 should be available helping in proper normalization of the com-

plete curves. In Fig. 8 results are shown for 296.65 K and 320.65 K; at this temperatures, dipole-dipole interactions, which may largely affect S_∞ ,⁴¹ are largely eliminated through rapid Li exchange. For the sake of completeness we also studied the decay at higher temperatures: similar curves were obtained. Interestingly, the S_2 curves, which can now correctly normalized, reveal final state amplitudes S_∞ ranging from 0.5 to 0.6. If related to $1/N$, we have to take into account the site occupancy of the available Li sites in LLZMO. There are two Li sites regularly occupied by Li^+ , the $24d$ and the $96h$ site. Neutron diffraction yields site occupancies of 0.51 and 0.31 that would expect S_∞ to take a value of 0.62 if we assume a two-site jump process being responsible for the final state amplitude. This is in good agreement with our experiments (Fig. 8), hence SAE NMR points to the involvement of the two electrically inequivalent sites in LLZMO. The observation of pronounced phase averaging during t_p indicates the quadrupole frequencies associated with the sites $24d$ and $96h$ are quite different. Then a small number of jumps suffices to cause the averaging observed. Note that S_∞ is influenced by dipolar couplings of the Li spins;⁴¹ only at sufficiently high T these couplings are averaged causing S_∞ to depend on T .

As a last remark: of course, at temperatures being equal or higher than 270 K the condition $t_p \ll \tau_{\text{SAE}}$ is violated. Thus, the influence of phase averaging, which predominantly affect the fraction of species moving fast on the scale set by the evolution time, cannot be neglected as it is shown in Fig. 7. Thus, there might be a fast spin reservoir because of heterogeneous dynamics rather than uniform Li^+ exchange that lead to $\overline{\omega}_Q(t_m) = \text{const.}$ giving rise to the second decay step seen.

3.4 Possible Li ion diffusion pathways and comparison of NMR activation energies with findings from theory

In order to ascribe the activation energies found to possible (microscopic) Li^+ diffusion pathways or elementary jump processes we firstly have to look at the crystal structure of LLZMO. The crystal structure ($Ia\bar{3}d$) and, most importantly, the Li site occupancies of our sample have been revealed by neutron diffraction. According to the refinement of neutron powder diffraction data, Mo ions and Zr ions are distributed over the 16a sites, La ions occupy the dodecahedra ($24c$). As mentioned above, according to the best refinement, Li ions reside on two sites, *viz.* $24d$ positions with 4-fold coordina-

Table 1: Possible elementary steps of Li ion hopping in LLZMO between next neighbors; tentative assignment of activation energies

sites	a (Å)	E_a (eV)	method	type/comment
$96h-48g-96h''^a$	0.7	< 0.1	T_1 (low- T)	“caged dynamics” ^b
$24d-96h^c$	1.66	0.15	T_1	forward, backward jumps ^d
$96h-24d(-96h')$	1.66	0.15	T_1	also detectable by SAE NMR (0.29 eV)
$24d-[96h]-24d^e$	2.34	0.27 - 0.29	$T_{1\theta}; \tau_{SAE}$	
	3.12			
$96h-96h'^f$	2.47	≥ 0.29	$T_{1\theta}; (\tau_{SAE})$	including paths bypassing the $24d$ site;
	2.9			curved pathway
	3.1			
	3.47			

^a Very fast jump process between similar sites most likely invisible for SAE NMR even at extremely low T .

^b Strictly localized motions of the split site $48g$, only one of the three sites within the pocket can be occupied by Li; E_a is expected to be extremely small; note, this movement has not been detected by NMR so far.

^c Fast jump process between similar sites most likely invisible for SAE NMR.

^d Localized two-site jump process.

^e Here, $[96h]$ denotes the split-atom site $96h-48g-96h''$, see first line in the table.

^f Presumably, this process, which bypasses the $24d$ site, involves temporary occupation of voids connecting the two $96h$ sites; it is most likely also visible by SAE NMR at low temperatures.

tion (site occupancy 0.51) and $96h$ sites with distorted 4-fold coordination (site occupancy 0.35). The occupancy of these two sites is in agreement with that found for other LLZO-type garnets.⁷² Possible Li^+ diffusion pathways, simply connecting the sites $24d$ and $96h$,^{71,72} are shown in Table 1.

The distribution of vacancies, ordered or disordered among the Li^+ sites, as well as repulsive Li^+-Li^+ Coulomb interactions – note that each occupied $24d$ site (see Fig. 9) blocks the occupation of next-neighbored $96h$ sites⁷³ – are expected to vary with the synthesis conditions.⁷⁴ Annealing temperatures and cooling rates may critically influence lithium ordering⁷⁴ and, thus, ionic conductivity that is assumed to depend on total Li^+ concentration rather than on the kind of doping ions present.¹⁹ In particular, the thermal history of the samples may also cause non-equilibrium Li^+ distributions over the available voids in garnet-type cubic LLZO that crucially influences its ion transport properties.⁷⁴ Thus, coming from real systems the comparison with results from calculations is by far not straightforward. We should also keep in mind that diffusion pathways chosen by the ions may change with increasing temperature as has been pointed out by Lai and co-workers for $\text{Li}_5\text{La}_3\text{Ta}_2\text{O}_{12}$ by using classical molecular dynamics simulations.⁷⁵

Recent theoretical investigations on overall ion conductivity, diffusion pathways and local hopping barriers reflect a highly complex picture of ion transport through LLZO. Long-range ion transport in cubic LLZO, to which (dc)-conductivity measurements

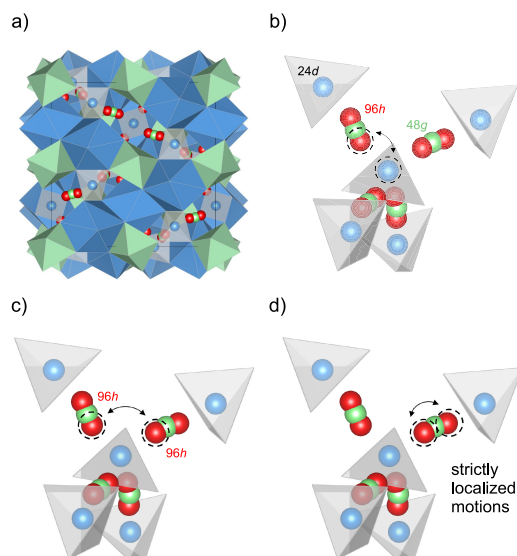


Figure 9: a) crystal structure of cubic LLZO (view along the a -axis), b) to d) selected Li elementary hopping steps between the sites $24d$ and $96h$ that are occupied by Li in LLZMO as evidenced from neutron diffraction. In b) the $24d-96h$ jump process is shown; in c) Li^+ diffusion between $96h$ sites of two different octahedral voids is illustrated. d) presents strictly localized Li motions within the $96h-48g-96h''$ arrangement.

are sensitive, is reported to be governed by an average activation energy of ca. 0.32 to 0.34 eV. The final result of Adams and co-workers (0.34 eV),⁷³ who studied

the 3D network pathway consisting of connected local $24d-96h-24d$ paths (see Table 1 and Fig. 9)), agrees well with the study performed by Jalem et al.⁷⁶ reporting on a concerted diffusion mechanism (0.33 eV); both groups used molecular dynamics simulations to describe Li^+ motions in the stabilized cubic polymorph at high temperatures. For Ta-bearing LLZO Ceder and co-workers report on an activation energy of 0.19 eV by considering the $96h-24d(-96h')$ pathway; this value points to the activation energy we observed via T_1 SLR NMR that is sensing short-range ion dynamics.⁷⁷

Two further studies have been published that focus on the *elementary* steps of ion hopping in LLZO-type garnets. The *ab initio* calculations based on density functional theory performed by Xu et al.⁷¹ differentiate between two possible Li ion hopping pathways. The first route describes Li ion hopping between $(96h/48g) - (96h/48g)'$ voids in garnets (Fig. 9 c)); this pathway is characterized by a rather large hopping barrier. According to the second route⁷¹ the Li ion moves through the $(96h/48g) - 24d$ border (Fig. 9 c)), thus, crossing the shared triangular face (0.25 eV). Then the ion shortly sticks at the corner of the $24d$ site before climbing over the other barrier finally reaching the empty $24d$ site, cf also the considerations of Awaka et al.⁷² This (edge pass-type) pathway would be consistent with that roughly denoted $96h-24d(-96h')$ in Table 1. The overall barrier reported by Xu et al.⁷¹ is 0.26 eV which is in excellent agreement to that what is seen via NMR relaxometry on our sample, see above. As suggested by Lai et al.,⁷⁵ in $\text{Li}_5\text{La}_3\text{Ta}_2\text{O}_{12}$ there might be a change from this edge-passing mechanism at low temperatures to a center-passing one at higher T . In the case of $\text{Li}_5\text{La}_3\text{Ta}_2\text{O}_{12}$ the authors, who used reverse Monte Carlo modelling and classical molecular dynamics to understand local lithium structure and dynamics, do not find any evidence for direct jumps between the octahedral voids, *i.e.*, bypassing the $24d$ bottleneck.⁷⁵ The latter has also been observed by Miara et al.⁷⁷

Coming back to our results from NMR relaxometry, in fact we observe, at least, two different relaxation rate peaks ($R_{1\rho}$). This might point to the situation that two types of Li ion dynamics play a role in our sample. Tentatively, we would assign the rate peak showing up at lower T to Li motions between $24d$ and $96h$ sites (Fig. 9 b)). The sites are separated by ca. 1.66 Å; because of Coulomb repulsion it is expected that they cannot be occupied simultaneously by two Li ions. Likely, the R_1 rates (0.15 eV) might also be influenced by this hopping process. From our measurements we do not find any indications that the Li ions on $24d$ sites do not participate in Li^+ diffusion as as-

sumed for, *e.g.*, $\text{Li}_5\text{La}_3\text{Nb}_2\text{O}_{12}$ on the basis of ^6Li 2D exchange NMR. It is common for the recent theoretical investigations that $24d$ sites do participate in Li^+ diffusion (see above). The second NMR relaxation rate peak observed via $R_{1\rho}$ might describe Li ion hopping between $96h$ sites either temporarily occupying or even bypassing the $24d$ sites (see Table 1). As pointed out by Meier et al.⁷⁸ short-distance jumps between face-sharing tetrahedra ($24d$) and octahedra ($96h/48g$) exhibit a slightly smaller energetic barrier than jumps between the neighbored, edge-sharing polyhedra ($96h$).

In detail, Meier et al. used *ab initio* molecular dynamics simulation, metadynamics, and nudged-elastic band calculations to systematically describe Li ion hopping in cubic and tetragonal LLZO.⁷⁸ While for the tetragonal modification the motion of Li ions is reported to be influenced by collective nature, they identified an asynchronous mechanism dominated by single-ion jumps and induced collective motion for cubic LLZO. On the assumption of individual jumps the activation energies for a series of elementary hopping processes along the Li^+ diffusion path in LLZO, involving the $24d$ and $(96h/48g)$ sites, are on the order of ca. 0.10 to 0.30 eV.⁷⁸ The activation energies of our NMR measurements fall perfectly into this range. These barriers are significantly smaller than the mean activation energy for Li ion hopping in the tetragonal modification (0.4 eV), for which 0.32 eV ($\omega_1\tau_c \gg 1$) and 0.48 eV ($\omega_1\tau_c \ll 1$) was recently found by our group using spin-lock NMR relaxometry (as mentioned above).³¹

As a last remark, the Li ions in the $(96h/48g)$ void, *i.e.*, the split site $96h-48g-96h'$, that can only be occupied by a single Li ion, might give rise to strictly localized Li^+ displacements (Fig. 9 d)). Such caged dynamics would give rise to a phenomenon that is frequently related to a nearly constant loss, that is, a frequency independent ϵ'' being the imaginary part of the complex permittivity. This translates into a temperature independent conductivity that linearly increases with temperature at sufficiently low T . For such motions activation energies below 0.1 eV are expected. It has to be checked in further studies whether this phenomenon can be detected in LLZO garnets.

4 Conclusion

$\text{Li}_{6.5}\text{La}_3\text{Zr}_{1.75}\text{Mo}_{0.25}\text{O}_{12}$ represents a new fast lithium ion conductor that crystallizes with cubic symmetry. The fact that it is stabilized in its cubic modification without doping with trivalent cations such as Al or Ga, leaves the Li sublattice untouched, *i.e.*, no blocking

dopants disturb the 3D network pathway used by Li ions for long-range diffusion.

We used various ^7Li solid-state NMR spectroscopic tools to analyze Li ion dynamics on both the short-range and long-range length scales. It is difficult to obtain such information from impedance spectroscopy that is usually applied to characterize ion transport in LLZO-based materials. Li diffusivity in LLZMO turns out to be remarkably high but has to be described by multiple Li ion dynamic processes taking place. Depending on the time window to which the different NMR methods are sensitive to (mean) activation energies were extracted that range from 0.15 eV (R_1) to 0.29 eV (R_{1Q} , SAE NMR).

In particular, the two-step damping of variable-temperature sin-sin correlation functions of SAE NMR reveals heterogenous dynamics. The applicability of SAE NMR, which is sensitive to ion hopping between electrically inequivalent sites in LLZO, shows that both $24d$ and $96h$ sites are involved in Li^+ diffusion. This is underlined by the two-step behavior observed. Echo damping at large preparation times might be added to find indications that a two-site jump process $96h-24d-96h'$ is present in LLZMO. At least for LLZMO, this rules out previous considerations about immobile Li ions residing on $24d$. The phase averaging observed during t_p clearly points to heterogeneous dynamics in LLZO.

The behavior of the R_{1Q} rates with temperature can be approximated at best with two BPP fits. The peak at 313 K points to an Li^+ jump rate of $4.2 \times 10^5 \text{ s}^{-1}$. This value is in perfect agreement with the jump rate expected from SAE NMR if we extrapolate the τ_{SAE}^{-1} rates toward higher T . The rate transforms into a self-diffusion coefficient D of ca. $1.9 \times 10^{-11} \text{ cm}^2 \text{ s}^{-1}$. Interestingly, the diffusion-induced rate peaks $R_{1Q}(1/T)$ observed appear to be more sharper than it is in the case of Al-doped LLZO indicating a less broad distribution of jump rates for LLZMO with a dopant-free Li sublattice. Extremely broad $R_{1Q}(1/T)$ are thus characteristic for Al-stabilized LLZO rather than for cubic-LLZO for which the Li sublattice is untouched.

The activation energies found have tentatively been assigned to possible elementary Li ion hopping processes between the neighbored Li^+ sites $24d$ and $96h$. Remarkably, our results agree with local hopping barriers in LLZO that have been calculated on the basis of density functional theory.

Author Contributions The authors from Salzburg have synthesised the sample. NMR measurements, data analysis and project planning was made in Graz. All

authors have given approval to the final version of the manuscript.

Acknowledgement We thank our colleagues at the TU Graz for valuable discussions. Financial support by the Deutsche Forschungsgemeinschaft (DFG Research Unit 1277, grant no. WI3600/2-2 and 4-1) as well as by the Austrian Federal Ministry of Science, Research and Economy, and the Austrian National Foundation for Research, Technology and Development is greatly appreciated. Moreover, we thank the Austrian Science Fund (FWF), project no. P25702 (D. Rettenwander, G. Amthauer) for financial support.

References

- (1) Larcher, D.; Tarascon, J.-M. Towards Greener and More Sustainable Batteries for Electrical Energy Storage. *Nature Chem.* **2015**, *7*, 19–29.
- (2) Adelhelm, P.; Hartmann, P.; Bender, C. L.; Busche, M.; Eufinger, C.; Janek, J. From Lithium to Sodium: Cell Chemistry of Room Temperature Sodium–Air and Sodium–Sulfur Batteries. *Beilstein J. Nanotechnol.* **2015**, *6*, 1016–1055.
- (3) Bruce, P. G.; Freunberger, S. A.; Hardwick, L. J.; Tarascon, J.-M. Li-O₂ and Li-S Batteries with High Energy Storage. *Nature Mater.* **2012**, *11*, 19–29.
- (4) Aricó, A. S.; Bruce, P.; Scrosati, B.; Tarascon, J.-M.; Schalkwijk, W. V. Nanostructured Materials for Advanced Energy Conversion and Storage Devices. *Nat. Mater.* **2005**, *4*, 366–377.
- (5) Whittingham, M. S. Lithium Batteries and Cathode Materials. *Chem. Rev.* **2004**, *104*, 4271–4301.
- (6) Knauth, P. Inorganic Solid Li Ion Conductors: An Overview. *Solid State Ion.* **2009**, *180*, 911–916.
- (7) Cao, C.; Li, Z.; Wang, X.-L.; Zhao, X.; Han, W.-Q. Recent Advances in Inorganic Solid Electrolytes for Lithium Batteries. *Front. Energy Res.* **2014**, *2*, 25–1–25–10.
- (8) Jung, Y. S.; Oh, D. Y.; Nam, Y. J.; Park, K. H. Issues and Challenges for Bulk-Type All-Solid-State Rechargeable Lithium Batteries using Sulfide Solid Electrolytes. *Israel J. Chem.* **2015**, *55*, 472–485.
- (9) Murugan, R.; Thangadurai, V.; Weppner, W. Fast Lithium Ion Conduction in Garnet-Type $\text{Li}_7\text{La}_3\text{Zr}_2\text{O}_{12}$. *Angew. Chemie Int. Ed.* **2007**, *46*, 7778–7781.

- (10) Kamaya, N.; Homma, K.; Yamakawa, Y.; Hirayama, M.; Kanno, R.; Yonemura, M.; Kamiyama, T.; Kato, Y.; Hama, S.; Kawamoto, K.; Mitsui, A. A Lithium Superionic Conductor. *Nature Mater.* **2011**, *10*, 682–686.
- (11) Mizuno, F.; Hayashi, A.; Tadanaga, K.; Tatsumisago, M. New, Highly Ion-Conductive Crystals Precipitated from $\text{Li}_2\text{S-P}_2\text{S}_5$ Glasses. *Adv. Mater. Materials* **2005**, *17*, 918–921.
- (12) Deiseroth, H.-J.; Kong, S.-T.; Eckert, H.; Vannahme, J.; Reiner, C.; Zaiß, T.; Schlosser, M. $\text{Li}_6\text{PS}_5\text{X}$: A Class of Crystalline Li-Rich Solids With an Unusually High Li^+ Mobility. *Angew. Chem. Int. Ed.* **2008**, *47*, 755–758.
- (13) Epp, V.; Gün, O.; Deiseroth, H.-J.; Wilkening, M. Highly Mobile Ions: Low Temperature NMR Directly Probes Extremely Fast Li^+ Hopping in Argyrodite-Type $\text{Li}_6\text{PSe}_5\text{Br}$. *J. Phys. Chem. Lett.* **2013**, *4*, 2118–2123.
- (14) Kaib, T.; Haddadpour, S.; Kapitein, M.; Bron, P.; Schröder, C.; Eckert, H.; Roling, B.; Dehnen, S. New Lithium Chalcogenidotetrelates, LiChT: Synthesis and Characterization of the Li^+ -Conducting Tetralithium ortho-Sulfidostannate Li_4SnS_4 . *Chem. Mater.* **2012**, *24*, 2211–2219.
- (15) Bron, P.; Johansson, S.; Zick, K.; Schmedt auf der Günne, J.; Dehnen, S.; Roling, B. $\text{Li}_{10}\text{SnP}_2\text{S}_{12}$: An Affordable Lithium Superionic Conductor. *J. Am. Chem. Soc.* **2013**, *135*, 15694–15697.
- (16) Sahu, G.; Lin, Z.; Li, J.; Liu, Z.; Dudney, N.; Liang, C. Air-Stable, High-Conduction Solid Electrolytes of Arsenic-Substituted Li_4SnS_4 . *Energy Environ. Sci.* **2014**, *7*, 1053–1058.
- (17) López, M. C.; Ortiz, G. F.; Arroyo-de Dompablo, E. M.; Tirado, J. L. An Unnoticed Inorganic Solid Electrolyte: Dilithium Sodium Phosphate with the Nalipoite Structure. *Inorg. Chem.* **2014**, *53*, 2310–2316.
- (18) Brant, J. A.; Massi, D. M.; Holzwarth, N. A. W.; MacNeil, J. H.; Douvalis, A. P.; Bakas, T.; Martin, S. W.; Gross, M. D.; Aitken, J. A. Fast Lithium Ion Conduction in Li_2SnS_3 : Synthesis, Physicochemical Characterization, and Electronic Structure. *Chem. Mater.* **2015**, *27*, 189–196.
- (19) Thangadurai, V.; Narayanan, S.; Pinzaru, D. Garnet-Type Solid-State Fast Li Ion Conductors for Li Batteries: A Critical Review. *Chem. Soc. Rev.* **2014**, *43*, 4714–4727.
- (20) Wolfenstine, J.; Allen, J. L.; Read, J.; Sakamoto, J. Chemical Stability of Cubic $\text{Li}_7\text{La}_3\text{Zr}_2\text{O}_{12}$ with Molten Lithium at Elevated Temperature. *J. Mater. Sci.* **2013**, *48*, 5846–5851.
- (21) Buschmann, H.; Dölle, J.; Berendts, S.; Kuhn, A.; Bottke, P.; Wilkening, M.; Heitjans, P.; Senyshyn, A.; Ehrenberg, H.; Lotnyk, A.; Duppel, V.; Kienle, L.; Janek, J. Structure and Dynamics of the Fast Lithium Ion Conductor “ $\text{Li}_7\text{La}_3\text{Zr}_2\text{O}_{12}$ ”. *Phys. Chem. Chem. Phys.* **2011**, *13*, 19378–19392.
- (22) Rettenwander, D.; Geiger, C. A.; Tribus, M.; Tropper, P.; Amthauer, G. A Synthesis and Crystal Chemical Study of the Fast Ion Conductor $\text{Li}_{7-3x}\text{Ga}_x\text{La}_3\text{Zr}_2\text{O}_{12}$ with $x = 0.08$ to 0.84. *Inorg. Chem.* **2014**, *53*, 6264–6269.
- (23) Wolfenstine, J.; Ratchford, J.; Rangasamy, E.; Sakamoto, J.; Allen, J. L. Synthesis and High Li-Ion Conductivity of Ga-Stabilized Cubic $\text{Li}_7\text{La}_3\text{Zr}_2\text{O}_{12}$. *Mater. Chem. Phys.* **2012**, *134*, 571–575.
- (24) Allen, J. L.; Wolfenstine, J.; Rangasamy, E.; Sakamoto, J. Effect of Substitution (Ta, Al, Ga) on the Conductivity of $\text{Li}_7\text{La}_3\text{Zr}_2\text{O}_{12}$. *J. Power Sources* **2012**, *206*, 315–319.
- (25) Jalem, R.; Rushton, M.; Manalastas, W.; Nakayama, M.; Kasuga, T.; Kilner, J. A.; Grimes, R. W. Effects of Gallium Doping in Garnet-Type $\text{Li}_7\text{La}_3\text{Zr}_2\text{O}_{12}$ Solid Electrolytes. *Chem. Mater.* **2015**, in press.
- (26) Rettenwander, D.; Geiger, C. A.; Amthauer, G. Synthesis and Crystal Chemistry of the Fast Li-Ion Conductor $\text{Li}_7\text{La}_3\text{Zr}_2\text{O}_{12}$ Doped with Fe. *Inorg. Chem.* **2013**, *52*, 8005–8009.
- (27) Bernstein, N.; Johannes, M. D.; Hoang, K. Origin of the Structural Phase Transition in $\text{Li}_7\text{La}_3\text{Zr}_2\text{O}_{12}$. *Phys. Rev. Lett.* **2012**, *109*, 205702–1–205702–5.
- (28) Rangasamy, E.; Wolfenstine, J.; Sakamoto, J. The Role of Al and Li Concentration on the Formation of Cubic Garnet Solid Electrolyte of Nominal Composition $\text{Li}_7\text{La}_3\text{Zr}_2\text{O}_{12}$. *Solid State Ion.* **2012**, *206*, 28–32.
- (29) Awaka, J.; Kijima, N.; Hayakawa, H.; Akimoto, J. Synthesis and Structure Analysis of Tetragonal $\text{Li}_7\text{La}_3\text{Zr}_2\text{O}_{12}$ with the Garnet-Related Type Structure. *J. Solid State Chem.* **2009**, *182*, 2046–2052.
- (30) Ramakumar, S.; Satyanarayana, L.; Manorama, S. V.; Murugan, R. Structure and Li^+ Dynamics of Sb-Doped $\text{Li}_7\text{La}_3\text{Zr}_2\text{O}_{12}$ Fast Lithium Ion Conductors. *Phys. Chem. Chem. Phys.* **2013**, *15*, 11327–11338.
- (31) Kuhn, A.; Narayanan, S.; Spencer, L.; Goward, G.; Thangadurai, V.; Wilkening, M. Li Self-Diffusion in Garnet-type $\text{Li}_7\text{La}_3\text{Zr}_2\text{O}_{12}$ as Probed Directly by Diffusion-Induced ^7Li Spin-Lattice Relaxation NMR Spectroscopy. *Phys. Rev. B* **2011**, *83*, 094302–1–094302–11.

- (32) Kuhn, A.; Epp, V.; Schmidt, G.; Narayanan, S.; Thangadurai, V.; Wilkening, M. Spin-Alignment Echo NMR: Probing Li^+ Hopping Motion in the Solid Electrolyte $\text{Li}_7\text{La}_3\text{Zr}_2\text{O}_{12}$ with Garnet-Type Tetragonal Structure. *J. Phys.: Condens. Matter* **2012**, *24*, 035901–1–035901–8.
- (33) Tang, X.-P.; Wu, Y. Alignment Echo of Spin-3/2 ^9Be Nuclei: Detection of Ultraslow Motion. *J. Magn. Res.* **1998**, *133*, 155–165.
- (34) Tang, X.-P.; Busch, R.; Johnson, W.; Wu, Y. Slow Atomic Motion in Zr-Ti-Cu-Ni-Be Metallic Glasses Studied by NMR. *Phys. Rev. Lett.* **1998**, *81*, 5358–5361.
- (35) Tang, X.-P.; Geyer, U.; Busch, R.; Johnson, W.; Wu, Y. Diffusion Mechanisms in Metallic Supercooled Liquids and Glasses. *Nature* **1999**, *402*, 160–162.
- (36) Böhmer, R.; Jörg, T.; Qi, F.; Titze, A. Stimulated Echo NMR Spectroscopy of Slow Ionic Motions in a Solid Electrolyte. *Chem. Phys. Lett.* **2000**, *316*, 419–424.
- (37) Qi, F.; Jörg, T.; Böhmer, R. Stimulated-Echo NMR Spectroscopy of ^9Be and ^7Li in Solids: Method and Application to Ion Conductors. *Solid State Nucl. Magn. Res.* **2002**, *22*, 484–500.
- (38) Böhmer, R.; Jeffrey, K.; Vogel, M. Solid-state Lithium NMR with Applications to the Translational Dynamics in Ion Conductors. *Prog. Nucl. Magn. Reson. Spectrosc.* **2007**, *50*, 87–174.
- (39) Wilkening, M.; Heitjans, P. From Micro to Macro: Access to Long-Range Li^+ Diffusion Parameters in Solids via Microscopic $^6\text{Li}/^7\text{Li}$ Spin-Alignment Echo NMR Spectroscopy. *Chem. Phys. Chem.* **2012**, *13*, 53–65.
- (40) Wilkening, M.; Küchler, W.; Heitjans, P. From Ultraslow to Fast Lithium Diffusion in the 2D Ion Conductor $\text{Li}_{0.7}\text{TiS}_2$ Probed Directly by Stimulated-Echo NMR and Nuclear Magnetic Relaxation. *Phys. Rev. Lett.* **2006**, *97*, 065901–1–065901–4.
- (41) Qi, F.; Diezemann, G.; Böhm, H.; Lambert, J.; Böhmer, R. Simple Modeling of Dipolar Coupled ^7Li Spins and Stimulated-Echo Spectroscopy of Single-Crystalline β -Eucryptite. *J. Magn. Res.* **2004**, *169*, 225–239.
- (42) Qi, F.; Rier, C.; Böhmer, R.; Franke, W.; Heitjans, P. Ion Hopping in Crystalline and Glassy Spodumene $\text{LiAlSi}_2\text{O}_6$: Spin-Lattice Relaxation and ^7Li Echo NMR Spectroscopy. *Phys. Rev. B* **2005**, *72*, 104301–1–104301–11.
- (43) Wilkening, M.; Heine, J.; Lyness, C.; Armstrong, A. R.; Bruce, P. G. Li Diffusion Properties of Mixed Conducting TiO_2 -B Nanowires. *Phys. Rev. B* **2009**, *80*, 064302–1–064302–8.
- (44) Wilkening, M.; Gebauer, D.; Heitjans, P. Diffusion Parameters in Single-Crystalline Li_3N as Probed by ^6Li and ^7Li Spin-Alignment Echo NMR Spectroscopy in Comparison with Results from ^8Li β -Radiation Detected NMR. *J. Phys.: Condens. Matter* **2008**, *20*, 022201–1–022201–6.
- (45) Wilkening, M.; Mühle, C.; Jansen, M.; Heitjans, P. Microscopic Access to Long-Range Diffusion Parameters of the Fast Lithium Ion Conductor Li_7BiO_6 by Solid State ^7Li Stimulated Echo NMR. *J. Phys. Chem. B* **2007**, *111*, 8691–8694.
- (46) Faske, S.; Koch, B.; Murawski, S.; Küchler, R.; Böhmer, R.; Melchior, J.; Vogel, M. Mixed-Cation $\text{Li}_x\text{Ag}_{1-x}\text{PO}_3$ Glasses Studied by ^6Li , ^7Li , and ^{109}Ag Stimulated-Echo NMR Spectroscopy. *Phys. Rev. B* **2011**, *84*, 024202–1–024202–9.
- (47) Brinkmann, C.; Faske, S.; Koch, B.; Vogel, M. NMR Multi-Time Correlation Functions of Ion Dynamics in Solids. *Z. Phys. Chem.* **2010**, *224*, 1535–1553.
- (48) Böhmer, R.; Qi, F. Spin Relaxation and Ultra-Slow Li Transport in an Aluminosilicate Glass Ceramic. *Solid State Nucl. Magn. Res.* **2007**, *31*, 28–34.
- (49) Wagner, R.; Rettenwander, D.; Welzl, W., A. Schmidt; Fleig, J.; Wilkening, M.; Amthauer, G. **2015**, to be published.
- (50) Fukushima, E.; Roeder, S. *Experimental Pulse NMR*; Addison-Wesley, Reading, 1981.
- (51) Heitjans, P.; Schirmer, A.; Indris, S. In *Diffusion in Condensed Matter – Methods, Materials, Models*, 2nd ed.; Heitjans, P., Kärger, J., Eds.; Springer, Berlin, 2005; Chapter 9, pp 369–415.
- (52) Ailion, D.; Slichter, C. P. Study of Ultraslow Atomic Motions by Magnetic Resonance. *Phys. Rev. Lett.* **1964**, *12*, 168–171.
- (53) Ailion, D. C.; Slichter, C. P. Observation of Ultra-Slow Translational Diffusion in Metallic Lithium by Magnetic Resonance. *Phys. Rev.* **1965**, *137*, A235–A245.
- (54) Slichter, C. P.; Ailion, D. Low-Field Relaxation and the Study of Ultraslow Atomic Motions by Magnetic Resonance. *Phys. Rev.* **1964**, *135*, A1099–A1110.
- (55) Epp, V.; Gün, O.; Deiseroth, H.-J.; Wilkening, M. Long-Range Li Dynamics in the Lithium Argyrodite Li_7PSe_6 as Probed by Rotating-Frame Spin-Lattice Relaxation NMR. *Phys. Chem. Chem. Phys.* **2013**, *15*, 7123–7132.

- (56) Stanje, B.; Epp, V.; Nakhal, S.; Lerch, M.; Wilkening, M. Li Ion Dynamics along the Inner Surfaces of Layer-Structured 2H-Li_xNbS₂. *ACS Appl. Mater. Interfaces* **2015**, *7*, 4089–4099.
- (57) Dunst, A.; Epp, V.; Hanzu, I.; Freunberger, S. A.; Wilkening, M. Short-Range Li Diffusion vs. Long-Range Ionic Conduction in Nanocrystalline Lithium Peroxide Li₂O₂ – the Discharge Product in Lithium-Air Batteries. *Energy Environ. Sci.* **2014**, *7*, 2739–2752.
- (58) Langer, J.; Epp, V.; Heitjans, P.; Mautner, F. A.; Wilkening, M. Li Motion in the Anode Material LiC₆ as Seen via Time-domain ⁷Li NMR. *Phys. Rev. B* **2013**, *88*, 094304–1–094304–9.
- (59) Jeener, J.; Broekaert, P. Nuclear Magnetic Resonance in Solids: Thermodynamic Effects of a Pair of rf Pulses. *Phys. Rev.* **1967**, *157*, 232–240.
- (60) Abragam, A. *The Principles of Nuclear Magnetism*; Clarendon, Oxford, 1961.
- (61) Wilkening, M.; Epp, V.; Feldhoff, A.; Heitjans, P. Tuning the Li Diffusivity of Poor Ionic Conductors by Mechanical Treatment: High Li Conductivity of Strongly Defective LiTaO₃ Nanoparticles. *J. Phys. Chem. C* **2008**, *112*, 9291–9300.
- (62) Küchler, W.; Heitjans, P.; Payer, A.; Schöllhorn, R. ⁷Li NMR Relaxation by Diffusion in Hexagonal and Cubic Li_xTiS₂. *Solid State Ion.* **1994**, *70/71*, 434–438.
- (63) Wilkening, M.; Heitjans, P. Li Jump Process in *h*-Li_{0.7}TiS₂ Studied by Two-Time ⁷Li Spin-Alignment Echo NMR and Comparison with Results on Two-Dimensional Diffusion from Nuclear Magnetic Relaxation. *Phys. Rev. B* **2008**, *77*, 024311–1–024311–13.
- (64) Bunde, A.; Dieterich, W.; Maass, P.; Meyer, M. In *Diffusion in Condensed Matter – Methods, Materials, Models*, 2nd ed.; Heitjans, P., Kärger, J., Eds.; Springer, Berlin, 2005; Chapter 20, pp 813–856.
- (65) Funke, K. Jump Relaxation in Solid Electrolytes. *Prog. Solid State Chem.* **1993**, *22*, 111–195.
- (66) Meyer, M.; Maass, P.; Bunde, A. Spin Lattice Relaxation: Non-BPP-Behavior by Structural Disorder and Coulomb Interactions. *Phys. Rev. Lett.* **1993**, *71*, 573–576.
- (67) Tse, D.; Hartmann, S. R. Nuclear Spin-Lattice Relaxation via Paramagnetic Centers without Spin Diffusion. *Phys. Rev. Lett.* **1968**, *21*, 511–514.
- (68) Ruprecht, B.; Billetter, H.; Ruschewitz, U.; Wilkening, M. Ultra-Slow Li Ion Dynamics in Li₂C₂ – On the Similarities of Results from ⁷Li Spin-Alignment Echo NMR and Impedance Spectroscopy. *J. Phys.: Cond. Matter* **2010**, *22*, 245901–1–245901–10.
- (69) Ruprecht, B.; Wilkening, M.; Uecker, R.; Heitjans, P. Extremely Slow Li Ion Dynamics in Monoclinic Li₂TiO₃ – Probing Macroscopic Jump Diffusion via ⁷Li NMR Stimulated Echoes. *Phys. Chem. Chem. Phys.* **2012**, *14*, 11974–11980.
- (70) Wagner, R.; Rettenwander, D.; Welzl, A.; Schmidt, W.; Fleig, J.; Wilkening, M.; Amthauer, G. A comparative study of the synthesis of coarse-grained Li_{6.4}M_{0.2}La₃Zr₂O₁₂ with M = Al, Ga, or Fe. **2015**, to be published.
- (71) Xu, M.; Park, M. S.; Lee, J. M.; Kim, T. Y.; Park, Y. S.; Ma, E. Mechanisms of Li⁺ Transport in Garnet-Type Cubic Li_{3+x}La₃M₂O₁₂ (M = Te, Nb, Zr). *Phys. Rev. B* **2012**, *85*, 052301–1–052301–5.
- (72) Awaka, J.; Takashima, A.; Kataoka, K.; Kijima, N.; Idemoto, Y.; Akimoto, J. Crystal Structure of Fast Lithium-ion-conducting Cubic Li₇La₃Zr₂O₁₂. *Chem. Lett.* **2011**, *40*, 60–62.
- (73) Adams, S.; Rao, R. P. Ion Transport and Phase Transition in Li_{7-x}La₃(Zr_{2-x}M_x)O₁₂ (M = Ta⁵⁺, Nb⁵⁺, x = 0, 0.25). *J. Mater. Chem.* **2012**, *22*, 1426–1434.
- (74) Rao, R. P.; Gu, W.; Sharma, N.; Peterson, V. K.; Avdeev, M.; Adams, S. In Situ Neutron Diffraction Monitoring of Li₇La₃Zr₂O₁₂ Formation: Toward a Rational Synthesis of Garnet Solid Electrolytes. *Chem. Mater.* **2015**, in press.
- (75) Wang, Y.; Klenk, M.; Page, K.; Lai, W. Local Structure and Dynamics of Lithium Garnet Ionic Conductors: A Model Material Li₅La₃Ta₂O₁₂. *Chem. Mater.* **2014**, *26*, 5613–5624.
- (76) Jalem, R.; Yamamoto, Y.; Shiiba, H.; Nakayama, M.; Munakata, H.; Kasuga, T.; Kanamura, K. Concerted Migration Mechanism in the Li Ion Dynamics of Garnet-Type Li₇La₃Zr₂O₁₂. *Chem. Mater.* **2013**, *25*, 425–430.
- (77) Miara, L. J.; Ong, S. P.; Mo, Y.; Richards, W. D.; Park, Y.; Lee, J.-M.; Lee, H. S.; Ceder, G. Effect of Rb and Ta Doping on the Ionic Conductivity and Stability of the Garnet Li_{7+2x-y}(La_{3-x}Rb_x)(Zr_{2-y}Ta_y)O₁₂ (0 ≤ x ≤ 0.375, 0 ≤ y ≤ 1) Superionic Conductor: A First Principles Investigation. *Chem. Mater.* **2013**, *25*, 3048–3055.
- (78) Meier, K.; Laino, T.; Curioni, A. Solid-State Electrolytes: Revealing the Mechanisms of Li-Ion Conduction in Tetragonal and Cubic LLZO by First-Principles Calculations. *J. Phys. Chem. C* **2014**, *118*, 6668–6679.

4 Zusammenfassung und Ausblick

Das Studium von Li-Bewegungsprozessen in Festkörpern ist mittlerweile ein wichtiges Gebiet der modernen Materialwissenschaften aufgrund der Anwendungsmöglichkeiten von Li-haltigen Festkörpern in neuen Energiespeichersystemen. NMR-spektroskopische Untersuchungen bieten in vielen Fällen einen verlässlichen Zugang zu den bulk-Transporteigenschaften mobiler Li-Ionen. Im Falle von nanokristallinen Proben ist es zudem möglich, die Li-Ionen in den Grenzflächenregionen separat von denen im Kristallinneren zu studieren. Mit den unterschiedlichen NMR-Techniken, zu denen vor allem die diversen Relaxationsmethoden gehören, können Li-Sprungprozesse mit Raten vom Sub-Hz bis in den GHz-Bereich erfasst werden. Generell eignen sich frequenzabhängige NMR-Messungen dazu, Informationen über die Dimensionalität, d. h. die Geometrie, des Diffusionsprozesses zu sammeln.

Die ^7Li NMR Relaxometrie ist ein vielseitiges, wenn auch teilweise zeitaufwändiges, Werkzeug zur Untersuchung kurz- und langreichweitiger Selbstdiffusionsprozesse in Festkörpern. Zusammen mit der Analyse von NMR-Linienformen, d. h. der Auswertung des sogenannten *motional averaging*, liefern NMR-relaxometrische Studien mitunter ein direktes Bild der atomaren Diffusionsprozesse (P4, P5, P6 und P7). Voraussetzung dafür sind Proben, die über den nötigen Temperaturbereich keine irreversiblen strukturellen Änderungen durchlaufen. Die erhaltenen Aktivierungsenergien können direkt mit Daten aus Leitfähigkeitsmessungen verglichen werden. In vielen Fällen ist es möglich, die absoluten Sprungraten aus NMR-Messungen mit Diffusionskoeffizienten aus Tracer-Messungen oder Leitfähigkeitsspektren zu vergleichen (P1 und Z1).

Idealer Weise enthält eine SLR-NMR-Studie T_1 - und $T_{1\rho}$ -Messungen, die über einen weiten Temperatur- und Frequenzbereich aufgenommen wurden. In der Praxis sind diese Methoden häufig durch die technischen Möglichkeiten oder die Temperaturstabilität der Materialien eingeschränkt. Für diese Fälle kann alternativ auf, z. B., 2D-MAS-EXSY-NMR (P1) und SAE-NMR (P4, P7) ausgewichen werden. Am Beispiel des LLZMoO (P7) konnte darüber hinaus gezeigt werden, in welcher Weise sich SAE-NMR eignet, Diffusionspfade aufzuzeigen und Beteiligungen einzelner Li-Plätze zu bestimmen. Es konnte gezeigt werden, dass die in der Literatur z. T. als unbeteiligt beschriebenen Plätze 24 *d* eindeutig zur hohen Diffusivität in oxidischen Granaten beitragen.

In den Publikationen P2 und P3 (siehe auch Z3) wurde die Struktur von den potentiellen Kathodenmaterialien Li_3VF_6 , Li_2NiF_4 , Li_2MnF_5 über hochauflösende 1D(2D)-MAS-NMR untersucht. Im Falle von $\beta\text{-Li}_3\text{VF}_6$ konnten ^6Li -2D-EXSY-NMR-Experimente entscheidend

dazu beitragen, die 1D-NMR-Spektren zu interpretieren, dass die NMR-Linien den fünf unterschiedlichen Gitterplätzen im Kristall zugeordnet werden konnten.

In allen untersuchten Proben der Titandioxid Nanoröhren wurden mittels $T_{1\rho}$ -Messungen eindeutige Hinweise für zwei zeitlich unterschiedlich ablaufende Li-Relaxationsprozesse gefunden. Dieses Verhalten ist bei der Probe E1 (elektrochemisch auf $x = 0.6$) am stärksten, nimmt bei C0 (chemisch auf $x = 0.3$) leicht ab und zeigt sich bei C1 (chemisch auf $x = 0.1$) nur noch schwach. Die den zwei Anteilen zugeordneten NMR-Relaxationsraten sind nicht temperaturabhängig. Dies zeigt den deutlichen Einfluss der paramagnetischen Ti-Zentren auf die Spin-Gitter-Relaxation. Im Allgemeinen werden im Falle quadrupolarer Relaxation (Li, $3/2$ -Spin) keine einfach-exponentiellen Transienten erwartet. In den vorliegenden Experimenten an den TiO_2 -Proben differieren die beiden erhaltenen Raten jedoch um mehrere Größenordnungen und müssen zwei unterschiedlichen Relaxationsprozessen zugeordnet werden. Die Anpassung der $T_{1\rho}$ -Transienten mit einer einfach gestreckten Exponentialfunktion liefert aus diesem Grunde keine verlässlichen Aktivierungsenergien.

In weiterführenden Studien sollte der Einfluss der Art der Li-Insertion (chemisch oder elektrochemisch), der Insertionsgrad und das Zusammenspiel von Aktivmaterial und Additiven (Leitruß und Binder) systematisch untersucht werden. Die vorliegenden temperaturabhängigen NMR-Messungen deuten auf eine irreversible Änderung der Proben während der Aufheizvorgänge hin. Zum Beispiel wäre eine elektrochemische Charakterisierung einer getemperten ($> 150\text{ °C}$) und einer nicht-getemperten Elektrode aufschlussreich. Diese Experimente könnten dazu beitragen, Fragen nach Änderungen des Li-Gehaltes und/oder der lokalen Umgebungen zu beantworten. Dies schließt auch die Frage ein, ob Li eher im bulk oder in Nähe der Oberflächenregionen mobil ist. Die Li-NMR-Linienformmessungen deuten darauf hin, dass die bulk-Li-Diffusivität für alle untersuchten Proben eher gering ausfällt.

Erste hochauflösende ^6Li -MAS-NMR-Messungen zeigen nur eine einzige NMR-Resonanz; weiterführende Messungen in Abhängigkeit von x sollen dazu beitragen, die lokale Umgebung der Li-Ionen näher zu bestimmen.

Literaturverzeichnis

- [1] Armand, M. and Tarascon, J.-M. *Nature* **451**, 652–657 (2008).
- [2] Tarascon, J.-M. *Philos. Trans. R. Soc. A Math. Phys. Eng. Sci.* **368**, 3227–3241 (2010).
- [3] Einstein, A. *Ann. Phys.* , 549–560 (1905).
- [4] Levitt, M. H. *Spin Dynamics: Basics of Nuclear Magnetic Resonance*. Wiley, Weinheim, 2nd edition (2008).
- [5] Blümich, B. *Essential NMR: for Scientists and Engineers*. (2005).
- [6] Bloembergen, N., Purcell, E. M., and Pound, R. V. *Nucl. Magn. Reson. Absorpt.* **37**, 679–712 (1948).
- [7] Solomon, I. *Phys. Rev.* **99**, 559–565 (1955).
- [8] Solomon, I. and Bloembergen, N. *J. Chem. Phys.* **25**, 261–266 (1956).
- [9] Bloembergen, N. *J. Chem. Phys.* **27**, 572–573 (1957).
- [10] Bloembergen, N. and Morgan, L. O. *J. Chem. Phys.* **34**, 842–850 (1961).
- [11] Richards, P. M. *Solid State Commun.* **25**, 1019–1021 (1978).
- [12] Richards, P. M. In *Phys. Superionic Conduct.*, Salamon, M., editor, volume 15 of *Topics in Current Physics*, 141–174. Springer Berlin Heidelberg (1979).
- [13] Chung, S. H. and Stevens, J. R. *Am J Phys* **59**, 1024–1030 (1991).
- [14] Heitjans, P. and Kärger, J., editors. *Diffusion in Condensed Matter*. (2005).
- [15] Baranovskii, S. D. and Cordes, H. *J. Chem. Phys.* **111**, 7546–7557 (1999).
- [16] Roling, B. *Phys. Chem. Chem. Phys.* **3**, 5093–5098 (2001).
- [17] Sidebottom, D. L. *Rev. Mod. Phys.* **81**, 999–1014 (2009).
- [18] Heitjans, P. and Kärger, J., editors. *Diffusion in Condensed Matter: Methods, Materials, Models*. Springer-Verlag Berlin Heidelberg (2005).

- [19] Jonscher, A. K. *Nature* **267**, 673–679 (1977).
- [20] Heitjans, P. *Solid State Ionics* **18 & 19**, 50–64 (1986).
- [21] Ailion, D. and Slichter, C. *Phys. Rev. Lett.* **12**, 168–171 (1964).
- [22] Ailion, D. D. and Slichter, C. C. *Phys. Rev.* **137**, A235 – A245 (1965).
- [23] Look, D. C. and Lowe, I. J. *J. Chem. Phys.* **44**, 2995–3000 (1966).
- [24] Rowland, T. J. and Fradin, F. Y. *Phys. Rev.* **182**, 760–770 (1969).
- [25] Wolf, D. *Phys. Rev. B* **10**, 2724–2732 (1974).
- [26] Fukushima, E. and Roeder, S. B. W. *Experimental Pulse NMR: A Nuts and Bolts Approach*. Westview Press; New Ed., Boulder (1993).
- [27] Allnatt, A. R. and Lidiard, A. B. *Atomic Transport in Solids*. Cambridge University Press (1993). Cambridge Books Online.
- [28] Hendrickson, J. R. and Bray, P. J. *J. Magn. Reson.* **9**, 341–357 (1973).
- [29] Waugh, J. S. and Fedin, E. I. *Sov. Phys. - Solid State* **4**, 1633–1636 (1963).
- [30] Spiess, H. W. *J. Chem. Phys.* **72**, 6755–6762 (1980).
- [31] Lausch, M. and Spiess, H. *J. Magn. Reson.* **54**, 466–479 (1983).
- [32] Böhmer, R. *J. Magn. Res.* **147**, 78–88 (2000).
- [33] Böhmer, R., Jörg, T., Qi, F., and Titze, a. *Chem. Phys. Lett.* **316**, 419–424 (2000).
- [34] Wilkening, M., Amade, R., Iwaniak, W., and Heitjans, P. *Phys. Chem. Chem. Phys.* **9**, 1239–1246 (2007).
- [35] Jeener, J. and Broekaert, P. *Phys. Rev.* **157**, 232–240 (1967).
- [36] Tang, X.-P. and Wu, Y. *J. Magn. Reson.* **133**, 155–165 (1998).
- [37] Böhmer, R., Jeffrey, K. R., and Vogel, M. *Prog. Nucl. Magn. Reson. Spectrosc.* **50**, 87–174 (2007).
- [38] Wilkening, M. and Heitjans, P. *ChemPhysChem* **13**, 53–65 (2012).
- [39] Bard, A. J. and Faulkner, L. R. *Electrochemical Methods: Fundamentals and Applications*. John Wiley & Sons, Inc., Weinheim, 2. edition (2001). Allen J. Bard, Larry R. Faulkner.
- [40] Heinze, J. *Angew. Chemie Int. Ed. English* **23**, 831–847 (1984).

- [41] Armand, M., Endres, F., MacFarlane, D. R., Ohno, H., and Scrosati, B. *Nat. Mater.* **8**, 621–629 (2009).
- [42] Epp, V., Nakhal, S., Lerch, M., and Wilkening, M. *J. Phys. Condens. Matter* **25**, 195402 1–7 (2013).
- [43] Xu, Z. and Stebbins, J. F. *Science (80-.)*. **270**, 1332–1334 (1995).
- [44] Hodeau, J., Marezio, M., Santoro, A., and Roth, R. *J. Solid State Chem.* **45**, 170–179 (1982).
- [45] Rietveld, H. M. *J. Appl. Crystallogr.* **2**, 65–71 (1969).
- [46] Dittrich, G. and Hoppe, R. *Zeitschrift für Anorg. und Allg. Chemie* **371**, 306–317 (1969).
- [47] Hellstrom, E. E. and Van Gool, W. *Solid State Ionics* **2**, 59–64 (1981).
- [48] Bielecki, A. and Burum, D. P. *J. Magn. Reson. Series A*, 215–220 (1995).
- [49] Guan, X. and Stark, R. E. *Solid State Nucl. Magn. Reson.* **38**, 74–76 (2010).
- [50] Kemp, T. F., Balakrishnan, G., Pike, K. J., Smith, M. E., and Dupree, R. *J. Magn. Reson.* **204**, 169–172 (2010).
- [51] Wilkening, M., Romanova, E. E., Nakhal, S., Weber, D., Lerch, M., and Heitjans, P. *J. Phys. Chem. C* **114**, 19083–19088 (2010).
- [52] Kohl, J., Wiedemann, D., Nakhal, S., Bottke, P., Ferro, N., Bredow, T., Kemnitz, E., Wilkening, M., Heitjans, P., and Lerch, M. *J. Mater. Chem.* **22**, 15819–15827 (2012).
- [53] Ren, Y., Hardwick, L. J., and Bruce, P. G. *Angew. Chemie Int. Ed.* **49**, 2570–2574 (2010).
- [54] Wagemaker, M., van de Krol, R., Kentgens, A. P. M., van Well, A. A., and Mulder, F. M. *J. Am. Chem. Soc.* **123**, 11454–11461 (2001).
- [55] Wagemaker, M., Kentgens, A. P. M., and Mulder, F. M. *Nature* **418**, 397–399 (2002).
- [56] Epp, V. and Wilkening, M. In *Handb. Solid State Batter.*, Dudney, N. J., West, W. C., and Nanda, J., editors, 133–190. WORLD SCIENTIFIC, 2nd edition (2015).
- [57] Rettenwander, D., Blaha, P., Laskowski, R., Schwarz, K., Bottke, P., Wilkening, M., Geiger, C. a., and Amthauer, G. *Chem. Mater.* **26**, 2617–2623 (2014).

A Verwendete Computerprogramme

Die im folgenden aufgeführten Programme wurden zur Aufnahme, Auswertung und Analyse der in dieser Arbeit präsentierten Ergebnisse, sowie deren Darstellung in geeigneter Form verwendet.

- **TopSpin 3.1** (Bruker BioSpin GmbH)
Aufnahme von NMR Experimenten an den Avance III Spektrometern; Berechnung und Phasenkorrektur der NMR Spektren (Fouriertransformation) sowie die Bestimmung der Linienbreiten. Export als ASCII-Dateien zur weiteren Analyse der Daten bzw. graphischen Darstellung.
- **WinDETA 5.73** (NOVOCONTROL Technologies GmbH & Co. KG)
Aufnahme aller impedanzspektroskopischen Experimente am Concept 80 System und Export der Messdaten.
- **IGOR Pro 6.36** (Wavemetrics Inc.)
Verarbeitung, Analyse, Auswertung und Darstellung aller Messdaten.
- **Diamond 3.2** (CRYSTAL IMPACT K. Brandenburg & M. Berndt GbR)
Visualisierung von Kristallstrukturen, sowie Auslesen von Sprungdistanzen.
- **CorelDRAW X5** (Corel Corporation)
Graphische Aufarbeitung von Darstellungen aus den oben genannten Programmen und Erstellung von Skizzen sowie Abbildungen in dieser Arbeit und allen Veröffentlichungen (siehe Anhang B).
- **T_EX Live 2014** (T_EX Users Group)
T_EX Textsatz-Distribution.
- **Texmaker 4.4.1** (Pascal Brachet)
L^AT_EX Editor mit dem diese Arbeit erstellt wurde.
- **Mendeley Desktop 1.14** (Mendeley Ltd.)
Verwaltung von Publikationen und Bereitstellung von Bibliotheken (*.bib) zur Erstellung des Literaturverzeichnisses im L^AT_EX Editor.
- **WSolids1 1.19.15** (Klaus Eichele)
Programm zur Simulation von Festkörper-NMR-Spektren.

B Konferenzbeiträge und Veröffentlichungen in Fachzeitschriften

B.1 Vorträge

1. **Ex situ NMR measurements of Li dynamics in TiO₂ anodes with an ordered hierarchical pore structure**
Bottke, P., Wilkening, M. »DocDay - Chemistry TU Graz – Österreich, 30.11.2012«
2. **Extremely slow Li exchange processes in diamagnetic Li₂ZrO₃ as monitored by ⁶Li 2D EXSY NMR**
Bottke, P., and Wilkening M. »Bunsentagung Karlsruhe – Deutschland, 09.05. – 11.05.2013«

B.2 Posterbeiträge

1. **Li diffusion in interface-dominated anodes of titanium dioxide**
Wittich O., Bottke, P., Wilkening, M., and Heitjans, P. »Bunsenkolloquium Goslar – Deutschland, 24.03. – 25.03.2011«
2. **Li diffusion in channel structured Li₂Ti₃O₇ as probed by NMR and impedance spectroscopy**
Heine, J., Bottke, P., Romanova, E., Wilkening, M., and Heitjans, P. »Solid State Ionics 18 Warschau – Polen, 03.07. – 08.07.2011«
3. **Revealing Li⁺ exchange in the β-modification of Li₃VF₆ by Li 2D MAS NMR spectroscopy**
Bottke, P., Nakhal, M., Lerch, M., Heitjans, P., and Wilkening, M. »Diffusion Fundamentals IV Troy, NY – USA, 21.08. – 24.08.2011« diffusion-fundamentals.org 16, 40 (2011).
4. **Li Diffusion in TiO₂ Nanotubes as Probed by NMR**
Bottke, P., Wittich, O., Wark, M., Wilkening, M., Ren, Y., and Bruce, P. G. »Bunsenkolloquium Hannover – Deutschland, 27.10. – 28.10.2011«

5. **Ex situ NMR Measurements of Li Dynamics in TiO₂ Anodes with an Ordered Hierarchical Pore Structure**
Bottke, P., Ren, Y., Bruce, P. G., and Wilkening, M. »GDCh-Fachtagung Darmstadt – Deutschland, 03.07. – 08.07.2012« *Z. Anorg. All. Chem.* **638**, 1607–1607 (2012).
6. **Li⁺ exchange in the β -modification of Li₃VF₆ as revealed by ⁶Li 2D MAS NMR spectroscopy**
Bottke, P., Nakhal, M., Lerch, M., Heitjans, P., and Wilkening, M. »MMCE Semmering – Österreich, 27.02. – 03.03.2013«
7. **Li ION DIFFUSION AND IONIC CONDCUTION IN NANOCRYSTALLINE, GLASSY AND NANOGLOSSY ALUMOLILICATE LiAlSi₄O₁₀**
Stanje, B., Bottke, P., Heitjans, P., Wilkening, M. »INCOME Krakau – Polen, 22.06. – 26.06.2014«
8. **Tracking down fas Li ions in composites of ionic liquids and Li salts by long-time ⁷Li NMR spin-lattice relaxation**
Stanje, B., Bottke, P., Hanzu, I. Marczewski, M.J., Johansson, P., Wilkening, M. »DIMAT Münster – Deutschland, 17.08. – 22.08.2014«

B.3 Veröffentlichungen in Fachzeitschriften

1. **Structure and dynamics of the fast lithium ion conductor "Li₇La₃Zr₂O₁₂"**
Buschmann, H., Dölle, J., Berendts, S., Kuhn, A., Bottke, P., Wilkening, M., Heitjans, P., Senyshyn, A., Ehrenberg, H., Lotnyk, A., Duppel, V., Kienle, L., and Janek J. *Phys. Chem. Chem. Phys.* **13**, 19378–19392 (2011).
2. **Synthesis of ternary transition metal fluorides Li₃MF₆ via a sol-gel route as candidates for cathode materials in lithium-ion batteries**
Kohl, J., Wiedemann, D., Nakhal, S., Bottke, P., Ferro, N., Bredow, T., Kemnitz, E., Wilkening, M., Heitjans, P., and Lerch, M. *J. Mater. Chem.* **22**, 15819–15827 (2012).
3. **Low-Temperature Synthesis, Characterization, and Stability of Spinel-Type Li₂NiF₄ and Solid-Solutions Li₂Ni_{1-x}Co_xF₄**
Kohl, J., Nakhal, S., Ferro, N., Bottke, P., Wilkening, M., Bredow, T., Heitjans, P., and Lerch, M. *Z. Anorg. Allg. Chem.* **639**, 326–333 (2013).
4. **Towards a lattice-matching solid-state battery: synthesis of a new class of lithium-ion conductors with the spinel structure**
Rosciano, F., Pescarmona, P. P., Houthoofd, K., Persoons, A., Bottke, P., and Wilkening, M. *Phys.Chem.Chem.Phys.* **15**, 6107–6112 (2013).

5. **Ultraslow Li Exchange Processes in Diamagnetic Li_2ZrO_3 As Monitored by EXSY NMR**
Bottke, P., Freude, D., and Wilkening, M. *J. Phys. Chem. C* **117**, 8114–8119 (2013).
6. **Li ion dynamics in TiO_2 anode materials with an ordered hierarchical pore structure – insights from ex situ NMR**
Bottke, P., Ren, Y., Hanzu, I., Bruce, P. G., and Wilkening, M. *Phys. Chem. Chem. Phys.* **16**, 1894–1901 (2014).
7. **DFT Study of the Role of Al^{3+} in the Fast Ion-Conductor $\text{Li}_{7-3x}\text{Al}_x^{3+}\text{La}_3\text{Zr}_2\text{O}_{12}$ Garnet**
Rettenwander, D., Blaha, P., Laskowski, R., Schwarz, K., Bottke, P., Wilkening, M., Geiger, C. A., and Amthauer, G. *Chem. Mater.* **26**, 2617–2623 (2014).
8. **Correlated fluorine diffusion and ionic conduction in the nanocrystalline F^- solid electrolyte $\text{Ba}_{0.6}\text{La}_{0.4}\text{F}_{2.4}$ — ^{19}F $T_{1(\rho)}$ NMR relaxation vs. conductivity measurements**
Preishuber-Pflügl, F., Bottke, P., Pregartner, V., Bitschnau, B., and Wilkening, M. *Phys. Chem. Chem. Phys.* **14**, 9580–9590 (2014).
9. **Novel amino propyl substituted organo tin compounds**
Pichler, J., Torvisco, A., Bottke, P., Wilkening, M., and Uhlig, F., *Can. J. Chem.* **92**, 565–573 (2014).
10. **Order vs. disorder—a huge increase in ionic conductivity of nanocrystalline LiAlO_2 embedded in an amorphous-like matrix of lithium aluminate**
Wohlmuth, D., Epp, V., Bottke, P., Hanzu, I., Bitschnau, B., Letofsky-Papst, I., Kriechbaum, M., Amenitsch, H., Hofer, F., and Wilkening, M. *J. Mater. Chem. A* **2**, 20295–20306 (2014).
11. **Small Change—Great Effect: Steep Increase of Li Ion Dynamics in $\text{Li}_4\text{Ti}_5\text{O}_{12}$ at the Early Stages of Chemical Li Insertion**
Schmidt, W., Bottke, P., Sternad, M., Gollob, P., Hennige, V., and Wilkening, M. *Chem. Mater.* **27**, 1740–1750 (2015).
12. **Li ion dynamics in nanocrystalline and structurally disordered Li_2TiO_3**
Brandstätter, H., Wohlmuth, D., Bottke, P., Pregartner, V., and Wilkening, M. *Z. Phys. Chem.* ahead of print, DOI: 10.1515/zpch-2014-0665 (2015).
13. **A simple and straightforward mechanochemical synthesis of the far-from-equilibrium zinc aluminate, ZnAl_2O_4 , and its response to thermal treatment**
Fabián, M., Bottke, P., Girman, V., Düvel, A., Da Silva, K. L., Wilkening, M. Hahn, H., Heitjans, P., and Šepelák, V. *RSC Adv.* **5**, 54321–54328 (2015).

14. **Access to spinel-type $\text{Li}_4\text{Ti}_5\text{O}_{12}$ nanoparticles prepared by low-temperature solid state synthesis**
Senna, M., Fabián, M., Turianicová, E., Briančin, J., Findoráková, L., Halamová, Dáša Kaňuchová, M., Bottke, P., Hirtler, G., Sternad, M., Wilkening, M., Baláž, P., and Šepelák, V. *J. Am. Ceram. Soc.* **submitted**, (2015).
15. **Ion dynamics in solid electrolytes: NMR reveals the elementary steps of Li^+ hopping in oxide garnets**
Bottke, P., Rettenwander, D., Amthauer, G., and Wilkening, M. *Chem. Mater.* **submitted**, (2015).

Lebenslauf



Dipl.-Chem. Patrick Bottke

Geburtsdaten: 02. September 1978 / D-31655 Stadthagen
Familienstand: Lebensgemeinschaft, 1 Kind
Nationalität: Deutsch

Ausbildung

- Februar 2012 - heute
Doktoratsstudium (Technische Chemie: *Dr. rer. nat.*)
Technische Universität Graz
Institut für Chemische Technologie von Materialien
„Zur Lithium-Selbstdiffusion in kristallinen Festkörpern“
Betreuer: Prof. Dr. Martin Wilkening
- Februar 2011 & März 2011
Forschungsaufenthalt in der Arbeitsgruppe von Prof. Dr. Peter G. Bruce
(St. Andrews, Schottland)
„Synthese und elektrochemische Charakterisierung von neuen TiO₂ Nanoröhren für Li-Ionen Batterien“
PROMOS Reisestipendium des DAAD
- Mai 2010 - Januar 2012
Promotionsstudium (Chemie: *Dr. rer. nat.*)
Institut für Physikalische Chemie & Elektrochemie
Leibniz Universität Hannover
„Festkörper-NMR und Impedanzspektroskopie an Li-Ionen-Leitern“
Betreuer: Dr. Martin Wilkening
- April 1999 - März 2010
Chemiestudium (Dipl.-Chem.)
Leibniz Universität Hannover
Abschluss: Diplom (15.04.2010)
„NMR-Spektroskopie an nanokristallinem, nanoglasigem und glasigem Eukryptit LiAlSiO₄“
- Juni 1998 - April 1999
Grundwehrdienst
- August 1991 - Juni 1998
Ratsgymnasium Stadthagen
Abschluss: Abitur (24.06.1998)

Berufserfahrung

Februar 2012 – heute	Technische Universität Graz Institut für Chemische Technologie von Materialien Universitätsassistent (Lehre, Forschung & Administration) außerdem: Verantwortlicher für Festkörper-NMR (Auftragsmessungen, Schulungen von neuen Mitarbeitern & Instandhaltung der Spektrometer)
Mai 2010 – Januar 2012	Leibniz Universität Hannover Institut für Physikalische Chemie & Elektrochemie Wissenschaftlicher Mitarbeiter
Februar 2005 – April 2010	Messeagentur Inter Cris GmbH Teamleiter (freiberuflich) Messen, Events & Hauptversammlung von Aktiengesellschaften
Februar 2008 – April 2010	Golfversand Hannover GmbH Produktberatung (inkl. Custom Fitting) & Verkauf
Dezember 2009 – Januar 2010	Leibniz Universität Hannover Institut für Physikalische Chemie & Elektrochemie Studentische Hilfskraft (Lehraufgaben)
Juli 2001 – Dezember 2008	REWE Großflächengesellschaft mbH Logistiker (Bestellung & Wareneingang)
April 2004 – November 2007	Medizinische Hochschule Hannover Institut für Zelluläre Chemie Studentische Hilfskraft (Lehraufgaben)
Juni 2003 – August 2003	Solvay GmbH Praktikant (Naturstoffsynthese / Women's Health)
August 1999 – Oktober 2002	Everlast Deutschland GmbH Berater (freiberuflich)

Väterkarenz

Juni 2014 – September 2014 Österreichische Version der Elternzeit

Sprachkenntnisse

Englisch: Verhandlungssicher
Französisch: Grundkenntnisse

EDV-Kenntnisse

MS Office, LaTeX, IGOR Pro, Corel Draw, TopSpin, MestReNova,
WinDETA, Diamond, WSolids1, dmfit, EC-Lab und Maccor Software

Hobbies

Basketball und Reisen

Graz, 8. August 2015

